Engineering topology and correlation in epitaxial thin film kagome metals

by

Minyong Han

B.S., Columbia University in the City of New York (2015)

Submitted to the Department of Physics
in partial fulfillment of the requirements for the degree of

Doctor of Philosophy

at the

MASSACHUSETTS INSTITUTE OF TECHNOLOGY

September 2022

Author .....
Department of Physics
Aug 03, 2022

Certified by .....
Joseph G. Checkelsky
Associate Professor of Physics
Thesis Supervisor

Accepted by .....
Deepto Chakrabarty
Associate Department Head of Physics

Engineering topology and correlation in epitaxial thin film kagome metals

by

Minyong Han

Submitted to the Department of Physics
on Aug 03, 2022, in partial fulfillment of the
requirements for the degree of
Doctor of Philosophy

Abstract

Along with the Landau paradigm of phase transitions, topology has been recognized as an important metric of classifying condensed matter systems, offering successful descriptions for systems with nontrivial energy gaps or protected band degeneracies. As much as topology has risen in significance, the study of correlation has also provided crucial insights for a number of may-body phenomena realized when the inter-particle interactions dominate the kinetic energies of individual constituents. The kagome lattice is a generalized lattice model whose characteristic atomic arrangement produces both topological Dirac bands and correlated flat bands. In search of its material realizations, kagome metals, a class of intermetallics containing the two-dimensional kagome networks of transition metal atoms, have shown promise in faithfully manifesting the original lattice model in their bulk electronic structures.

In this thesis, we present our works on engineering topology and correlation in two representative kagome metals, FeSn and Ni_3In, stabilized in epitaxial thin film form. We characterize via transport, thermodynamic, and spectroscopic probes the emergent quantum phenomena arising from the key band structure singularities and further exploit various thin film tuning parameters to manipulate them. With systematic control of chemical potential and spin structure, we elucidate the pivotal roles of the lattice-driven Dirac and flat bands in generating magnetic instabilities and topological edge modes. We also demonstrate how the kagome spectrum reconstructs upon intense inter-kagome hybridization or broken crystallographic symmetry, eventually giving rise to new types of flat bands and their derived anomalies. To track the origins of these, we incorporate films into spintronic or ion-battery devices and monitor their responses under different conditions. These results will construct an important framework in designing topological and correlated electronic states and further driving them towards the regime suitable for functional device applications.

Thesis Supervisor: Joseph G. Checkelsky
Title: Associate Professor of Physics

Acknowledgments

This thesis research would not have been possible without invaluable supports from many people. First and foremost, I would like to express my deepest gratitude to my advisor Prof. Joe Checkelsky. I am extremely blessed to have been educated under his scientific guidance that encompasses the entire process of identifying intellectually-inspiring problems, designing experimental protocols, performing the experiments the right way, and finally communicating the results in a way that engages the most effectively with the audience. The approach that Joe taught me will be one of the most powerful assets for my life, not restricted to the research in condensed matter physics. I also appreciate him for his moral support that helped me survive through a tide after another in the past six years. In both scientific and non-scientific contexts, he has kept me up with caring advice at times or playful conversations at other times. I also wish to thank Prof. Riccardo Comin and Prof. Vladan Vuletic for serving as my thesis committee members.

I thank the former and current members of the Checkelsky group as well as some of my closest collaborators. Among all, I am most deeply indebted to Hisashi Inoue for his mentorship during the early stage of my PhD journey. For most of my first experiments in the group − the first film growth, the first transport measurement, the first Maglab trip, and many more − he was always there with me patiently helping a young graduate student learn every necessary step the proper way. His presence during the formative phase of my career will have an everlasting impact on my life. I am grateful to Takehito Suzuki, Linda Ye, and Aravind Devarakonda for passing down their profound knowledge and experience on material growth and characterization when I first joined the lab. I thank Linda Ye in particular for pioneering some of the foundational works that motivated my experiments. I appreciate Caolan John for sharing with me all the up and down moments in the latter part of my PhD journey. In hindsight, I truly cherish the memories of us as a duo going through day-to-day grinds of research, continuously discussing over data and brainstorming new ideas. The works presented here are made possible thanks to active theory inputs from Shiang

Fang (within the group), Madhav Ghimire (from Tribhuvan Univ.), Manuel Richter (from IFW Dresden), and Junwei Liu (from HKUST). As well as their immense supports on the subject matters of research, their profound expertise and whole-hearted mindset to science in general have always been inspiring to me. I enjoyed all the scientific discussions and casual coffee-talks I had with Takashi Kurumaji, Mallika Randeira, Alejandro Ruiz, Jingxu Kent Zheng, Shu Yang Frank Zhao, Junbo Zhu, Paul Neves, Joshua Wakefield, Yuki Tatsumi, Pheona Williams, Max Debbas, Boris Tsang, Alan Chen, and Ryan McTigue.

I wish to acknowledge contributions from external supports. I would like to thank Mun Chan and Dave Graf from the National High Magnetic Field Laboratory for their technical assistances on high field experiments. I thank Charlie Settens, Alan Schwartzman, and Kevin Woller for managing shared characterization facilities. I appreciate SVTA for their product development and instrument maintenance for the MBE chamber in 13-2080, the bread and butter of my thesis research. I am glad that the chamber sustained till I make it to the finish line without any catastrophic crash. I thank ACE for their prompt and high quality TEM measurements. I wish to express my gratitude to Prof. Philip Kim at Harvard for letting me use the heterostructure fabrication setup for one of my projects (and also for inspiring me to study condensed matter physics in the early days).

I would like to thank people in the CMX community. I appreciate Prof. Nuh Gedik for providing me appropriate guidance as an academic advisor. I thank Monica Wolf and Gerry Miller for their administrative and mental supports. Among all colleagues in CMX, special thanks go to Heunmo Yoo an Dongsung Choi for sharing many difficult moments with me in the past six year.

Finally, I would like to thank my parents, grandmother, and brother for their love and support. I would like to appreciate my wife Eunice for being on my side thus far and forever. This has been a long journey and I would not have reached at this point without helps from these people.

Contents

List of Figures

List of Tables

Chapter 1

Introduction

1.1 Topology as a metric of phase classification

The traditional paradigm of phase transition in condensed matter systems is based on the symmetries of the order parameters. A solid−liquid phase boundary can be delineated by the presence or absence of lattice translational symmetry, whereas a ferromagnet−paramagnet transition is accompanied by the change in time-reversal symmetry. Within this framework, two systems with the identical symmetry parameters are assumed to be adiabatically connected to each other with no phase transition between them. In a broader context, however, symmetry is not the unique criterion for classifying different objects. In mathematics, topology characterizes the properties of a geometric object robust against various deformations. For instance, any closed surface can be assigned a genus $g = 0, 1, 2, \ldots$, corresponding to the number of holes in the structure, which cannot be changed unless by creating or removing a hole (Fig. 1-1(a)). This idea has been formalized in the Gauss−Bonnet theorem such that $1 - g = \frac{1}{4\pi} \int K_G ds$, where K_G is the Gaussian curvature at the surface (Fig. 1-1(b)) [3].

In recent decades, the concept of topology has been introduced as a new metric of classifying electronic phases of matter. One of the central ideas was that one can define a set of mathematical invariants in the electronic structure of a solid associated with the Berry curvature of the underlying wavefunction. The invariants and the Berry curvature can be understood as momentum space analogs of g and K_G. In

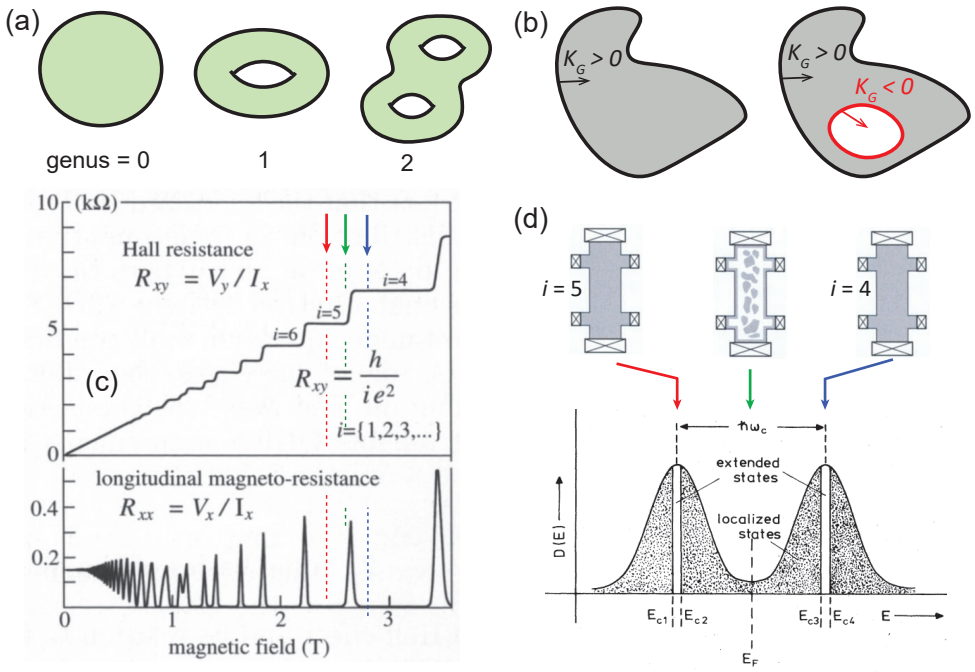

Figure 1-1: **Topological classification of electronic states**

(a) Geometric objects with genus $g = 0$, 1, 2. (b) Schematic description of the Gauss-Bonnet theorem. (c) The quantum Hall effect in a two-dimensional electronic system. (b) Schematic of the density of states in the Landau level spectrum (bottom) and the real space charge distributions at corresponding energies (top). The features that are correlated between (c) and (d) are marked with the color-coded arrows. (c),(d) are adapted from [1, 2].

this paradigm, two states with distinct topological invariants are assumed to have a well-defined phase boundary between them even when they have the identical symmetry properties. This mathematical concept provided key insights in interpreting the quantum Hall effect, in which each Hall plateau with the quantized conductance $\sigma_{xy} = i(e^2/h)$ is associated with the topological index of the Landau level (LL) wavefunction (Fig. 1-1(c),(d)) [4, 5]. Furthermore, it was discovered that the quantization of σ_{xy} originates from a series of chiral edge modes circulating around an insulating bulk when the chemical potential crosses the energy gap between two consecutive LLs. This realization constituted an important insight that in general an energy gap separating two or more topologically distinct states generate topologically protected surface/edge modes via bulk−boundary correspondence.

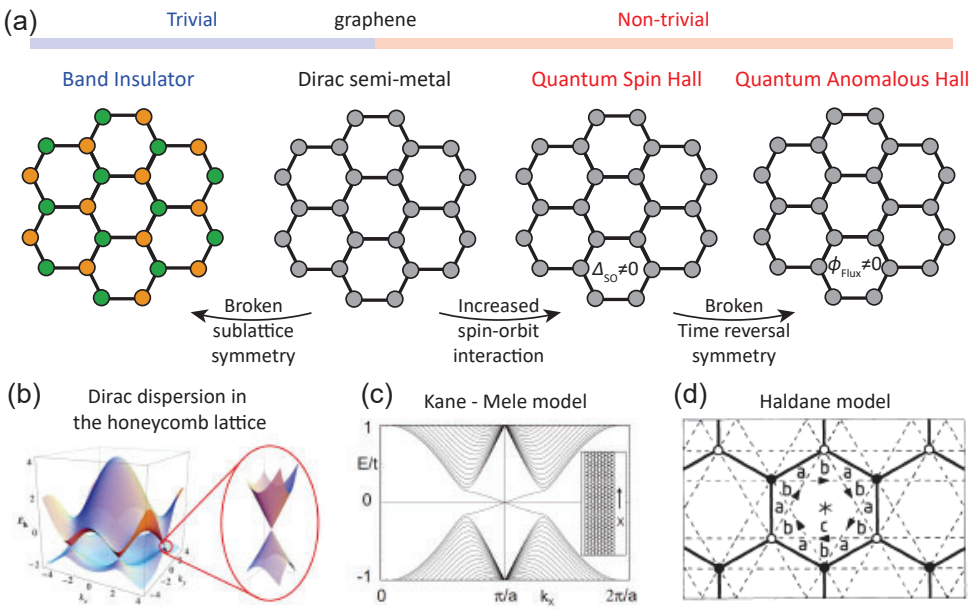

Figure 1-2: **Topological phases on the honeycomb lattice**

(a) Cascade of topological phase transitions in the honeycomb lattice triggered by lattice distortion (left), spin-orbit coupling (middle), or time-reversal symmetry breaking (right). (b) The Dirac band in the honeycomb lattice [6]. (c) The quantum spin Hall phase and the helical edge modes predicted from the Kane-Mele model [7]. (d) The honeycomb lattice with a staggered flux pattern studied in the Haldane model [8]. This model predicted a phase conceptually equivalent to the quantum anomalous Hall phase.

With the quantum Hall effect being a pioneering example, a great amount of work has been done towards predicting and stabilizing other topological electronic states realized under zero magnetic field. One of the leading candidate platforms has been the honeycomb lattice. With the symmetry-protected Dirac crossing in the band structure (Fig. 1-2(b)) [6], the honeycomb lattice was shown to be a candidate to generate nontrivial energy gaps. Along this line, it was predicted from the Kane-Mele model that a sizable spin-orbit coupling (SOC) can in fact open a topologically nontrivial gap at the Dirac point in the honeycomb lattice, giving rise to the quantum spin Hall (QSH) phase with two helical modes counter-propagating around the edge of the insulating bulk (Fig. 1-2(a),(c)) [7]. This phase is characterized by the topological index $Z_2 = 1$, distinguished from the ordinary $Z_2 = 0$ state realized when the Dirac crossing is gapped trivially via *e.g.* broken sublattice symmetry. Extending

this further, with additional breaking of time-reversal symmetry, the QSH phase is anticipated to give way to a different type of topological phase called the quantum anomalous Hall (QAH) phase characterized by the Chern index $C = 1$ and a chiral edge mode − the process considered earlier in the Haldane model by assuming a staggered flux pattern in the honeycomb lattice (Fig. 1-2(a),(d)) [8]. Inspired by these predictions, there have been active efforts to experimentally realize the QSH and QAH phase in graphene, the two-dimensional honeycomb network of carbon. One of the major challenges, however, was the small SOC strength of carbon ($\sim$40 μeV); this has been overcome in part in certain van der Waals heterostructures [9]. While graphene in its isolated form may not harbor the required material parameters, the extensive studies on the honeycomb lattice and its related platforms have established a critical insight that in general an inclusion of large SOC to a system with a Dirac-like band degeneracy has a potential to drive the system into a topological phase.

Though studied initially in the honeycomb lattice platform, the first experimental realization of the zero-field topological phase appeared in narrow gap semiconductors containing heavy mass elements more likely to generate large SOC. It was identified in certain Bi-based semiconductors that some of the energy gaps therein originate from the SOC-driven band mixings and as a result show inverted band orderings in vicinity of the gap (Fig. 1-3(a), right) [13]. This realizes a situation where the eigenstates of the conduction band minimum (or the valence band maximum) manifest a dominant orbital character of what originally accounts for the valence band (or the conduction band) far away from the gap − the energy hierarchy that cannot be realized in other ordinary semiconductors (Fig. 1-3(a), left). This process of band inversion involves a gradual closure of an ordinary gap and a subsequent reopening of an inverted gap as SOC strength is increased in the system. The zero-gap state dividing the two regimes (Fig. 1-3(a), middle) is conceptually equivalent to the Dirac state in the honeycomb lattice. Furthermore, the regime of an inverted gap is found to harbor a non-zero Z_2 index, also similar to the honeycomb lattice with strong SOC. This scheme of generating nontrivial topology has led to the discovery of a Dirac surface state in a three-dimensional topological insulator $Bi_2(Se{:}Te)_3$ (Fig. 1-3(b)) [11, 14] and helical

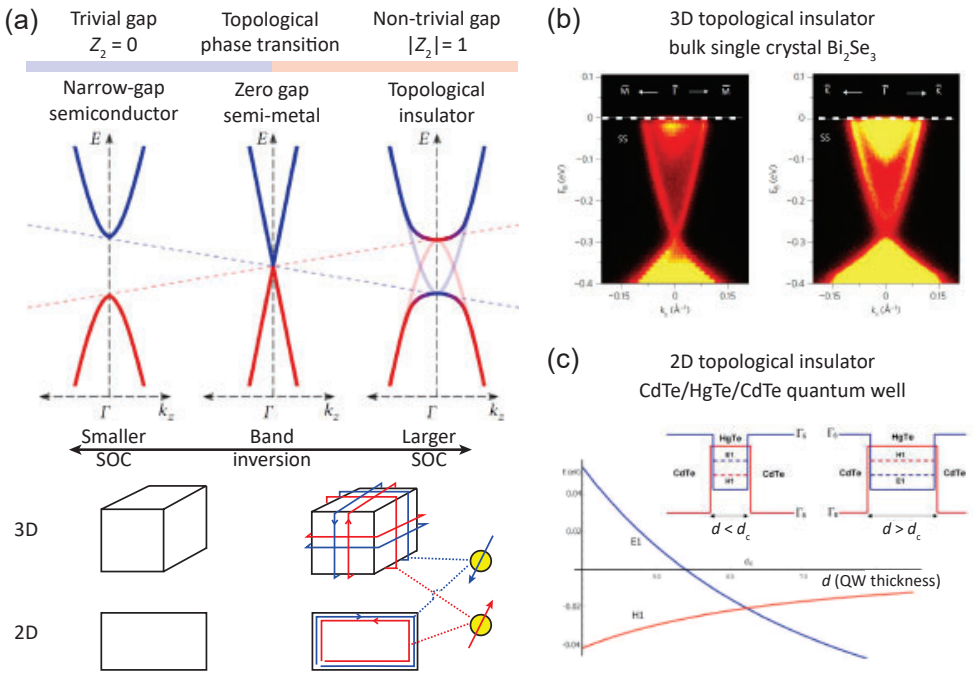

Figure 1-3: **Topological phase transition via band inversion**

(a) Top: Schematic of topological phase transition via band inversion driven by the spin-orbit coupling (adapted from [10]). Bottom: Schematic depiction for the presence (or absence) of helical surface/edge modes in the $Z_2 = 1$ (or $Z_2 = 0$) state in three- and two-dimensional systems. Up/down spin directions are locked with the mode propagation directions and color-coded red/blue. (b) Photoemission spectra of a three-dimensional topological insulator Bi_2Se_3 [11]. (c) Schematic of band orderings in a CdTe/HgTe/CdTe quantum well with different HgTe thicknesses d (adapted from [12]). A band inversion is expected for d above the critical thickness d_c.

edge modes in quantum wells of CdTe/HgTe/CdTe (Fig. 1-3(c)) [12, 15]. We note that the band inversion in the latter is assisted by the characteristic band alignment of the three constituent layers.

1.2 Correlation at the origin of emergent phenomena

As much as topology has risen to great importance in the past decades, the study of correlation has developed with a longer history, providing foundational insights for various emergent phases arising from different inter-particle interactions. These include the Stoner ferromagnetism from the Coulomb repulsion between itinerant elec-

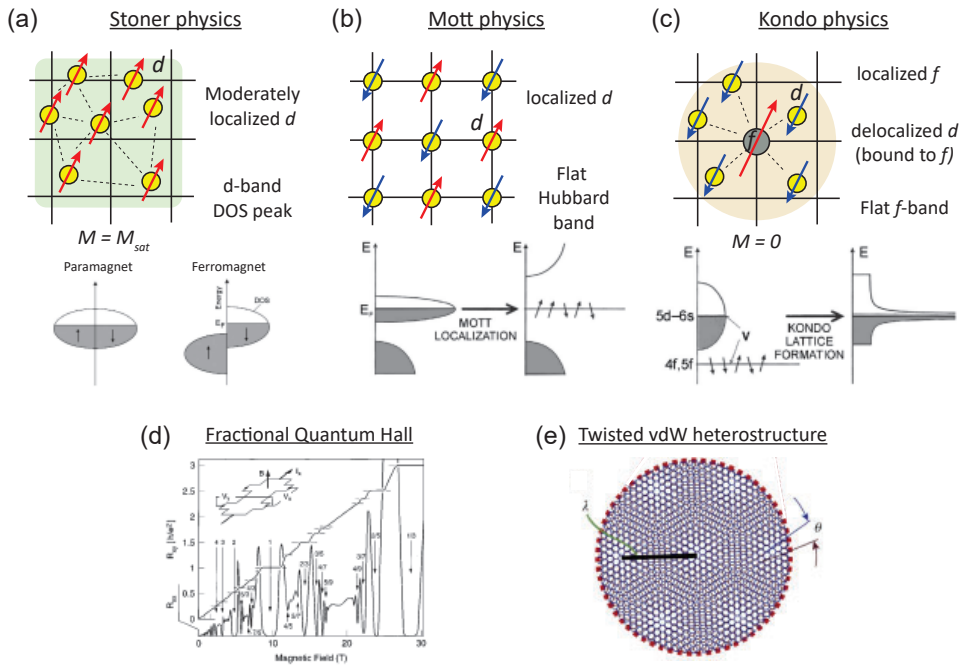

Figure 1-4: **Emergent phases from electronic correlations**

Schematic depictions of real space charge/spin arrangements for (a) the Stoner ferromagnet, (b) the Mott insulator, and (c) the Kondo singlet. Bottom insets in (a) (adapted from [17]) and (b),(c) (from [18]) are schematic band structures that give rise to the respective phenomena. (d) The fractional quantum Hall effect in a two-dimensional electronic system [19]. (e) Schematic of the magic angle twisted bilayer graphene (adapted from [20]).

trons, the Mott transition from the on-site energy of localized d-electrons ($U_{\mathrm{on-site}}$), and the Kondo hybridization from the virtual exchange interaction between localized f-electrons and itinerant d-electrons (U_{d-f}) [16].

Whereas each phenomenon concerns a distinct type of interaction, a general consensus is that these effects are enhanced when the interaction energy of an ensemble of electrons (parametrized by the generic interaction parameter U) dominates the kinetic energy of individual electrons (parameterized by the generic hopping parameter t) – the condition likely to be satisfied in a flat band with suppressed dispersion in momentum space and localized wavefunction in real space. For example, the Mott transition is preceded by the Hubbard splitting of the flat d-band with $U_{\mathrm{on-site}} > t$ enforcing the single occupancy of electrons per atomic site. The generation of the

Kondo hybridization gap is also aided by the extreme flatness of the f-band. Once the itinerant electrons (with $U_{d-f} < t$ originally) bind to localized f-moments, the effective t of the many-body Kondo singlet becomes dramatically suppressed and the system eventually satisfies $U_{d-f} > t$. In addition, Stoner ferromagnetism, though itinerant in nature, can still be projected onto this paradigm in that the magnetic instability is most enhanced when the Fermi level (E_{F}) crosses the density of states (DOS) peak, typically expected at the energy the band is relatively flat. Under such conditions, the net exchange energy gain tends to be bigger than the net kinetic energy loss. Aside from the flat bands originating from the d- or f-orbital degrees of freedom, there exist a variety of methods to realize flat bands. For example, a cascade of interaction-driven fractional quantum Hall states can be realized when electrons are first confined to the Landau levels, a type of a flat band generated by magnetic field [19]. More recently, a number of correlated phases have been discovered in magic angle twisted bilayer graphene, in which a flat band from the Moire localization is anticipated [20, 21]. Furthermore, there has been a growing interest in constructing a generalized lattice model that can universally produce flat bands and their associated correlated phenomena, even in the absence of compact atomic orbitals, high magnetic field, or inter-layer twist angle [22–27].

1.3 Lattice-driven topology and correlation in the kagome lattice

In this thesis, we explore one example of a two-dimensional lattice model whose characteristic atomic arrangement deterministically generates Dirac and flat bands in the electronic structure. We examine the implications of these symmetry-enforced band singularities in giving rise to different types of topological and correlated phases.

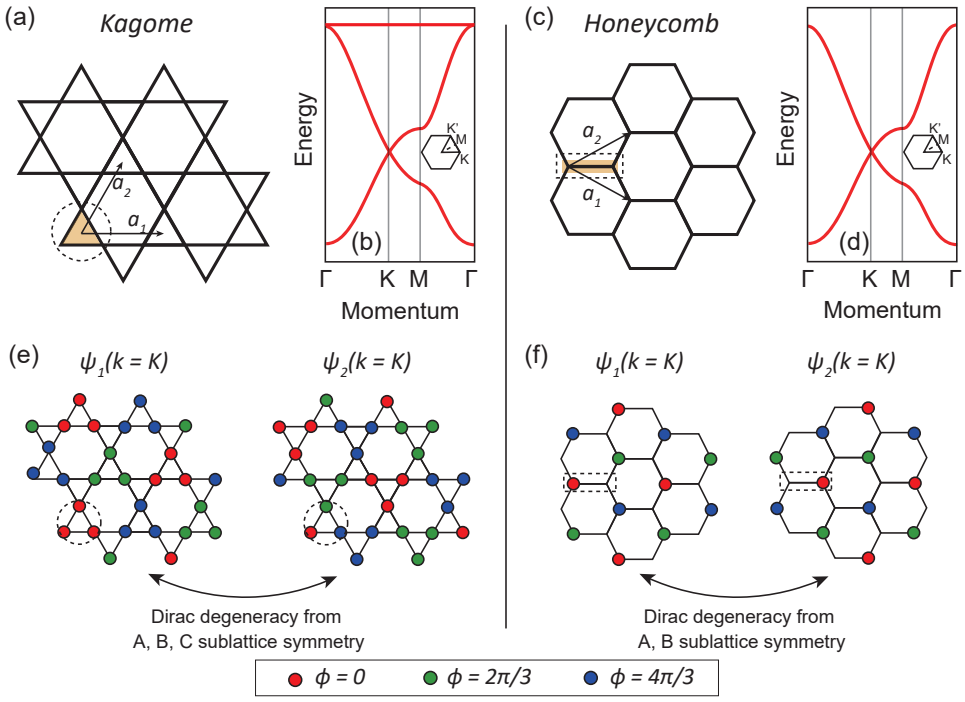

Figure 1-5: **Dirac electrons in the kagome lattice and the honeycomb lattice**

Schematic (a) lattice structure and (b) electronic band structure of the kagome lattice. Schematic (c) lattice structure and (d) electronic band structure of the honeycomb lattice. Phase arrangements of the degenerate eigenstates at Dirac point in (e) the kagome lattice and (f) the honeycomb lattice.

1.3.1 Symmetry-enforced band structure singularities

The kagome lattice is a two-dimensional hexagonal network of corner-sharing triangles (Fig. 1-5(a)). This lattice structure can be viewed equivalently as three interpenetrating triangular sublattices originating from the three atoms in the unit cell; we define this as A, B, C sublattice degrees of freedom in the kagome lattice. Many structural similarities can be identified between the kagome lattice and the honeycomb lattice. In a similar fashion as in the kagome lattice, the honeycomb lattice can be constructed with two interpenetrating triangular sublattices from its two basis atoms; we define this as A, B sublattice degrees of freedom in the honecomb lattice (Fig. 1-5(c)). In both lattice systems, the atoms within the basis are indistinguishable (enclosed in the dashed lines in Fig. 1-5(a),(c)) and the sublattices can be mapped onto each other via various rotation and mirror symmetry operations belonging to the D_{6h} point group.

The band structure of the kagome lattice can be obtained from a simple tight-binding Hamiltonian:

$$H_{[i,j]} = \sum t_{ij}(c_i^\dagger c_j + h.c.) \tag{1.1}$$

where t is the nearest neighbor hopping integral, $c^\dagger$ (c) is the creation (annihilation) operator, and $h.c.$ denotes the Hermitian conjugate of $c_i^\dagger c_j$. i and j are indices for the sites involved in the hopping process. As shown in the schematic band structure in Fig. 1-5(b), the kagome lattice contains three bands originating from its three sublattices, two of them forming Dirac branches with a degeneracy at the K-point and the other one forming a flat band. The flat band is energetically isolated from the Dirac band except at the quadratic band touching at the Γ-point. The energy of the flat band is higher or lower than the Dirac band depending on the sign of t, which in real materials is determined by the detailed orientation and phase arrangement of the orbitals in the lattice. By comparison, the honeycomb lattice harbors a Dirac band, accounted for by its two sublattice degrees of freedom, and no other band is expected (Fig. 1-5(c)).

Fig. 1-5(e) displays schematic real space phase arrangements of the two degenerate eigenstates at the Dirac point in the kagome band structure (ψ_1 and ψ_2), with the phase $\phi = 0$, $2\pi/3$, and $4\pi/3$ color-coded with red, green, and blue, respectively [28]. Focusing first on the local phase arrangement within the basis, the three basis atoms in ψ_1 and ψ_2 (dashed circles in Fig. 1-5(e)) are in-phase and out-of-phase, respectively, thus forming bonding- or anti-bonding-type molecular orbital states depending on the sign of t. Disregarding the kinetic energy contribution from the crystal momentum, the energies of the isolated eigenbases will be different. When they are tiled periodically with $\vec{k} = \vec{K}$ phase oscillations, however, ψ_1 and ψ_2 eventually harbor the same energy; the overall phase arrangements in the two states become indistinguishable from each other by a combination of inversion symmetry (P) and translation symmetry (T). Expressed differently, the A vs. B vs. C sublattice symmetry of the kagome lattice protects the combined PT symmetry and guarantees the Dirac cross-

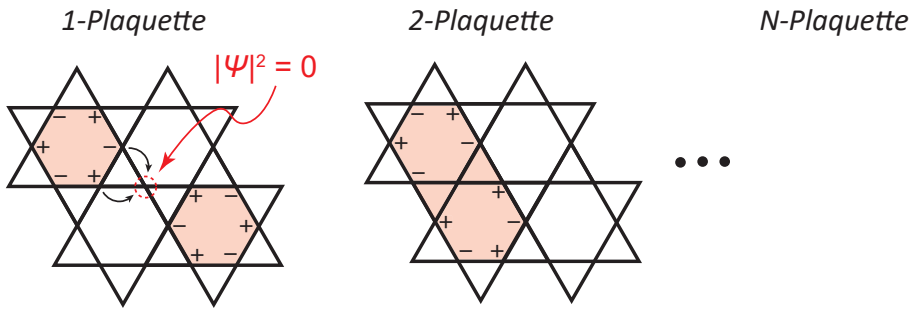

Figure 1-6: **Flat band wavefunctions in the kagome lattice**

Schematic of localized eigenstates for the flat band electrons in the kagome lattice. Destructive phase interference of hopping pathways localize charge clusters containing 1, 2, ..., N kagome hexagons (or plaquettes).

ing in the band structure. We compare this to the equivalent momentum eigenstates of the Dirac electrons in the honeycomb lattice (Fig. 1-5(f)). There, ψ_1 and ψ_2 show A- and B-sublattice polarization, respectively, and the degeneracy of the two states are guaranteed by the A vs. B sublattice symmetry, analogous to the case of the kagome lattice manifesting the three-atom-basis version of this [28].

In addition to the Dirac band, the kagome lattice hosts a flat band in the band structure. The flat band in the kagome lattice is generated by the destructive interference of electronic hopping pathways in the frustrated lattice geometry, as will be described below. The absence of dispersion in the momentum space leads to a wavefunction localization in real space and a sharp peak in DOS in the energy spectrum. The momentum eigenstates at each $\vec{k}$ extracted from the tight-binding calculations do not intuitively represent the manner in which the electrons are localized; $\vec{k}$, by definition, generates a non-zero phase oscillation in the real space. However, one can construct a linear combination of multiple momentum eigenstates each weighted by respective phase factor and construct real space representations of the flat band [29]. This process can also be viewed as a calculation of the localized Wannier state from the Fourier transform of the Bloch states.

In Fig. 1-6, we present schematics of some of the localized eigenstates. The most fundamental form is the 1-plaquette state with the phase factor alternating

between ±1 within the kagome hexagon. An intriguing observation can be made at the nearest neighbor site outside the kagome hexagon (red dashed circle in Fig. 1-6). There, the wavefunction amplitude is effectively cancelled (*i.e.* $|\psi^2| = 0$) by the two frustrated hopping pathways from the kagome hexagons with +1 phase and -1 phase. The same phenomenon occurs at all six equivalent sites and this as a result traps the charge clusters within the kagome hexagons. We note that the 1-plaquette state is not the unique eigenstate of the flat band electrons. There exist other possible plaquette states with n = 2, 3, ... , N kagome hexagons enclosed within a localized charge cluster, which can be constructed by formulating the Wannier state from the momentum eigenstates differently.

The Dirac and flat bands in the kagome lattice, generated from the lattice symmetry, are expected to be robust against external perturbations (*e.g.* disorder, thermal fluctuation, and atomic degrees of freedom). Such robustness makes the kagome lattice a promising platform to explore various topological and correlated states born of these band singularities.

1.3.2 Topological phases in the kagome lattice

As described in section 1.1, the Dirac crossing, a symmertry-protected zero-gap state, situates the honeycomb lattice on the verge of various topological gap openings. The Dirac band in the kagome lattice, analogous to that in the honeycomb lattice, also has a potential to produce different gapped states at the Dirac point with distinct topological characters. In this section, we introduce two types of low energy phases in the kagome lattice, one nontrivial phase arising from the interplay of magnetism and SOC and the other trivial phase arising from a lattice distortion.

We first consider the case of ferromagnetic kagome lattice with SOC (Fig. 1-7(a)) using the modified tight-binding Hamiltonian:

$$H_{[i,j]} = \sum (t_{ij} + i\lambda\nu_{ij})(c^{\dagger}_{i,\uparrow}c_{j,\uparrow} + h.c.) \tag{1.2}$$

where λ is the intrinsic SOC strength and ν_{ij} = +1 (-1) for counter-clockwise (clock-

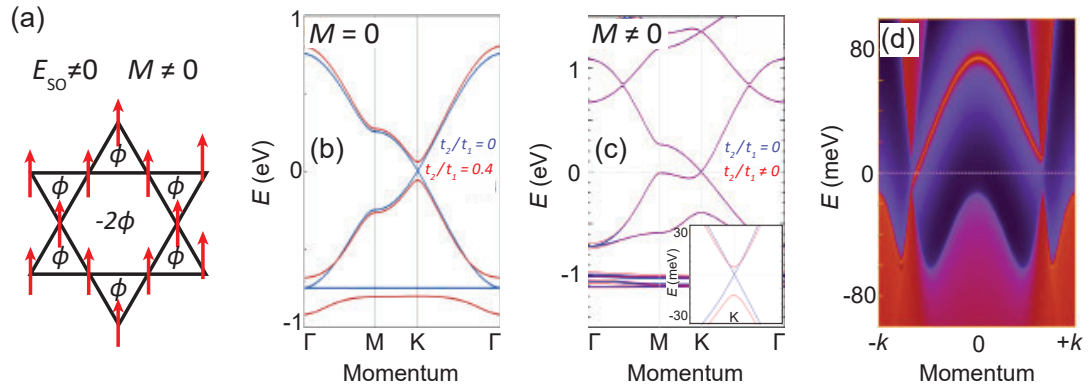

Figure 1-7: **Nontrivial gap openings on the ferromagnetic kagome lattice**

(a) Schematic of the ferromagnetic kagome lattice with spin-orbit coupling. Effective magnetic flux ϕ (or -2ϕ) threads through the kagome triangles (or hexagons). The band structure of the (b) nonmagnetic and (c) ferromagnetic kagome lattices calculated with and without spin-orbit coupling. (d) One-dimensional projection of the band structure in (c), manifesting a chiral edge mode. (b)-(d) are adapted from [30].

wise) hopping direction assuming the magnetization ($\vec{M}$) is along the $+z$. The chirality of ν_{ij} is set by the relative orientation of the local crystal field ($\vec{E}$) and $\vec{M}$. A relativistic electron hopping along the bonds in the kagome lattice experiences distinct crystal environments on the hexagon side and the triangle side. Such imbalance results in the non-zero $\vec{E}$ acting as a spin-dependent magnetic field in the relativistic regime and the overall the sign of the interaction is determined by $(\vec{k} \times \vec{E}) \cdot \vec{M}$. The SOC term in the Hamiltonian ($i\lambda\nu_{ij}$), being an imaginary quantity, gives rise to the phase accumulation equivalent to the effective magnetic flux $\Phi = 3\tan^{-1}(\lambda/t)$ (or -2Φ) threading through the triangles (or hexagons). The spatial variation of flux is related to the bond-dependent $\vec{E}$ direction in the lattice. Such staggered flux pattern (with the net flux across the unit cell summing up to 0) is conceptually similar to that assumed in the Haldane model.

Fig. 1-7(b) shows an example tight-binding band structure of a $M = 0$ state with ($\lambda = 0.1$ eV; red) and without (λ =0; blue) SOC and $t = 0.25$ eV [30, 31]. We find that gaps are created at the Dirac point and the Dirac−flat quadratic band touching point. The low energy band structure near the gapped Dirac point is expected to resemble that in the QSH phase from the Kane−Mele model. We now consider a $M \neq 0$ state.

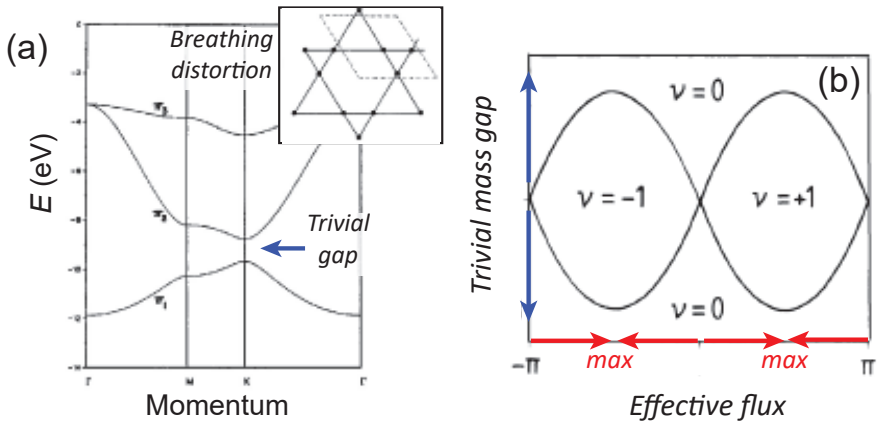

Figure 1-8: **Trivial gap openings on the distorted kagome lattice**

(a) Band structure of the kagome lattice with breathing distortion. Inset: schematic of the breathing distortion (adapted from [28]). (b) A generic topological phase diagram in the presence of two energy scales that generate a trivial gap (blue) and a nontrivial gap (red) (adapted from [8])

Focusing on the low energy dispersions (Fig. 1-7(c), inset), the spin-polarized Dirac electrons acquire mass with non-zero SOC, similar to the phenomenology of the QAH phase. From the one-dimensional projection of this bands structure, we identify a chiral edge state reflecting the non-trivial topology of the Dirac mass gap with Chern number $C = 1$.

While the $Z_2 = 1$ or $C = 1$ gap can be generated at the Dirac point with $\lambda \neq 0$ or $\vec{M}$ // z, a different type of gap can also be created with a symmetry-breaking lattice distortion. Fig. 1-8(a) shows a band structure of a distorted kagome network with three of the triangles expanded and the other three compressed − the form known as the breathing kagome lattice (see the inset) [28]. In this state, the PT symmetry is broken (it maps the large triangles onto the small triangles) and the degeneracy is no longer protected at the Dirac point. Unlike in case described in Fig. 1-7, the process here drives the system to become a trivial band insulator.

Having explored two distinct pathways to Dirac mass gap generation, we map them onto the phenomenologically similar phase diagram proposed in the Haldane model [8]. The topological character of the gap is determined by the relative strengths of the asymmetric lattice potential (giving rise to the trivial gap) and the SOC (giving

rise to the effective flux through the lattice). In the regime the latter is stronger than the former, the $C = 1$ state can be realized. This suggests a key message that larger SOC strength can make the nontrivial topology of a system even more robust against lattice deformations or other perturbations.

1.3.3 Correlated phases in the kagome lattice

In the previous section, we have examined the topological characters of different gapped Dirac states in the kagome lattice. In this section, we survey theoretical predictions on how different parts of the kagome band structure can incur correlated phenomena. We split the discussion into four representative categories each based on a different assumption.

- (i) *Mapping the flat band to the frustrated Hubbard band*
  The real space eigenstates of the flat band electrons can be viewed as triangular networks of localized charge clusters. Based on this insight, many authors have mapped the inter-cluster hopping in the kagome flat band to the inter-site hopping on a triangular lattice with $U/t \gg 1$. This is phenomenologically equivalent to the Hubbard model, which in the case of square lattice gives rise to the Mott insulating phase with an antiferromagnetic spin structure. In the triangular lattice Hubbard model, the magnetic frustration complicates a simple antiferromagnetic spin arrangement. Adopting the approaches taken for frustrated Heisenberg antiferromagnets (with an assumption that each atomic site contains one spin), the prospects of spin liquid and its related phases have been raised [32–35].

- (ii) *Mapping the flat band to quantum Hall states*
  In the presence of SOC, the quadratic band touching between the Dirac and flat bands gaps out. Given that the nontrivial topology of the Dirac band is intermixed to the flat band, E. Tang *et al.* proposed that the kagome flat band may act as a zero-field analog of the LL [36]. When further enriched with

interaction effects, inherently relevant for a flat band with $U/t \gg 1$, the LL-like flat band may generate a high temperature fractional quantum Hall effect.

- (iii) *The flat band stabilizing an extreme limit of the Stoner ferromagnetism*
  Aside from the implications of wavefunction localization (critical to the Hubbard physics and the quantum Hall physics), one can also consider the impacts of the concentrated DOS within an extremely narrow energy range. Many authors have proposed that the flat band may realize an extreme limit of the Stoner ferromagnetism. This treatment was also found to be analogous to the special case of the Hubbard model on a partially flat band with non-singular $U_{\mathrm{on-site}}$ and DOS peak [37–40].

- (iv) *Imposing strong interactions to other parts in the band structure*
  While the flat band may act as a *hot spot* of electronic correlations, other parts in the band structure (*e.g.* Dirac point, van Hove singularity), if strong interactions are imposed, may also generate exotic phases. By enforcing an interaction-driven gap opening at these key band singularities, many authors have predicted exotic orders such as unconventional superconductivity or chiral density waves [41–43].

In general, a precise *a priori* prediction of correlation effects requires a delicate balance of multiple competing interactions, which without any knowledge of actual material parameters may encounter an immense challenge. This calls for material realizations of the kagome lattice and further experimental verifications of these predicted phases.

1.3.4 The kagome metals

As an ideal material platform to explore the kagome physics, we focus on a class of intermetallics that contains the kagome network of transition metal elements as one of its constituent layers − the compounds henceforth referred to as "kagome metals."

Several known kagome metals are realized in a hexagonal crystal structure with a formula unit $X_mY_nZ_k$ (m, n = 1, 2, 3, 5, 6; k= 0, 1) and contain the two-dimensional

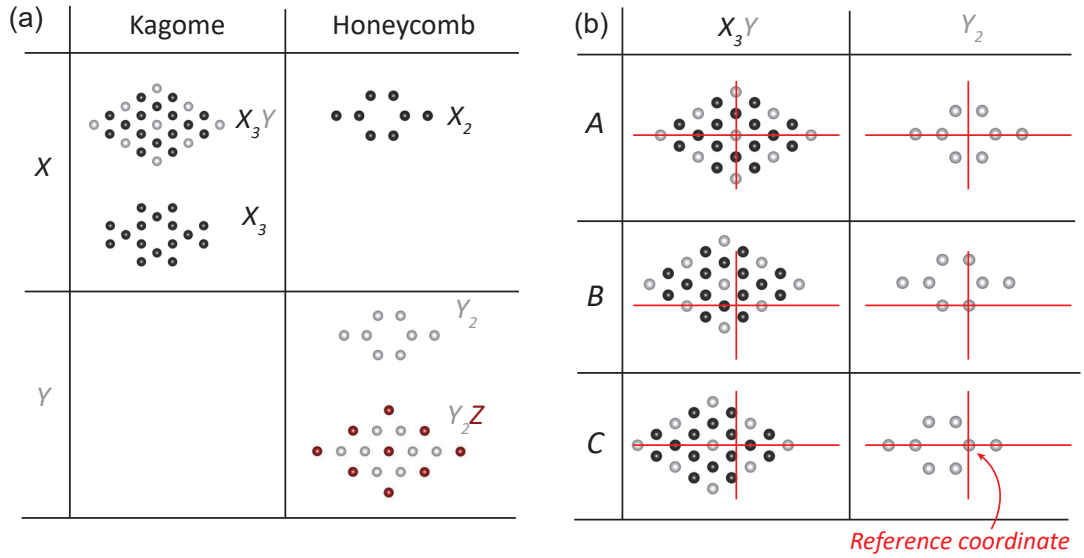

Figure 1-9: **Two-dimensional building block layers for kagome metals**

(a) Two-dimensional kagome and honeycomb layers of X- and Y-atoms. (b) Three types of stacking configurations for the kagome and honeycomb layers.

kagome networks of X-atoms. The left column in Fig. 1-9(a) displays examples of the X-kagome networks: the X_3Y-layer and the X_3-layer with and without the Y-atoms at the center of the kagome hexagons, respectively. The other non-kagome building block layers are the honeycomb networks of X- or Y-atoms, which in certain kagome metals function as spacer layers that suppress hybridizations between consecutive kagome layers (the right column in Fig. 1-9(a)). Some of the examples are the X_2-layer, the Y_2-layer, and the Y_2Z-layer ($\equiv$ the Y_2-layer with the Z-atoms at the center of the honeycomb hexagons).

These fundamental building block layers can be assembled to formulate a variety of crystal structures. There exist three possible configurations for stacking these layers. To demonstrate this, we set an arbitrary reference coordinate and define configuration A to have the reference point at the center of the kagome/honeycomb hexagon (Fig. 1-9(b), the first row). When the X_3Y-layer and the Y_2-layer are AA-stacked, for example, their hexagons will be concentric. Other configurations can be defined by displacing the center of kagome/honeycomb hexagon from the reference point by a fraction of unit cell vectors. Such acquired configuration B and configuration C are

Formula unit	# of layers / unit cell	Unit cell	Stacking Sequence	Examples
X_1Y_1	2	X_3Y - Y_2	AA	FeSn, CoSn, RhPb
X_5Y_1	2	X_3Y - X_2	AA	YCo_5, $CaPd_5$
$X_3Y_2Z_1$	3	X_3 - Y_2Z	AA	$LaRu_3Si_2$
$X_6Y_6Z_1$	4	X_3Y - Y_2 - X_3Y - Y_2Z	A′AA″A	$TbMn_6Sn_6$,
$X_3Y_5Z_1$	4	Y_2 - X_3Y - Y_2 - Z_1	AAAA	KV_3Sb_5
X_3Y_2	9	(X_3Y - Y_2 - X_3Y) - (X_3Y - Y_2 - X_3Y) - (X_3Y - Y_2 - X_3Y)	(AAA) - (BBB) - (CCC)	Fe_3Sn_2, V_3Sb_2
X_3Y_1	2	X_3Y - X_3Y	AB	Mn_3Sn, Ni_3In
$X_3Y_2Z_2$	6	(X_3Y - Z_2Y) - (X_3Y - Z_2Y) - (X_3Y - Z_2Y)	(A$\overline{C}$) -(B$\overline{A}$) -(C$\overline{B}$)	$Co_3Sn_2S_2$ $Rh_3Pb_2S_2$

Table 1.1: **Layer-by-layer arrangements in kagome metals**

shown in the second and third rows of Fig. 1-9(b), respectively. When two X_3Y-layers are AB-stacked, for example, the kagome hexagon in one layer will sit on top of the kagome triangle in the other layer.

$X_mY_nZ_k$ with different $m : n : k$ stoichiometry can be generated from various permutations of constituent layers and their stacking sequences. Table 1.3.4 lists some of the prototype structures. X_1Y_1, X_5Y_1, $X_3Y_2Z_1$ consist of alternating AA-stacks of the kagome layers and the honeycomb spacer layers. Such a crystal structure is predicted to generate a quasi-two-dimensional electronic structure with the key features of the original two-dimensional lattice model manifested intact. This prediction has been verified experimentally in some of the model compounds (Co:Fe)Sn (X = Co, Fe; m = 1; n = 1) [44–46] and YCo_5 (X = Co; m= 5; n = 1) [47].

$X_3Y_5Z_1$ is conceptually similar to the above three, but with two additional spacer layers per unit cell with respect to X_1Y_1. The increased kagome-to-kagome separation is expected to enhance the electronic/structural two-dimensionality. Potentially related to this, one of the model compounds (K:Cs)V_3Sb_5 (X = V; m = 3; n = 5; k = 1) has shown a relatively stronger tendency to be exfoliated than most X_1Y_1 compounds [48, 49].

$X_6Y_6Z_1$ also has a similar stacking sequence to X_1Y_1. The unit cell, however,

contains two kagome layers, one with the Y-atoms buckled upwards (configuration $A^{'}$) and the other with the Y-atoms buckled downwards (configuration $A^{''}$). Given that the the degree of buckling is small, the overall electronic structure is nearly analogous to that of X_1Y_1 as confirmed from a model compound $TbMn_6Sn_6$ (X = Mn; $m = 6$; $n = 6$; $k = 1$) [50].

X_3Y_2 is known to stabilize in a complex stacking sequence. Its unit cell consists of nine layers, which can be split into three sets of kagome−spacer−kagome trilayer. The identical stacking configuration is maintained within each trilayer, but the three consecutive trilayer bundles are ABC-stacked; this stacking pattern gives the nine-layer arrangement of AAABBBCCC. The consequence of this peculiar stacking sequence has been studied by S. Fang *et al*. [51]; the presence of the spacer layers in this crystal structure still preserves the electronic two-dimensionality as experimentally verified in a model compound Fe_3Sn_2 (X = Fe; $m = 3$; $n = 2$) [52–55].

Lastly, we examine X_3Y_1 and $X_3Y_2X_2$. X_3Y_1 consists of AB-stacked kagome layers with no spacer layer in the structure and is expected give rise to a three-dimensional electronic structure. $X_3Y_2X_2$ also harbors a three-dimensional electronic structure as the Y-atoms in the Z_2Y spacer layers buckle significantly out-of-plane and mediate strong hybridizations between the X_3Y_1-layers. In Table 1.3.4, we distinguish these buckled Z_2Y-layers from other planar layers by denoting their configurations as $\overline{A}$, $\overline{B}$, or $\overline{C}$. It has been identified in a number of X_3Y_1 or $X_3Y_2X_2$ compounds that their three-dimensional electronic structures support new types of band features including Weyl nodes (*e.g.* Mn_3Sn, $Co_3Sn_2S_2$) [56–59]) or anisotropic flat bands (*e.g.* Ni_3In) [60].

1.4 Thin film engineering of quantum materials

Thin films offer a unique platform to manipulate physical properties of quantum materials in a highly controlled fashion. Such versatility comes from their reduced sample dimensions, strong film−substrate epitaxial interaction, as well as ultra-precise and ultra-clean synthesis processes associated with thin film synthesis. In this thesis, we

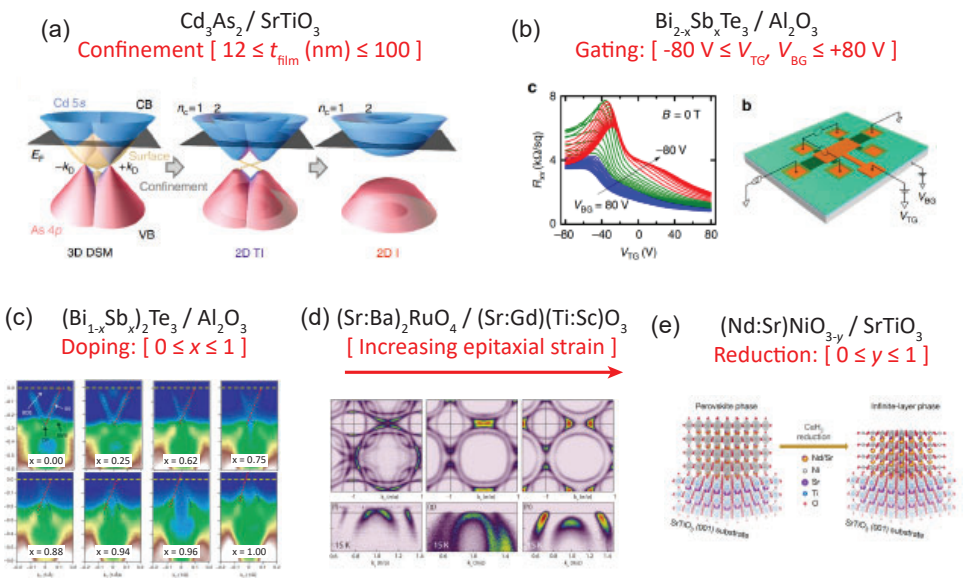

Figure 1-10: **Manipulating properties of thin film quantum materials**

(a) Two-dimensional subband splittings in Cd_3As_2 thin films via quantum confinement [61]. (b) Gate control [62] and (c) doping control [63] of the chemical potential in Bi_2Te_3 thin films. (d) Manipulation of Fermi surface morphology with epitaxial strain in $(Sr:Ba)_2RuO_4$ thin films [64]. (e) Topotactic transition of $(Nd:Sr)NiO_3$ thin films into $(Nd:Sr)NiO_2$ via reduction chemistry [65].

stabilize some of the representative kagome metals in epitaxial thin film form and engineer the topological and correlated electronic states therein with different experimental tuning knobs.

One of the consequences of confining electrons within a thin slab is the quantization of crystal momentum along the thickness direction (k_z) and the subsequent subband splittings. In the thickness regimes where the splitting exceeds the Fermi energy in original band structure, electrons collapse to the lowest subband with a single-valued k_z and the system can be treated as a two-dimensional system. Recently, thin films of a three-dimensional Dirac semimetal Cd_3As_2 have been driven into such regime, where non-canonical quantum Hall behaviors were observed. These anomalies have been ascribed to the characteristic cyclotron orbits of Dirac and Weyl fermions (Fig. 1-10(a)) [61, 66].

In addition to the changes in the band structure, thinning down a film to below

the Thomas-Fermi screening length, in conjunction with simultaneous reduction of sheet carrier density, dramatically enhances the gate-tunability. For decades, field effect transistors have offered a key working principle for binary logic gates: small vs. large electrical conductivity when E_{F} is inside vs. outside the gap. With a goal of deciphering the topological nature of the gap, the identical electrostatic gating experiments have been performed on three-dimensional topological insulator thin films. By continuously sweeping E_{F} within the gap, anomalous in-gap states were observed and further identified as the topological Dirac surface states (Fig. 1-10(b)) [62, 67–69].

A similar E_{F}-tuning can also be performed via chemical doping. Thin film synthesis involves ultra-fine calibration of element-specific concentration, allowing sub-% control of stoichiometry. Furthermore, owing to the epitaxial stabilization energy, the synthesis may take place at a temperature significantly lower than that used for bulk synthesis. Such non-thermodynamic growth mode facilitates stabilization of heavily doped compounds despite their inherent instabilities. Taking advantage of these aspects, E_{F} of $Bi_{2-x}Sb_xTe_3$ thin films has been engineered across an energy range larger than what is available with gating alone (Fig. 1-10(c)) [63].

The choice of substrate offers another important axis along which the film properties can change. For reliable epitaxy, the substrates are generally chosen to have the same in-plane crystallographic symmetry and similar lattice constants with the films. Given a small but finite lattice mismatch, the films experience coherent tensile/compressive strains within the plane due to the film−substrate interactions. For instance, the epitaxial strain has proven effective in manipulating the Fermi surface morphology of a strongly correlated oxide $(Sr{:}Ba)_2RuO_4$ (Fig. 1-10(d)) [64].

More recently, phase changing phenomena in thin films have also been highlighted. One of the pioneering works concerns converting a thin film correlated oxide $RENiO_3$ (RE = rare-earth) into $RENiO_2$ via reduction chemistry (Fig. 1-10(e)) [65]. The samples were found to maintain homogeneity and single-crystallinity due to reduced thickness and film−substrate bonding energy, respectively. After this topotactic transition, the system revealed superconductivity unattained in its original structure.

Finally, we comment on the heterostructure engineering of thin film quantum ma-

Figure 1-11: **Heterostructure engineering of thin film quantum materials**

(a) Two-dimensional electron gas at the polar interface of $LaAlO_3/SrTiO_3$ [70]. (b) Skyrmionic spin texture stabilized in a magnetic multi-layer [71]. (c) Magnetic proximity effect in a topological insulator heterostructure [72].

terials. Abrupt changes in dielectric, magnetic, and symmetry environments across thin film heterointerfaces have given rise to peculiar states confined at the interfacial layer. Two-dimensional electron gas at the $LaAlO_3/SrTiO_3$ polar interface (Fig. 1-11(a)) [70] and skyrmionic spin textures in magnetic multi-layers (Fig. 1-11(b)) [71] both belong to this category. Furthermore, when the constituent layers in the heterostructure are sufficiently thin, the influence of one layer may proximitize the entirety of the neighboring layer, not restricted to the two-dimensional interface. An example of the proximity effect can be found in $CrGeTe_3/(Bi:Sb)_2Te_3/$ $CrGeTe_3$ heterostructure, in which the encapsulated topological insulator layer manifested a magnetism-induced gap opening upon influence of the neighboring ferromagnetic layers (Fig. 1-11(c)) [72].

1.5 Thesis outline

In this thesis, we present our approaches in engineering the topological and correlated electronic states in certain intermetallic compounds containing the two-dimensional kagome networks of transition metal elements as one of its constituent layers – the class of materials referred to as kagome metals. For versatile control of their material parameters, we first stabilize these compounds in epitaxial thin film form and track their physical properties as a function of different experimental tuning knobs.

The viewpoints proposed herein are expected to (i) shed light onto the physics of the kagome lattice placed under various symmetry conditions and electromagnetic environment as well as (ii) drive the candidate kagome metals towards the regime more suitable for electronic/spintronic device incoporation.

In chapter 2, we discuss the experimental techniques employed in this thesis. In chapter 3, we present our extensive works on synthesis and characterization of epitaxial thin film FeSn, an antiferromagnetic kagome metal with quasi-two-dimensional electronic structure. In this chapter, we present a systematic doping control of the chemical potential and spin structure in FeSn, through which we elucidate the roles of the lattice-driven Dirac and flat bands in shaping the electromagnetic properties of this system. In chapter 4, we describe the characteristic atomic arrangement of FeSn realized at the film−substrate heterointerface and probe its local electronic structure with planar tunneling spectroscopy. A significant portion of the discussions in chapter 3 and 4 are based on [73–75]. In chapter 5, we describe the emergence of a new type of flat band and the associated non-Fermi-liquid behaviors in a paramagnetic kagome metal Ni_3In stabilized in epitaxial thin film form. We discuss the relevance of the flat band in generating the observed Fermi surface breakdown. In chapter 6, we introduce an alternative non-kagome-originated approach in commingling topology and correlation in a single material platfom by the spatial coexistence of different atomic degrees of freedom [76]. In chapter 7, we summarize the frameworks of understandings on various kagome metals and comment on the future prospects for more advanced thin film engineering in this family of compounds and beyond.

Chapter 2

Experimental methods

2.1 Molecular Beam Epitaxy

Thin films of intermetallic compounds are synthesized here with molecular beam epitaxy (MBE). MBE is a physical vapor deposition technique for growing a crystalline overlayer on a substrate in an epitaxially registered fashion. The process takes place in an ultra high vacuum chamber in order to provide ultraclean and highly controlled synthesis environment. The MBE system used for this thesis research has a typical base pressure of $\sim 10^{-10}$ torr and consists of three compartments: the load-lock chamber, the preparation chamber, and the growth chamber. The former two are typically used for sample exchange, storage, and pre-annealing, whereas the latter is where the film deposition takes place. Fig. 2-1(a) illustrates a schematic diagram of the growth chamber.

For film growth, a substrate is mechanically clamped onto an Inconel sample holder and loaded into the system. After appropriate pre-annealing treatments, the sample holder is transferred to the growth chamber with the substrate facing downward. At the bottom of the growth chamber are inserted solid source effusion cells. Each effusion cell contains a crucible made from alumina or boron nitride and is heated by resistive coils up to the temperature that allows vaporization of the raw material therein. The cell temperatures are controlled with power supplies and PID control units, a set of two assigned to every cell. The beam equivalent pressures (BEPs) of the

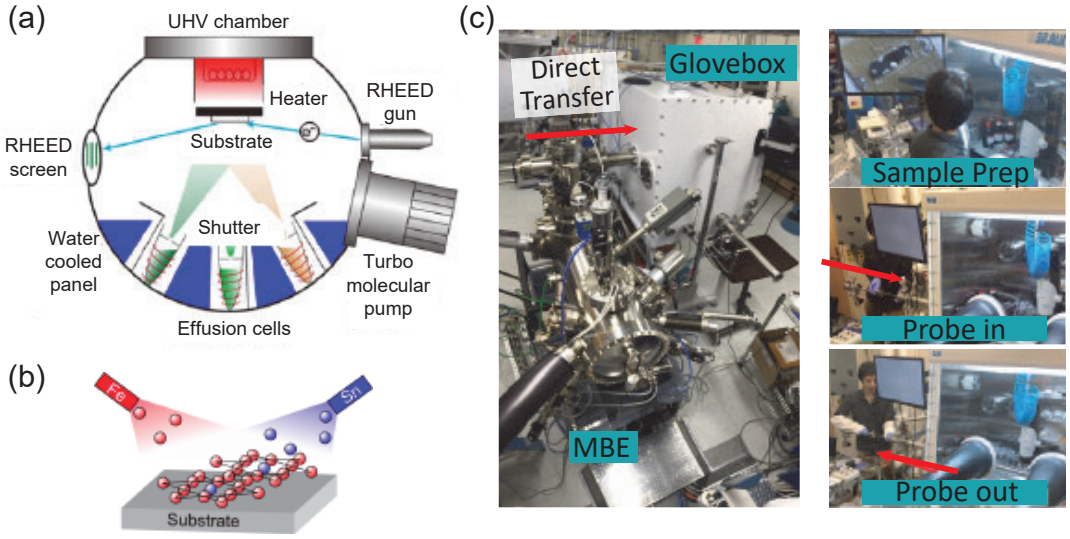

Figure 2-1: **Molecular beam epitaxy**

(a),(b) Schematic of thin film deposition process in a molecular epitaxy beam (MBE) system. (c) Pictures describing the direct sample transfer from the MBE to an Argon-filled glovebox (left) and from the glovebox to a cryogenic probe (right).

evaporated elements are calibrated before every film growth with a flux monitor to ensure the correct deposition rate and stoichiometry. The raw materials evaporated in this chamber for this thesis research include BaF_2, Bi, Fe, Gd, In, Mg, Mn, Ni, and Sn.

To initiate/terminate the film deposition, pneumatically controlled shutters for the relevant effusion cells are opened/closed. The sample holder is fixed at an optimized temperature for the growth (also PID-controlled) as the beam fluxes are irradiated onto the substrate (Fig. 2-1(b)). The deposition temperature ranges from as low as the room temperature to as high as 700 °C, depending on the detailed growth dynamics of the target compound. During the deposition, the sample holder is rotated at a rate 0 - 5 rotations per minute using an *ex-situ* stepper motor mechanically connected to an *in-situ* rotation unit. The rotation is critical in producing a film with uniform stoichiometry across a macroscopic length scale. The rate of deposition and the process of crystallization are monitored in real time with a quartz crystal monitor (QCM) and reflection high energy electron diffraction (RHEED). Most of

the components involved in the MBE operation are continuously water-cooled to maintain normal operation parameters. After the deposition, the sample holder is cooled down to the room temperature and the effusion cells down to the standby temperature of 400 °C, at which all of the elements have negligible vapor pressures. To avoid any risk of crucible deformation or damage during solidification/melting, the standby temperature is chosen to be sufficiently higher than the melting points of some of the low melting point elements (*e.g.* Bi, Sn, In). The sample holder is transferred from the growth chamber to the load-lock chamber so that the films can be taken out of the MBE.

The compounds studied in chapter 3 - 5 of this thesis are relatively stable in air. The one studied in chapter 6, however, is extremely air-sensitive; thin films of this compound degrade in air within a few seconds. To preserve the sample quality, we transfer those films directly from the load-lock chamber to an Argon-filled glovebox without any air exposure. They are processed inside the glovebox for different types of measurements and finally loaded onto cryogenic probes, which themselves are also inserted into the glovebox in an air-free manner. The pictures in Fig. 2-1(c) show the experimental protocols for glovebox transfer, sample preparation, and probe loading in our MBE-glovebox-cryostat assembly system.

2.2 Structural characterizations

In this thesis, we employ different experiment techniques to characterize various structural aspects of our thin film samples. Symmetric X-ray diffraction (XRD) offers the highest throughput metric to examine the film quality. The symmetric scattering geometry entails the following constraints: $k_{\text{plane,in}} = k_{\text{plane,in}}$ and $k_{\text{perp,in}} = -k_{\text{perp,in}}$, where $k_{\text{plane,in}}$ and $k_{\text{perp,in}}$ (or $k_{\text{plane,out}}$ and $k_{\text{perp,out}}$) denote the in-plane and out-of-plane momentums of the X-ray beam projecting into (or scattering out of) the sample. An example of the symmetric XRD measurement can be found in Fig. 2-2(a) where a pronounced Bi (003) diffraction peak is identified from a Bi film deposited on a BaF_2 substrate, reflecting both the hexagonal orientation of the film as well as its

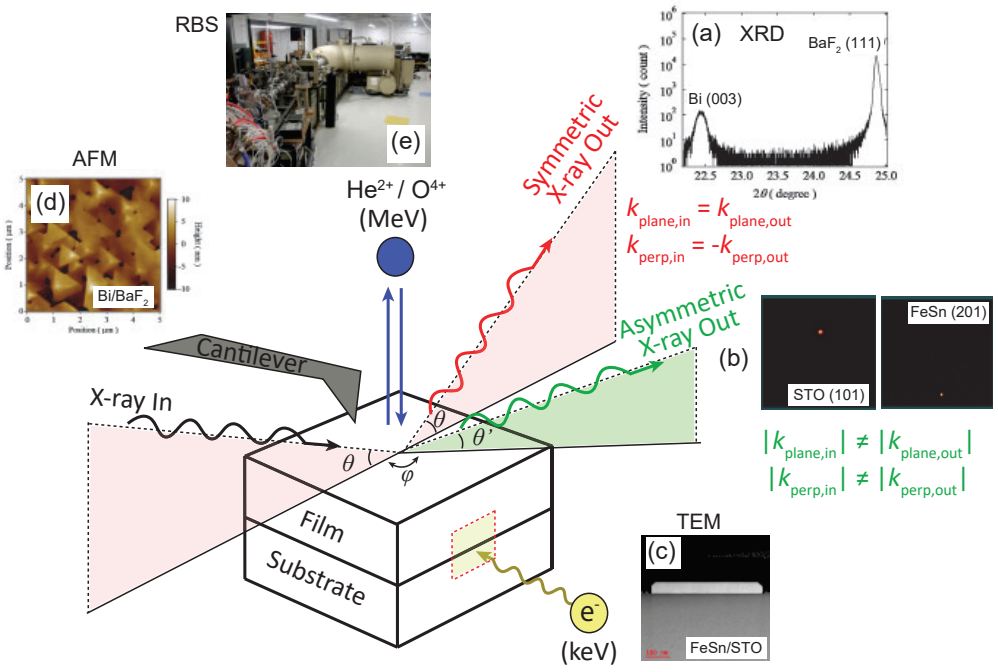

Figure 2-2: **Structural characterizations on thin film samples**

Schematic sample structure (center) and measurement schemes for various characterization techniques. (a) Symmetric and (b) asymmetric X-ray diffractions. (c) Cross-sectional transmission electron microscopy. (d) Atomic force microscopy. (e) Rutherford backscattering. The data and pictures in (a)-(e) are described in the main text.

high crystalline quality. To complement this information, we perform X-ray reflectivity (XRR) measurements under the same scattering geometry but with grazing incident beam angles ($0 < 2\theta < 5°$). The oscillations in XRR can be used to extract the film thickness. In addition, some of the high quality films are characterized with asymmetric XRD measurements. The asymmetric scattering geometry entails a different set of constraints: $|k_{\text{plane,in}}| \neq |k_{\text{plane,in}}|$, $|k_{\text{perp,in}}| \neq |k_{\text{perp,in}}|$, and $\phi \neq 0$, where ϕ is the azimuthal angle. Fig. 2-2(b) shows the asymmetric XRD peaks for FeSn (201) and $SrTiO_3$ (101) at the same ϕ, manifesting an epitaxial alignment of in-plane orientations between the materials.

As well as diffraction mediated approaches, more direct real space imaging techniques are employed. Cross-section images of the films are acquired by cross-sectional transmission electron microscopy (TEM) using keV electrons. Fig. 2-2(c) shows a

TEM image of an island-segregated FeSn film deposited on a $SrTiO_3$ substrate, revealing the sharp film−substrate interface. Typically, TEM tools are equipped with an *in-situ* electron energy loss spectroscopy (EELS) capability. After every TEM measurement, samples are also characterized with EELS for chemical identification. Surface morphologies of the films are probed with atomic force microscopy (AFM). Fig. 2-2(d) shows an AFM image of a Bi film deposited on a BaF_2 substrate. AFM is helpful in optimizing films for electrical transport measurements; for example, films with disconnected morphologies are not suitable and further optimization is required.

The information from the above are corroborated with Rutherford backscattering (RBS) measurements taken in the class 1.7 MV tandem ion accelerator at Cambridge Laboratory for Accelerator Surface Science at Massachusetts Institute of technology (CLASS at MIT) (Fig. 2-2(e)). The measurements are conducted by projecting MeV He^{2+} or O^{4+} ion beams towards the sample along the film normal direction and detecting the energy loss from the reflected beams. The beam flux and energy are calibrated separately using a Au film on a Ge substrate. The experimental spectra are compared with the simulated spectra using the SIMNRA software, developed by the Max Planck Institute for Plasma Physics [77]. For the simulation, we use the scattering cross-section database from Ion Beam Analysis Nuclear Data Library (IBANDL) [78]. RBS offers information about film thickness, chemical contents, and their relative stoichiometry.

2.3 Electrical transport measurements

Electrical transport properties of thin film samples are characterized in a typical Hall bar geometry. As-grown samples with 5×5 mm^2 lateral dimensions are cut into smaller pieces with rectangular shapes. In most occasions, we define the Hall bar shape by scratching off other areas of the film using a diamond scribe. In case more precise sample geometry is required, we pattern a device shape with a standard photolithography, followed by either acid dip or Argon ion milling to etch other areas of the film. The samples are mounted on sapphire pads using GE varnish. Prior

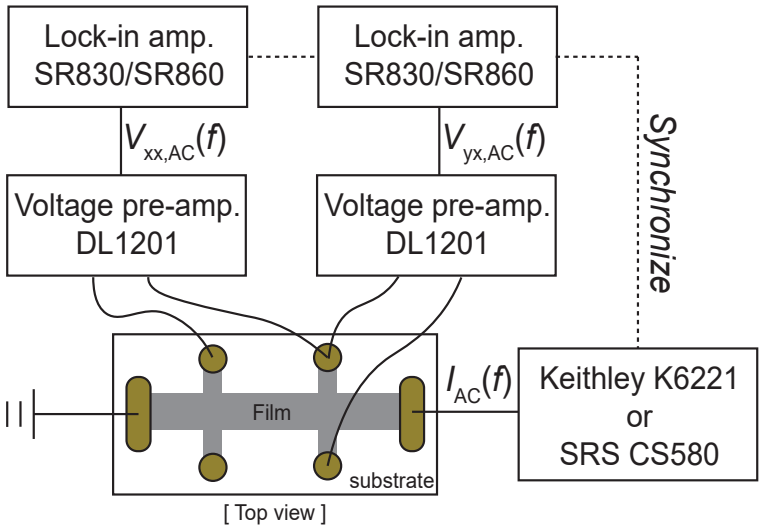

Figure 2-3: **Schematic of transport measurement on thin film samples**

Schematic diagram of the five-terminal electrical transport measurement using a standard lock-in technique.

to sample mounting, several Au wires are mechanically fixed on the sapphire pads with a two-part epoxy (Epotek). Electrical contacts are made by applying Ag paint (DuPont 4922N) to the joints between the film contact areas and the Au wires. For certain measurements that require more stable electrical contacts, Ti (5 - 10 nm thick) and Au (20 - 100 nm thick) are evaporated sequentially onto the contact areas with electron beam evaporation. The contact patterns are defined with custom-made shadow masks from Al foils or teflon tape (or with another step of patterning for lithographically-defined devices).

A standard lock-in technique is used for transport measurements. An excitation current with the frequency 5 Hz $< f <$ 50 Hz was supplied along the elongated direction of the sample using Keithey K6221 or Stanford Research System CS580 current source. The current amplitude is determined for each measurement depending on the sample resistance. The voltage drops along the longitudinal (V_{xx}) and transverse (V_{yx}) directions are amplified with Ithaco DL1201 voltage pre-amplifiers. Then the amplified signals are measured with Stanford Research System SR860 (or SR830) lock-in amplifiers synchronized to the current source. Longitudinal resistivity

(ρ_{xx}) and transverse resistivity (ρ_{xx}) are obtained by normalizing V_{xx} and V_{yx}, respectively, with the excitation current and the sample dimensions. The schematic of this measurement configuration can also be found in Fig. 2-3. In some cases, the identical measurement scheme is conducted by the built-in functionalities of a Physical Properties Measurement System (PPMS) (Quantum Design, Inc.).

For magnetotransport measurements, a field-symmetric (field-asymmetric) response is assumed for ρ_{xx} (ρ_{yx}). To subtract off background signals, the raw ρ_{xx} (ρ_{yx}) data are symmetrized (anti-symmetrized) with respect to the magnetic field. When relevant, longitudinal conductivity (σ_{xx}) and transverse conductivity (σ_{xy}) are extracted from ρ_{xx} and ρ_{yx} using the following relation:

$$\sigma_{xx} = \frac{\rho_{xx}}{\rho_{xx}^2 + \rho_{yx}^2} \tag{2.1}$$

$$\sigma_{xy} = \frac{\rho_{yx}}{\rho_{xx}^2 + \rho_{yx}^2} \tag{2.2}$$

Based on the measured (ρ_{xx}, ρ_{yx}, σ_{xx}, σ_{xy}) under various temperature and magnetic field conditions, we extract different transport parameters representing either the electronic structure of the sample or the scattering processes therein.

2.4 Thermoelectric measurements

To complement the electrical transport measurements, we perform thermoelectric measurements. Fig. 2-4(a) is a schematic diagram of a typical measurement setup and Fig. 2-4(b) is an optical micrograph of a setup prepared for a Bi thin film sample.

A thermal gradient is generated by heating up one end of the sample to T_{hot} with a resistive heater while the other end is clamped to a Cu block fixed at T_{cold}. The heater has a typical resistance of 1 kΩ and is attached to the sample with stycast (ES-2-20, Lakeshore cryotronics). Additional thermal joint compound (type 120 silicone, Wakefield solution) is applied onto the sample−heater junction and the sample−Cu block junction to ensure efficient thermalization. DC electrical current is applied across the resistive heater with Keithley K6221 current source. The sample is kept in

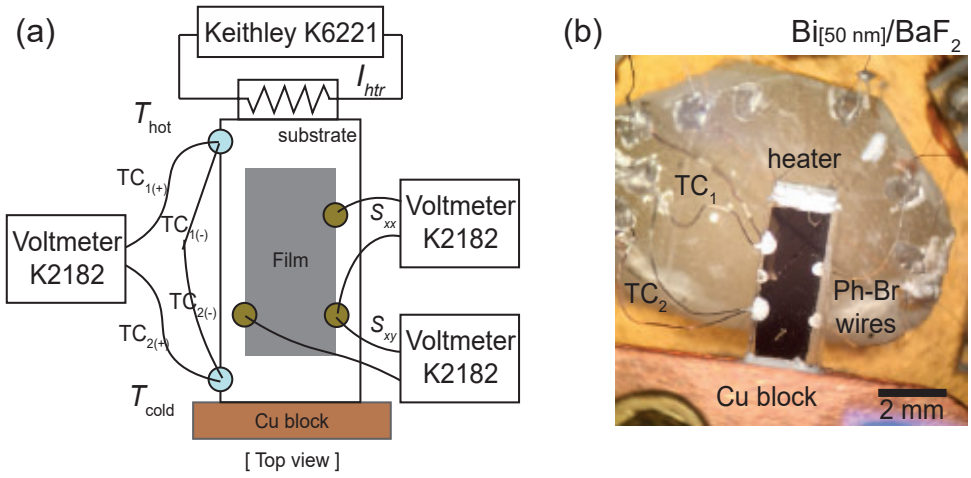

Figure 2-4: **Thermoelectric characterizations on thin film samples**

Schematic diagram of a measurement setup. The thermal gradient is generated with a resistive heater and measured with thermocouples connected in a differential measurement configuration. (b) An optical micrograph of the setup in (a) prepared for a Bi thin film sample.

a high vacuum environment and electrical connection is made with a Phosphor-Bronze wire to suppress unintended heat leaks. The thermal gradient is measured with two type-E thermocouples (TC), one attached near the hot end and the other near the cold end. The negative leads of the TCs are electrically shorted and the voltage difference between the positive leads is measured with Keithley K2182 voltmeter (*i.e.* differential measurement configuration). The thermal joint compound is applied at the TC−sample junctions. The Seebeck voltage (S_{xx}) and the Nernst voltage (S_{xy}) are measured with Keithley K2182 voltmeters across the longitudinal and transverse directions of the sample, respectively. Electrical connections between the contact areas in the film and the Phosphor-Bronze wires are made with Ag paint.

In this thesis, we measure the thermoelectric coefficients of our films under various temperature and magnetic field conditions. In chapter 3, we detect from the temperature dependence of S_{xx} the magnetic transition in FeSn. In chapter 5, we identify from the field dependence of S_{xx} the interplay of magnetic field and local moments in Ni_3In.

2.5 Shubnikov-de Haas oscillation

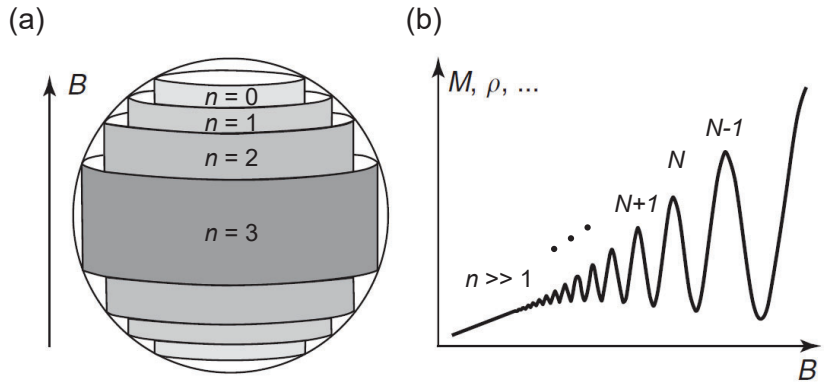

Figure 2-5: **Landau quantization and Shubnikov-de Haas oscillation**

(a) Schematic of the Landau quantization in a spherical Fermi surface. (b) Schematic of resistivity oscillation as the Fermi surface crosses a cascade of Landau levels. (a),(b) are from [79].

When a metallic system is placed under a high magnetic field B, electronic cyclotron orbit perpendicular to the field direction becomes quantized and the Fermi surface (FS) splits into Landau levels (LL). Fig. 2-5(a) shows a schematic of the Landau quantization in a spherical FS. Its energy spectrum is known to follow the quantum harmonic oscillator spectrum and the energy of the n^{th} LL can be expressed as $E_n = \hbar\omega_c(n + 1/2)$, where $\omega_c = eB/m^\star$ is the cyclotron frequency for electrons with the effective mass $m^\star$.

As B increases, the energy spacing between the consecutive LLs increases and FS crosses a cascade of LLs with decreasing n. As a result, the density of states (DOS) at FS oscillates periodically, manifesting a peak when FS crosses the LL and a valley when it is within the gap. This periodic modulation in DOS manifests as modulations in various physical observables and that for resistivity is called the Shubnikov-de Haas (SdH) oscillation (schematic illustration in Fig. 2-5(b)). An equivalent modulation in magnetic susceptibility is called the de Haas-van Alphen effect. Given a characteristic quantum lifetime τ_{Q}, SdH oscillations are likely to be observed in the regime $\omega_c\tau_{\text{Q}} > 1$.

Within a semi-classical picture, this criterion can be understood as a requirement for electrons to complete at least one cyclotron orbit before losing their coherence. For this criterion to be met, one generally needs high sample quality and low temperature (to raise τ_{Q}) as well as high magnetic field (to raise ω_c). The SdH oscillation is known to be periodic in $1/B$. Based on the Onsager relation, the cross-section area of the original FS perpendicular to B (A_k) can be extracted from the frequency of the oscillation $f = (h/2\pi e)A_k$. In chapter 3, we resolve the SdH oscillations in FeSn thin films and extract from their temperature, field, and angle dependence the morphology and the scattering lifetime of the associated Fermi pocket. The details of the analyses will be provided in the corresponding chapter.

2.6 Capacitive torque magnetometry

In this thesis, we utilize capacitive torque magnetometry to detect magnetic responses of our thin film samples. The schematic measurement configuration is shown in Fig. 2-6(a). A sample is attached at the end of a cantilever using Ag paint and a magnetic field H is applied at an angle θ slightly tilted from the film normal direction. The cantilever is custom-made from a Au or BeCu foil and is positioned in parallel to a rigidly fixed Au pad. The magnetic torque $\vec{\tau} = V(\vec{M} \times \vec{B})$ exerted to the sample (with volume V) bends the cantilever towards or away from the Au pad and the resultant change in capacitance (ΔC) is measured by Andeen-Hagerling 2500A capacitance bridge. τ is calculated from ΔC using mechanical conversion factors (*e.g.* Young's modulus of the cantilever material, cantilever shape, and dimensions).

When the sample has an isotropic magnetic susceptibility $\chi_x = \chi_y$ (here, x // film in-plane and y // film normal), $\vec{M}$ // $\vec{H}$ and $\tau = 0$ is expected (Fig. 2-6(b)). For $\chi_x \neq \chi_y$, however, the imbalance between χ_x and χ_y displaces $\vec{M}$ away from $\vec{H}$ as $\tan^{-1}(\frac{M_x}{M_y}) > \theta$ for $\chi_x > \chi_y$ (Fig. 2-6(c)) and $\tan^{-1}(\frac{M_x}{M_y}) < \theta$ for $\chi_x < \chi_y$ (Fig. 2-6(d)). Here, H_x and $M_x = \chi_x H_x$ (H_y and $M_y = \chi_y H_y$) are the components of $\vec{H}$ and $\vec{M}$ along the x direction (y direction). As a result, $\tau > 0$ ($\tau < 0$) is expected for $\chi_x > \chi_y$ ($\chi_x < \chi_y$) and the capacitance increases (decreases). Given the above, τ and

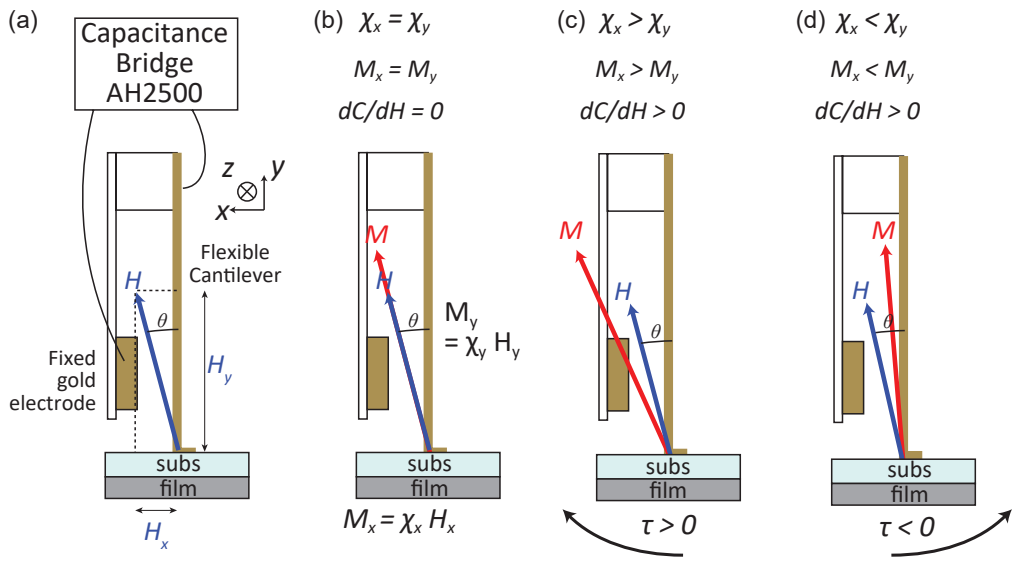

Figure 2-6: **Schematic of torque measurement on thin film samples**

(a) Schematic diagram of a capacitive torque magnetometry on thin film samples. Schematic description of torque responses for (b) $\chi_x = \chi_y$, (c) $\chi_x > \chi_y$, and (d) $\chi_x < \chi_y$, where χ_x and χ_y are magnetic susceptibilities along the x and y directions. The coordinate system here is defined in (a).

relates to the torque susceptibility $\chi_\tau \propto \chi_x$ - χ_y and the torque magnetization $M_\tau \propto \chi_\tau H$ rather than the absolute values of χ and M. In the case of field independent χ_τ, τ shows a quadratic field dependence.

A typical measurement setup is presented in the picture in Fig. 2-7(a). Fig. 2-7(b),(c) are representative magnetic field dependent torque data ($\tau(H)$) from a Gd film deposited on a BaF_2 substrate measured at $T = 2$ K (red) and 100 K (black). $\tau(H)$ reveals a sharp increase near 0 T and flattens out to a nearly constant value above $\sim$ 2 T (Fig. 2-6(b)). M_τ manifests a consistent response with an abruptly changing signal in the low field regime giving way to a diminishing signal entering the high field regime (Fig. 2-6(c)). These observations can be understood as a competition of shape anisotropy dominating at $H < 2$ T and field-polarization of ferromagnetic moments dominating at $H > 2$ T. The former generates an easy-plane anisotropy in samples with reduced thickness (*i.e.* $\chi_x > \chi_y$ in the low field) until the latter enforces the alignment of $\vec{M}$ and $\vec{H}$ (*i.e.* $\chi_x \sim \chi_y$ in the high field). In addition,

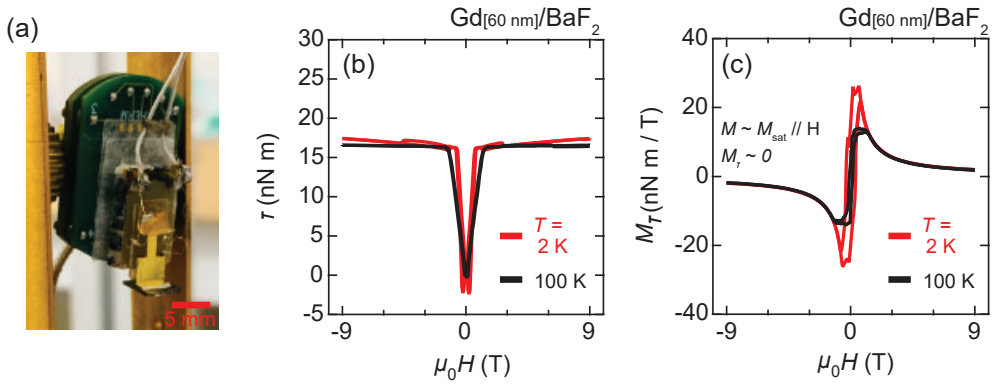

Figure 2-7: **Representative torque measurements on thin film samples**

(a) An optical micrograph of an FeSn thin film sample attached to a Au cantilever. (b),(c) Magnetic torque response of a Gd thin film sample. (b) and (c) are torque τ and torque magnetization M_τ at $T = 2$ K (red) and 100 K (black).

hysteretic responses are observed in both τ and M_τ, consistent with the expectation that the film is ferromagnetic. As indicated from this representative example, torque magnetometry offers an extremely sensitive probe of anisotropic magnetic response, particularly useful in extracting the sample signal from a large but relatively isotropic background signal.

2.7 Planar tunneling spectroscopy

We probe the electronic structure of some of the thin film samples via planar tunneling spectroscopy. For this purpose, we characterize the tunnel conductance of electrons traveling between the target layer and the electrode layer across an insulating barrier. The net conductance (I) of a tunnel junction is given by:

$$I(V_{\mathrm{J}}) \propto \int_{E_{\mathrm{F,target}}-eV_{\mathrm{J}}}^{E_{\mathrm{F,target}}} T_{\mathrm{barrier}} D_{\mathrm{target}}(\varepsilon)_{\mathrm{electrode}}(\varepsilon) d\varepsilon \tag{2.3}$$

where V_{J}, $E_{\mathrm{F,target}}$, T_{barrier} are the junction voltage, the Fermi energy of the target layer, and the tunneling efficiency of the barrier, respectively. In a typical tunnel junctions, ($E_{\mathrm{F,target}}$ - eV_{J}) = $E_{\mathrm{F,electrode}}$, where $E_{\mathrm{F,electrode}}$ is the Fermi energy of the electrode layer. $D_{\mathrm{target}}(\varepsilon)$ and $D_{\mathrm{electrode}}(\varepsilon)$ are the DOS at $E = \varepsilon$ of the target layer

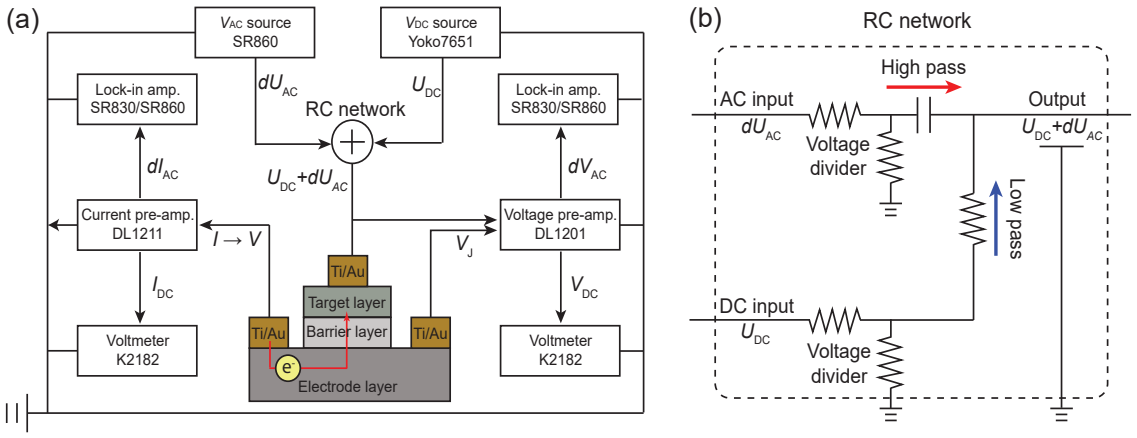

Figure 2-8: **Measurement configuration for planar tunneling spectroscopy**

(a) Schematic diagram of the three-terminal tunneling measurement configuration. (b) Circuit diagram of the resistor-capacitor (RC) network.

and the electrode layer, respectively. While I entails the net contribution from all electronic states within $E_{\mathrm{F,electrode}} \leq E \leq E_{\mathrm{F,target}}$, the energy-resolved DOS can be inferred from the differential conductance dI/dV:

$$\frac{dI}{dV}(V_{\mathrm{J}}) \quad \propto \quad D_{\mathrm{target}}(E_{\mathrm{F,target}} - eV_{\mathrm{J}}) \tag{2.4}$$

Fig. 2-8(a) shows a schematic diagram of a three-terminal tunneling measurement configuration used to extract I and dI/dV in our tunnel junctions. In order to probe the differential current dI in response to the differential voltage dV at a given V_{J}, we mix a small AC bias voltage (dU_{AC}) to a DC bias voltage (U_{DC}) with a custom-made resistor-capacitor (RC) network consisting of voltage dividers, a low pass filter, and a high pass filter (Fig. 2-8(b)). U_{DC} and dU_{AC} are generated from Yokogawa 7651 DC voltage source and Stanford Research Systems SR860 lock-in amplifier equipped with an AC voltage source, respectively. Typically $|\mathrm{d}U_{\mathrm{AC}}| \ll |U_{\mathrm{DC}}|$ to ensure reliable difference conductance characterization.

As the net bias voltage of ($U_{\mathrm{DC}} + \mathrm{d}U_{\mathrm{AC}}$) is applied onto the tunnel layer, the actual I and V_{J} across the junction are measured simultaneously (note that $|U_{\mathrm{DC}}| > |V_{\mathrm{J}}|$ due to non-junction-related voltage drops). I is first converted to an equivalent voltage

signal with a current amplifier Ithaco DL1211 and $V_{\rm J}$ is also passed through a voltage pre-amplifier Ithaco DL1201. The DC components, $I_{\rm DC}$ and $V_{\rm DC}$, are extracted with Keithley K2182 voltmeters and the AC components, $\mathrm{d}I_{\rm AC}$ and $\mathrm{d}V_{\rm AC}$, are extracted with an SR860 (or SR830). By taking the numerical ratio of $\mathrm{d}I_{\rm AC}$ and $\mathrm{d}V_{\rm AC}$, we extract the $\mathrm{d}I/\mathrm{d}V$ spectrum, closely correlated with the intrinsic DOS at the target layer.

Chapter 3

Engineering the kagome band structure in FeSn

In this chapter, we investigate the roles of the kagome band structure in shaping the electrical and magnetic properties of FeSn. The recent experimental observations of the lattice-driven Dirac and flat bands in TSn (T = Fe, Co) revealed the effectiveness of its quasi-layered crystal structure in preserving the physics of the two-dimensional kagome lattice model. In the first part, we provide comprehensive descriptions of the synthesis and characterization of high quality epitaxial thin film FeSn. In the second part, we demonstrate systematic control of the chemical potential and spin structure of FeSn in a highly controlled fashion, thereby elucidating the impacts of the Dirac and flat band electrons in generating magnetic instability and anomalous transport responses in this system.

3.1 Properties of TSn (T = Fe, Co)

FeSn is a quasi-layered transition metal stannide consisting of an alternating stack of Fe_3Sn kagome layers and Sn_2 honeycomb layers (Fig. 3-1(a)-(c)). The consecutive kagome layers in FeSn are AA-stacked, distinguished from those in its Sn-deficient cousin compounds Fe_3Sn_2 (AAABBBCCC-stacking) and Fe_3Sn (AB-stacking). This crystal structure is a prototype of a wider class of kagome metals XY (X = transition

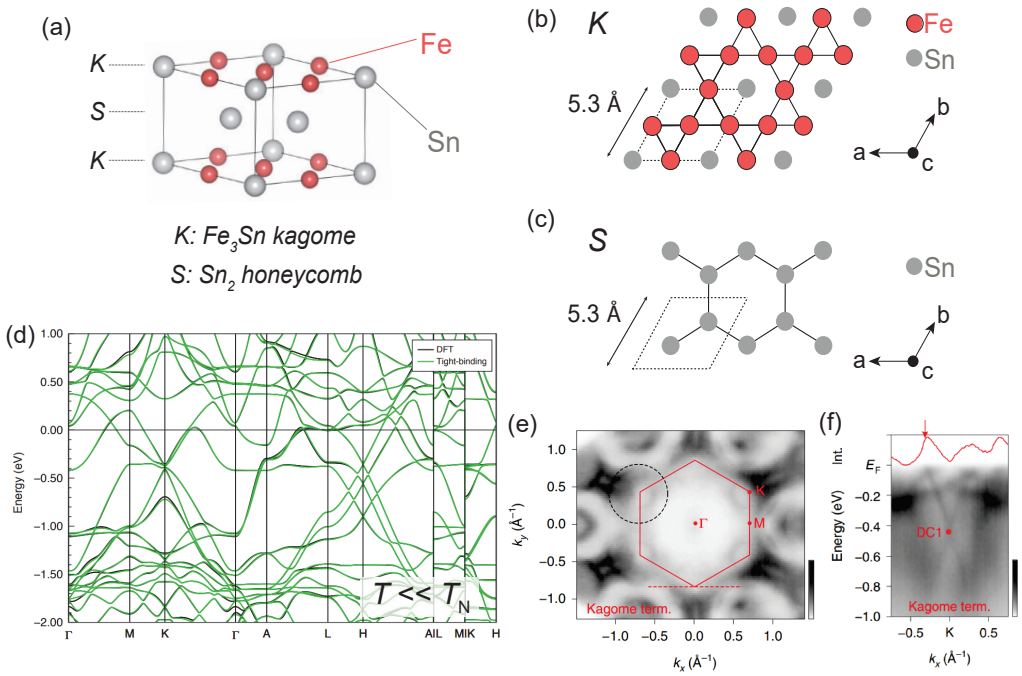

Figure 3-1: **Antiferromagnetic kagome metal FeSn**

(a) Crystal structure of FeSn. Schematic atomic arrangements of (b) the Fe_3Sn kagome layer and (c) the Sn_2 honeycomb layer. (d) DFT electronic structure of FeSn in the antiferromagnetic state. (e,f) Fermi surface of FeSn at the kagome termination measured by photoemission experiments. The kagome-derived Dirac points can be identified at the K-point. (d)-(f) are from [44].

metal; Y = group III, IV elements).

Below T_N = 365 K, FeSn becomes a type-II antiferromagnet, in which the Fe spin moments align ferromagnetically within a single kagome plane but antiferromagnetically from those in the neighboring planes [80–84]. While FeSn has shown limited exfoliation capability potentially owing to the three-dimensional bonding network of Sn therein, the hybridization between the consecutive kagome layers is expected to be strongly suppressed by the stanene spacer layers, giving rise to a bulk band structure with the kagome-derived Dirac crossings and flat bands clearly visible. Corroborating this insight, density-functional theory (DFT) band structure calculations of FeSn in the antiferomagnetic state manifest near the Fermi level (E_F) quasi-two-dimensional Dirac and flat bands with the associated Dirac points and the density of state (DOS) peak at $E \sim$ -0.4 eV and $E \sim$ 0.6 eV, respectively (Fig. 3-1(d)). In recent pho-

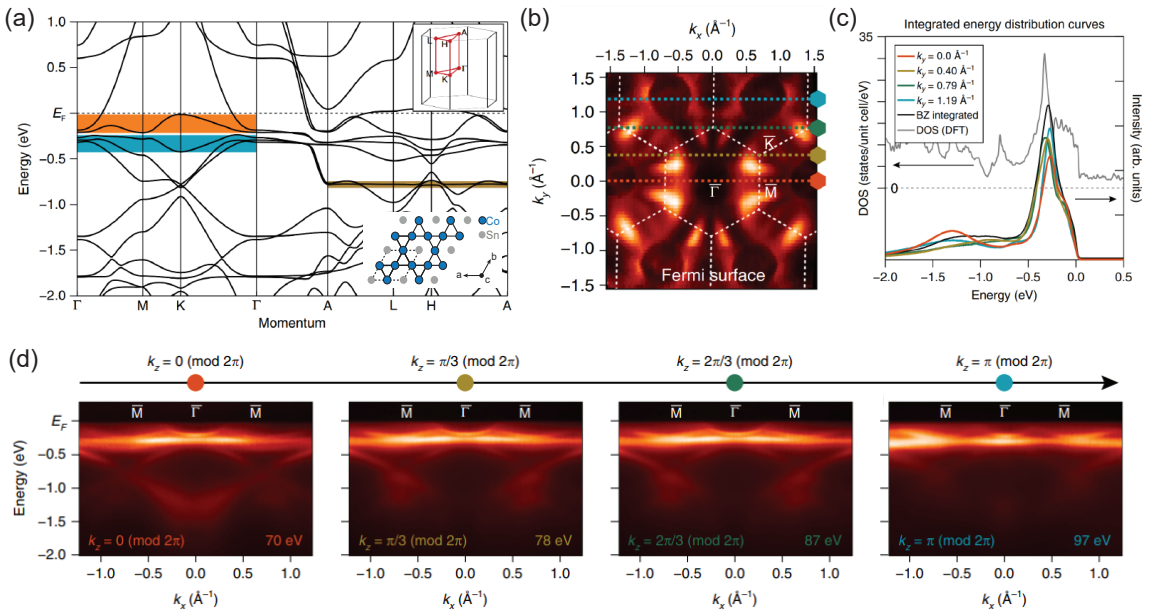

Figure 3-2: **Paramagnetic kagome metal CoSn**

(a) DFT electronic structure of CoSn in the nonmagnetic state. The kagome-derived flat bands of different *d*-orbital origins are enclosed in colored boxes. (b) Fermi surface of CoSn measured by photoemission experiments. (c) DOS peak from the flat bands. (d) Direct visualization of the flat bands from different momentum cuts in (b). (a)-(d) are all from [45].

toemission experiments on bulk single crystal FeSn, the predicted Dirac bands have been observed, confirming the validity of the long-sought conceptual model in a real material (Fig. 3-1(e),(f)) [44]. The access to the flat bands, however, has been limited as they are expected above E_F of FeSn. Paramagnetic kagome metal CoSn, an isostructural compound to FeSn, was then proposed as an alternative testbed material to detect the flat bands. Containing one extra electron per formula unit with respect to FeSn, CoSn's E_F was predicted to be above the energies of the flat bands (Fig. 3-2(a)). Another set of photoemission experiments have been performed on bulk single crystal CoSn and in fact the lattice-driven flat bands were directly visualized (Fig. 3-2(b)-(d)) [45].

The faithful representation of the original kagome lattice model reveals that *T*Sn offers an ideal material platform to explore the topology and correlation originating from the Dirac and flat band electrons. In either FeSn or CoSn, however, the im-

plications of the key band features to the macroscopic physical properties have not been discussed thus far, largely owing to their energies being deviated from E_F. In the following sections, we present our approaches in stabilizing FeSn in epitaxial thin film form (section 3.2), the morphology compatible with various experimental control parameters, and bringing the kagome-derived band singularities to E_F (section 3.3). Based on the results, we discuss their relevance to different types of emergent phenomena in this system.

3.2 Synthesis and characterization of FeSn epitaxial thin films

To engineer the kagome band structure, we first synthesize epitaxial thin films of FeSn using molecular beam epitaxy (MBE). This section provides a description of the synthesis and characterization of high quality FeSn thin films.

3.2.1 Epitaxial thin film synthesis of FeSn

For reliable epitaxy to take place, FeSn with hexagonal symmetry is deposited on (111) facet of cubic perovskite $SrTiO_3$. Inter-atom distance of the Sr network on (111) planes of $SrTiO_3$ was 5.5 Å, 3.9% larger than the in-plane lattice parameter of FeSn (a_{FeSn} = 5.3 Å). The reasonable match between the two length scales make $SrTiO_3$ (111) a lattice-matched substrate platform for FeSn (Fig. 3-3(a)).

Prior to film synthesis, $SrTiO_3$ (111) substrates (Shinkosha Co.) are dipped into Buffered Oxide Etch for 8 min and then rinsed with deionized water. This chemical etching procedure is followed by 1 h annealing in air at 1300 °C. The substrates prepared this way has flat and step-terraced surface morphologies suitable for subsequent film deposition (Fig. 3-3(b)). After loading to the growth chamber, the substrates are pre-annealed at 600 °C for 1 h to remove any residual moisture and adsorbate. Then, the substrate temperature is changed to the deposition temperature (T_d), at which Fe and Sn are co-deposited with the optimal beam equivalent pressure (BEP)

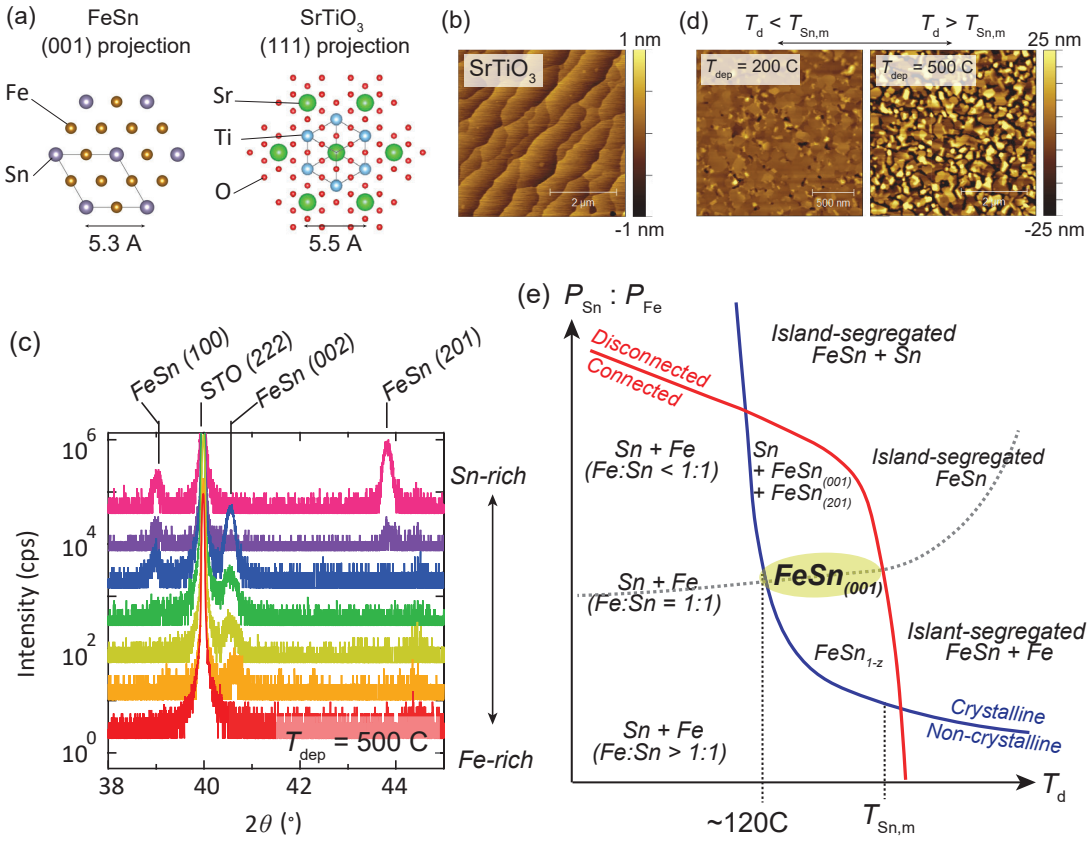

Figure 3-3: **Optimization of FeSn thin film synthesis**

(a) Schematic atomic arrangements on the FeSn (001) plane (left) and the $SrTiO_3$ (111) plane (right). (b) Atomic force microscopy (AFM) image of an annealed $SrTiO_3$ (111) substrate. (c) X-ray diffraction spectra of FeSn films synthesized with different BEP ratios. (d) AFM images of FeSn films deposited at T_d = 200 °C (left) and 500 °C (right). (e) Schematic growth phase diagram of FeSn thin films. An optimized film has high crystallinity (above the blue boundary), connected in-plane morphology (below the red boundary), and 1:1 stoichiometry (along the black dashed line). The region that satisfies these conditions is shaded yellow.

ratio $P_{\mathrm{Sn}} : P_{\mathrm{Fe}}$, where P_{Sn} and P_{Fe} are BEPs for Sn and Fe, respectively. After the deposition, some of the films are additionally capped with BaF_2 and post-annealed at $T_{\mathrm{a}} = 500$ °C to enhance crystalline quality.

The growth optimization requires precise calibrations of T_{d} and $P_{\mathrm{Sn}} : P_{\mathrm{Fe}}$. Fig. 3-3(c) shows the X-ray diffraction (XRD) spectra of a series of samples synthesized with different $P_{\mathrm{Sn}} : P_{\mathrm{Fe}}$ ($T_{\mathrm{d}} = 500$ °C fixed). The wavelength of the incident X-ray beam is $\lambda = 0.154$ nm. All of the traces show $SrTiO_3$ (222) XRD peaks at $2\theta = 39.98°$. In vicinity of the substrate peaks are observed film peaks, including those associated with the desired FeSn (002) orientation ($2\theta = 40.52°$). When films are synthesized under Sn-rich conditions, the (002) peak intensity becomes significantly suppressed. This is accompanied by the emergence of other undesired peaks from FeSn (201) ($2\theta = 44.70°$) and FeSn (100) ($2\theta = 38.90°$). By comparison, when films are synthesized under Fe-rich conditions, all of the peak intensities diminish and the films manifest nearly non-crystalline characters. At a given T_{d}, the optimal $P_{\mathrm{Sn}} : P_{\mathrm{Fe}}$ is obtained by maximizing the (002) peak intensity and minimizing the parasite peak intensities.

Turning to the optimization of T_{d}, Fig. 3-3(d) shows the atomic force microscopy (AFM) images of two films deposited at $T_{\mathrm{d}} = 200$ °C $< T_{\mathrm{Sn,melt}}$ (left) and $T_{\mathrm{d}} = 500$ °C $> T_{\mathrm{Sn,melt}}$ (right), where $T_{\mathrm{Sn,melt}} = 231$ °C is the melting point of Sn. The formation of FeSn is driven by the kinetic energies of impinged Fe and Sn atoms − the reason why higher T_{d} in general produces a film with higher crystallinity. This, however, is also accompanied by the impetus of surface tension tending to segregate the film into disconnected islands. This tendency becomes pronounced when the kinetic energy of the constituent atoms is large *e.g.* when Sn becomes a liquid at $T_{\mathrm{d}} > T_{\mathrm{Sn,melt}}$ (see Fig. 3-3(d), right). To attain high crystallinity and connected film morphology simultaneously, 120 °C $\leq T_{\mathrm{d}} < T_{\mathrm{Sn,melt}}$ is used. This is the T_{d} range between the blue boundary and the red boundary in Fig. 3-3(e), the former dividing the crystalline vs. non-crystalline phases and the latter dividing the connected vs. disconnected phases. The optimal $P_{\mathrm{Sn}} : P_{\mathrm{Fe}}$ is different for each T_{d}, mainly due to temperature dependent sticking coefficient of Fe and Sn to $SrTiO_3$ surface (see the black dashed

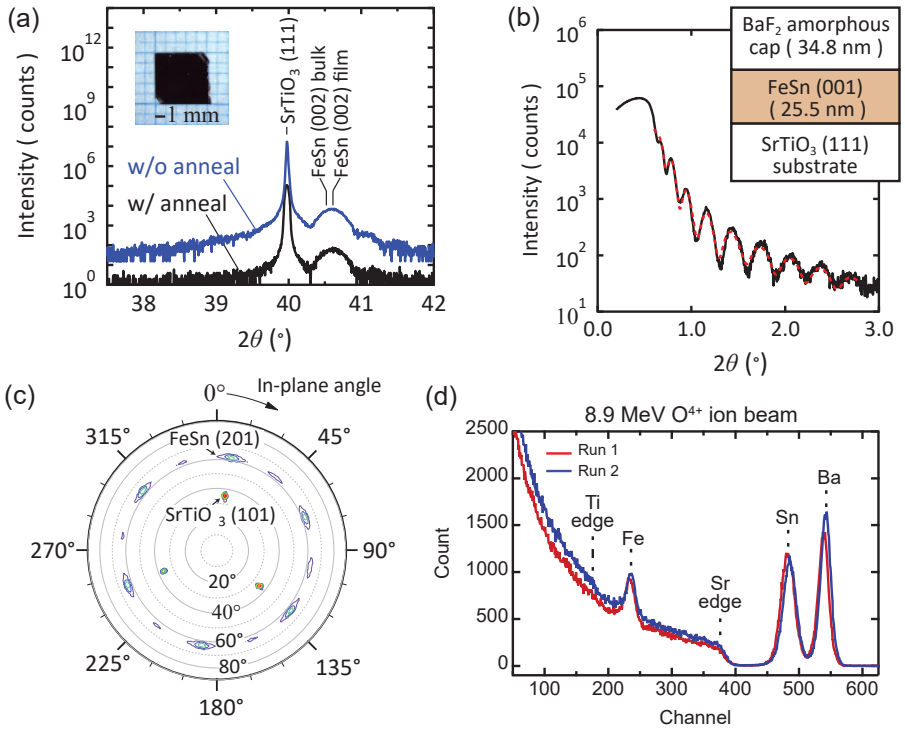

Figure 3-4: **Structural characterizations of FeSn films**

(a) X-ray diffraction spectra of FeSn films with and without the post-annealing treatment. Inset: optical micrograph of an FeSn film (scale bar: 1 mm). (b) X-ray reflectivity oscillation measured on the annealed FeSn film in (a). The best fit to the data is shown as the red dashed curve. Inset: schematic sample structure. (c) Pole figure of an FeSn film, showing the in-plane crystallographic orientation of the film with respect to that of the $SrTiO_3$ substrate. (d) Rutherford backscattering spectra of an FeSn film measured with 8.9 MeV O^{4+} beam.

line in Fig. 3-3(e)). The P_{Sn} : P_{Fe} is optimized to be $\sim$ 3:1 within the chosen T_{d} range. The optimum growth parameters need to be periodically recalibrated to keep track of time-varying chamber conditions.

3.2.2 Structural characterizations

Figure 3-4(a) shows XRD spectra of optimized FeSn films synthesized with and without the BaF_2 cap and post-annealing. Both of these samples were synthesized at T_{d} = 150 °C with an optimal BEP ratio. The pronounced film peaks are identified at $2\theta = 40.60°$ for both samples, $\sim$ 0.2% deviated from the (002) diffraction peak po-

sition of bulk FeSn. The film peaks show Laue interference fringes, indicating sharp interfaces. In a symmetric scattering configuration, peaks other than $SrTiO_3$ (lll) and FeSn ($00l$) are not observed, indicating these films are singly oriented. Fig. 3-4(b) shows the X-ray reflectivity (XRR) measurements on the annealed FeSn film. The spectrum shows a clear oscillation due to the interference of reflected X-ray beams, indicating the flat film morphology. By comparing the data to a simulated curve using the model structure (Fig. 3-4(b), inset), we determine the thicknesses of the FeSn layer and the BaF_2 layer to be $t_{\mathrm{FeSn}} = 25.5$ nm and $t_{\mathrm{BaF2}} = 34.8$ nm, respectively.

The in-plane orientation of FeSn with respect to the $SrTiO_3$ is determined by asymmetric XRD measurements. As shown in the pole figure in Fig. 3-4(c), the (201) diffraction peaks of FeSn exhibit a six-fold rotation symmetry while the (101) diffraction peaks of $SrTiO_3$ show a three-fold rotation symmetry as expected from their crystal structures. The in-plane angles of the FeSn (201) peaks match with those of the $SrTiO_3$ (101) peaks, indicating the epitaxial alignment of in-plane crystallographic orientations between the two layers. We observe small but finite intensities between the consecutive FeSn (201) peaks, likely originating from a minor domain rotated by 30° with respect to the major domain.

To further confirm the sample structure, we perform a Rutherford backscattering (RBS) measurement. Fig. 3-4(d) shows RBS spectra from 8.9 MeV O^{4+} experiments, manifesting pronounced peaks from Fe, Sn, and Ba, as well as Sr and Ti continua from the substrate contributions. By comparing the experimental traces to the simulated curves, we find the expected 1:1 stoichiometry between Fe and Sn as well as the thickness value consistent with the XRR fitting result.

3.2.3 Magnetic characterizations

Having characterized structural aspects of our FeSn films, we now investigate their magnetic properties. FeSn in its antiferromagnetic phase is reported to have an extremely high saturation field $\mu_0 H_{\mathrm{sat}} \sim 300$ T. Kakihana *et al.* have confirmed from magnetization (M) measurements of bulk single crystal FeSn that $M < 0.1\ \mu_{\mathrm{B}}$/Fe at $\mu_0 H = 10$ T and $M < 0.35\ \mu_{\mathrm{B}}$/Fe at $\mu_0 H = 50$ T with field along any high symmetry

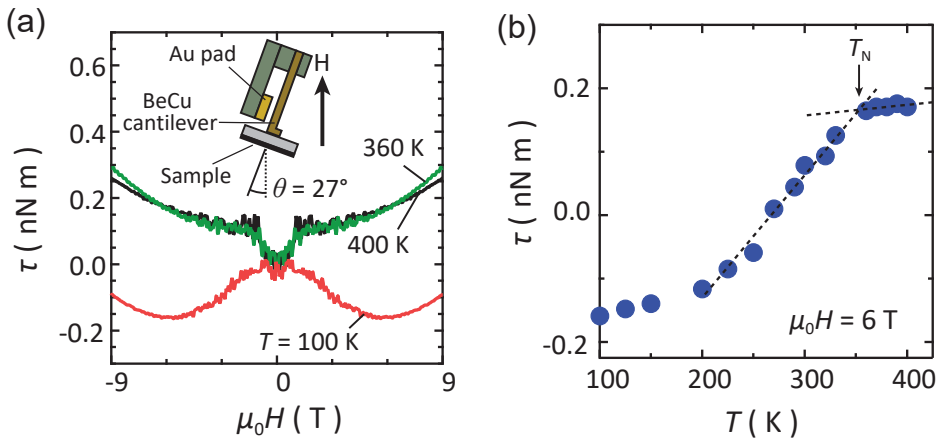

Figure 3-5: **Magnetic torque of an FeSn film**

(a) Magnetic torque τ of an FeSn film. Inset: schematic of the measurement setup. (b) Temperature dependence of τ at $\mu_0 H = 6$ T. Dashed lines show linear fits for $T \leq 330$ K and $T \geq 360$ K, whose intersection gives an estimate for T_{N}.

direction [85]. This is much smaller than the saturation magnetization $M_{\mathrm{sat}} = 1.8$ μ_{B}/Fe observed in ferromagnetic Fe_3Sn_2 at $\mu_0 H \geq 1$ T. Additionally, the small sample volume (*e.g.* 6.5×10^{-8} mol for a film with $t_{\mathrm{FeSn}} = 25$ nm and 5 mm $\times$ 5 mm area) imposes additional practical challenge in detecting M of FeSn films.

In order to probe signatures of magnetic phase transition in our films, we utilize magnetic torque τ. In the current measurement configuration, $\tau \propto \chi_\tau H^2 = (\chi_{ab} - \chi_c)H^2$, where χ_{ab} and χ_c are magnetic susceptibilities along the film in-plane and the film normal direction, respectively (Fig. 3-5(a), inset). In Fig. 3-5(a), we plot magnetic field dependent torque $\tau(H)$ of an annealed FeSn film with $t_{\mathrm{FeSn}} = 25.5$ nm. Disregarding the cusp-like anomaly within $|\mu_0 H| < 1.5$ T (which we attribute to a mechanical instability of the cantilever), $\tau(H)$ exhibits a quadratic response with nearly temperature independent positive curvature above $T = 360$ K. This reflects a weak $\chi_\tau > 0$ (or $\chi_{ab} > \chi_c$) component in the high temperature regime.

Below $T = 360$ K, $\tau(H)$ starts to deviate from a simple parabola and at 100 K it develops a negative dip around $\mu_0 H = 6$ T. This non-quadratic $\tau(H)$ below 360 K can be understood as an emergence of a $\chi_\tau < 0$ (or $\chi_{ab} < \chi_c$) component in the low field regime, which eventually gives way to the net $\chi_\tau > 0$ response in the high field

regime. This behavior can also be seen from the temperature dependent torque $\tau(T)$ at a fixed magnetic field $\mu_0 H = 6$ T (Fig. 3-5(b)). $\tau(T)$ shows a kink-like anomaly around 360 K, suggesting an onset of a distinct magnetic response. We attribute this to the appearance of an antiferromagnetic order. By linearly extrapolating the slopes of $\tau(T)$ below and above 360 K and identifying their intercepts, we find that the Neel temperature of the film is $T_{\mathrm{N,film}} \sim 353$ K, close to $T_{\mathrm{N}} = 365$ K in bulk FeSn.

3.2.4 Electrical characterizations

Electrical transport properties of FeSn films are characterized within 2 K $\leq T \leq$ 390 K and 0 T $\leq |\mu_0 H| \leq$ 9 T. Figure 3-6 shows the temperature dependent electrical resistivity $\rho_{xx}(T)$ of three different samples: a lithographically defined Hall-bar device (blue), a bare annealed film (red), and a bare unannelaed film (green). The film thicknesses in all three samples are 25.5 nm. All samples show metallic behavior with ρ_{xx} monotonically decreasing as temperature decreases ($d\rho_{xx}/dT < 0$). ρ_{xx} at 300 K (2 K) of the annealed and unannealed films are 194 $\mu\Omega$ cm (8.1 $\mu\Omega$ cm) and 102 $\mu\Omega$ cm (9.5 $\mu\Omega$ cm), respectively. This gives residual resistivity ratio RRR ($\equiv \rho_{xx}$(300 K)/ρ_{xx}(2 K)) of 24 for the annealed film and 10.7 for the unannealed film. The factor of ~ 2 increase in RRR signifies the improved quality after the post-annealing treatment. The resistivity of the Hall-bar device at 300 K (2 K) is 328 $\mu\Omega$ cm (13.7 $\mu\Omega$ cm). It exhibits $RRR = 24$, identical to that of the bare annealed film, indicating the sample quality is unaffected by the device fabrication procedures.

A close inspection of $\rho_{xx}(T)$ of the Hall-bar device reveals a kink around $T = 358$ K. To illustrate this more clearly, the derivative of $\rho_{xx}(T)$ as a function of temperature is shown in Fig 3-6(b). $d\rho_{xx}/dT$ shows a clear feature at $T = 358$ K, close to $T_{\mathrm{N,film}} =$ 353 K detected from the magnetic torque. A similar kink-like drop in $\rho_{xx}(T)$ has been observed in bulk FeSn as it enters the antiferromagnetic phase [84]. It was understood that the formation of a long-range order diminishes the spin fluctuations in the system and leads to the decrease in scattering cross-section for conduction electrons.

Figure 3-6(c) shows the magnetoresistance (MR $\equiv \frac{\Delta\rho_{xx}}{\rho_{\mathrm{xx}}(H=0)} = \frac{\rho_{\mathrm{xx}}(H)-\rho_{\mathrm{xx}}(H=0)}{\rho_{\mathrm{xx}}(H=0)}$) of the annealed FeSn film with magnetic field along the film normal direction. At T

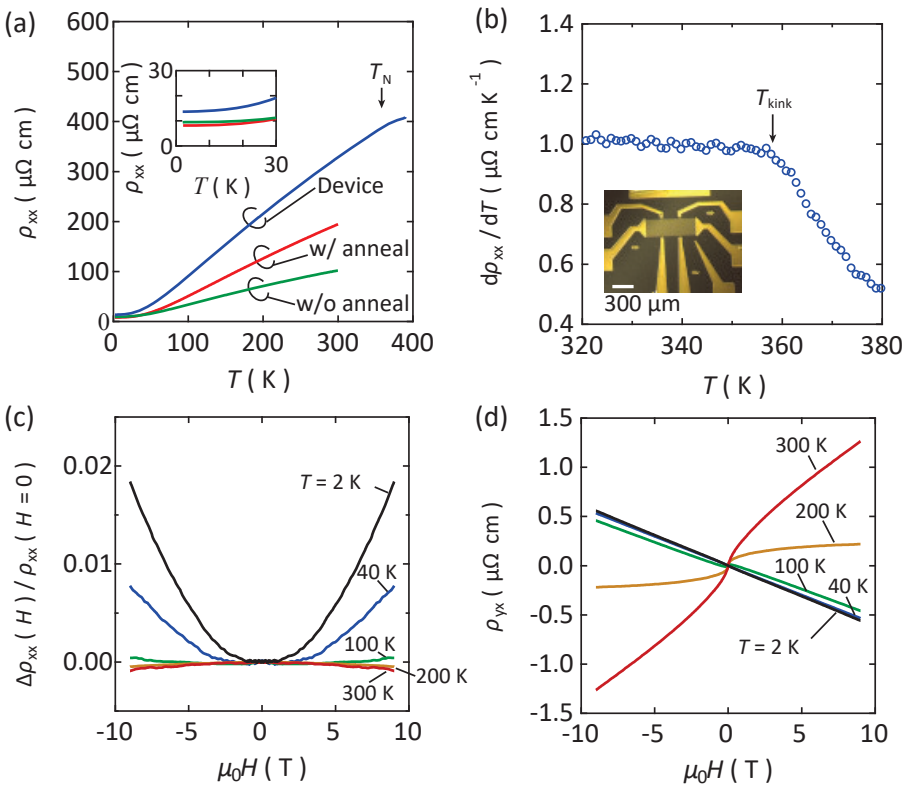

Figure 3-6: **Electrical transport of FeSn films**

(a) Temperature dependent electrical resistivity $\rho_{xx}(T)$ of a Hall-bar device (blue), a bare annealed film (red), and a bare unannealed film (green). Inset: magnified view of $\rho_{xx}(T)$ at low temperature. (b) Derivative of $\rho_{xx}(T)$ with respect to T of the Hall-bar device. Inset: optical micrograph of the Hall-bar device (scale bar: 300 μm). (c) Magnetoresistance and (d) Hall effect of the annealed film at selected temperatures.

= 300 K, we see a small quadratic negative MR with -0.09% amplitude at $\mu_0 H$ = 9 T. This negative MR suppresses as temperature decreases and becomes positive below T = 100 K. Below 100 K, the positive MR monotonically grows and reaches up to +1.84% amplitude at $\mu_0 H$ = 9 T. The quadratic negative MR response in the high temperature regime is suspected to arises from the field-suppression of magnetic fluctuations and the resultant modulation of ρ_{xx} [86]. Once the temperature drops far below T_N, the negative MR component is sufficiently suppressed and the Lorentz-force-induced positive MR component dominates.

Fig. 3-6(d) shows the Hall curves of the annealed film. The Hall coefficient R_H ($\equiv d\rho_{yx}/dH$), extracted from the linear slope near $\mu_0 H$ = 9 T, changes sign from

positive to negative as temperature decreases below $T = 200$ K. Within a single band approximation, the Hall carrier density at $T = 2$ K is estimated to be $N_H = 9.9 \times 10^{21}$ cm^{-3} (electron-like) with the corresponding mobility $\mu = 78$ cm^2 V^{-1} s^{-1}. The observed temperature dependence of R_{H} can be attributed to the temperature dependent evolution of the sublattice magnetization (M_{Fe}) in antiferromagnetic FeSn, combined with complex mobility contributions from multiple bands. We discuss the former effect in detail in section 3.3.2.

3.2.5 Quantum oscillations

To investigate the Fermi surface morphology, some of the highest quality FeSn films are characterized at the National High Magnetic Field Laboratories (NHMFL). Figure 3-7(a) shows the high field MR of an annealed film with $t_{\mathrm{FeSn}} = 25.5$ nm. The overall response is quadratic in magnetic field with growing magnitude from $T = 40$ K to $T = 0.58$ K, originating from an enhanced mobility at lower temperatures. Shubnikov-de Haas (SdH) oscillations are also observed with an onset field of $\mu_0 H \sim 30$ T. Figure 3-7(b) shows the extracted SdH oscillations at different temperatures, from which the effective mass of $m^\star = 0.38\ m_0$ can be extracted using the Lifshitz-Kosevich (LK) formula (Fig. 3-7(c), inset):

$$A\left(T\right) = A_0 \frac{2\pi^2 m^\star k_{\mathrm{B}} T}{e\hbar\mu_0 H} \sinh^{-1}\left(\frac{2\pi^2 m^\star k_{\mathrm{B}} T}{e\hbar\mu_0 H}\right) \tag{3.1}$$

where A is the SdH oscillation amplitude, A_0 is a temperature independent pre-factor, m_0 is the electron rest mass, k_{B} is the Boltzmann constant, and $\hbar$ is the reduced Planck constant. The oscillation frequency, extracted by the Fast Fourier Transformation (FFT), was $f = 145$ T (Fig. 3-7(c)). The oscillation frequency and the quantum lifetime (τ_{Q}) of the detected Fermi surface can also be estimated by fitting the field-dependent SdH amplitudes to the Dingle formula: $A\left(T, H\right) = A_1 R_T R_D \sin\left(\frac{2\pi f}{\mu_0 H} + \gamma\right)$, where A_1 is a temperature and field independent pre-factor, R_T is the thermal damping factor, R_D is the Dingle damping factor, and γ is the

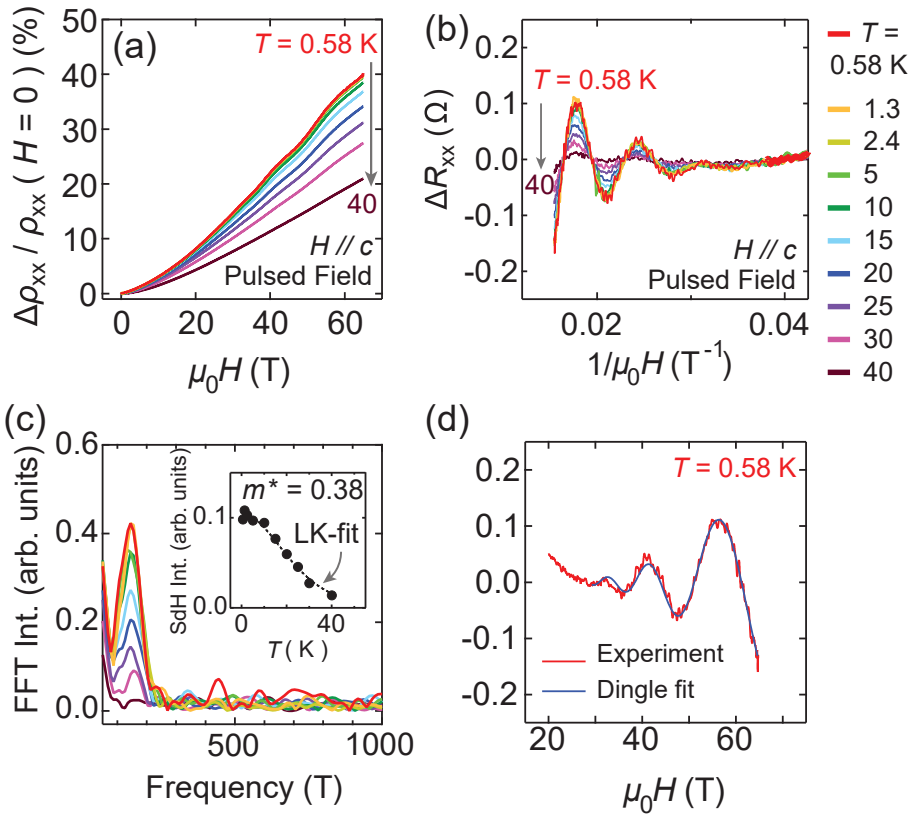

Figure 3-7: **High magnetic field transport of an FeSn film**

(a) High field magnetoresistance of an FeSn film at different temperatures. (b) Shubnikov-de Haas (SdH) oscillations at different temperatures, extracted from (a). (c) Fast Fourier Transform (FFT) of the SdH oscillations in (b). The inset shows the temperature dependent SdH oscillation amplitudes (marker) and their fit to the Lifshitz-Kosevich (LK) formula (dashed line). (d) The SdH oscillation at $T = 0.58$ K (red) and their fit to the Dingle formula (blue).

phase of the oscillation. R_{T} and R_{D} are defined as:

$$R_T = \frac{2\pi^2 m^\star k_{\mathrm{B}} T}{e\hbar\mu_0 H}\left(\sinh\left(\frac{2\pi^2 m^\star k_{\mathrm{B}} T}{e\hbar\mu_0 H}\right)\right)^{-1} \tag{3.2}$$

$$R_D = \exp\left(-\frac{2\pi^2 m^\star k_{\mathrm{B}} T_{\mathrm{D}}}{e\hbar\mu_0 H}\right) \tag{3.3}$$

where T_{D} is the Dingle temperature. Fig. 3-7(d) shows the SdH oscillation at $T = 0.58$ K and their best fit to the Dingle formula. The fit results give $T_{\mathrm{D}} = 34$ K and $f = 153$ T, the latter close to the value extracted from the FFT analysis. From the

	f_{FFT}	$m^{\star}_{\mathrm{LK}}$ (m_0)	f_{Dingle}	T_{Dingle}	Reference
Bulk α_1-pocket	1310	5.4			[44]
Bulk α_2-pocket	3641.5	3.1		4	[44]
Bulk α_3-pocket	6755.3	4.3			[44]
Bulk δ-pocket	132	0.26		30	[44]
Film#1	145	0.38	153	34	this work
Film#3	145	0.37			this work
Film#4	143	0.33	157	28	this work

Table 3.1: **Band parameters of bulk and thin film FeSn**

(Row 1−4): band parameters of bulk FeSn reported in [44]. The parameters undisclosed in [44] are left as blanks. (Row 5−7): band parameters of thin film FeSn. f_{Dingle} and T_{Dingle} for Film#3 are not available due to insufficient signal-to-noise ratio in the experimental data. Film#4 is a lithographically defined device.

extracted T_{D}, we infer $\tau_{\mathrm{Q}} = \frac{\hbar}{2\pi k_{\mathrm{B}} T_{\mathrm{D}}} = 3.6 \times 10^{-14}$ s.

The band parameters extracted from all measured samples are summarized in Table 3.2.5 (Film#1 corresponding to the one shown in Fig. 3-7). For comparison, we also include some of the reported band parameters from a de Haas-van Alphen (dHvA) experiment on bulk FeSn [44]. f and $m^{\star}$ extracted from all measured films are in good agreement with those of the δ-pocket observed in bulk, indicating comparable electronic structure and Fermi level position. The higher frequency α-pockets are not detected in our films. In the dHvA study, the α_2-pocket was identified as one of the kagome-derived Dirac bands.

To investigate the geometry of the observed Fermi surface, we perform field angle dependent SdH measurements at T = 0.35 - 0.55 K. Figure 3-8(a),(b) shows SdH oscillations of FeSn films at different magnetic field angles θ with respect to the c-axis (*i.e.* H // c corresponds to θ = 0, 180 °). Fig. 3-8(a) is the data acquired from Film #2 in the 45 T DC magnet system at T = 0.35 K, whereas Fig. 3-8(b) is the one acquired from Film#1b in the 65 T pulsed magnet system at T = 0.55 K (Film#1b is prepared by rewiring Film#1). Considering T_{D} = 34 K, two orders of magnitude higher than T = 0.35 - 0.55 K, the 0.2 K variation between the two measurement temperatures is not expected to generate a significant difference in $\Delta R_{\mathrm{xx}}/R_{\mathrm{xx}}$.

As magnetic field is tilted away from the c-axis, the oscillation frequency grad-

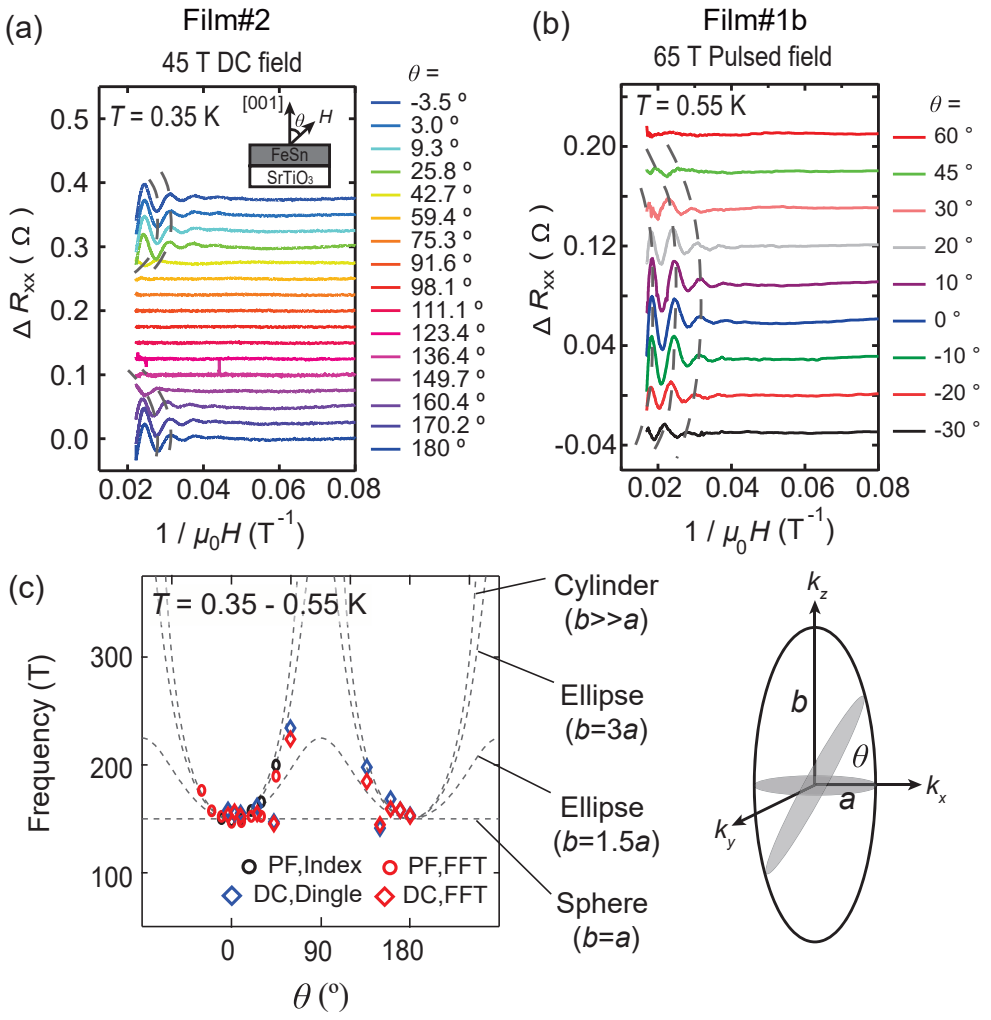

Figure 3-8: **Field angle dependent Shubnikov-de Haas oscillations**

SdH oscillations with different magnetic field angles (θ) measured (a) from Film#2 in the 45 T DC magnet system and (b) from Film#1b in the 65 T pulsed magnet system (vertical offsets are added for clarity). Dashed lines indicate the trajectories of peaks and dips. (c) θ dependent SdH oscillation frequencies. The overlaid dashed lines denote expected Fermi surface cross sections assuming different ellipticities. a and b respectively are minor and major axis of the ellipse.

ually increases, while its amplitude becomes suppressed. The change in the oscillation frequency is seen clearly from the gradual shift in the peak/dip positions of the oscillations. Each peak/dip position follows an elliptical trajectory (grey dashed lines), reflecting an anisotropic Fermi surface elongated along the c-axis. Figure 3-8(c) shows a scatter plot of the oscillation frequencies at different θ extracted from Fig. 3-8(a),(b). As well as the FFT (red) and the Dingle fitting (blue), the peak/dip indexing method (black) is applied by identifying the number of peaks/dips within a certain interval of the inverse magnetic field: $f_{\text{index}} = \left(\frac{\text{Number of oscillations}}{(1/\mu_0 H)_{\text{max}} - (1/\mu_0 H)_{\text{min}}}\right)$, where $(1/\mu_0 H)_{\text{max}}$ and $(1/\mu_0 H)_{\text{min}}$ respectively denote the maximum and minimum inverse magnetic field values at which peak/dip occurs. The overall trend is consistent with an elongated pocket with $b \sim 3a$, where a and b are minor and major axis of the ellipse, respectively (see the schematic in Fig. 3-8(c), right). This reflects the electronic hopping anisotropy in FeSn originating from its quasi-layered crystal structure.

3.3 Complete control of the kagome spectrum in FeSn

In the previous section, we have presented extensive discussions on synthesis and characterization of FeSn films. In this section we demonstrate a systematic doping control of FeSn films, which enables versatile tuning of the chemical potential and the spin structure in this system.

3.3.1 Complete coverage of doping in $(\mathbf{Fe}_{1-x-y}\mathbf{Mn}_x\mathbf{Ni}_y)(\mathbf{Sn}_{1-z})$

While the quasi-layered crystal structure of FeSn (or CoSn) has proven effective in preserving the lattice-driven Dirac and flat bands in its bulk electronic structure, its chemical potentials is deviated from the key band features. With an objective of stabilizing a system with the lattice-borne band singularities at E_{F} and further exploring their impacts on electrical and thermodynamic properties, we incorporate a wide range of chemical doping into the parent FeSn matrix.

As the effects of chemical doping include the enhancement/suppression of magnetic order as well as the change in band filling, it is instructive to first consider the

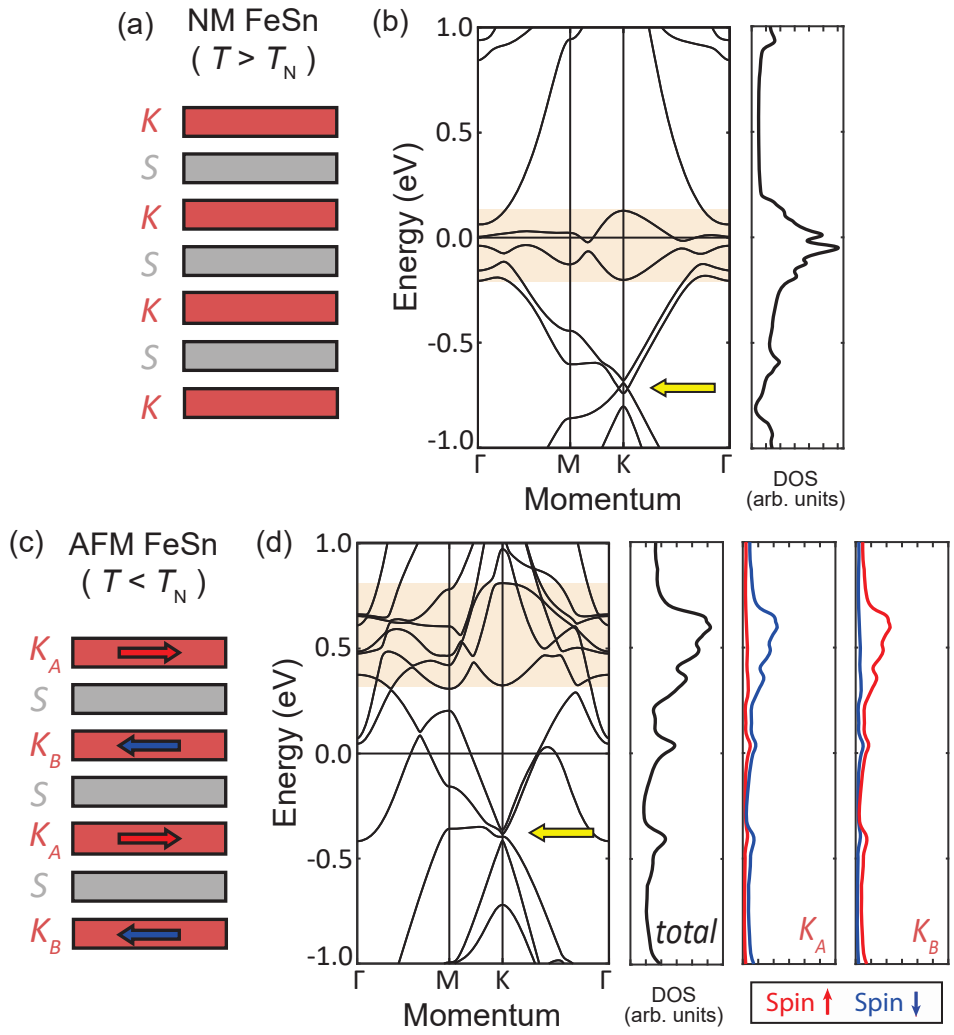

Figure 3-9: **Band structures of nonmagnetic and antiferromagnetic FeSn**

(a) Schematic stacking sequence in FeSn crystal structure, consisting of an alternating stack of the Fe_3Sn kagome layers (K, red) and the Sn_2 honeycomb layers (S, grey). (b) The $k_z = 0$ plane band structure of FeSn in the nonmagnetic state. The right column is DOS. (c) Schematic spin arrangement and (d) the $k_z = 0$ plane band structure of FeSn in the antiferromagnetic state with fully saturated Fe moments. The right columns in (d) are total and spin-/layer-resolved DOS. The Dirac points and flat bands in (b),(d) are marked with yellow arrows and orange shaded boxes, respectively. The $k_z = \pi$ plane band structures are qualitatively similar to those in (b),(d). The calculations for (b),(d) are performed by S. Fang in [75].

electronic structures of undoped FeSn in both the high temperature paramagnetic phase ($T > T_{\mathrm{N}}$; Fig. 3-9(a)) and the low temperature antiferromagnetic phase ($T \ll T_{\mathrm{N}}$; Fig. 3-9(c)) − the former harboring $M_{\mathrm{Fe}} = 0$ and the latter harboring $M_{\mathrm{Fe}} = M_{\mathrm{sat}}$. In the nonmagnetic state of FeSn, DFT band structure calculations predict that E_{F} is located within the DOS peak arising from the flat band complex (Fig. 3-9(b)). This flat band complex was identified in previous bulk single crystal studies to be a combination of two distinct kagome-derived flat bands with the d_{xz}/d_{yz}- and d_{xy}/d_{x2-y2}-orbital origins [44–46]. Also originating from multiple d-orbitals in the system, two copies of nearly iso-energy Dirac points are expected at the K-point around $E \simeq$ -700 meV. Both of these band features are quasi-two-dimensional owing to the layer-decoupled crystal structure and show qualitatively similar morphologies at the $k_z \neq 0$ planes. In the antiferromagnetic state of FeSn (Fig. 3-9(c)), exchange energy generates a spin-split band structure at each spin-polarized kagome layer, while the majority/minority spin direction is flipped between the A (K_{A}) and B (K_{B}) sublattices (Fig. 3-9(d), right). There, most of the majority spin bands shift far below E_{F}, leaving the flat bands and the Dirac points with minority spin at $E \simeq 600$ meV and $E \simeq$ -400 meV, respectively (Fig. 3-9(d), left). Focusing on the antiferromagnetic band structure, we aim to bring the Dirac points (or the flat bands) to E_{F} with an appropriate hole-doping (or electron-doping), accomplished by substituting the Fe-site in FeSn with heterogeneous 3d transition metal elements.

Epitaxial thin films of $(\mathrm{Fe}_{1-x-y}\mathrm{Mn}_x\mathrm{Ni}_y)(\mathrm{Sn}_{1-z})$ with varying doping concentrations x, y, and z are deposited on $SrTiO_3$ substrates by MBE. High degree of stoichiometric control involved in MBE synthesis facilitates the ultra-precise doping on the lattice. The films used for the doping experiments are deposited at $T_{\mathrm{d}} = 140$ - 210 °C but are not post-annealed. Bringing thermodynamically unstable doped films (especially those with high doping concentrations) to elevated temperatures tend to segregate the dopants from the parent matrix. Fig. 3-10(a) shows the XRD peak positions of $(\mathrm{Fe}_{1-x-y}\mathrm{Mn}_x\mathrm{Ni}_y)(\mathrm{Sn}_{1-z})$ films at different doping concentrations. At (x, y, z) = (0, 0, 0), the FeSn (002) diffraction peak is observed at $2\theta = 40.60°$ (black trace in Fig. 3-10(a), inset). Upon chemical doping, the position of the FeSn (002)

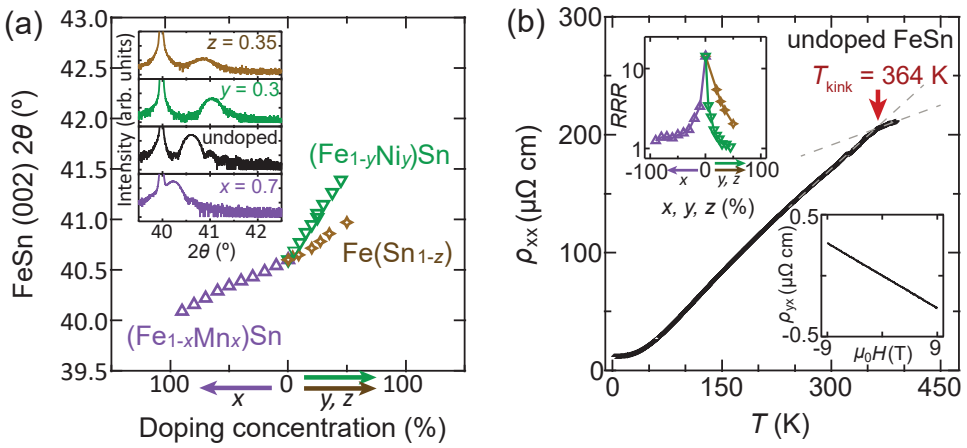

Figure 3-10: **Epitaxial stabilization of $(Fe_{1-x-y}Mn_xNi_y)(Sn_{1-z})$ films**

(a) Doping dependent (002) X-ray diffraction (XRD) peak positions of $(Fe_{1-x-y}Mn_xNi_y)(Sn_{1-z})$ films. The inset shows the XRD spectra of samples with $x = 0.7$ (purple), $y = 0.3$ (green), $z = 0.35$ (amber), and $(x, y, z) = (0, 0, 0)$ (black). (b) $\rho_{xx}(T)$ of an undoped FeSn film. The top inset shows doping dependent residual resistivity ratio of Mn-doped (purple), Ni-doped (green), and Sn-deficient (amber) samples. The bottom inset shows magnetic field dependent Hall resistivity of the undoped FeSn at $T = 2$ K.

diffraction peak shifts linearly, reflecting a gradual expansion or compression of the c-axis lattice constant. With Mn-substitution ($0 \leq x \leq 0.9$) (Fig. 3-10(a), purple markers), the peak position moves from $2\theta = 40.60°$ at $x = 0$ to $2\theta = 40.09°$ at $x = 0.9$ as the inter-layer spacing expands ($\Delta(2\theta)/\Delta x$ = -0.0057°/%). Conversely, with Ni-substitution ($0 \leq y \leq 0.45$) (Fig. 3-10(a), green markers), it moves from $2\theta = 40.60°$ at $y = 0$ to $2\theta = 41.39°$ at $y = 0.45$ as the inter-layer spacing compresses ($\Delta(2\theta)/\Delta y$ = 0.0175°/%), similar to what was observed previously in Co-doped FeSn bulk single crystal studies [87]. The systematic compression or expansion of the inter-layer spacing as a function of Mn- or Ni-substitution is in accordance with the atomic radii trend of Mn, Fe, and Ni. In addition to the Fe-site substitution, we also introduce Sn-site vacancies into the system ($0 \leq z \leq 0.5$) (Fig. 3-10(a), amber markers) and observe a peak shift from $2\theta = 40.60°$ at $z = 0$ to $2\theta = 41.97°$ at $z = 0.5$ ($\Delta(2\theta)/\Delta z$ = 0.0074°/%). This is consistent with the decrease of the inter-layer spacing when bulk single crystal FeSn ($c/2 = 2.24$) becomes Sn-deficient by 33% and 66% in Fe_3Sn_2 ($c/9 = 2.21$) and Fe_3Sn ($c/2 = 2.18$), respectively, as the kagome−stanene stacking

sequence is altered in the latter two compounds. Complete sets of XRD and XRR spectra for all measured $(Fe_{1-x-y}Mn_xNi_y)(Sn_{1-z})$ samples can be found in Fig. 3-11 and Fig. 3-12, respectively.

Fig. 3-10(b) shows the electrical transport properties of the undoped FeSn; these are the initial conditions prior to doping and are qualitatively similar to those from the annealed film presented in section 3.2.4. ρ_{xx}(T) reveals a metallic character with $RRR = 14$ (Fig. 3-10(b)). The RRR decreases as a function of doping concentration, likely due to an increased number of scattering centers in doped films. We note that RRR decreases more rapidly in Mn- and Ni-substituted samples (purple and green traces in Fig. 3-10(b), top inset) than in Sn-deficient samples (amber trace in Fig. 3-10(b), top inset). This is consistent with the expectation that the Fe_3Sn kagome layers are the active conduction channels in this system with the majority of carrier density concentrated therein. Contrary to modulation doping effect in semiconductor heterostructures, placing dopants directly at the channel layer has a more detrimental effect on the electronic mobility of the sample [88]. A kink in $\rho_{xx}(T)$ was observed at $T = 364$ K, suggestive of the antiferromagnetic order setting in. Across the entire range of x and y, the antiferromagnetic order was preserved though with modified T_N. In section 3.3.4, we present the doping dependence of T_N and interpret it in relation to the flat band driven magnetic instability. The Hall effect of FeSn measured at $T = 2$ K was linear up to $\mu_0 H = 9$ T with the Hall coefficient R_H = -3.0 $\times$ 10^{-8} Ω cm T^{-1} and the single band Hall carrier density $N_H = 2 \times 10^{22}$ cm^{-3} (electron-like). In section 3.3.3, we utilize R_H in the linear Hall regime as an indicator for doping dependent E_F positions and other signatures of band singularities.

Before investigating the doping dependent electrical transport (section 3.3.2 - 3.3.4), we wish to conclude this section by commenting from a synthesis-oriented perspective on how such a wide range of doping has been made possible. Unlike FeSn, MnSn and NiSn are thermodynamically unstable compounds and therefore do not exist in bulk single crystal form. Such instability typically obstructs reliable incorporation of Mn and Ni dopants into the FeSn matrix. When $(Fe_{1-x-y}Mn_xNi_y)Sn$ is stabilized in thin film form, however, epitaxial stabilization energy from film−substrate

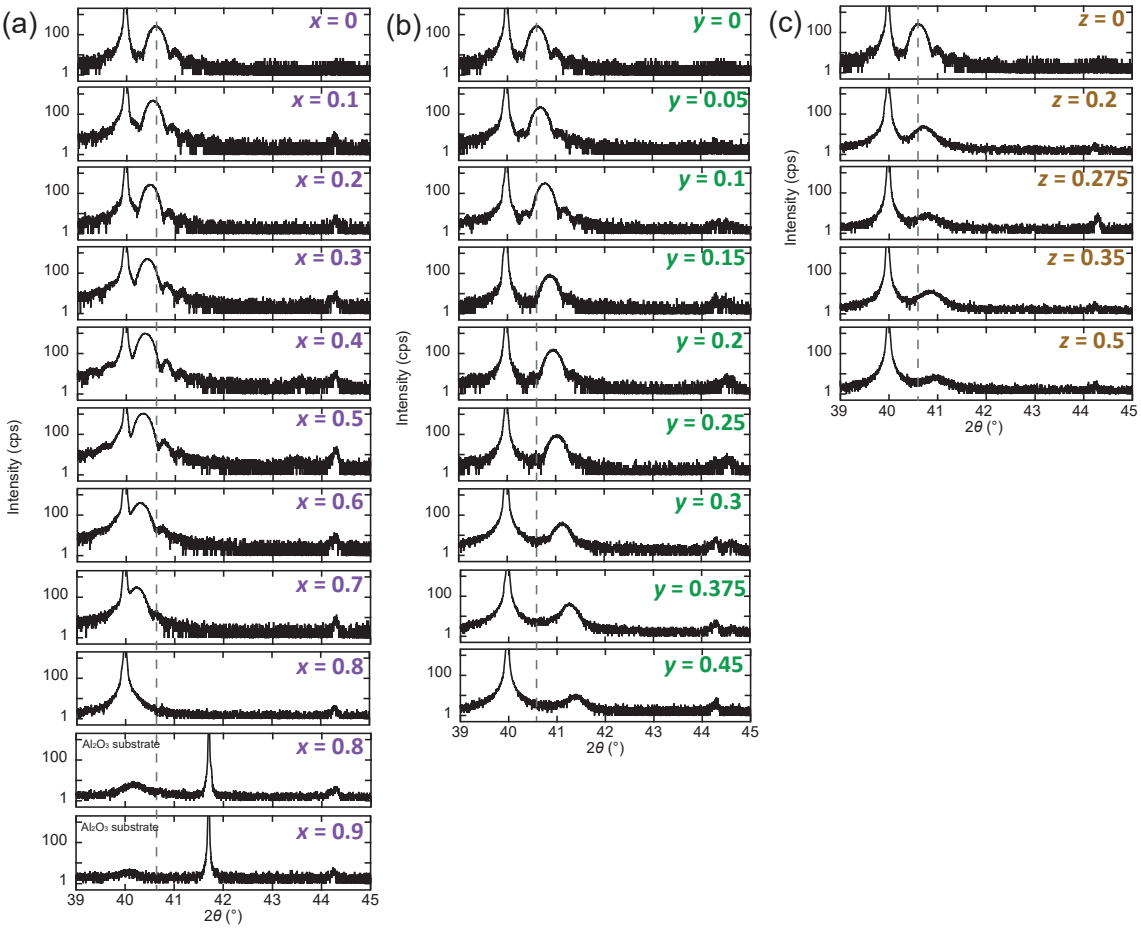

Figure 3-11: **X-ray diffraction spectra of $(Fe_{1-x-y}Mn_xNi_y)(Sn_{1-z})$ films**

X-ray diffraction spectra of (a) $(Fe_{1-x}Mn_x)Sn$, (b) $(Fe_{1-y}Ni_y)Sn$, and (c) $Fe(Sn_{1-z})$ films. All of the films are grown on $SrTiO_3$ (111) substrates except for the two films with $x = 0.8$ and 0.9 grown on Al_2O_3 (001) substrates (ninth and tenth rows in (a)).

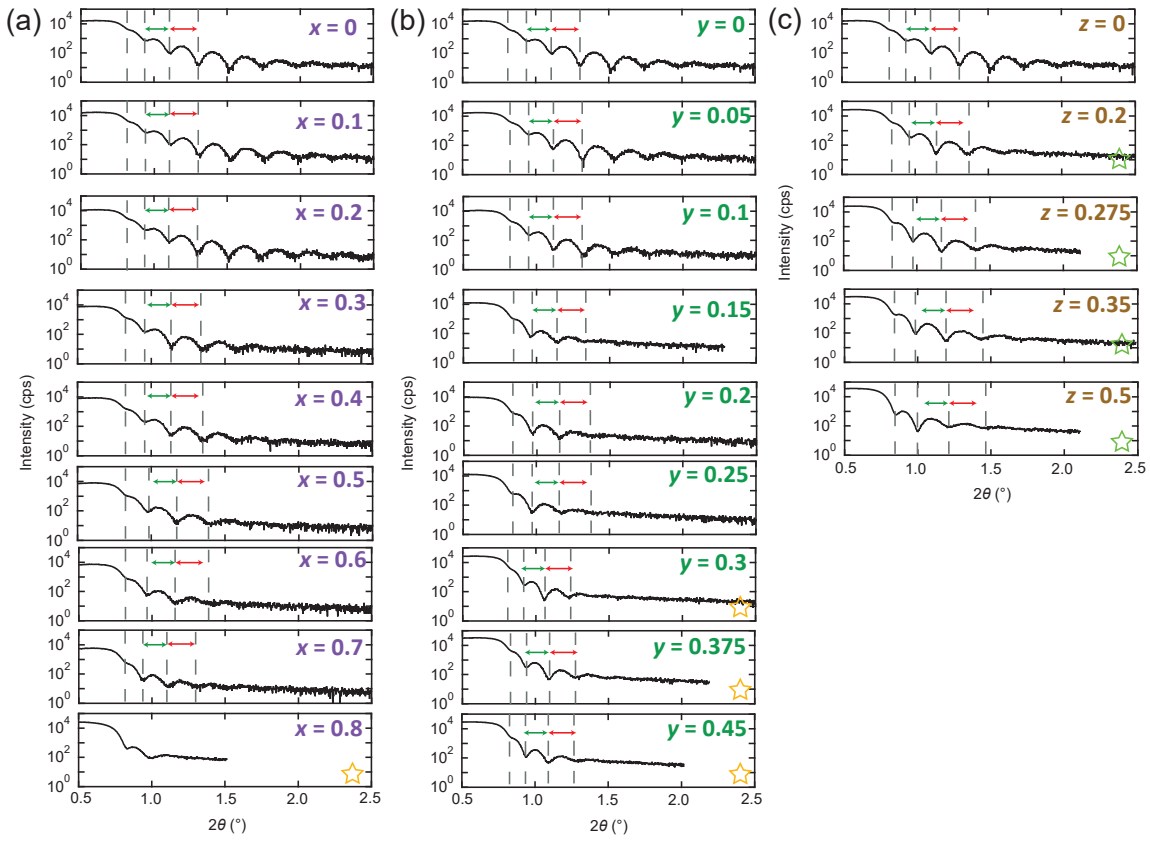

Figure 3-12: **X-ray reflectivity spectra of $(Fe_{1-x-y}Mn_xNi_y)(Sn_{1-z})$ films**

X-ray reflectivity (XRR) oscillations of (a) $(Fe_{1-x}Mn_x)Sn$, (b) $(Fe_{1-y}Ni_y)Sn$, and (c) $Fe(Sn_{1-z})$ films. Intended film thicknesses for $0 \leq x \leq 0.7$ and $0 \leq y \leq 0.25$ are 25.5 nm, while those for $0.8 \leq x \leq 0.9$ and $0.3 \leq y \leq 0.45$ (marked with yellow stars) are 31 nm. Film deposition times for $Fe(Sn_{1-z})$ (marked with lime stars) are identical as those for $(Fe_{1-x-y}Mn_xNi_y)Sn$ samples with 31 nm thickness, but their resultant thicknesses are smaller due to Sn-deficiency. Pronounced XRR oscillation is not observed for $x = 0.9$.

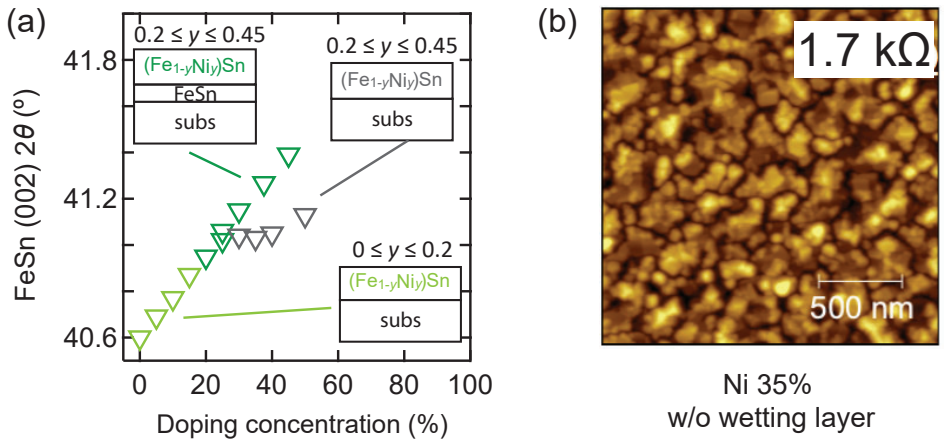

Figure 3-13: **Wetting layer assisted synthesis for heavily doped films**

(a) XRD peak positions of $(Fe_{1-y}Ni_y)Sn$ films. Results from $y \leq 0.2$, $y \geq 0.2$ with wetting layer, and $y \geq 0.2$ without wetting layer are color-coded as lime, green, and grey, respectively. Their schematic sample structures are shown in the insets. (b) AFM image of a $y = 0.35$ sample without the wetting layer.

interaction, together with limited kinetic energy of the impinged atoms given a low substrate temperature (*i.e.* 140−210°C in the present case), realizes a highly non-thermodynamic growth process. In such a regime, energy constraints in bulk synthesis can be overcome and in some cases unstable dopants can be embedded into the parent matrix with high doping efficiency (lime markers in Fig. 3-13(a)).

Even aided by the epitaxial stabilization energy, we encountered a finite solubility limit for certain dopants. Beyond $y \geq 0.2$, for instance, the XRD peak ceased to shift at the same rate as it did within $y \leq 0.2$ (grey markers in Fig. 3-13(a)). Accompanied by this behavior, a dramatic increase in film's 2-probe resistivity is observed. As can be seen from the AFM image of a nominally Ni 35%-substituted FeSn film (Fig. 3-13(b)), $y \geq 0.2$ typically results in a mixed phase film consisting of segregated islands of $(Fe_{0.8}Ni_{0.2})Sn$ and elemental Ni (which gives rise to high apparent 2-probe resistivities). To go beyond the natural solubility limit, we have employed a wetting layer assisted growth. We first coated the substrate with a less than 2 nm thick undoped FeSn. Then, using the ultrathin undoped FeSn as a wetting/seed layer, we deposited $(Fe_{1-y}Ni_y)Sn$ with $y \geq 0.2$. This restored the linear XRD peak shift as well as connected film morphologies (green markers in Fig. 3-13(a)). Given that

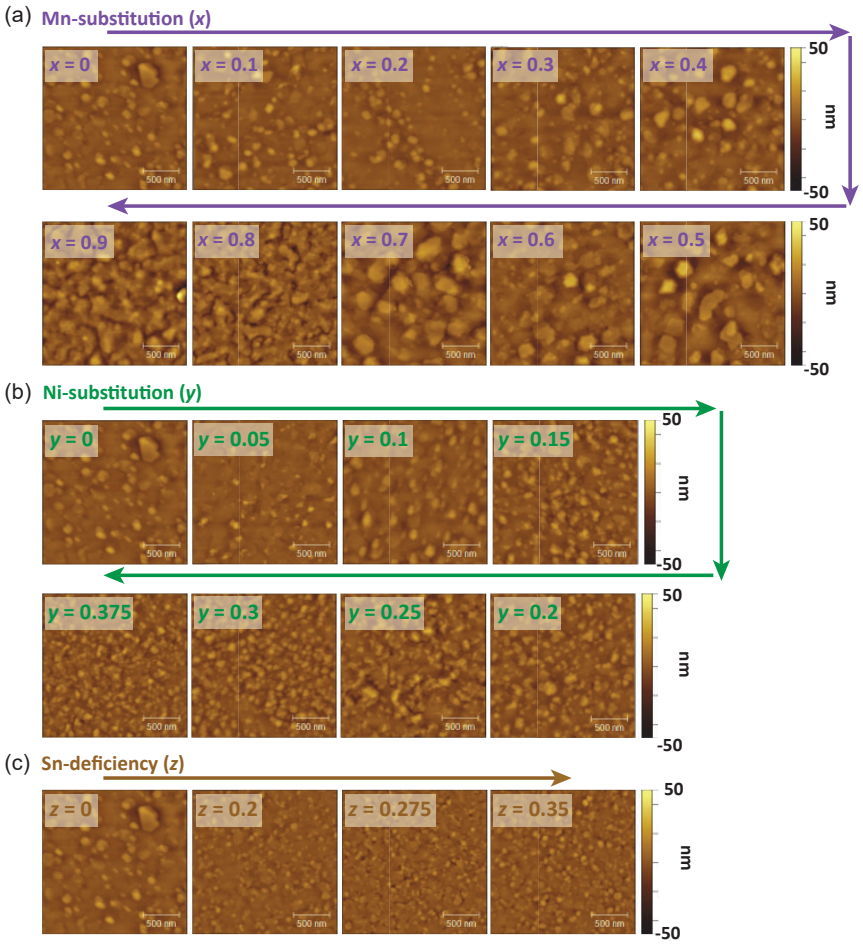

Figure 3-14: **Surface morphologies of $(Fe_{1-x-y}Mn_xNi_y)(Sn_{1-z})$ films**

AFM images of (a) $(Fe_{1-x}Mn_x)Sn$, (b) $(Fe_{1-y}Ni_y)Sn$, and (c) $Fe(Sn_{1-z})$ films.

the wetting layer is much thinner than the doped layer above, electrical transport is always dominated by the latter. A set of AFM images for $(Fe_{1-x-y}Mn_xNi_y)(Sn_{1-z})$ samples is shown in Fig. 3-14.

3.3.2 Magnetotransport properties of $(Fe_{1-x-y}Mn_xNi_y)Sn$

Having acquired a series of doped FeSn films, we now characterize their electrical transport properties. In this section, we present the complex magnetotransport properties of $(Fe_{1-x-y}Mn_xNi_y)Sn$ films across the entire range of temperature, field, and doping.

Fig. 3-15 shows the MR responses of $(Fe_{1-x}Mn_x)Sn$ films. As x increases, the

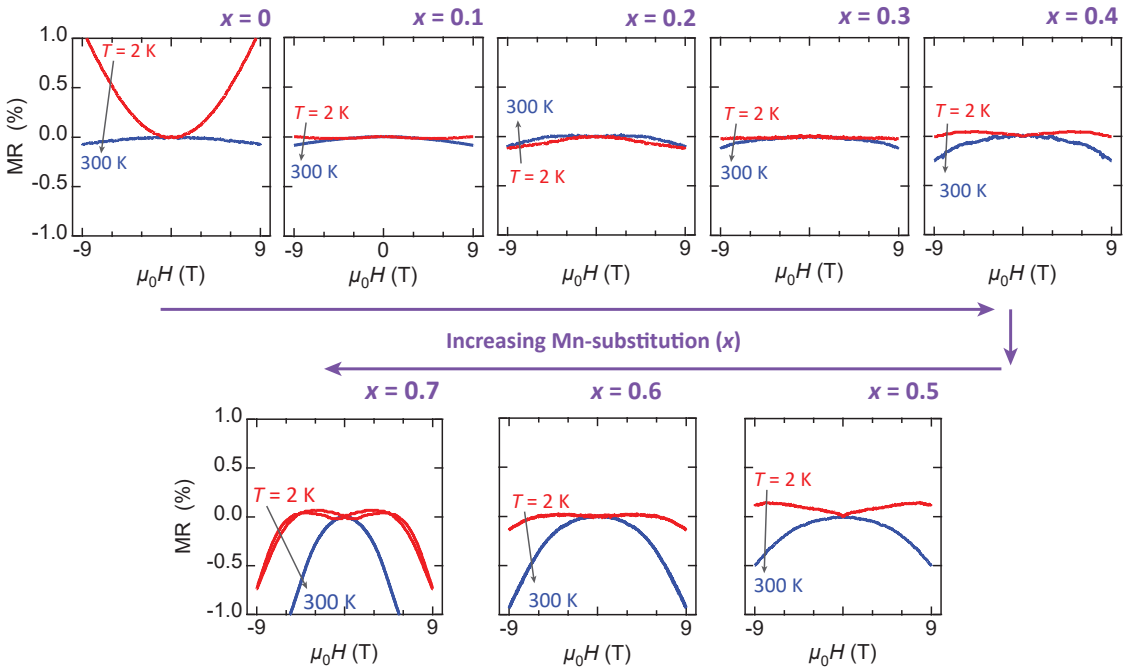

Figure 3-15: **Magnetoresistance of $(Fe_{1-x}Mn_x)Sn$**

Magnetoresistiance of $(Fe_{1-x}Mn_x)Sn$ films at $T = 2$ K (red) and $T = 300$ K (blue).

positive quadratic MR at $T = 2$ K at $x = 0$ rapidly suppresses in magnitude until it gives way to the negative quadratic MR at $x = 0.2$. This observed trend reflects the suppression of positive MR component due to decreased electronic mobility and the concurrent onset of negative MR component arising from field-suppression of fluctuating spin disorders [86]. Beyond $x = 0.2$, another cusp-like positive MR component appears in the low field in addition to the negative MR component, giving rise to an inflection point at an intermediate field range. As $x \to 0.7$, the negative MR component grows more rapidly than the cusp-like component, resulting in the net negative response at $\mu_0 H = 9$ T. We note that a similar MR response was observed in YMn_6Sn_6, a structurally similar compound to MnSn, and was ascribed to field-induced spin flop phenomena [89]. In both FeSn and YMn_6Sn_6, $T = 300$ K MR was reported to be negative. Consistent with those observations, the MR responses of all the $(Fe_{1-x}Mn_x)Sn$ films at $T = 300$ K are negative with increasing magnitude at higher x. The gradual disappearance of the characteristic MR response of FeSn and

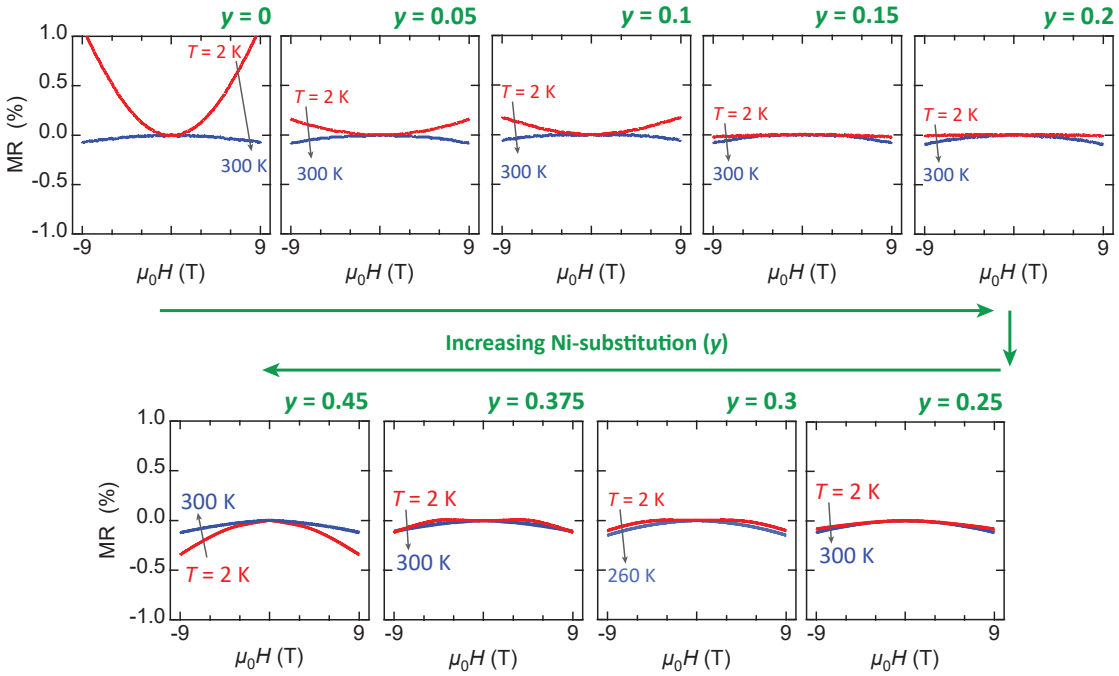

Figure 3-16: **Magnetoresistance of $(Fe_{1-y}Ni_y)Sn$**

Magnetoresistiance of $(Fe_{1-y}Ni_y)Sn$ films at $T = 2$ K (red) and $T = 300$ K (blue). For $y = 0.3$, 260 K data (light blue) are shown instead of 300 K data.

the emergence of a new type of response reminiscent of YMn_6Sn_6 indicate that our $(Fe_{1-x}Mn_x)Sn$ films realize a stable solid solution of FeSn and MnSn.

Fig. 3-16 shows the MR responses in $(Fe_{1-y}Ni_y)Sn$ films (Fig. 3-16). At $T = 2$ K, the positive quadratic MR at $y = 0$ gradually suppresses until it gives way to the negative quadratic MR beyond $y = 0.2$. At $T = 300$ K, the negative quadratic response mildly increases in magnitude as y increases. In both temperature regimes, the tendency of the negative MR component to enhance at higher doping concentration is analogous to that observed in $(Fe_{1-x}Mn_x)Sn$, except no signature of potential spin flop is observed in Ni-doping series. Overall, the doping dependence of MR in $(Fe_{1-x-y}Mn_xNi_y)Sn$ represents the systematic evolution of electrons' scattering processes as FeSn is continuously transformed to MnSn or NiSn.

Next, we investigate the Hall responses of $(Fe_{1-x-y}Mn_xNi_y)Sn$ films (Fig. 3-17). Across a wide temperature and doping range, extremely rich behaviors are observed. At $T = 2$ K, the negative Hall slope at $(x, y) = (0, 0)$ changes its magnitude and sign

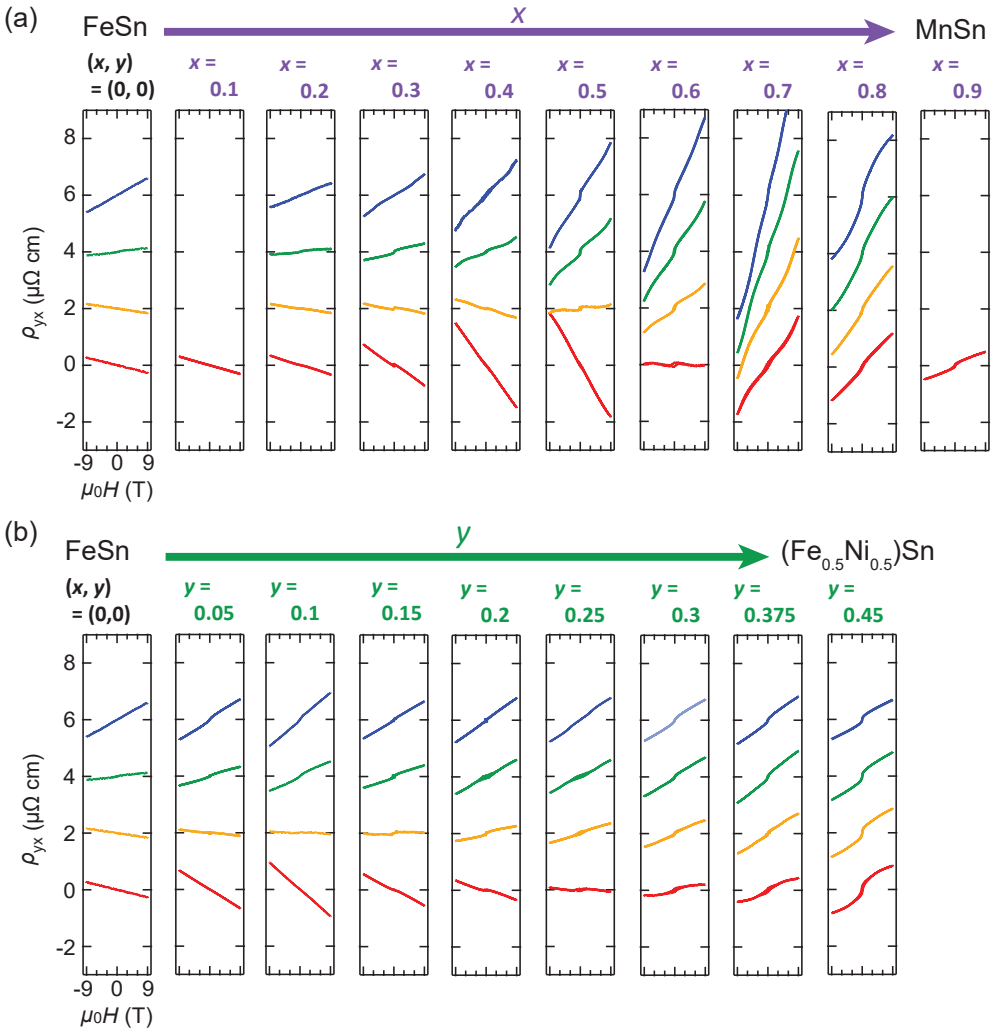

Figure 3-17: **Hall effect of $(Fe_{1-x-y}Mn_xNi_y)Sn$ within 2 K $\leq T \leq$ 300 K**

Hall resistivity ρ_{yx} of $(Fe_{1-x-y}Mn_xNi_y)Sn$ films across the full doping range. Measurements are taken between $T = 2$ K and $T = 300$ K and representative data at 2 K (red), 100 K (yellow), 200 K (green), and 300 K (navy) are shown. For $y = 0.3$, 280 K data (light blue) are shown instead of 300 K data.

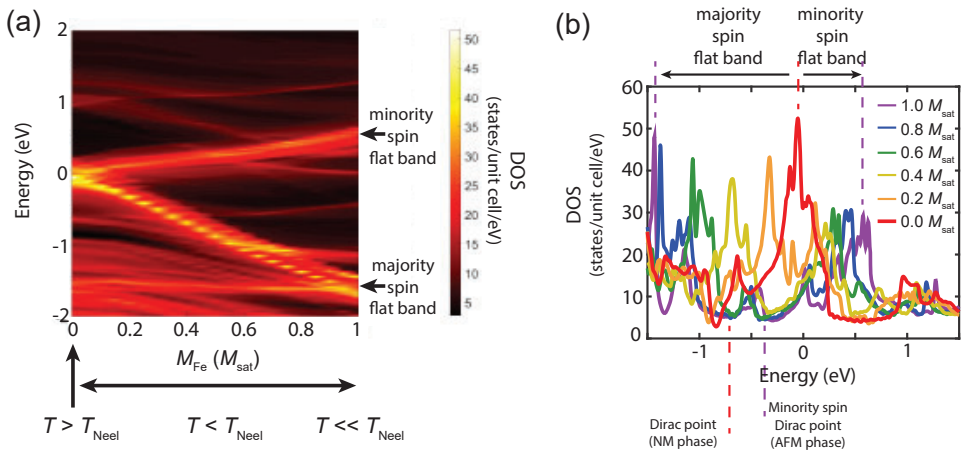

Figure 3-18: **Density of states of FeSn with varying M_{Fe}**

(a) M_{Fe}-dependent density of states of FeSn. M_{Fe} is in the unit of M_{sat}. (b) Line cut of (a) at certain M_{Fe}. The calculations here are performed by S. Fang in [75].

in a highly nonmonotonic fashion as x and y are varied, suggesting nontrivial changes in the Fermi surface morphology and carrier polarity. At $T = 300$ K, the Hall slope is consistently positive throughout the entire range of x and y, though with different magnitude at each (x, y). The Hall response within 2 K $< T <$ 300 K represents a gradual evolution between the $T = 2$ K response and the $T = 300$ K response at respective doping concentration.

The intricate temperature dependence of the Hall response can be ascribed to the strong temperature dependence of the electronic structure of FeSn; as temperature decreases below T_{N}, M_{Fe} at each spin-polarized kagome layer begins to increase and the layer-resolved band structure gradually spin-splits. To illustrate this, we perform DFT calculations of the DOS of FeSn as M_{Fe} is varied from 0 ($T > T_{\mathrm{N}}$) to M_{sat} ($T \ll T_{\mathrm{N}}$). Upon increasing M_{Fe}, the spin degenerate flat band complex, located at E_{F} for $M_{\mathrm{Fe}} = 0$, splits into the majority and minority spin species. The splitting between the two increases as a function of M_{Fe} until they settle at $E \sim$ -1.6 eV (majority) and $E \sim +0.6$ eV (minority) as $M_{\mathrm{Fe}} \rightarrow M_{\mathrm{sat}}$ at $T \ll T_{\mathrm{N}}$ (Fig. 3-18(a)). The Dirac bands also undergo a similar spin splitting. As shown in Fig. 3-18(b), the DOS dip associated with the Dirac points shift significantly as a function of M_{Fe}. Given the strong M_{Fe}-dependence (thus temperature dependence) of the band structure, electrical transport

of $(Fe_{1-x-y}Mn_xNi_y)Sn$ is expected to be highly temperature dependent, consistent with the observed Hall response (Fig. 3-17).

A challenge in tracking E_F vs. (x, y) arises from doping-dependent variation of T_N. At an arbitrary $T = T_0$ in the intermediate temperature range, M_{Fe} (correlated with T_0/T_N) and the resultant exchange splitting will be different for each doping concentration. This accounts for the seemingly non-systematic doping-dependence of the Hall slopes within 100 K $\leq T \leq$ 300 K. Despite the complication in the intermediate temperature range, however, a reliable comparison can be made between different doping concentrations in the $T \ll T_N$ regime, where M_{Fe} is sufficiently converged to M_{sat} regardless of T_N at each (x, y). In the following section, we probe the systematic shift in the chemical potential in $(Fe_{1-x-y}Mn_xNi_y)Sn$ by limiting the analysis to $T \ll T_N$ − the regime where the chemical potential of the antiferromagnetic band structure can be shifted upward or downward as a function of doping without any significant change in the exchange splitting.

3.3.3 Chemical potential tuning in $(Fe_{1-x-y}Mn_xNi_y)Sn$

To explore the chemical potential shift of $(Fe_{1-x-y}Mn_xNi_y)Sn$ in the antiferromagnetic phase, we investigate the doping dependence of R_H in the linear Hall regime, focusing primarily on the $T = 2$ K $\ll T_N$ behaviors. Fig. 3-19 shows ρ_{yx} of $(Fe_{1-x-y}Mn_xNi_y)Sn$ samples measured at $T = 2$ K across the entire Fe-site doping range ($0 \leq x \leq 0.9$, $0 \leq y \leq 0.45$). In the low doping concentration regime (x, $y \leq 0.1$), ρ_{yx} is linear up to $\mu_0 H = 9$ T. At higher doping concentrations, a small hysteresis appears at $|\mu_0 H|$ ≤ 1 T. The anomalous Hall conductivity associated with this anomaly ($\sigma_{AH} < 5$ S cm^{-1}) is significantly smaller than that of ferromagnetic kagome metal Fe_3Sn_2 (σ_{AH} > 1000 S cm^{-1} at $T = 2$ K) [52]. We identify this as arising from weak spin canting as is frequently observed in antiferromagnets [90], and thus extract the linear slope of ρ_{yx} at $|\mu_0 H| \geq 3$ T for R_H.

Overall, R_H reveals a nonmonotonic doping dependence with a few notable singular behaviors. On the hole-doping side (*i.e.* $(Fe_{1-x}Mn_x)Sn$) (along the purple arrow in Fig. 3-19), we observe a negative R_H which increases in magnitude from R_H = -3.0

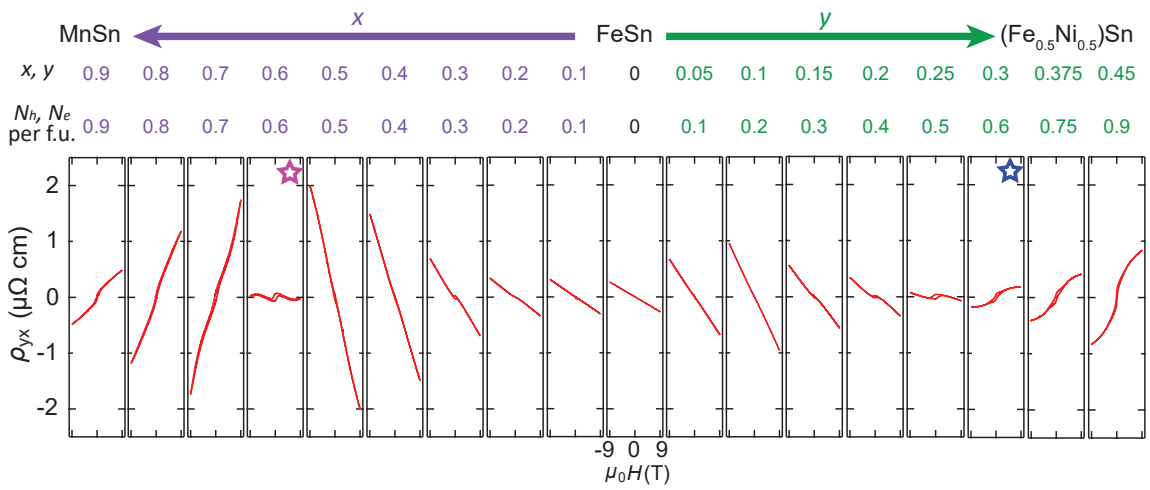

Figure 3-19: **Hall effect of $(Fe_{1-x-y}Mn_xNi_y)Sn$ at $T = 2$ K**

Magnetic field dependent ρ_{yx} of $(Fe_{1-x-y}Mn_xNi_y)Sn$ films across the entire range of (x, y) measured at $T = 2$ K. Magenta and blue stars mark the doping concentrations around which ρ_{yx} changes sign.

$\times 10^{-8}$ Ω cm T^{-1} at $x = 0$ to R_H = -2.01 $\times 10^{-7}$ Ω cm T^{-1} at $x = 0.5$, reflecting the decrease in the effective electron-like carrier density in this regime. With further increase in x, the negative R_H abruptly reverses sign from R_H = -2.01 $\times 10^{-7}$ Ω cm T^{-1} at $x = 0.5$ to $R_H = 2.11 \times 10^{-7}$ Ω cm T^{-1} at $x = 0.7$, beyond which the magnitude of positive R_H starts to decrease. This indicates the presence of an effective electron-hole compensation point beyond which hole-like carrier density increases in size with further Mn-doping. Between the two large but sign-reversed R_H values at $x = 0.5$ and 0.7, we observe a near-zero R_H value of -9.3 $\times 10^{-9}$ Ω cm T^{-1} at $x = 0.6$ (magenta star in Fig. 3-19). The behavior of R_H and $1/R_H$ on the hole-doping side of FeSn is plotted in Fig. 3-20(a) and Fig. 3-20(b), respectively, in which R_H reverses sign in a singular fashion and $1/R_H$ crosses zero smoothly around 0.6 hole-doping per formula unit (f.u.) ($x = 0.6$; magenta star and dashed line in Fig. 3-20). We note that the observed trend for R_H recalls a semimetallic ambipolar Hall signal with two oppositely signed peaks appearing on either side of $R_H = 0$ Ω cm T^{-1} as the chemical potential is swept across a charge neutral point via electrostatic gating [91–93], as observed for graphene, topological insulator Bi_2Te_3 [68, 69], and Dirac semimetal Cd_3As_2 [94].

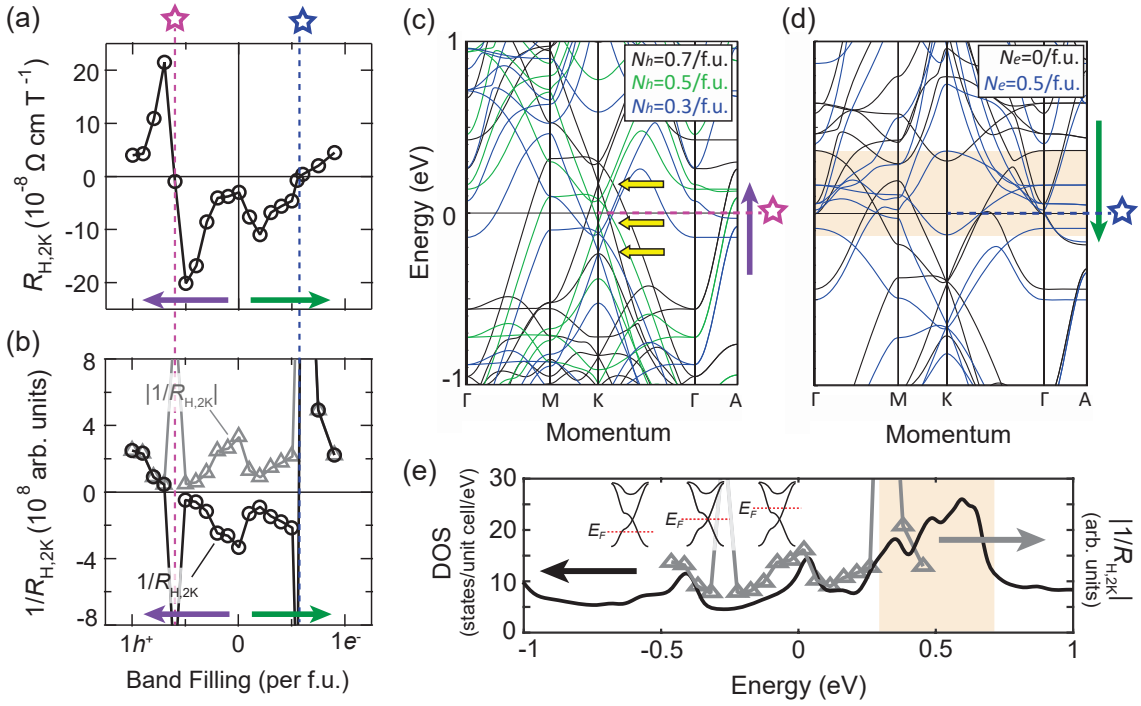

Figure 3-20: **Chemical potential tuning in $(Fe_{1-x-y}Mn_xNi_y)Sn$**

Band filling dependent (a) Hall coefficient R_H, (b) $1/R_H$ (black), and its absolute value $|1/R_H|$ (grey) extracted from Fig. 3-19 within the linear Hall regime. As the Hall carrier density is ill-defined when E_F is at the charge neutral point, a discontinuity in $1/R_H$ is expected at $x = 0.6$ as R_H crosses 0 within $0.5 < x < 0.7$. Singularities in (a),(b) are marked with magenta and blue stars and dashed lines. Band structures of $(Fe_{1-x-y}Mn_xNi_y)Sn$ with different (c) hole- and (d) electron-doping concentrations per formula unit. The Dirac points at the K-point are marked with the yellow arrows in (a). The flat band complex at $N_e = 0.5$ per f.u. is enclosed in the orange shaded box in (b). (e) Energy dependent density of states (DOS) of undoped FeSn (black). The grey trace in Fig. 3-20(b) is overlaid here. The inset depicts schematic chemical potential shift across the Dirac points. The calculations for (c),(d) are performed by M. P. Ghimire and M. Richter in [75]. The calculations for (e) are performed by S. Fang in [75].

A different type of nonmonotonic doping dependence is observed on the electron-doping side (*i.e.* $(Fe_{1-y}Ni_y)Sn$) (along the green arrow in Fig. 3-19). As y increases up to 0.1, negative R_H at $y = 0$ increases in magnitude from R_H = -3.0 $\times$ 10^{-8} Ω cm T^{-1} to R_H = -1.09 $\times$ 10^{-7} Ω cm T^{-1}. This trend, however, is reversed beyond $y > 0.1$ and R_H monotonically changes to 4.51 $\times$ 10^{-8} Ω cm T^{-1} with sign reversal occurring between $y = 0.25$ and $y = 0.3$ (blue star in Fig. 3-19). When converted to $1/R_H$, one can identify a signature consistent with an increase in carrier density as R_H changes sign. This behavior is also plotted in Fig. 3-20, with R_H smoothly crossing zero and $1/R_H$ sharply peaking around 0.55 electron-doping per f.u. ($y = 0.275$; blue star and dashed line in Fig. 3-20). This singularly spiked $1/R_H$ (or smoothly changing R_H) at $y = 0.275$ is contrasted with the singularly spiked R_H (or smoothly changing $1/R_H$) at $x = 0.6$.

To correlate the features identified from R_H and $1/R_H$ to the band structure of FeSn, we performed DFT electronic structure calculations of $(Fe_{1-x-y}Mn_xNi_y)Sn$ based on the virtual crystal approximation (VCA). The antiferromagnetic band structures of $(Fe_{1-x-y}Mn_xNi_y)Sn$ on the hole-doping and electron-doping sides are shown in Fig. 3-20(c) and Fig. 3-20(d), respectively. With hole-doping, the band features originally located below E_F of FeSn, including the Dirac points at the K-point close to $E \simeq$ -400 meV, move upward (Fig. 3-20(c)). Consistent with the Hall data, the band structure at E_F is dominantly electron-like for < 0.5 hole-doping per f.u. and hole-like for > 0.5 hole-doping per f.u.. One of the key contributing factors to this is that the Dirac points cross E_F between 0.5 and 0.7 hole-doping per f.u. (at all k_z planes; see Fig. 3-20(c)). As the Dirac bands with high Fermi velocity likely dominate the transport in the low field regime, the carrier polarity switching across the Dirac points may give rise to the Hall sign reversal at $x = 0.6$. We note that contributions from other bands may generate a finite mismatch between the energies of the Dirac points and the actual electron-hole carrier compensation; in the present case, however, the mismatch was found to be smaller than the minimum resolution of 0.1 hole-doping per f.u.. Throughout the entire Mn-doping range, these Dirac electrons are expected to be nearly massless considering the collinear easy-plane antiferromagnetism and large

saturation field (*i.e.* estimated to be $\mu_0 H_{\rm sat} \sim 300$ T based on previous single crystal studies), which enforce the preservation of combined symmetry $\Theta T_{1/2}$ within $|\mu_0 H| \leq 9$ T where Θ is time reversal symmetry and $T_{1/2}$ is fractional translation symmetry [95]. By comparison, electron-doping shifts downward the band features originally located above $E_{\rm F}$ of FeSn (Fig. 3-20(d)). Around 0.5 electron-doping per f.u., the bottom edge of the flat band complex at the K-point (at ~ 0.3 eV in undoped FeSn) moves to below $E_{\rm F}$, potentially correlated with the surge in $1/R_{\rm H}$ around $0.25 \leq y \leq 0.3$ from the Hall data. With further electron-doping, the flattest part of the flat band complex between the Γ-point and the M-point (at ~ 0.6 eV in undoped FeSn) is expected to cross $E_{\rm F}$.

The electronic properties of doped FeSn are subject to both the electron count and the details of its microscopic structure. Since VCA does not capture the latter, the obtained band dispersion stays qualitatively the same for all doping levels (Fig. 3-20(c),(d)). Within this simplified rigid band shift picture, the band filling dependent DOS of $(Fe_{1-x-y}Mn_xNi_y)Sn$ at $E_{\rm F}$ is expected to follow the energy dependent DOS of undoped FeSn. In fact, the absolute value of $1/R_{\rm H}$ at different band fillings (grey trace in Fig. 3-20(b) replotted in Fig. 3-20(e)) qualitatively tracks the energy dependent DOS of undoped FeSn, including the dip near the Dirac points and the peak at the flat band complex. These altogether show that $(Fe_{1-x-y}Mn_xNi_y)Sn$ in the antiferromagnetic phase allows extensive $E_{\rm F}$ tuning, covering the salient band features expected from a single kagome layer.

3.3.4 $T_{\rm N}$ tuning in $(Fe_{1-x-y}Mn_xNi_y)Sn$

Despite versatile tuning of $E_{\rm F}$ across the energies of the Dirac points, Dirac electrons therein are expected to stay massless as indicated by the negligible anomalous Hall response. To address the electronic structure features supporting the persistence of type-II antiferromagnetism and associated $\Theta T_{1/2}$ symmetry in $(Fe_{1-x-y}Mn_xNi_y)Sn$, we investigate the doping dependence of $T_{\rm N}$. Fig. 3-21 shows magnetic transition temperatures at different band fillings extracted from anomalies (kinks or inflections) observed in various physical quantities as well as theoretical magnetic stabilization

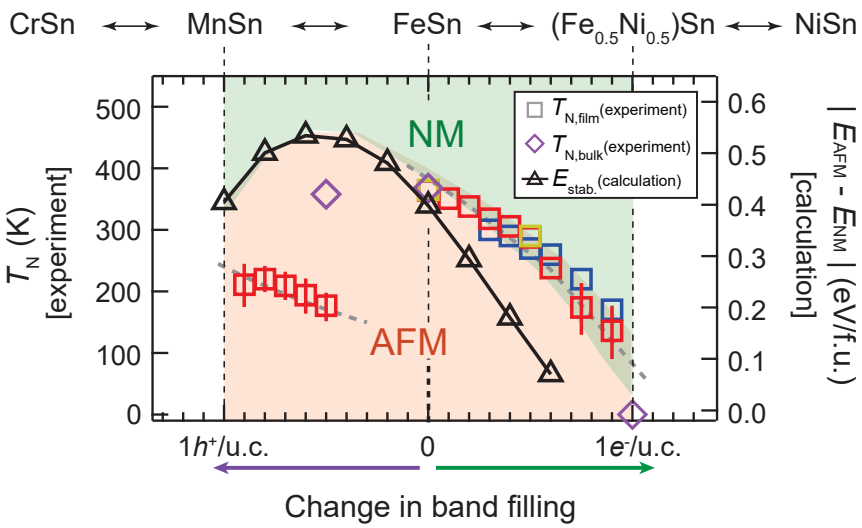

Figure 3-21: **Magnetic phase diagram of $(Fe_{1-x-y}Mn_xNi_y)Sn$**

Magnetic transition temperatures at different band fillings inferred from experiments (squares) and calculations (black triangles; by M. Richter in [75]) on $(Fe_{1-x-y}Mn_xNi_y)Sn$. Neel temperatures of bulk single crystal FeSn [44], CoSn [45], and YMn_6Sn_6 [89, 96] are also plotted at their corresponding band fillings (purple diamonds). Experimental transition temperatures are extracted from the anomalies in electrical resistivity ρ_{xx} (red) and Seebeck coefficient S_{xx} (yellow) as well as the onset of canting-induced hysteresis (blue). The transition temperatures are correlated with the calculated magnetic stabilization energies (E_{stab}), defined by the energy difference between the nonmagnetic state and the antiferromagnetic state per formula unit (f.u.). Hypothesized paramagnetic and antiferromagnetic regions are shaded with green and orange, respectively.

energies (E_{stab}). E_{stab} is defined as the energy difference of nonmagnetic FeSn and antiferromagnetic FeSn and is acquired from VCA. As magnetic phase sets in when there is a significant energy gain, E_{stab} was assumed to be correlated with T_N within a simplified Stoner-like picture. A complete set of $\rho_{xx}(T)$ traces used for identifying T_N in all measured $(Fe_{1-x-y}Mn_xNi_y)Sn$ samples can be found in Fig. 3-22. Other experimental means of extracting T_N can be found in appendix A.

The collection of experimental T_N and calculated E_{stab} delineate a phase boundary between the high temperature paramagnetic phase and the low temperature antiferromagnetic phase. Upon Ni-doping (along the green arrow in Fig. 3-21), T_N monotonically decreases from $T = 364$ K at $(x, y) = (0, 0)$ to $T \simeq 140$ K at $(x, y) = (0,$

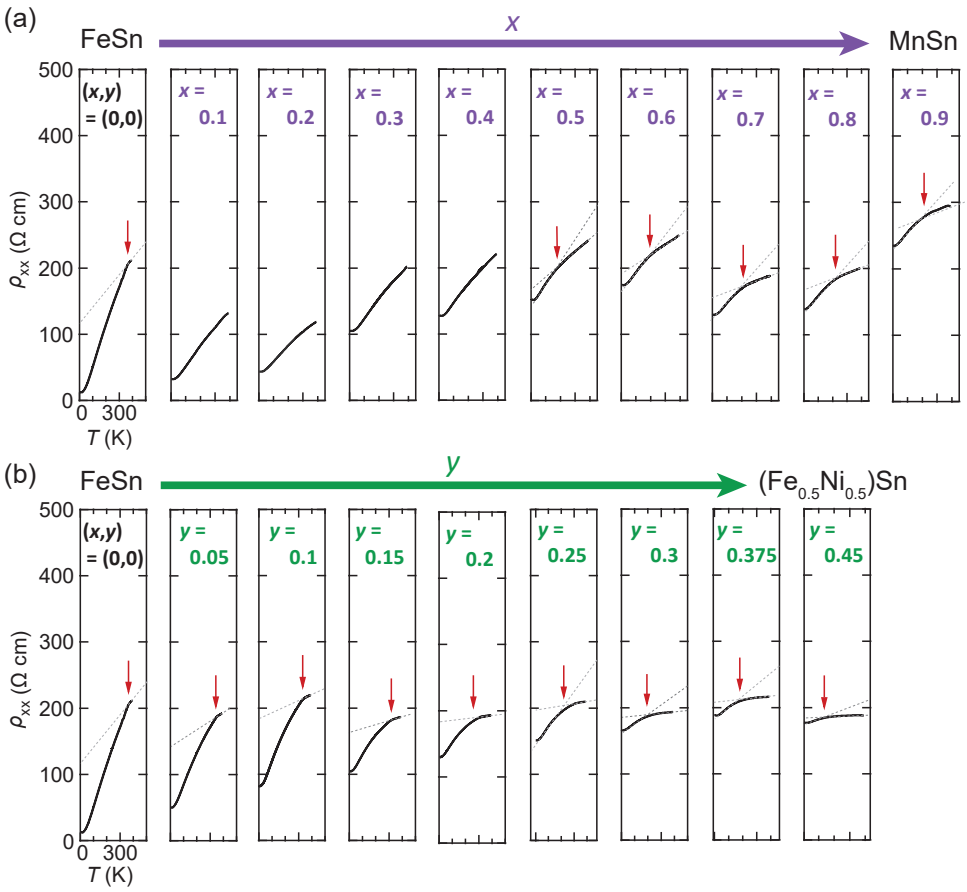

Figure 3-22: **Extracting T_{N} from $\rho_{xx}(T)$ of $(\mathbf{Fe}_{1-x-y}\mathbf{Mn}_x\mathbf{Ni}_y)\mathbf{Sn}$**

Temperature dependent electrical resistivities of $(\mathrm{Fe}_{1-x-y}\mathrm{Mn}_x\mathrm{Ni}_y)\mathrm{Sn}$ films across the entire doping range. Extracted magnetic transition temperatures are marked with the red arrows. Dashed lines are guides to the eye that denote asymptotic linear slopes above and below the suspected transition temperatures.

0.45). This trend is consistent with gradually diminishing E_{stab} upon electron doping. We ascribe the deviation between the experimental T_{N} values and the trend of E_{stab} to inability of VCA to take into account distinct local moments for different atoms in the alloy, combined with imperfect doping efficiencies in real samples. We note that a similar collapse of type-II antiferromagnetism was also observed in previous Co-doped FeSn bulk single crystal studies [87]. Upon Mn-doping (along the purple arrow in Fig. 3-21), we encounter experimental difficulties in extracting the precise phase boundary potentially occurring near or above $T = 400$ K (instrument limits). However, the projected phase boundary approaching $(x, y) = (0, 0)$ from the Ni-doping side

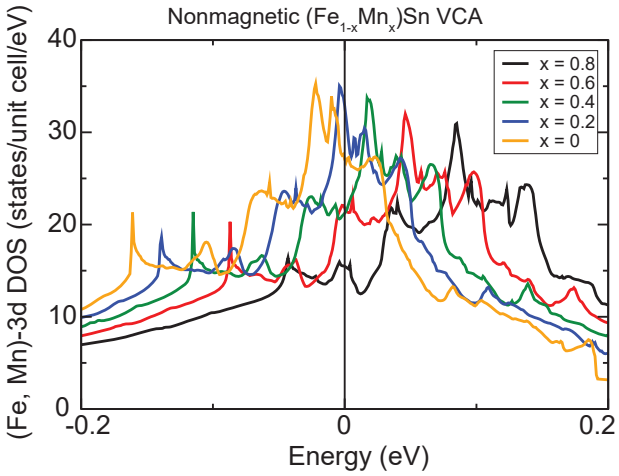

Figure 3-23: **Density of states of nonmagnetic FeSn at different band fillings**

The shift in the density of states near E_F in nonmagnetic $(Fe_{1-x}Mn_x)Sn$. The calculation is perfomed with the virtual crystal approximation (by M. Richter in [75]). Note that the apex of the flat band DOS peak crosses E_F around $x = 0.3$.

shows a tendency of T_N to continuously increase as FeSn is hole-doped, resembling the behavior of E_{stab} upon hole-doping. The persistence of canting-induced hysteresis up to $T = 300$ K (Fig. 3-17), together with the inflection in $\rho_{xx}(T)$ observed for $0.5 \leq x \leq 0.9$ around $T \simeq 200$ K reminiscent of spin reorientation transition (Fig. 3-22), provides consistent evidence of magnetic phase setting in near or above $T = 400$ K. Additionally, we find that E_{stab} shows an apex around $x = 0.5$. This indicates a broad dome-like magnetic phase boundary formed around the T_N maximum on the hole-doping side of FeSn, though the exact band filling at which T_N is maximized may deviate from $x = 0.5$ (*e.g.* insufficiency of E_{stab} in fully accounting for doping dependent magnetic interactions). Regarding the spin structure, the absence of significant σ_{AH} throughout the entire x and y reveals that the observed magnetic phase can be adiabatically connected to the antiferromagnetic phase of undoped FeSn, rather than a ferromagnetic or ferrimagnetic phase.

In order to understand the doping dependence of T_N and the persistence of the antiferromagnetic spin structure, we recall that the magnetic transition is determined by the instabilities in the high temperature paramagnetic phase. From VCA on nonmagnetic FeSn, we find that the apex of the flat band DOS peak crosses E_F of nonmagnetic

FeSn with appropriate hole-doping (Fig. 3-23), close to the band filling at which the T_{N} maximum is anticipated. Based on these findings, we hypothesize the following nature of magnetism in FeSn. An isolated nonmagnetic unit cell of FeSn, consisting of an Fe_3Sn-Sn_2 bilayer, hosts the kagome-derived flat bands and the associated DOS peak at E_{F} (Fig. 3-24(a)). This as a result provides a sufficient condition to incur an instability within each kagome layer. When a number of unit cells stack to constitute bulk FeSn, the Sn_2 layers mediate interactions between consecutive kagome layers, each of which harboring the flat band at E_{F}. Previous neutron scattering measurements, magnetization measurements, and dynamic mean field theory calculations on bulk single crystal FeSn have all corroborated the presence of an in-plane ferromagnetic exchange ($J_{\mathrm{ab}} > 0$) and an out-of-plane antiferromagnetic exchange ($J_{\mathrm{c}} < 0$) [97, 98]. In the current framework, the former can be related to the instability driven by the flat band in each layer and the latter can be related to the manner in which the Sn_2 layers mediate the kagome−kagome exchange (Fig. 3-24(b)). T_{N}, as determined by the convolution of J_{ab} (driving the intra-layer ferromagnetic spin arrangement) and J_{c} (driving the inter-layer antiferromangetic spin arrangement), may decrease as E_{F} is shifted away from the flat band DOS peak, but the global spin structure stays nearly identical as long as Sn_2 layers stay intact. Conversely, when E_{F} is shifted towards it, as in hole-doped FeSn, T_{N} may become maximized.

This interpretation can account for magnetism in a number of related quasi-layered kagome metals as well as that in $(Fe_{1-x-y}Mn_xNi_y)Sn$ films. For instance, CoSn is reported to be paramagnetic, which can be attributed to its E_{F} being deviated from the flat band DOS peak, thus failing to satisfy the Stoner criterion [45]. YMn_6Sn_6, a structurally similar compound to hypothetical MnSn with paramagnetic Y atoms intercalated every four atomic layers, is reported to host a qualitatively similar spin structure with FeSn below $T = 358$ K [89, 96]. The difference in T_{N} may originate from distinct E_{stab}, while the global spin structure (as mediated by Sn_2 layers) stays nearly identical. The realization that FeSn is an antiferromagnetic stack of quasi-two-dimensional flat band ferromagnets formulates a design principle that fine engineering of kagome−kagome exchange with different choice of spacer layer can generate a global

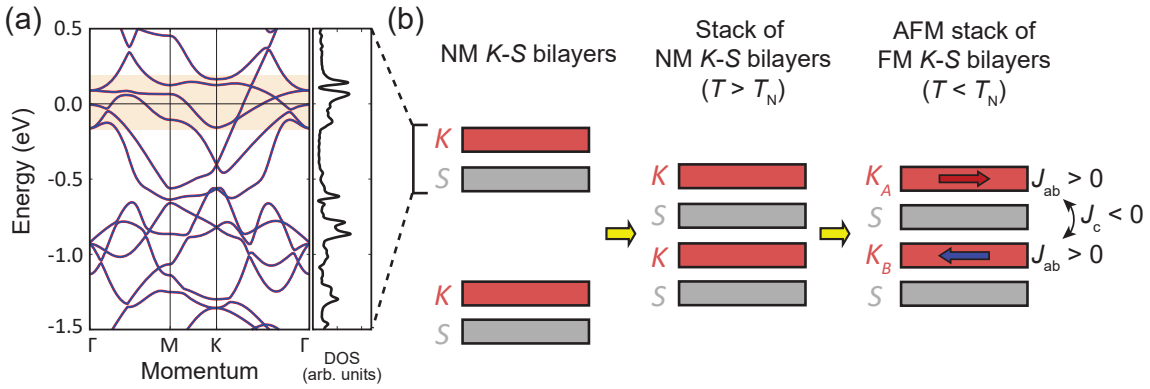

Figure 3-24: **Flat band driven nature of magnetism in FeSn**

(a) Band structure (left) and density of states (right) of a nonmagnetic $Fe_3Sn(K)-Sn_2(S)$ bilayer (by S. Fang in [75]). (b) Schematic depiction of long-range order formation in FeSn. Nonmagnetic $K-S$ bilayers (left) stack vertically to constitute nonmagnetic FeSn at $T > T_N$ (middle). A cooperation of the intra-layer ferromagnetic exchange J_{ab} (driven by the flat band within each kagome layer) and the inter-layer antiferromagnetic exchange J_c (via the S layer) stabilizes the type-II antiferromagnetism at $T < T_N$ (right).

spin structure of desire.

3.3.5 Spin structure tuning in $Fe(Sn_{1-z})$

Having identified the role of stanene layers in determining the global spin arrangement, we now explore how magnetism evolves as we introduce Sn-deficiency into the system (*i.e.* $Fe(Sn_{1-z})$). For this, we tune the number of Sn-atoms in the film, while keeping the number of Fe-atoms constant. The percentage change in the c-axis lattice constant, inferred from the XRD peak position (amber markers in Fig. 3-10(a)), is plotted in Fig. 3-25(a) (black trace). As z increases, the c-axis lattice constant gradually decreases and crosses the value expected for bulk single crystal Fe_3Sn_2 (green marker in Fig. 3-25(a)) around $z = 0.35$. Whereas the atomic inter-layer spacing diminishes by $\sim$ 1-2%, the film thickness, inferred from the XRR oscillations, decreases by $\sim$ 30% (Fig. 3-25(a), blue trace) . This stark discrepancy can be understood if the original kagome−stanene stacking sequence in FeSn becomes altered and certain stanene layers are skipped in $Fe(Sn_{1-z})$, forcing kagome layers to neighbor another

kagome layer on one side and a stanene layer on the other side.

To complement this interpretation, we perform a structural stability analysis of several possible configurations of $FeSn_{0.66}$. To simplify the comparison, we only consider limiting cases where all of the Sn-vacancies form on the identical Sn-site in each configuration. In configuration 1 (Fig. 3-26(a),(e)), all of the Sn vacancies are formed at the Fe_3Sn kagome layers. The system as a result consists of an alternating stack of Fe_3 layers (with void at the center of each kagome hexagon) and Sn_2 layers. In configuration 2 (Fig. 3-26(b),(f)), all of the Sn vacancies are formed at the Sn_2 honeycomb layers. Therefore, the system consists of an alternating stack of Fe_3Sn layers and Sn_1 layers (with half of the atoms missing). Configuration 1 and 2 maintain the original stacking sequence of FeSn, despite a high density of voids in each layer. Unlike configuration 1 and 2, configuration 3 (Fig. 3-26(c),(g)) assumes no atomic defects in either Fe_3Sn layers or Sn_2 layers. Instead, every other Sn_2 layers are skipped and a $-Fe_3Sn-Fe_3Sn-Sn_2-$ stacking sequence is realized. Configuration 4 (Fig. 3-26(d),(h)) is the stacking sequence of bulk Fe_3Sn_2. It is nearly identical to configuration 3, but has an ABC-type in-plane staggering; see section 1.3.4 for the characteristic stacking sequence of X_3Y_2.

The structural energy of each configuration, normalized by three Fe atoms and two Sn atoms (*i.e.* Fe_3Sn_2), with respect to that of configuration 3 is plotted in Fig. 3-26(i). We find that configuration 1 and 2 are less stable than the configuration 3 by 2.31 eV and 1.40 eV per Fe_3Sn_2, respectively. This prediction is consistent with our inference from the X-ray experiments that for $FeSn_{0.67}$ it is energetically more favorable to eliminate every other stanene layers, rather than to create voids at 33% of Sn-sites. With the original stacking sequence becoming naturally modified, Sn-deficient film synthesis offers a unique method to manipulate the nature of the kagome−kagome exchange interaction through layer order control. Our calculations suggest that configuration 4 is more stable than configuration 3. It remains unclear whether the kagome layers in our $FeSn_{0.66}$ films stack in a staggered fashion as in bulk Fe_3Sn_2 and further studies are required to elucidate their in-plane arrangements.

Fig. 3-25(b) shows $T = 2$ K Hall conductivity σ_{xy} for $Fe(Sn_{1-z})$ samples. σ_{xy} is

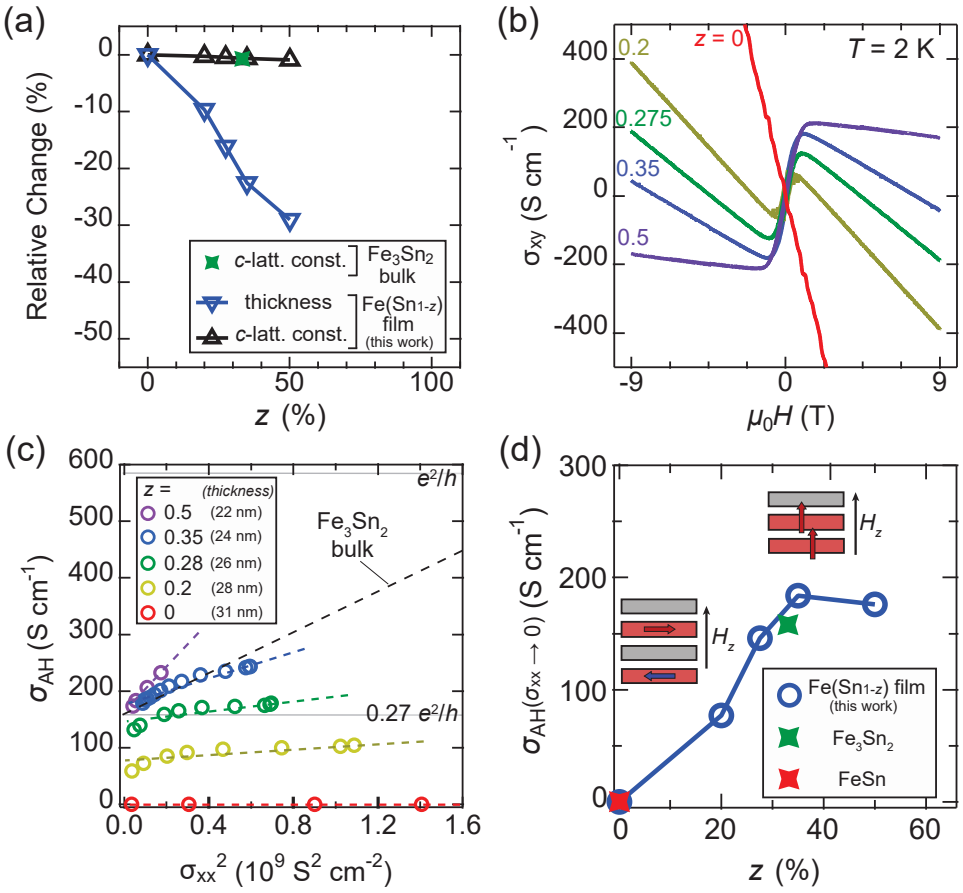

Figure 3-25: **Antiferromagnet-to-ferromagnet crossover in Fe(Sn_{1-z})**

(a) z-dependent percentage change in the c-axis lattice constant (black) and the film thickness (blue) of Fe(Sn_{1-z}) samples. The relative size of the c-axis lattice spacing in Fe_3Sn_2 with respect to that in FeSn is also indicated as green marker.(b) Magnetic field dependent Hall conductivity of Fe(Sn_{1-z}) samples measured at $T = 2$ K. (c) σ_{AH} vs. σ_{xx}^2 scaling relations of Fe(Sn_{1-z}) samples. Each color-coded dashed lines are guides to the eye for linear scaling curves. The black dashed line marks the scaling curve observed from bulk single crystal Fe_3Sn_2 in [52]. (d) $\sigma_{\mathrm{AH}}^{\mathrm{int}}$ at different z values extracted from the intercepts in (c). $\sigma_{\mathrm{AH}}^{\mathrm{int}}$ observed from Fe_3Sn_2 [52] and FeSn [44, 73] are indicated as green and red markers, respectively. Inset is a schematic depiction of spin orientations for $z \sim 0$ (left) and $z \sim 0.33$ (right) in the presence of small magnetic field along the c-axis.

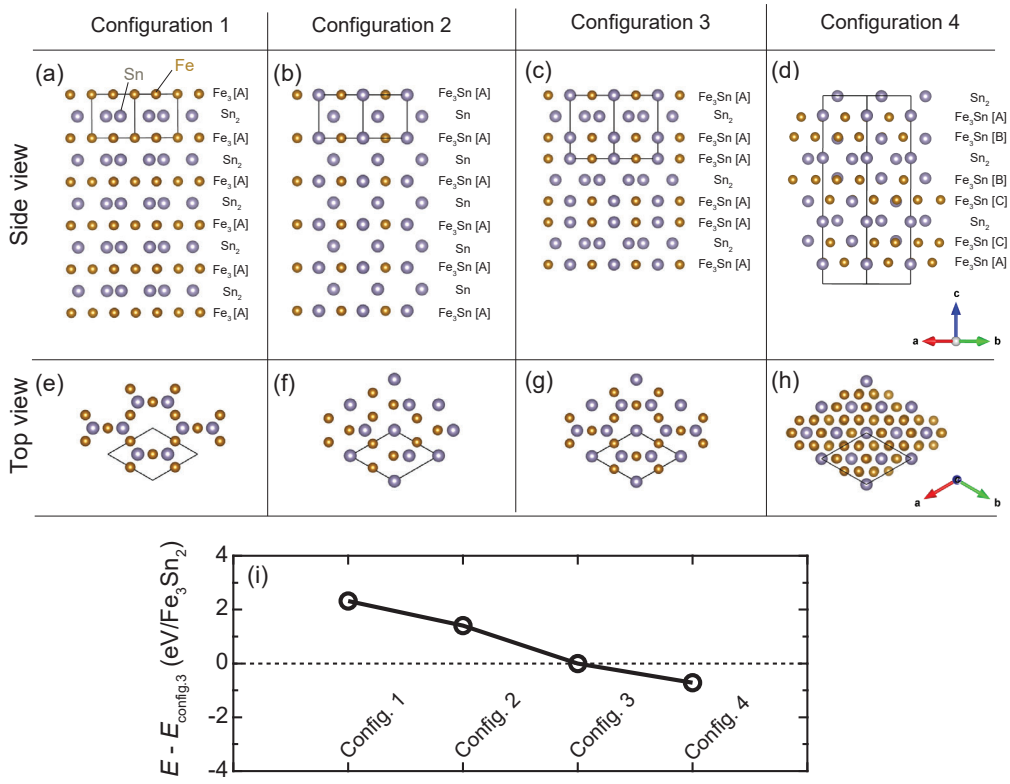

Figure 3-26: **Structural stability analysis of Sn-vacancies in $FeSn_{0.66}$**

Possible configurations of Sn-vacancies in $FeSn_{0.66}$. (a)-(d) are side views and (e)-(h) are top views of each configuration. In configuration 1 and 2, Sn-vacancies are formed at Fe_3Sn layers and Sn_2 layers, respectively. In configuration 3 and 4, every other Sn_2 layers are skipped, with no atomic defect at each constituent layer. Fe_3Sn layers in configuration 4 are stacked in a staggered fashion. (i) Structural energies of configuration 1-4 compared to that of configuration 3. These energies are normalized with respect to three Fe atoms and two Sn atoms (*i.e.* Fe_3Sn_2). The calculations for (i) are performed by S. Fang in [75].

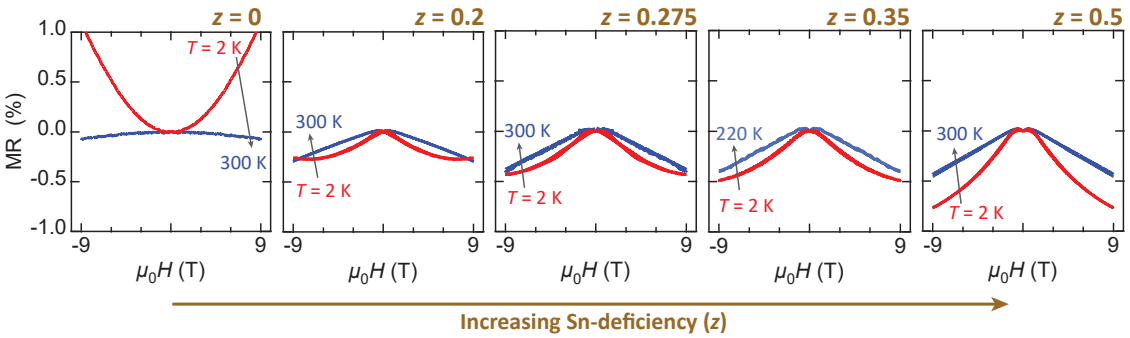

Figure 3-27: **Magnetoresistance of Fe(Sn_{1-z})**

Magnetoresistiance of Fe(Sn_{1-z}) films measured at $T = 2$ K (red) and $T = 300$ K (blue). For $z = 0.35$, $T = 220$ K data is shown instead of $T = 300$ K data.

B-linear at $z = 0$, but pronounced step-like responses within $\mu_0 H_{\rm sat} \sim 2$ T emerges at $z \geq 0.2$. $\sigma_{\rm AH}$, defined by the size of the step, increases up to 250 S cm^{-1} at $z = 0.35$ and tends to saturate beyond that. This evidences a crossover from a strong easy-plane type-II antiferromagnet at $z = 0$ to a soft ferromagnet as $z \rightarrow 0.35$. The same conclusion can drawn from the MR responses in Fe(Sn_{1-z}) (Fig. 3-27). As z increases, the positive quadratic MR at $T = 2$ K at $z = 0$ rapidly transforms into the negative linear MR at $z \geq 0.2$ with increasing magnitude at larger z. Such negative linear MR is commonly observed in ferromagnets upon field-suppression of spin fluctuation and is distinguished from the quadratic negative MR in antiferromagnetic ($Fe_{1-x-y}Mn_xNi_y$)Sn [99]. As spin fluctuations are sufficiently suppressed at higher magnetic field, it eventually gives way to nonlinear responses.

A closer examination of $\sigma_{\rm AH}$ in Fe(Sn_{1-z}) reveals a gradual topological gap opening as z increases. The net $\sigma_{\rm AH}$ consists of contributions from extrinsic ($\sigma_{\rm AH}^{\rm ext}$) and intrinsic ($\sigma_{\rm AH}^{\rm int}$) origin [100]. The former, being a scattering-originated quantity, is known to scale linearly with σ_{xx}^2. Fig. 3-25(c) shows the scaling behaviors for samples with different z. The slope of $\sigma_{\rm AH}$ vs. σ_{xx}^2 is steeper at higher z, indicating increased saturation magnetization $M_{\rm sat}$ and the associated anomalous Hall response. $\sigma_{\rm AH}^{\rm int}$, however, is a scattering-independent quantity originating from the Berry curvature in the electronic structure. For a system with significant Berry curvature, the $\sigma_{\rm AH}$ vs. σ_{xx}^2 scaling curve terminates at an intercept of size $\sigma_{\rm AH}^{\rm int}$ as $\sigma_{xx} \rightarrow 0$. As z increases,

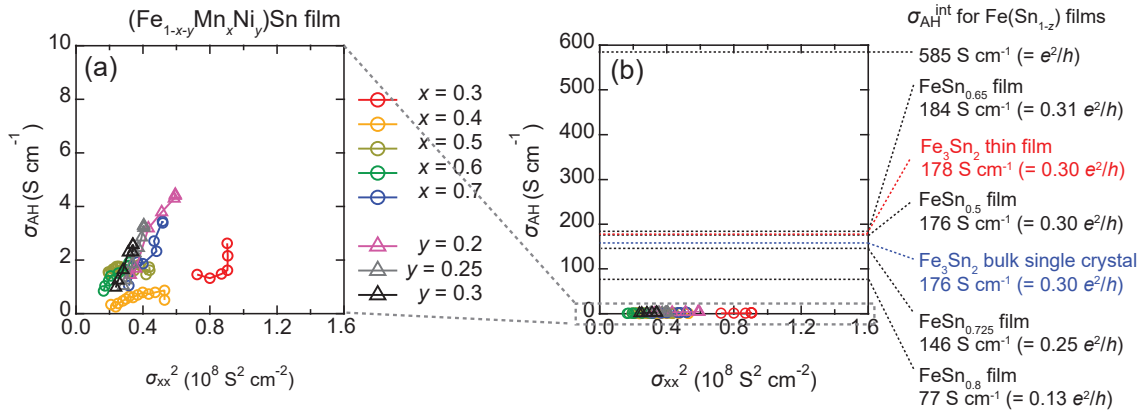

Figure 3-28: σ_{AH} **vs.** σ_{xx}^2 **scaling in** $\mathbf{(Fe_{1-x-y}Mn_xNi_y)(Sn_{1-z})}$

(a) σ_{AH} vs. σ_{xx}^2 scaling curves for $(Fe_{1-x-y}Mn_xNi_y)Sn$ films. (b) Comparison of (a) with $\sigma_{\mathrm{AH}}^{\mathrm{int}}$ for $Fe(Sn_{1-z})$ films (black) and Fe_3Sn_2 (bulk, blue [52]; film, red [101]).

the intercept also grows in magnitude to 185 S cm^{-1} (= 0.31 e^2/h) at z = 0.35 (Fig. 3-25(c),(d)). This is close to 158 S cm^{-1} (= 0.27 e^2/h) observed in bulk single crystal Fe_3Sn_2 [52] and 178 S cm^{-1} (= 0.30 e^2/h) observed in thin film Fe_3Sn_2 [101]. There, the observed $\sigma_{\mathrm{AH}}^{\mathrm{int}}$ were associated with the Berry curvature generated from the Chern gap at the Dirac point below E_{F} of Fe_3Sn_2. Given the similar magnetism and stoichiometry with Fe_3Sn_2, we hypothesize that $\sigma_{\mathrm{AH}}^{\mathrm{int}}$ in $FeSn_{0.65}$ may share the same topological origin.

Within the perspective that the Chern gap is generated in $Fe(Sn_{1-z})$, we compare the massless Dirac fermions in antiferromagnetic $(Fe_{1-x-y}Mn_xNi_y)Sn$ and massive Dirac fermions in ferromagnetic $Fe(Sn_{1-z})$. In $(Fe_{1-x-y}Mn_xNi_y)Sn$, $\sigma_{\mathrm{AH}}^{\mathrm{int}} \sim 0$ is observed across the entire doping range despite $M_{\mathrm{Fe}} = M_{\mathrm{sat}}$ within each spin-polarized kagome layer (Fig. 3-28(a)). As the effective spin-orbit gap at the Dirac point is determined by $(\vec{k} \times \vec{E}) \cdot \vec{M}$ (see section 1.3.2), the in-plane ferromagnetic moments ($M_z \sim 0$) cannot generate a gap and the Dirac electrons stay massless. In ferromagnetic $Fe(Sn_{1-z})$, a small B // B_z polarizes spins along the z-direction ($M = M_z$) and $(\vec{k} \times \vec{E}) \cdot \vec{M}$ acquires a non-zero value. This gives rise to a sizable $\sigma_{\mathrm{AH}}^{\mathrm{int}}$ determined by the relative distance between E_{F} and the Chern gap (Fig. 3-28(b)). If E_{F} of $Fe(Sn_{1-z})$ is tuned to the gap, we anticipate that $\sigma_{\mathrm{AH}}^{\mathrm{int}}$ will approach the quantized value.

3.4 Conclusions and outlook

In this chapter, we presented a comprehensive study on engineering the kagome band structure in antiferromagnetic FeSn. To facilitate systematic tuning of materials parameter, we synthesized epitaxial thin films of FeSn using MBE and confirmed their high quality with various experimental probes. Further, we demonstrated the full control of the band filling and magnetism of FeSn via site-selective chemical doping. With a wide range of Mn-/Ni-substitution, the chemical potential crossed a large energy range while maintaining the antiferromagnetic spin structure, thus allowing E_{F} to be precisely positioned at the Dirac point or at the flat band. On the other hand, Sn-deficiency gradually altered the original kagome−stanene stacking sequence of FeSn, thereby triggering the antiferromagnet-to-ferromagnet crossover as well as the onset of intrinsic anomalous Hall response. These findings altogether construct a framework of understanding that the spin structure in FeSn originates from the cooperation of flat band induced instability within each kagome layer and kagome−kagome exchange couplings mediated by the stanene layers.

A promising future direction would be to induce global ferromagnetic spin structure with simultaneous E_{F} tuning to the Dirac mass gap, so that quantized anomalous Hall response can be observed. We anticipate that a combination of Sn-deficiency and Mn-substitution can accomplish this, with the former inducing the ferromagnetic order and the latter tuning E_{F} without perturbing the global spin structure. In attaining purely edge-mode-dominated quantum transport, driving the system towards the extreme two-dimensional limit, for example by stabilizing ultrathin films, will be helpful in restricting contributions from trivial bulk bands. In a broader context, the viewpoint presented herein on long-range order formation in a quasi-layered kagome metal can be generalized as a design principle to create complex order parameters with exotic symmetries/periodicities in a wider class of kagome-based compounds. Additionally, the capability to manipulate band filling and spin structure in kagome metals will facilitate systematic evaluation of spin-orbit torque generation efficiency of the lattice-borne Dirac and flat bands under various electromagnetic environments.

Chapter 4

Surface electronic structure of FeSn

In chapter 3, we have investigated the lattice-driven Dirac and flat bands in FeSn, wherein the quasi-layered crystal structure preserves the original lattice model in its bulk electronic structure. In this chapter, we study the effects of broken inversion symmetry on the kagome band structure. From transmission electron microscopy, we identify an atomic arrangement at the heterointerface of FeSn and $SrTiO_3$ satisfying such a symmetry condition. Employing a Schottky heterojunction made from FeSn and Nb-doped $SrTiO_3$, we probe via planar tunneling spectroscopy the local density of states at the interfacial layer. We observe an anomalous enhancement in tunneling conductance within a narrow energy range and analyze the results in conjunction with first-principles calculations to reveal the presence of a two-dimensional flat band and other band reconstructions at the surface/interface of FeSn.

4.1 Interfacial atomic arrangement

Thin film heterointerface has frequently been a venue of exotic electronic states unexpected from either of the constituent layers, including Rashba spin splitting [102], two-dimensional electron gas at oxide heterointerfaces [70, 103], and complex spin texture [71]. At the origin of these interface-localized phenomena are abrupt changes in symmetry conditions, crystal environments, and electromagnetic properties across the boundary of two distinct materials. We have synthesized FeSn thin films on

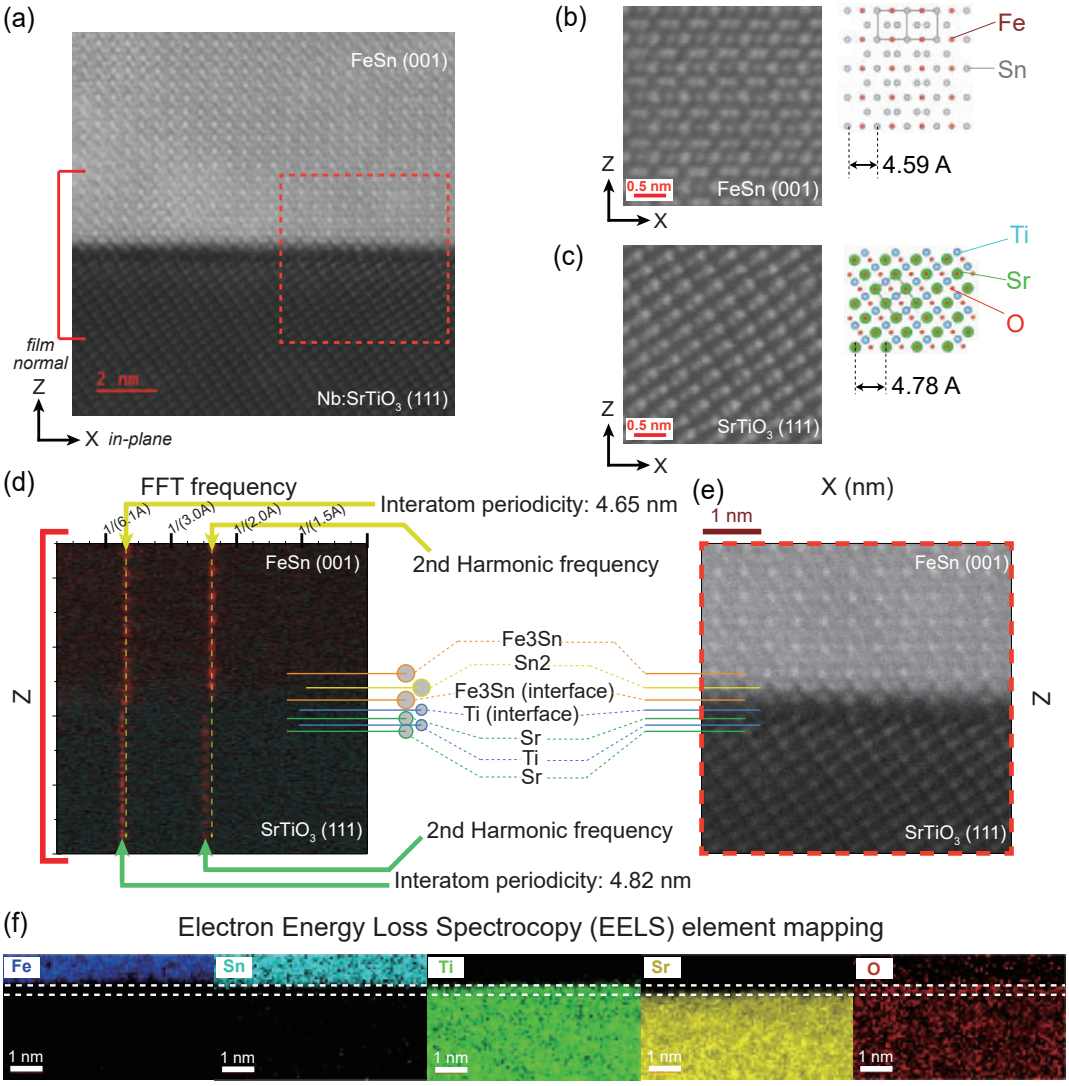

Figure 4-1: **Interface characterizations of FeSn/$SrTiO_3$**

(a) Cross-sectional transmission electron microscopy (TEM) image of a FeSn/$SrTiO_3$ (scale bar: 2 nm). Higher magnification TEM images of bulk parts of (b) the FeSn film and (c) the $SrTiO_3$ substrate (scale bars: 0.5 nm). The schematics on the right depict model atomic arrangements of (b) and (c). (d) Fast Fourier Transform (FFT) intensity color map of the selected region in (a) (marked with the red bracket). (e) Magnified view of the selected region in (a) (enclosed with the red dashed line). Horizontal color-coded lines in (d) and (e) mark Fe_3Sn layers (orange) and Sn_2 layers (yellow) in FeSn and Ti-rich layers (blue) and Sr-rich layers (green) in $SrTiO_3$ near the interface. (f) Element-specific mapping of the region near the interface, acquired from a electron energy loss spectroscopy (EELS) measurement (scale bars: 1 nm).

$SrTiO_3$ substrates (abbreviated as FeSn/$SrTiO_3$ hereon) and confirmed that the in-plane crystallographic orientations of the two materials are epitaxially locked (see section 3.2.2). This provides a sufficient condition to form a coherent film−substrate heterointerface with a well-defined symmetry conditions. To understand the detailed interface morphology of FeSn/$SrTiO_3$, we conduct cross-sectional transmission electron microscopy (TEM) measurements. The films used for this measurement are deposited at $T_d = 500$ °C in order to maximize the crystalline quality in the atomic scale. Fig. 4-1(a) is a high-angle annular dark-field TEM image of a region near the interface. It confirms that FeSn film is highly crystalline down to the interface without a polycrystalline or amorphous buffer layer. The cross-sectional views in the bulk part of FeSn and $SrTiO_3$ are shown in Fig. 4-1(b) and (c), respectively. The observed atomic arrangements are consistent with the film−substrate epitaxial relation indicated from the pole figure in section 3.2.2.

The Fe_3Sn kagome layer is found to be the preferred first-formed layer of FeSn immediately above the Ti-rich surface of $SrTiO_3$ (111). Fig. 4-1(e) is a magnified view of the selected area in Fig. 4-1(a) (enclosed with a red dashed line). From the magnified view, it is evident that the bottom-most Fe_3Sn layer has formed above the Ti-rich layer of $SrTiO_3$ and below the Sn_2 layer of FeSn. Unlike the bottom-most layer, the top-most layer of the film shows a mixture of the Fe_3Sn-termination and the Sn_2-termination. The strong tendency of the Fe-containing layer to be the first-formed layer may be related to starkly different sticking coefficients of Fe and Sn on $SrTiO_3$ at $T_d = 500$ °C. We anticipate that the observed interfacial atomic configuration will become less prominent at $T_d \ll 500$ °C.

Fig. 4-1(a),(e) show that the lattice strain is completely relaxed in FeSn. The inter-atom distance of the triangular network of Ti on $SrTiO_3$'s (111) surface is +3.9% bigger than the hexagonal lattice constant of FeSn, while the observed lattice spacing in FeSn is identical to that of a strain-free bulk FeSn. To investigate more thoroughly the exact manner through which the lattice strain is relaxed, we perform a Fast Fourier Transform (FFT) analysis for each horizontal linecut in Fig. 4-1(a) and construct a two-dimensional color map of FFT intensities (Fig. 4-1(d)). The extracted peak

frequency from the FFT analysis is expected to represent the crystal periodicity of each atomic layer. The color map shows that the lattice strain is relaxed from the interface, manifested as a discontinuity in the FFT peak frequency with a $\sim 4\%$ jump between the bottom-most Fe_3Sn layer in FeSn (orange linecut) and the top-most Sr-rich layer in $SrTiO_3$ (green linecut). From the FFT peak frequencies, we extract the corresponding inter-atom distances of 0.465 nm in FeSn and 0.482 nm in $SrTiO_3$, both approximately matched with those of bulk values (Fig. 4-1(b),(c)). The Ti-rich layer at the interface (blue linecut), sandwiched between the two layers with distinct lattice spacings, shows broadened intensities between two FFT frequencies, suggesting they retain crystallinity with distortions to accommodate chemical bonding between Sn and Sr, typical of lattice strains relaxed at the epitaxial interface.

To complement the structural analysis from TEM, we perform electron energy loss spectroscopy (EELS) measurements. The element-specific mapping in Fig. 4-1(f) shows the existence of a Ti-rich region at the interface protruding above the upper boundary of the Sr-rich region and terminating below the onset of the Sn-rich region. This is in agreement with the layer-by-layer arrangement of constituent layers revealed from TEM. The interfacial Fe_3Sn layer in $FeSn/SrTiO_3$ offer a unique platform to study the local electronic structure of the kagome layer placed under broken inversion symmetry. In the following, we demonstrate our approach in probing selectively a single atomic layer buried at the interface.

4.2 Tunneling spectroscopy across Schottky heterojunctions

In order to study the interfacial electronic structure, we synthesize another set of FeSn films on degenerate semiconductor $SrTi_{1-x}Nb_xO_3$ (Nb:$SrTiO_3$) with varying Nb concentrations ($x = 0.05, 0.2, 0.5, 0.7$ wt.%). Unlike insulating $SrTiO_3$, Nb:$SrTiO_3$ is conductive as the Fermi level ($E_{\mathrm{F,STO}}$) is located above the conduction band edge. Nb:$SrTiO_3$ substrates (Shinkosha Co.) are prepared the same way as described in

section 3.2.1 and a complete set of structural characterizations are performed to confirm that FeSn/Nb:$SrTiO_3$ have comparable qualities to FeSn/$SrTiO_3$. When the two materials come in contact, a depletion layer is formed at the Schottky interface, creating an insulating barrier useful for tunneling measurements [104–108]. Utilizing this barrier, we perform a planar tunneling spectroscopy with Nb:$SrTiO_3$, FeSn, and the Schottky barrier each serving the role of tip, sample, and vacuum in scanning tunneling microscopy. In the present case, the strain-relaxed interface (Fig. 4-1) is expected to eliminate the momentum preservation constraint for electrons tunneling across the Schottky barrier. This facilitates the energy-resolved density of states (DOS) spectroscopy of FeSn; for a strained interface, in contrast, resonant tunneling occurs only between the identical momentum states, which limits the region in the Brillouin zone accessible via tunneling spectroscopy.

Figure 4-2(a) shows a schematic of the measurement setup in a three-terminal configuration, consisting of tunnel (middle), current (right), and reference (left) electrodes. For the current and reference electrodes (or the tunnel electrode), we evaporate 10 nm thick Ti onto the Nb:$SrTiO_3$ substrate (or the FeSn film) and cap it with 100 nm thick Au. Ti is chosen as it is known to form an ohmic contact with Nb:$SrTiO_3$ owing to its low work function [109]. Upon applying a voltage on the tunnel electrode, a tunnel current flows between the tunnel and current electrodes across the Schottky barrier. Simultaneously, the reference potential with respect to the reference electrode is measured in order to precisely estimate the junction voltage V_J. As the tunnel current is determined by the total number of electronic states which electrons can tunnel into, the differential tunnel conductance $\mathrm{d}I/\mathrm{d}V$ encodes the energy-resolved DOS of FeSn overlaid onto a monotonic background signal arising from *e.g.* energy-dependent DOS of the tunnel electrode [110]. As will be described below, the background contribution is expected to negligible in the V_J regime or interest in this study.

Figure 4-2(b) shows the current-voltage (I-V) characteristics of FeSn/Nb:$SrTiO_3$ junctions with different Nb concentrations, all acquired at temperature $T = 2$ K. All of the I-V traces show nonlinear behavior, reflecting the tunneling transport process

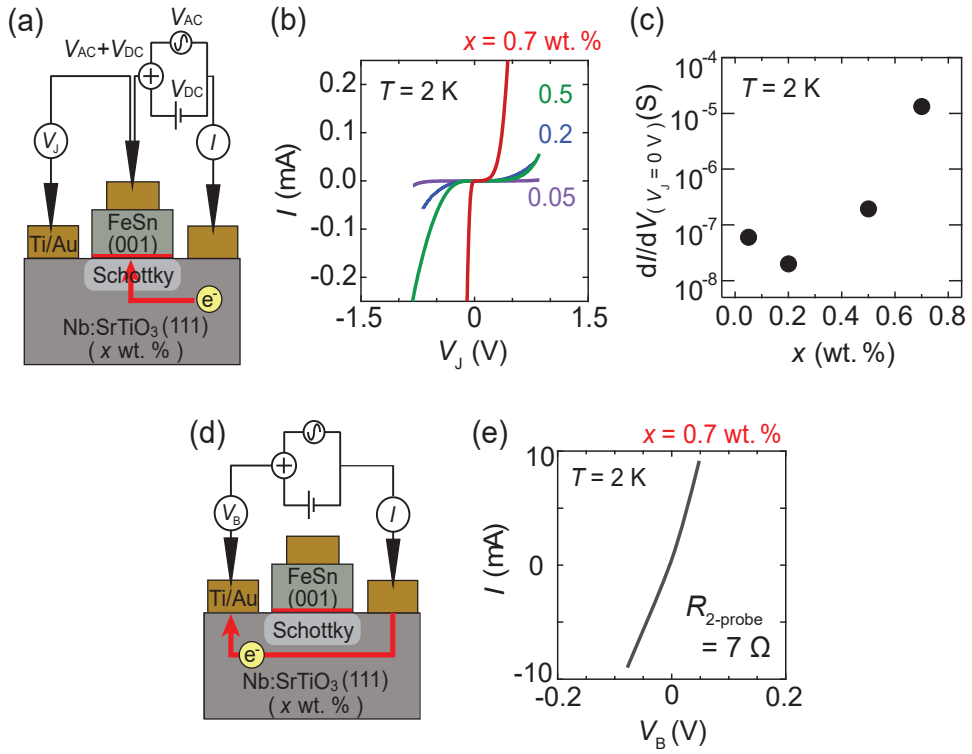

Figure 4-2: **Tunneling across FeSn/Nb:SrTiO$_3$ heteterointerfaces**

(a) Schematic of the three-terminal tunneling measurement configuration. (b) Current-voltage (I-V) characteristics of FeSn/Nb:SrTiO$_3$ junctions with different Nb concentrations. (c) Nb concentration dependent zero bias differential tunnel conductance (dI/dV(V_J = 0 V)) (d) Schematic of the two-terminal contact resistance measurement configuration. (b) I-V curve of the Ti/Nb:SrTiO$_3$ junctions. The red arrows in (a),(b) denote schematic conduction pathways of electrons. The measurements in (b),(c),(e) are taken at T = 2 K.

across these junctions. Typical tunnel resistance of a FeSn/Nb:SrTiO$_3$ (x = 0.5 wt.%) junction at T = 2 K and V_J = 0 V is > 1 MΩ with minor variance between different devices. These suggest the presence of a depletion layer at the FeSn/Nb:SrTiO$_3$ interface. Contrary to the nonlinear tunnel conductance, 7 Ω two-terminal resistance is observed across the current and the reference electrodes (Fig. 4-2(d),(e)). Subtracting the pre-calibrated series resistance of Nb:SrTiO$_3$ and the measurement electronics, we infer the contact resistance of each Ti/Nb:SrTiO$_3$ junction to be ∼ 2−3 Ω, several orders of magnitude more conductive than typical FeSn/Nb:SrTiO$_3$ tunnel contacts. This ensures reliable operation of the three-terminal measurement scheme.

Figure 4-2(c) shows the exponential growth of the zero bias differential tunnel conductance at $T = 2$ K for Nb concentration from $x = 0.05$ wt.% to $x = 0.7$ wt.%. We ascribe this to the cooperative action of increased carrier density (N_{d}) and suppressed dielectric permittivity (ϵ) in highly doped Nb:$SrTiO_3$ dramatically shortening the depletion layer width $W_{\mathrm{d}} = \sqrt{\frac{2\epsilon\Delta\Psi_{\mathrm{WF}}}{qN_d}}$ at the Schottky interface, where q is elementary charge and $\Delta\Psi_{\mathrm{WF}}$ is work function difference between FeSn and Nb:$SrTiO_3$ [111, 112]. Consistent with our observation, recent studies have shown that $W_{\mathrm{d}} \sim 5$ nm in Pt/Nb:$SrTiO_3$ ($x = 0.7$ wt.%) Schottky junctions [113], in contrast with $W_{\mathrm{d}} > 100$ nm in metal/Nb:$SrTiO_3$ Schottky junctions with lower Nb concentrations [114–116].

4.2.1 Temperature dependent tunnel conductance

Figure 4-3(a) and 4-3(b) show I-V curves and $\mathrm{d}I/\mathrm{d}V$ spectra, respectively, at different temperatures for the FeSn/Nb:$SrTiO_3$ ($x = 0.5$ wt.%) junction (the device micrograph is shown in Fig. 4-3(a) inset). The overall tunnel conductance, as revealed from both I and $\mathrm{d}I/\mathrm{d}V$, gradually increases as T increases, owing to the exponential growth of thermionic emission (TE) and thermionic field emission (TFE) contributions (Fig. 4-3(e)). This resembles the behavior of a conventional Schottky junction in which enhanced thermal activation probability of electrons at high temperature boosts the junction current [117]. We note that TE and TFE are non-resonant processes ($E_{\mathrm{initial}} \neq E_{\mathrm{final}}$, where E_{initial} and E_{final} are the energy of electrons before and after the tunneling, respectively) and therefore the resulting broadened $\mathrm{d}I/\mathrm{d}V$ spectra at high temperatures obscure fine DOS features of FeSn.

When TE and TFE are sufficiently suppressed at low T, the $\mathrm{d}I/\mathrm{d}V$ spectra reveal an anomalous behavior beyond that expected for conventional Schottky barriers. Figure 4-3(c),(d) show the temperature dependent $\mathrm{d}I/\mathrm{d}V$ for negative and positive V_{J}, respectively. While $\mathrm{d}I/\mathrm{d}V$ over the entire range of V_{J} decreases exponentially as T decreases, within the finite range -400 mV $< V_{\mathrm{J}} <$ -100 mV, the exponential suppression of $\mathrm{d}I/\mathrm{d}V$ at $T > 100$ K gives way to an upturn in $\mathrm{d}I/\mathrm{d}V$ at $T < 100$ K. This feature is also manifested as a broad peak in the $\mathrm{d}I/\mathrm{d}V$ spectra at $T = 2$ K ($V_{\mathrm{J,peak}}$

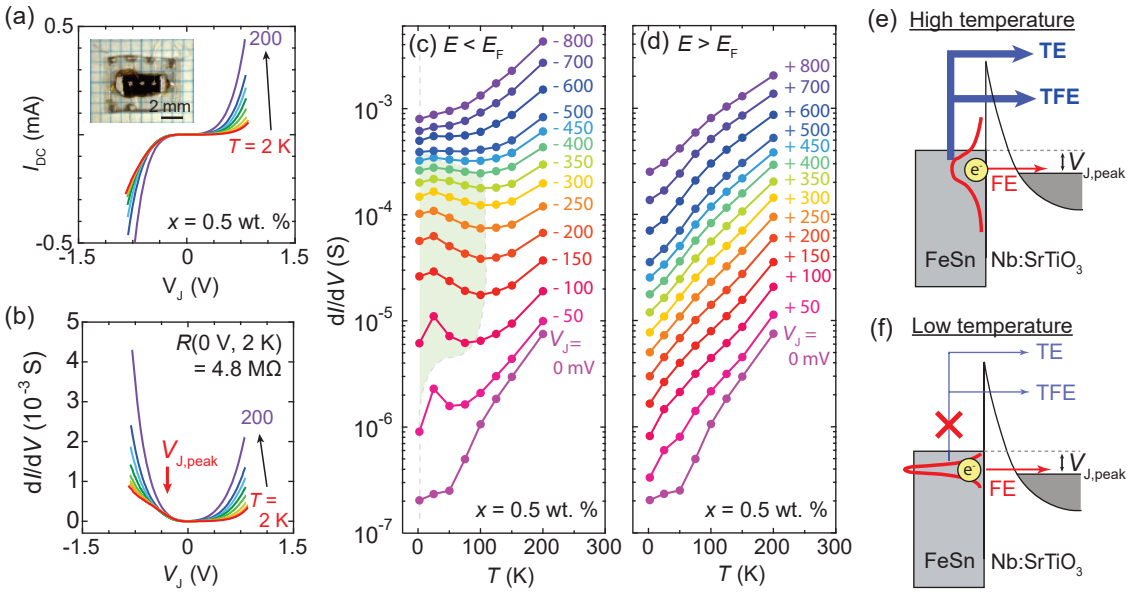

Figure 4-3: **Temperature dependent tunneling in a $x = 0.5$ wt.% junction**

(a) I-V characteristics and (b) dI/dV spectra at different temperatures for a FeSn/Nb:SrTiO$_3$ junction with $x = 0.5$ wt.%. The measurements are taken at T = 2, 25, 50, 75, 100, 125, 150, 200 K. The inset is an optical micrograph of the measured device. The red arrow in (b) marks $V_{\mathrm{J,peak}}$, the position of the broad peak at low temperature. (c),(d) Temperature dependent dI/dV for negative and positive V_{J}. The green-shaded area denotes the region in which dI/dV increases as temperature decreases. Schematic of the tunneling mechanisms across the Schottky barrier at (e) high and (f) low temperatures. Non-resonant thermionic emission (TE) and thermionic field emission (TFE) processes dominate in the high temperature regime, whereas resonant field emission (FE) process through the barrier dominates in the low temperature regime.

= -250 mV) that eventually broadens and diminishes at higher T. Qualitatively, this feature can be understood as combination of an anomalous enhancement of dI/dV in the negative bias range with the conventional rectifying behavior of Schottky diodes in the positive bias range. The enhancement in dI/dV in the low T regime suggests a dominant field emission (FE) contribution to the tunneling conductance for $T < 100$ K (Fig. 4-3(f)). FE is a resonant process ($E_{\mathrm{initial}} = E_{\mathrm{final}}$) that becomes more pronounced at lower T when thermal band broadening in FeSn and inelastic scattering events within the tunnel barrier both diminish. The upturn in dI/dV around $V_{\mathrm{J,peak}}$ = -250 mV for $T < 100$ K suggests high DOS concentrated at this energy in FeSn,

manifested more clearly as the FE dominates the tunneling process.

4.2.2 Barrier width dependent tunnel conductance

To elucidate the origin of the anomaly in $\mathrm{d}I/\mathrm{d}V$ seen in Fig. 4-3, we investigate the tunneling characteristics of two junctions with different Nb concentrations: $\mathrm{d}I/\mathrm{d}V$ spectra for $x = 0.2$ wt.% and $x = 0.7$ wt.% are shown in Fig. 4-4(a) and Fig. 4-4(b), respectively (I-V curves consistent with these $\mathrm{d}I/\mathrm{d}V$ spectra can be found in Fig. 4-5). The prominent peak in $\mathrm{d}I/\mathrm{d}V$ is resolved around $V_{\mathrm{J,peak}}$ = -180 mV at $T = 2$ K for $x = 0.7$ wt.%, whilst for $x = 0.2$ wt.% the feature is absent. We hypothesize that the 20-fold enhancement of the overall tunneling conductance from $x = 0.2$ wt.% to $x = 0.7$ wt.% originates from the difference in the depletion layer widths. The peak in $\mathrm{d}I/\mathrm{d}V$ at $T = 2$ K for the $x = 0.7$ wt.% junction occurs at a similar energy range as the broad peak in $\mathrm{d}I/\mathrm{d}V$ for the $x = 0.5$ wt.% junction ($V_{\mathrm{J,peak}}$ = -250 mV, Fig. 4-3), indicating a common origin of the two conductance anomalies. If originating from a peak in the DOS of FeSn, it would be expected that the associated peak feature in $\mathrm{d}I/\mathrm{d}V$ would become less prominent for junctions with lower Nb concentrations, as electron tunneling across the thicker depletion layer involves more inelastic scattering events (Fig. 4-4(d),(e)). This is in fact what is observed as the Nb concentration is changed from $x = 0.7$ wt.% to $x = 0.2$ wt.%. Therefore, we conclude that the enhancement in $\mathrm{d}I/\mathrm{d}V$ at $V_{\mathrm{J,peak}}$ = -180 mV originates from a large, narrowly peaked DOS at this energy in FeSn.

Figure 4-4(c) shows the temperature dependence of $\mathrm{d}I/\mathrm{d}V$ peak positions and full widths at half maximum of the $x = 0.7$ wt.% junction. In addition to the peak broadening from TE and TFE contributions, the peak position gradually shifts from $V_{\mathrm{J,peak}}$ = -180 mV at $T = 2$ K to $V_{\mathrm{J,peak}}$ = -560 mV at $T = 200$ K. Though the triangular shape of the tunnel barrier and nonlinear dielectric properties of $SrTiO_3$ in metal/Nb:$SrTiO_3$ Schottky junctions are known to displace the energy axis of the tunneling spectra from the actual DOS spectra by $\sim$10 mV at high temperature, this is insufficient to explain the large shift of $|\Delta V_{\mathrm{J,peak}}| = 380$ mV. We instead explain this shift in relation to the modulation of the surface band structure by considering spin

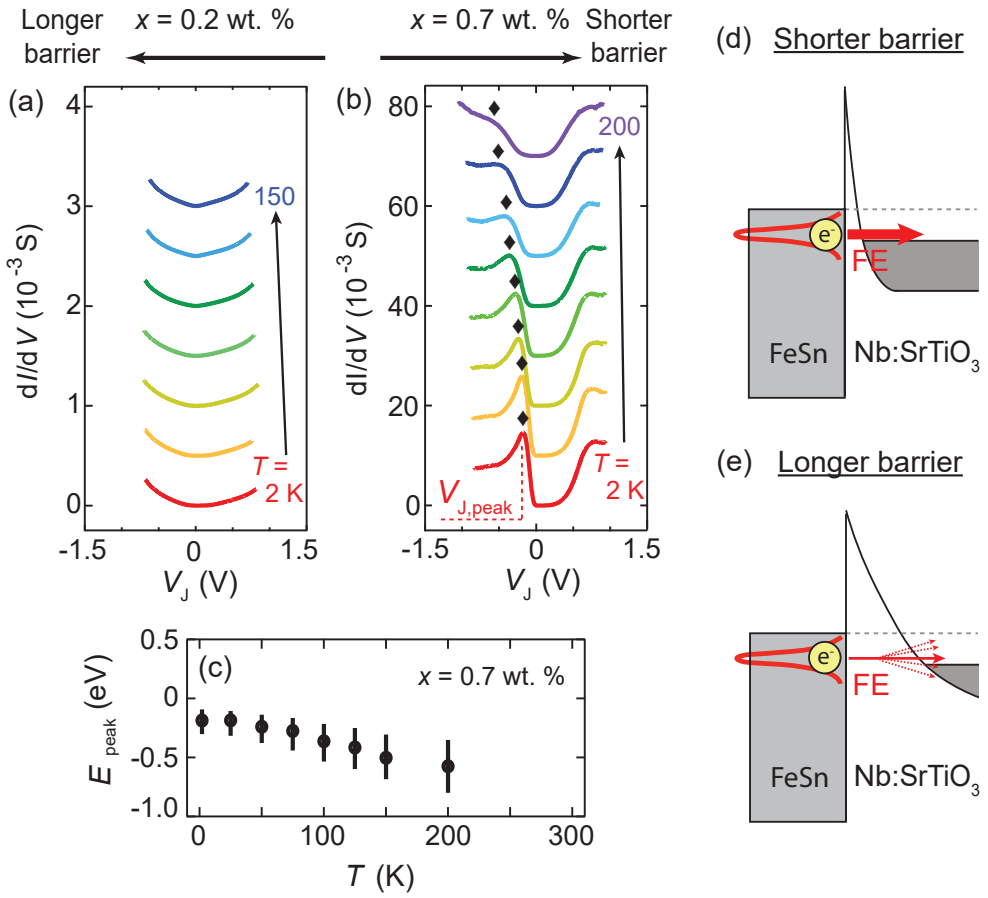

Figure 4-4: **Tunneling in $x = 0.2, 0.7$ wt.% junctions**

$\mathrm{d}I/\mathrm{d}V$ spectra at different temperatures for FeSn/Nb:$SrTiO_3$ junctions with (a) $x =$ 0.2 wt.% and (b) $x = 0.7$ wt.%. The measurements are taken at $T = 2$, 25, 50, 75, 100, 125, 150, 200 K. Each curve is offset vertically by equal amount with respect to the $T = 2$ K trace for clarity. The peaks of interest in (b) are marked with diamonds. (c) Temperature dependent $\mathrm{d}I/\mathrm{d}V$ peak positions (E_{peak}) (circles) and corresponding full widths at half maximum (vertical bar), extracted from (b). Schematic of the tunneling mechanisms across the Schottky barrier with (d) short and (e) long depletion layers. Inelastic scattering events within the long depletion layer obstruct the field emission (FE) process.

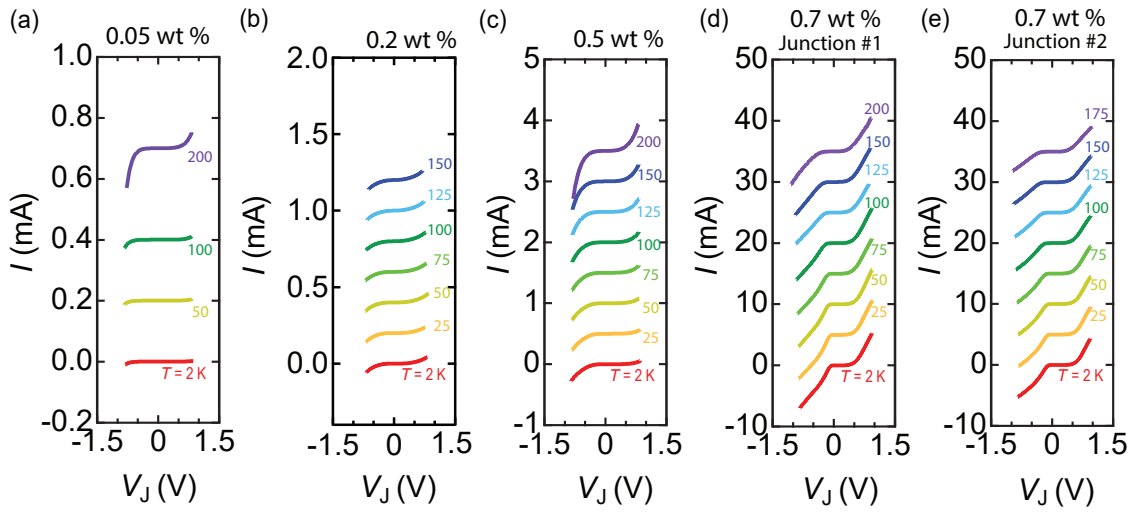

Figure 4-5: I-V **characteristics of FeSn/Nb:SrTiO$_3$ junctions**

I-V curves of FeSn/Nb:SrTiO$_3$ junctions with different Nb doping concentrations. Vertical offsets are added with respect to the $T = 2$ K trace for clarity.

polarization-dependent band reconstruction. In the following sections, we examine this assumption with model junction simulations (section 4.2.3) and correlate the observed spectra to the electronic structure of FeSn (section 4.2.4).

4.2.3 Schottky junction simulations

We have thus far presented the tunneling anomalies in FeSn/Nb:SrTiO$_3$ Schottky heterojunctions. Before directly correlating the tunneling spectra to the intrinsic DOS of FeSn, we first examine the validity of this analysis by establishing both qualitative and quantitative understanding on tunneling spectroscopy in Schottky junctions. The usage of a semiconducting electrode distinguishes the present case from conventional tunneling spectroscopy that uses a metallic electrode and an attention must be taken in determining which (V_J, $E_\mathrm{F,STO}$) regime allows reliable comparison between dI/dV and DOS. Fig. 4-6 depicts schematic tunneling processes and the relation between the DOS of FeSn and the tunneling spectra is summarized as follows:

If $E_\mathrm{F,STO} \gg |V_\mathrm{J}|$ (*i.e.* metallic electrode) :

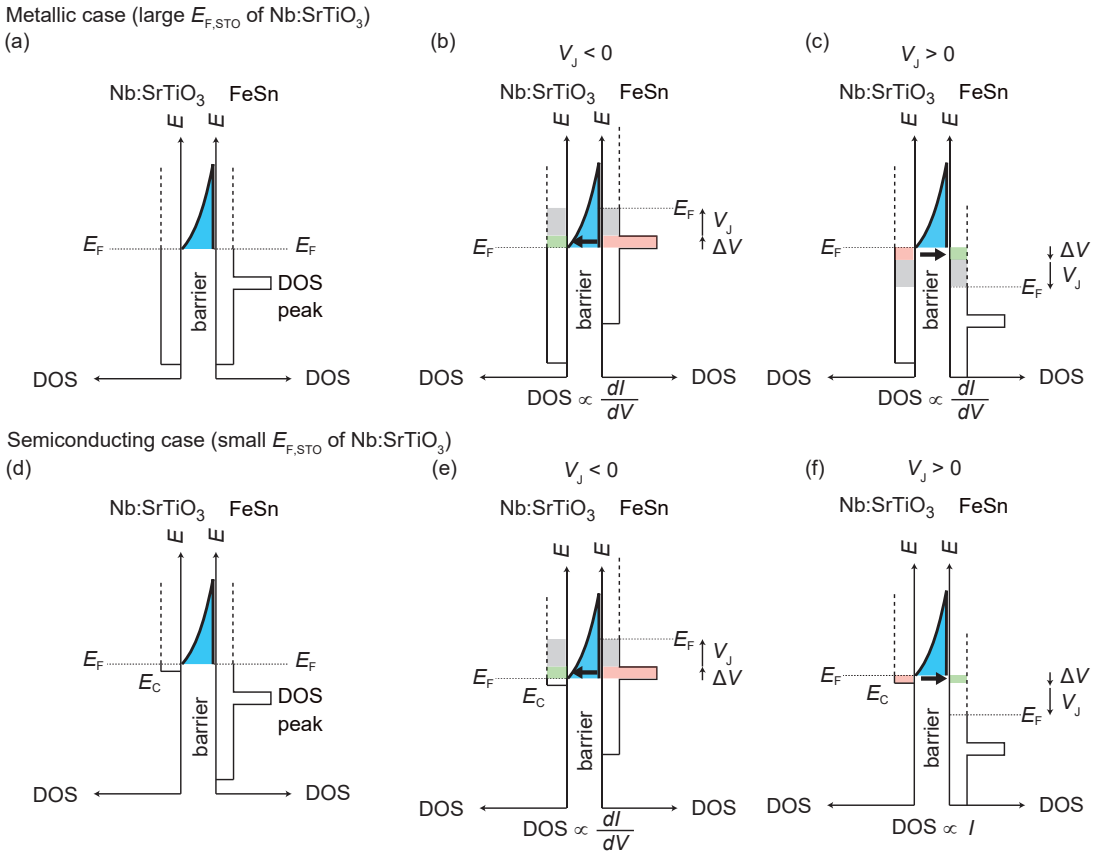

Figure 4-6: **Tunneling spectroscopy across a Schottky barrier**

(a-c) describe spectroscopy for the case of a metallic electrode at (b) negative bias $V_J < 0$ and (c) positive bias $V_J > 0$. (d-f) describe spectroscopy for the case of a semiconducting electrode at (e) negative bias $V_J < 0$ and for (f) positive bias $V_J > 0$.

- $V_J < 0$ (tunneling from FeSn to Nb:SrTiO$_3$):

  DOS of FeSn corresponds to dI/dV,

- $V_J > 0$ (tunneling from Nb:SrTiO$_3$ to FeSn):

  DOS of FeSn corresponds to dI/dV.

If $E_{F,STO} \ll |V_J|$ (*i.e.* semiconducting electrode) :

- $V_J < 0$ (tunneling from FeSn to Nb:SrTiO$_3$):

  DOS of FeSn corresponds to dI/dV + smooth background,

- $V_J > 0$ (tunneling from Nb:SrTiO$_3$ to FeSn):

  DOS of FeSn corresponds to I.

First, we consider the case of Nb:$SrTiO_3$ being in the metallic regime, where $E_{F,STO}$ is much larger than $|V_J|$ and the DOS of Nb:$SrTiO_3$ is nearly constant in energy (Fig. 4-6(a)). Under $V_J < 0$ applied to FeSn (Fig. 4-6(b)), electrons tunnel from $E < E_F$ of FeSn to the empty states in the conduction band continuum of Nb:$SrTiO_3$ above $E_{F,STO}$ (grey boxes in Fig. 4-6(b)). Similarly for $V_J > 0$, electrons tunnel from $E < E_{F,STO}$ of Nb:$SrTiO_3$ to the empty states at $E > E_F$ of FeSn (grey boxes in Fig. 4-6(c)). Increasing or decreasing the bias voltage by ΔV induces additional tunnel current ΔI to flow from FeSn (Nb:$SrTiO_3$) to Nb:$SrTiO_3$ (FeSn). Since each ΔI is determined by the number of states participating additionally to the tunneling process in response to ΔV, DOS is approximately proportional to dI/dV for any V_J.

We now consider the case of Nb:$SrTiO_3$ being in the semiconducting regime, where the $E_{F,STO}$ is much smaller than $|V_J|$ (Fig. 4-6(d)). Under $V_J < 0$ applied to FeSn (Fig. 4-6(e)), the situation is still equivalent to the case described in Fig. 4-6(b) − electrons flow from $E < E_F$ of FeSn to the empty states in the conduction band continuum of Nb:$SrTiO_3$, except the DOS of Nb:$SrTiO_3$ now has a finite energy dependence. The net tunnel conductance is determined by the convolution of Nb:$SrTiO_3$'s DOS and FeSn's DOS, the former generating a smooth and nearly featureless background signal and the latter generating a variety of sharp features. We therefore expect that the tunneling process still resembles the metallic electrode case and dI/dV captures most of the key signatures in FeSn's DOS. A caution must be taken for $V_J > 0$ in this regime (Fig. 4-6(f)). Electrons at $E < E_F$ of Nb:$SrTiO_3$ flow into FeSn, but the maximum number of electrons that can tunnel is bounded by the total number of electrons present in Nb:$SrTiO_3$'s conduction band (*i.e.* no electronic states below the conduction band edge E_C). Given that $E_{F,STO} \ll V_J$, tunneling occurs only within a narrow energy region $E_C \leq E \leq E_{F,STO}$, making I, rather than dI/dV, to be proportional to the DOS of FeSn.

$E_{F,STO} \sim 75$ meV (for $x = 0.7$ wt.%) situates our FeSn/Nb:$SrTiO_3$ in the intermediate regime between the two limits described above. This makes the interpretation of either dI/dV or I in the $V_J > 0$ range challenging and we refrain from correlating the spectral features in the $V_J > 0$ range to the DOS of FeSn. Regardless of $E_{F,STO}$,

however, $\mathrm{d}I/\mathrm{d}V$ in the $V_\mathrm{J} < 0$ regime can always be connected to the DOS of a target material. Given that the tunneling anomalies are observed around $V_\mathrm{J} = -180$ meV < 0, they can be connected to the DOS of FeSn.

Focusing primarily on the $V_\mathrm{J} < 0$ range, we now verify with model junction simulations that the background contributions to $\mathrm{d}I/\mathrm{d}V$ are in fact negligible compared to the major spectral features. For the simulations, we use the Wentzel-Kramers-Brillouin (WKB) approximation [118]. The shape of the Schottky barrier $\phi(z)$ is modeled by the self-consistent Poisson equations with the nonlinear dielectric constant

$$\begin{aligned} \frac{d}{dz}\left(\varepsilon(F)\frac{d}{dz}\phi(z)\right) &= -e(n_\mathrm{e}(z) - n_\mathrm{d}), \\ n_\mathrm{e}(z) &= \int D_1(E + e\phi(z))f_1(E)dE, \end{aligned} \tag{1}$$

where n_e and n_d are the electron and donor densities, respectively, and D_1 and f_1 are the DOS and Fermi distribution functions of $SrTiO_3$, respectively. The electric field dependent permittivity has the form $\varepsilon(F) = (1 + a/\sqrt{b + F^2})\varepsilon_0$, where F is the electric field, ε_0 is the electric permittivity of vacuum, and a and b are the temperature dependent coefficients [112]. A parabolic dispersion is assumed for $SrTiO_3$'s band structure. Tunnel current is given by

$$\begin{aligned} I(V) \sim &\iint v_{z1}(E_z)T_{1\to2}(E_z)g(D_1(E), D_2(E + eV))f_1(E)f_2(E + eV)dE \\ &- \iint v_{z2}(E_z)T_{2\to1}(E_z)g(D_1(E - eV), D_2(E))f_1(E - eV)f_2(E)dE, \end{aligned} \tag{2}$$

where D_2 and f_2 are the DOS and Fermi distribution function of FeSn, respectively, v_{z1} and v_{z2} are the velocities of electrons in $SrTiO_3$ and FeSn, respectively, and $T_{1\to2}$ and $T_{2\to1}$ are the tunneling probabilities from $SrTiO_3$ to FeSn and FeSn to $SrTiO_3$, respectively. $g(D_1, D_2)$ is a function that satisfies $g(D_1, D_2) \to D_1$ for $D_2 \to \infty$ and $g(D_1, D_2) \to D_2$ for $D_1 \to \infty$. Here we use a functional form $g(D_1, D_2) = D_1D_2/(D_1 + D_2)$.

Examples of simulated I-V and $\mathrm{d}I/\mathrm{d}V$ are shown in Fig. 4-7(a) and Fig. 4-7(b),

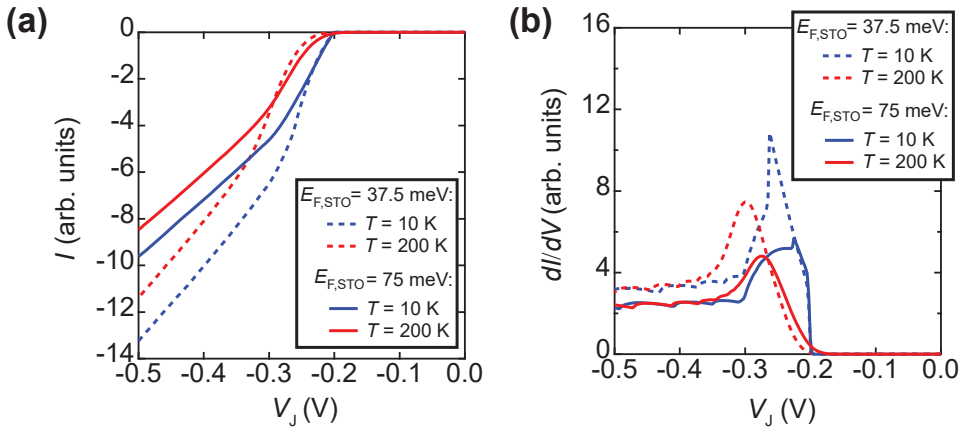

Figure 4-7: **Model Schottky junction simulations**

Simulated (a) I-V curves and (b) $\mathrm{d}I/\mathrm{d}V$ spectra for different temperatures and E_{STO}. The calculations assume a DOS peak 0.2 eV below E_{F} of FeSn. The shape of the barrier is determined by self-consistent Poisson equations.

respectively, assuming different $E_{\mathrm{F,STO}}$: 37.5 meV (dotted line; $x < 0.7$ wt.%) and 75 meV (solid line; $x = 0.7$ wt.%). In these calculations, we create a truncated parabolic band with the bandwidth of 0.1 eV and the top edge at 0.2 eV below E_{F} of FeSn. This band generates a peak in DOS, which manifests as pronounced peaks (or humps) in the simulated $\mathrm{d}I/\mathrm{d}V$ (or I-V) curves. This feature becomes absent when the peak is removed from DOS, suggesting the electric field dependence of ε alone cannot account for the observed spectral feature, though it may generate a small mismatch between the peak positions in DOS and $\mathrm{d}I/\mathrm{d}V$.

The mismatch between the two increases in magnitude at elevated temperatures, owing to the temperature dependence of ε. Whereas the peak in DOS is fixed in energy, the apparent peak in $\mathrm{d}I/\mathrm{d}V$ shifts to more negative energy by ~ 0.050 eV for $E_{\mathrm{F,STO}} = 75$ meV and by ~ 0.038 eV for $E_{\mathrm{F,STO}} = 37.5$ meV, respectively, as temperature increases from $T = 10$ K to $T = 200$ K. The shift, however, is an order of magnitude smaller than the observed shift in the $\mathrm{d}I/\mathrm{d}V$ peak $|\Delta V_{\mathrm{J}}| = 0.38$ eV (Fig. 4-4(c)). This provides an additional evidence that dielectric effects of $SrTiO_3$ cannot solely explain the major aspects of the tunneling spectra.

Finally, we use the above methodology to consider small but finite junction effects and further refine the actual position of the DOS peak at each temperature. We focus

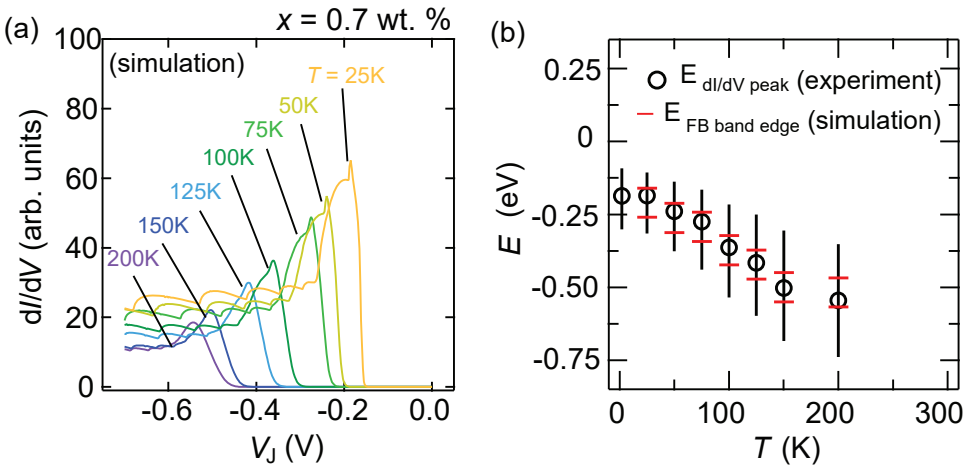

Figure 4-8: **Comparison of experimental and simulated tunnel spectra**

(a) Simulated dI/dV spectrum at each temperature for the $x = 0.7$ wt.% junction. The DOS peak positions in the simulation are adjusted so as to match the experimental dI/dV peak positions. (b) Top/bottom edges of the simulated DOS peaks (red horizontal bars) overlaid onto the experimental data in Fig. 4-4(c).

on the $x = 0.7$ wt.% junction with $E_{\mathrm{F,STO}} = 75$ meV. Iterative processes are taken at each temperature: (i) simulate a dI/dV spectrum at a given temperature with the DOS peak at an arbitrary energy, (ii) compare it with the experimental dI/dV spectrum at that temperature, and (iii) simulate again with a modified DOS peak position. This process is repeated until a reasonable match is attained between the simulation and the experiment (Fig. 4-8(a)). As presented in Fig. 4-8 and Table 4.1, the correction factors are found to be small at all temperatures and the experimental dI/dV peaks always appear within the simulated bandwidth of the DOS peak. This indicates that the experimental dI/dV is consistently a good indicator of the actual DOS of FeSn across the entire temperature range.

4.2.4 Slab band structure calculations

The previous sections have laid solid experimental, conceptual, and computational foundations on which we can analyze the tunneling spectra in close comparison with the intrinsic electronic structure of FeSn. For this, we perform first-principles electronic structure calculations of a slab containing eight crystallographic unit cells of

	$E_{\mathrm{dI/dV}}$ (meV) experiment	$E_{\mathrm{FB,top}}$ (meV) simulation	$E_{\mathrm{FB,bottom}}$ (meV) simulation
25K	-185	-160	-260
50K	-239	-212	-312
75K	-275	-243	-343
100K	-363	-323	-423
125K	-416	-372	-472
150K	-503	-450	-550
200K	-560	-468	-568

Table 4.1: **Band parameters from simulations and experiments**

Top (middle column) and bottom (right column) edges of the simulated DOS peaks in comparison with the experimental $\mathrm{d}I/\mathrm{d}V$ peak positions (left column).

FeSn ($1 \leq L \leq 8$), where L denotes the layer index (Fig. 4-9(a)). The slab has the Fe_3Sn kagome layers at layer index sites with the Sn_2 honeycomb (stanene) layers inserted between. This structure terminates with the Fe-kagome layer on one surface ($L = 1$) and the stanene layer on the other surface ($L = 8$). The slab calculations presented in this section are performed by S. Fang in [74].

The $\mathrm{d}I/\mathrm{d}V$ spectrum for the $x = 0.7$ wt.% junction at $T = 2$ K (Fig. 4-9(c)) is compared with the calculated DOS spectra at the kagome-terminated surface ($L = 1$; Fig. 4-9(d)), the Sn-terminated surface ($L = 8$; Fig. 4-9(e)), and the bulk part of the slab ($L = 4$, 5; Fig. 4-9(f)). Within the energy range of the $\mathrm{d}I/\mathrm{d}V$ peak (green-shaded box across Fig. 4-9(c)-(f)), the kagome-terminated surface hosts a clear peak in DOS at E = -125 meV (diamonds in Fig. 4-9(c),(d)) whereas the other two do not manifest any pronounced feature. The layer-resolved DOS color map in Fig. 4-9(b) also shows a surface-localized band at $L = 1$ containing high DOS concentrated within a narrow energy around E = -125 meV. In addition, a shoulder-like feature in $\mathrm{d}I/\mathrm{d}V$ is observed at V_{J} = -560 mV nearby the satellite peak in DOS at the kagome-terminated surface at E = -525 meV, reinforcing the correlation between the traces in (c) and (d) (asterisks in Fig. 4-9(c),(d)). These suggest that the major features in the tunneling spectra including the peak at $V_{\mathrm{J,peak}}$ = -180 mV originate from the electronic states at the kagome-terminated surface of FeSn; this is also consistent with

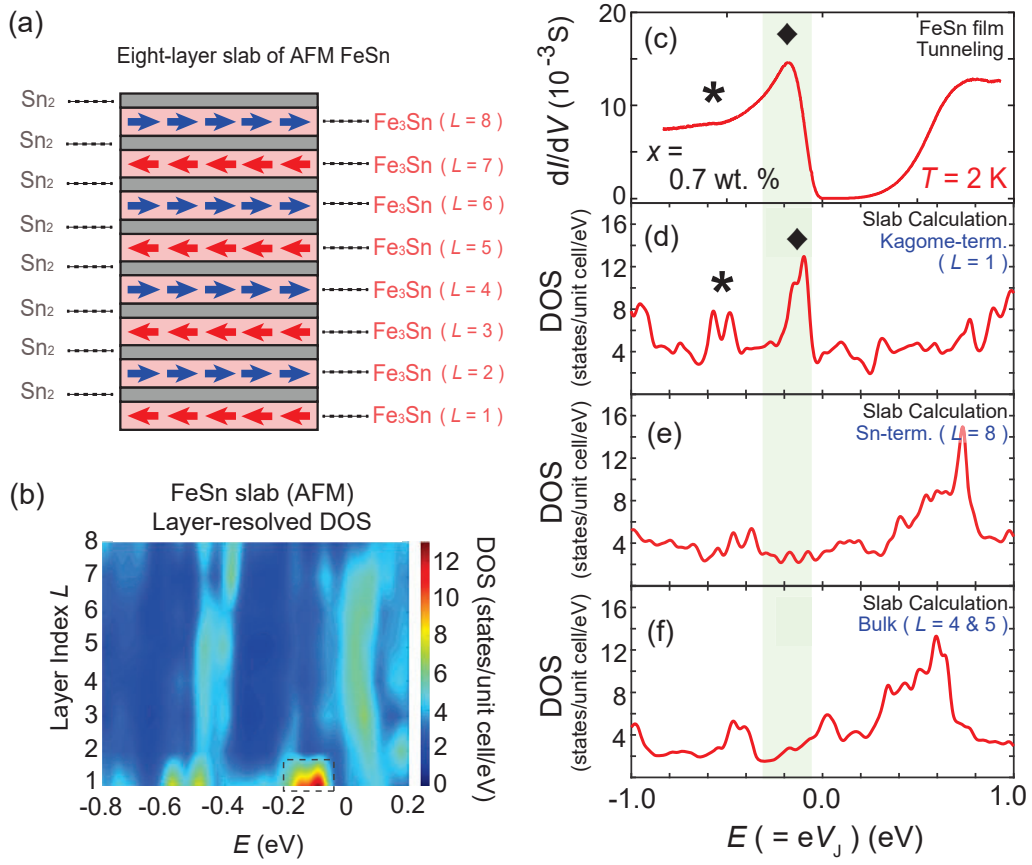

Figure 4-9: **Slab band structure calculation of FeSn**

(a) Schematic of the eight-layer slab of antiferromagnetic FeSn. (b) Layer-resolved density of states (DOS) color map in the eight-layer slab. (c) $\mathrm{d}I/\mathrm{d}V$ spectrum for the $x = 0.7$ wt.% junction at $T = 2$ K. Energy dependent DOS at (d) the kagome-terminated surface, (e) the Sn-terminated surface, and (f) the bulk of the eight-layer slab. The green-shaded box across (c-f) denotes the energy window in which the peak feature in $\mathrm{d}I/\mathrm{d}V$ is observed. Diamonds and asterisks mark the positions of noticeable features that correlate between (c) and (d).

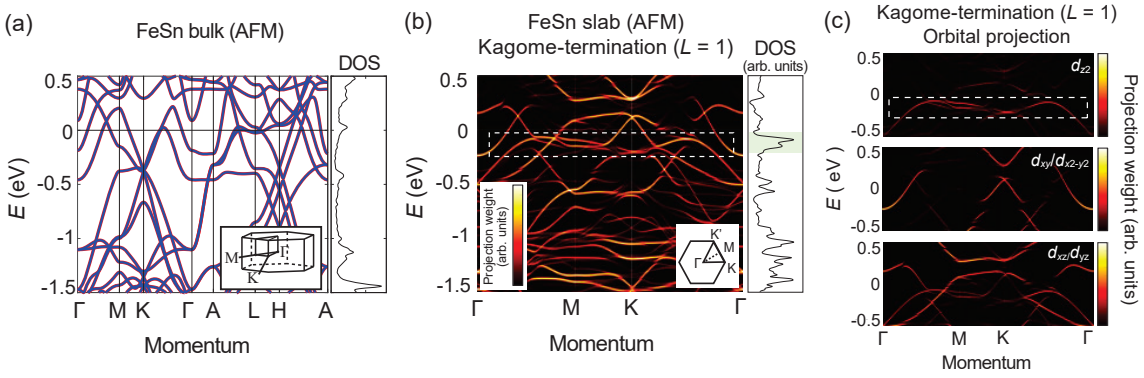

Figure 4-10: **Bulk vs. surface band structure of FeSn**

Band structure and DOS of (a) bulk FeSn in the antiferromagnetic state and (b) the kagome-terminated surface of the eight-layer slab. Insets in (a),(b) are schematics of the corresponding Brillouin zones. Spin down/up bands are color-coded blue/red in (a). The DOS peak and the flat band in (b) are marked with the green-shaded box and the dashed line, respectively. (c) Orbital projected band structure of (b). The intensity denotes d-orbital projection weights.

the inference from TEM that the Fe-kagome layer is the preferred first-formed layer at the film−substrate interface immediately above the depletion layer in Nb:$SrTiO_3$ (see section 4.1).

To understand the origin of the DOS peak at the surface, it is instructive to compare the bulk and surface electronic structures of FeSn. Figure 4-10(a) shows the bulk band structure of FeSn in the antiferromagnetic state; this is identical to the band structure we investigated in chapter 3. To underscore some of the highlights, it harbors the Dirac points at the K-point near $E \sim$ -400 meV and the flat band complex centered around $E \sim 600$ meV. As discussed in section 3.3.1, the latter originates from the d_{xz}/d_{yz}- and d_{xy}/d_{x2-y2}-orbitals and is responsible for the prominent peak in DOS around $E \sim 600$ meV in Fig. 4-9(e) [44]. Around $E =$ -125 meV, we do not find any band with suppressed dispersion.

Turning to the kagome-terminated surface band structure in Fig. 4-10(b), near the energy at which the DOS peak is expected, a highly non-dispersive band is observed (enclosed with the dashed line). The orbital projection analysis reveals that the major contribution to this surface flat band comes from the d_{z2}-orbital, distinct from the

orbital character of the bulk flat band (Fig. 4-10(c)). Considering the vertically elongated shape of d_{z2}-orbital and its hybridization with Sn p-orbitals in neighboring stanene layers, it is expected to gain a sizable dispersion along z when placed inside the bulk, resulting in a dilution of the spectral weight in energy. However, at the surface the translational invariance is broken and k_z-dispersion is quenched, thereby allowing a surface state non-dispersive within the ab-plane as well as along the c-axis.

4.3 Origin of the surface band reconstruction

4.3.1 Comparison with kagome−stanene bilayers

To gain further insight into the surface flat band, we consider an isolated ferromagnetic kagome−stanene bilayer, which constitutes half of the magnetic unit cell of FeSn. The band structure of the ferromagnetic kagome−stanene bilayer is shown in Fig. 4-11(a), showing a reasonably match with that of the kagome-terminated surface band structure in Fig. 4-10(b). It also exhibits a non-dispersive band (enclosed with the dashed line in Fig. 4-11(a)) that nearly coincides in shape and energy with the surface flat band. A more direct connection between the flat band and the DOS peak can be made here. In Fig. 4-11(b),(c), we show the DOS distributions across the Brillouin zone at E = -170meV and E = -105 meV, both of which are located within the DOS peak. Notably, a significant fraction of DOS at E = -170 meV (or E = -105 meV) is concentrated near the K-point (or the M-point), indicating a section of the flat band near the K-point (or the M-point) is responsible for the DOS peak.

The resemblance between 4-10(b) and 4-11(a) reflects the layered crystal structure of FeSn in which hybridization between the consecutive kagome layers is suppressed by the stanene layers. This as a result allows FeSn band structure to be well described by the minimal constituent of kagome−stanene bilayer. Furthermore, we note that the intrinsically inversion asymmetric kagome−stanene bilayer is most precisely represented by the kagome layer at the surface (or Schottky heterointerface) that neighbors a stanene on one side and vacuum (or Nb:$SrTiO_3$) on the other side. However,

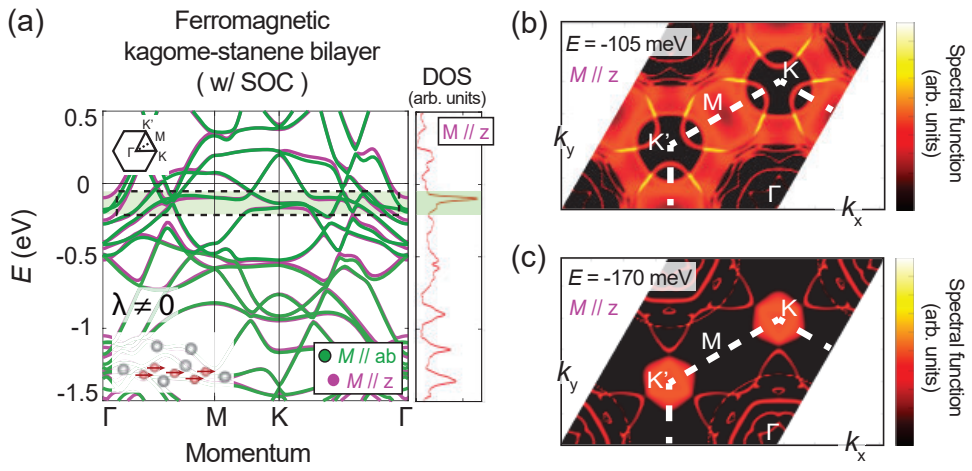

Figure 4-11: **Band structure of the ferromagnetic kagome−stanene bilayer**

(a) Band structure and DOS of a ferromagnetic kagome−stanene bilayer with spins along the *c*-axis (purple) and within the *ab*-plane (green). Spin-orbit coupling is included here. The flat band and the DOS peak are enclosed in green-shaded boxes. DOS distribution across the Brillouin zone at (b) E = -170 meV and (c) E = -105 meV for the band structure in (a). The intensities in (b),(c) correspond to spectral function amplitudes. The calculations here are performed by S. Fang in [74].

kagome layers in the bulk, being sandwiched by two stanene layers, are situated in an inversion symmetric environment and therefore give rise to the band structure deviated from that of the kagome−stanene bilayer. Rather, their environment can be approximated more precisely by that of an isolated kagome monolayer or an isolated stanene−kagome−stanene trilayer. The band structures of the Sn-terminated surface of FeSn (Fig. 4-12(a),(b)) and the ferromagnetic stanene−kagome−stanene trilayer (Fig. 4-12(c)), both consisting of a kagome layer encapsulated by two stanene layers in a symmetric fashion, resemble each other and in fact capture many features of the bulk band structure in Fig. 4-10(a) projected onto the two-dimensional Brillouin zone. The striking distinction between the bilayer dispersion (or analogously, the L = 1 dispersion) and the trilayer dispersion (or analogously, the bulk and the L = 8 dispersions) suggests that the kagome−stanene interaction under an inversion asymmetric environment has an important influence in generating the surface/interface-localized flat band in FeSn.

In addition to the peculiar chemical environment created by Sn and Nb:$SrTiO_3$,

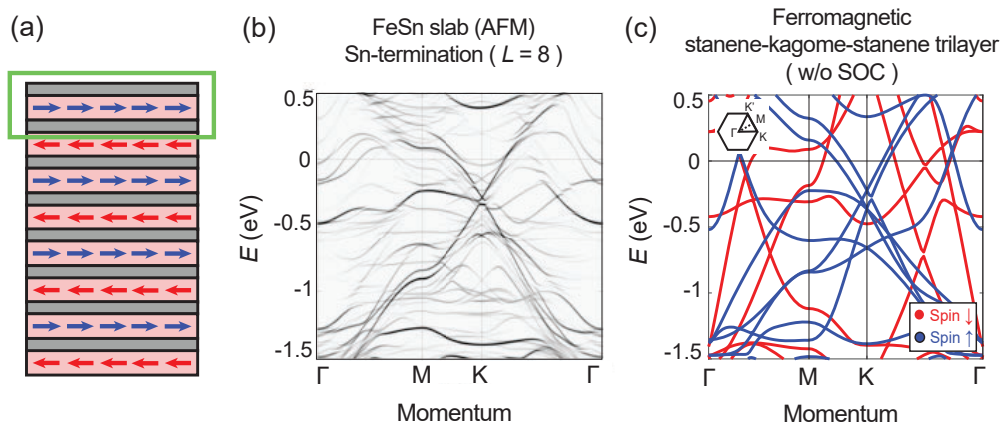

Figure 4-12: **Kagome layers in inversion symmetric environments**

(a) Schematic depiction and (b) band structure of the Sn-terminated surface of the slab in Fig. 4-9(a). (c) Band structure of a ferromagnetic stanene−kagome−stanene trilayer. Spin down/up bands are color-coded blue/red and spin-orbit coupling is not included here for the spin-resolved calculation. The calculations for (b),(c) are performed by S. Fang in [74].

the characteristic spin arrangement of FeSn generates a spin-split band structure at the surface. Such magnetic environment gives an opportunity to investigate how the two-dimensional band structure of the kagome−stanene bilayer changes as a function of the sublattice magnetization (M_{Fe}). To examine this, we perform spin-resolved band structure calculations of the kagome−stanene bilayers with varying M_{Fe}. When M_{Fe} is equal to the saturation magnetization (M_{sat}) (*i.e.* $T \ll T_{\mathrm{N}}$), we find that the flat band is fully spin-polarized (enclosed with the green-shaded box in Fig. 4-13(a)). When $M_{\mathrm{Fe}} = 0$ (*i.e.* $T > T_{\mathrm{N}}$), however, a spin-degenerate flat with similar but deformed morphology can be identified at E = -875 meV (enclosed with the green-shaded box in Fig. 4-13(b)). We show in Fig. 4-13(c) that the position of the DOS peak associated with the flat band shifts to higher binding energy from E = -110 meV to E = -480 meV as M_{Fe} reduces from M_{sat} to 0.5 M_{sat}. We attribute this as a potential origin of the temperature dependent shift in the dI/dV peak position observed in the tunneling experiment (Fig. 4-9(c)). Gradual depolarization of M_{Fe} at the interface upon thermal fluctuation and the consequent reduction of the local exchange field may explain the shift from $V_{\mathrm{J,peak}}$ = -180 mV at T = 2 K to $V_{\mathrm{J,peak}}$ =

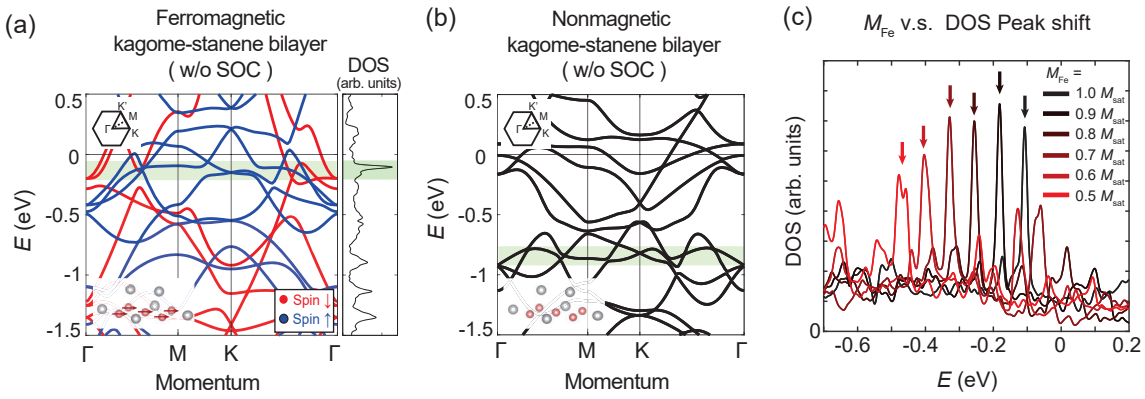

Figure 4-13: M_{Fe}**-dependent band structure of the bilayer**

Band structures and DOS of (a) ferromagnetic and (b) nonmagnetic kagome−stanene bilayers. Spin down/up bands are color-coded blue/red in (a). Spin-orbit coupling is not included here for the spin-resolved calculation. The flat bands and the DOS peak in (a),(b) are enclosed in green-shaded boxes. (c) M_{Fe}-dependent DOS of the kagome−stanene bilayer. The DOS peak associated with the flat band shifts to higher binding energy as M_{Fe} depolarizes. The calculations here are performed by S. Fang in [74].

-560 mV at $T = 200$ K. By estimating M_{Fe} at each temperature from $V_{\mathrm{J,peak}}$, we find that the magnetic transition at the surface kagome layer effectively occurs around 316 K, reduced from the T_{N} of FeSn extracted from bulk-sensitive measurements on bulk single crystals [44] and thin films (see chapter 3).

4.3.2 Continuous tuning of kagome−stanene interactions

We now investigate the manner through which the kagome−stanene interaction gives rise to the peculiar bilayer dispersion based on the calculations performed by S. Fang in [74]. Fig. 4-14(a) shows the evolution of the ferromagnetic kagome−stanene bilayer band structure with variable kagome−stanene interaction strength (only the minority spin bands presented here for clarity). The interaction strength is controlled parametrically by the inter-layer spacing $z_{\mathrm{K-S}}$ that tunes the orbital overlap between the two layers. Fig. 4-14(b)-(e) show the orbital compositions of the band structures at different $z_{\mathrm{K-S}}$ and Fig. 4-15 summarizes the $z_{\mathrm{K-S}}$-dependent band parameters extracted from Fig. 4-14. When $z_{\mathrm{K-S}}$ is large (Fig. 4-14, $z_{\mathrm{K-S}} = 6.0$ Å), the inter-layer

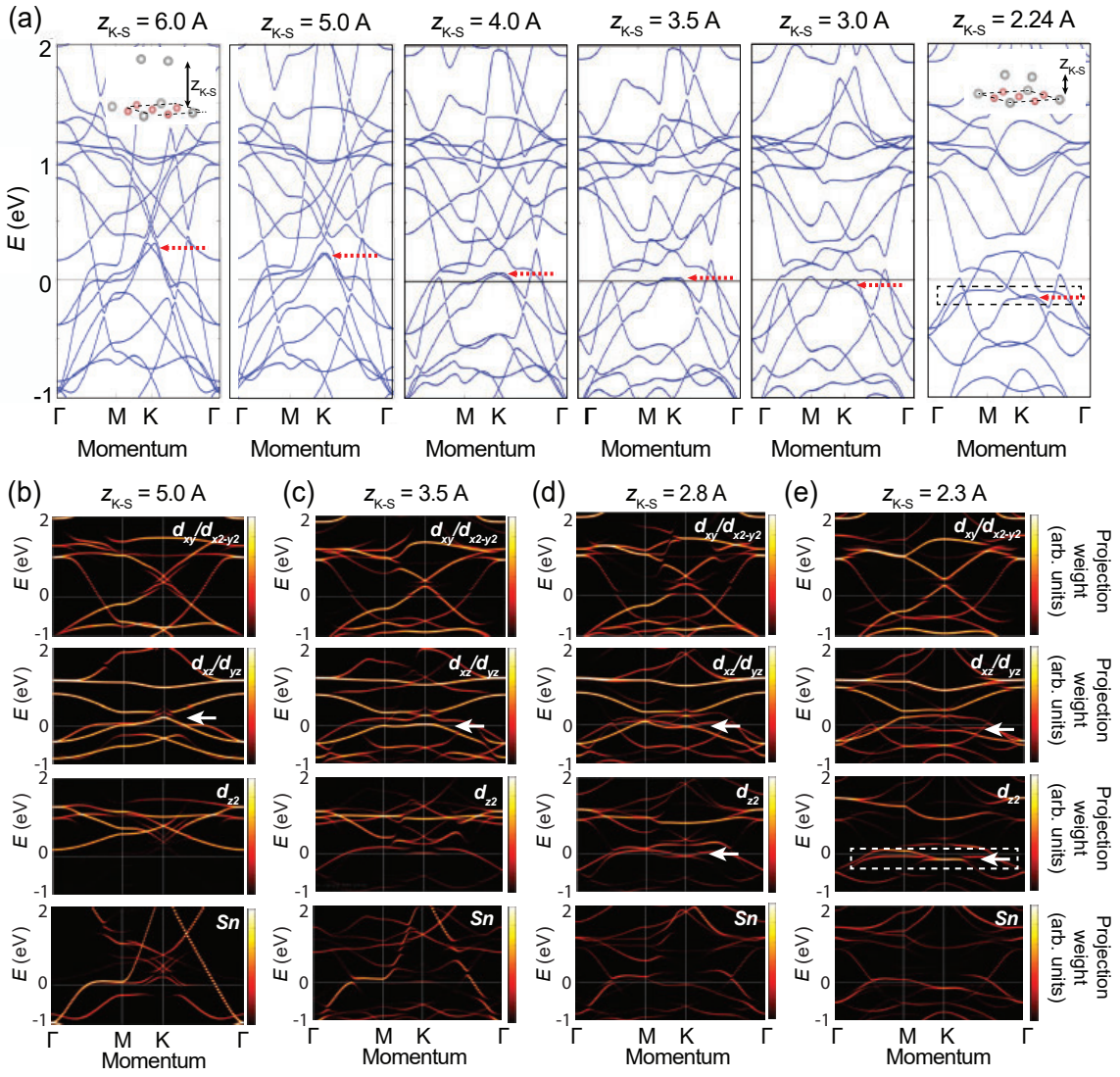

Figure 4-14: **Continuous tuning of the kagome−stanene interaction**

(a) Electronic structures of ferromagnetic kagome−stanene bilayers with different inter-layer spacings $z_{\mathrm{K-S}}$ (only the minority spin bands are shown). Increasing $z_{\mathrm{K-S}}$ reduces the kagome−stanene interaction and the bilayer band structure continuously evolves into the isolated monolayer band structure. The red arrows mark the positions of the band crossing that is relevant to the flat band observed in the experiment. (b)-(e) Orbital decomposed kagome−stanene bilayer band structures with different $z_{\mathrm{K-S}}$. The white arrows mark the dominant orbital components of the flat band at each $z_{\mathrm{K-S}}$.

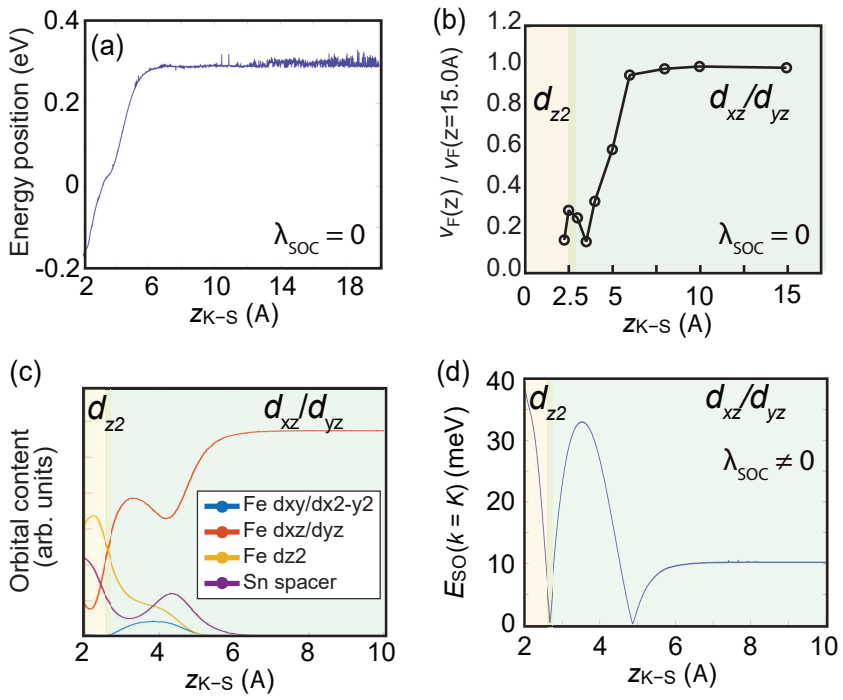

Figure 4-15: **Evolution of the Dirac-like crossing within the bilayer flat band**

$z_{\mathrm{K-S}}$-dependent (a) energy position, (b) normalized Fermi velocity v_{F} (along the M-K direction), (c) orbital composition, and (d) spin-orbit gap size E_{SO} of the Dirac-like crossing within the bilayer flat band.

interaction is weak and the band structure asymptotically converges to that of an isolated kagome monolayer. In contrast, as $z_{\mathrm{K-S}}$ approaches the actual inter-layer spacing in FeSn (Fig. 4-14(a), $z_{\mathrm{K-S}}$ = 2.24 Å), it restores the band structure of a realistic bilayer that represents the kagome-terminated surface band structure detected in FeSn/Nb:$SrTiO_3$.

When $z_{\mathrm{K-S}}$ = 6.0 Å, the band structure reveals several Dirac crossings at the K-point originating from different d-orbitals in the Fe_3Sn kagome network, including d_{xy}/d_{x2-y2}, d_{xz}/d_{yz}, and d_{z2} orbitals (Fig. 4-14(a),(b)). Here we focus specifically on one of the Dirac crossings located around $E \sim$ 300 meV at $z_{\mathrm{K-S}}$ = 6.0 Å. As $z_{\mathrm{K-S}}$ reduces from 6.0 Å to 2.24 Å, the position of the crossing gradually shifts down to E = -110 meV, the energy around which the DOS peak was observed in the tunneling experiments (red arrows in Fig. 4-14(a)). Fig. 4-15(a) shows the continuous shift of its position as a function of $z_{\mathrm{K-S}}$. Simultaneously, the bandwidth shrinks and the Fermi

velocity v_{F} near the K-point decreases by more than five-fold (Fig. 4-15(b)). After the energy shift and band flattening, the Dirac band of interest eventually transforms into the bilayer flat band discussed thus far. This suggests that the bilayer flat band (or equivalently the kagome-terminated surface flat band) can be viewed as a flattened Dirac band.

While the crossing stays robust at all $z_{\mathrm{K-S}}$ (in the absence of spin-orbit coupling λ_{SOC}), a significant amount of its orbital spectral weight originally concentrated in the d_{xz}/d_{yz}-orbital sector in the $z_{\mathrm{K-S}} \gg 2.24$ Å limit transfers to the d_{z2}-orbital sector as $z_{\mathrm{K-S}} \to 2.24$ Å (white arrows in Fig. 4-14(b)-(e)). This demonstrates that the complex kagome−stanene interaction and the consequent orbital hybridization are critical factors in generating the bilayer flat band. In the presence of λ_{SOC} and the magnetization vector along the z, a spin-orbit gap (E_{SO}) opens at the crossing point, reminiscent of the Dirac mass gap openings in graphene and other systems. This gap opening further enhances the local band flatness near the K-point. E_{SO} in the bilayer limit ($z_{\mathrm{K-S}} \to 2.24$ Å) is larger than that in the monolayer limit ($z_{\mathrm{K-S}} \gg 2.24$ Å), as the relatively large atomic number of Sn yields a stronger λ_{SOC} in the former case. While E_{SO} is in general larger at smaller $z_{\mathrm{K-S}}$, the $z_{\mathrm{K-S}}$-dependence of E_{SO} shows a non-monotonic trend (Fig. 4-15(d)). We note that E_{SO} closes and reopens whenever the orbital spectral weight at the crossing point redistributes between $d_{\mathrm{xz}}/d_{\mathrm{yz}}$, $d_{\mathrm{xy}}/d_{\mathrm{x2-y2}}$, and d_{z2} and Sn sectors. In particular, such behavior is most pronounced around $z_{\mathrm{K-S}} = 2.7$ Å, the critical inter-layer spacing across which the dominant orbital character of the band crossing changes from d_{xz}/d_{yz} to d_{z2} and Sn (Fig. 4-15(c)). We hypothesize that the sign (or complex phase) of λ_{SOC} is different between these orbitals, whose competition determines the size of positive, real-valued E_{SO} in the resultant band structure.

Finally, we comment on the merger of topology and correlation. It is noteworthy that while v_{F} is significantly quenched in the bilayer flat band, E_{SO} is still comparable to that of dispersive Dirac bands in ferromagnetic kagome metal Fe_3Sn_2 (~ 30 meV) [52]. A preliminary calculation suggests that a significant Berry curvature is concentrated within the gap, potentially endowing a nontrivial topology to the flat

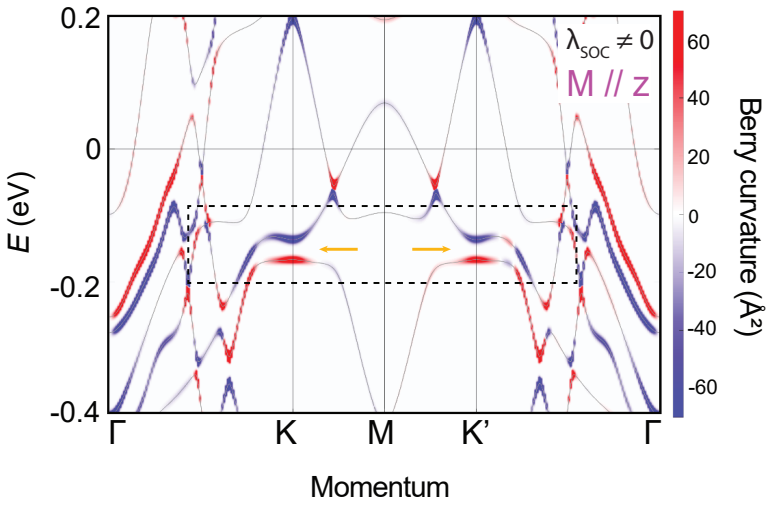

Figure 4-16: **Berry curvature analysis of the bilayer flat band**

Berry curvature (BC) distribution in the ferromagnetic kagome−stanene bilayer band structure (M // z here). With spin-orbit coupling, the band crossing within the flat band (enclosed with the dashed line) gaps out and BC emerges within the gap.

band electrons (Fig. 4-16). In general, the regime of high spin-orbit interaction and strong electronic correlation has been pointed out as a promising parameter space to blend nontrivial band topology and interaction-driven quantum phases into a single material [119]. The kagome−stanene interaction under inversion asymmetric environment proposes a potential pathway to flatten a highly spin-orbit coupled Dirac-like band and eventually drive it towards the strong correlation regime. With the key ingredients naturally built-in, the surface/interface of FeSn, as well as the isolated kagome−stanene bilayer, offers a unique physical platform to realize novel types of edge modes and correlated flat bands.

4.4 Conclusions and outlook

In this chapter, we probed the local DOS of FeSn at the Schottky heterointerface with an n-type semiconductor Nb:$SrTiO_3$. Using planar tunneling spectroscopy, we detected an anomalous enhancement of the tunnel conductance $\sim$ 180 meV below the

Fermi level of FeSn, which in conjunction with the slab band structure calculations revealed an evidence for a two-dimensional flat band residing at the bottom-most kagome layer of FeSn at the interface − consistent with the interface atomic arrangement identified from the TEM measurements. Our numerical calculations suggested that the observed surface flat band corresponds to a d_{z2} orbital derived spin-polarized flat band expected in the ferromagnetic kagome−stanene bilayer.

While our findings constitute consistent signatures of the proposed surface flat band, a critical future direction would be to directly probe the spin texture and electronics structure of the interfacial layer via space-, spin-, and layer-resolved high resolution spectroscopy techniques. Furthermore, it is of significant interest to stabilize an isolated kagome−stanene bilayer, which would most readily facilitate the direct investigation of the surface flat band discussed herein. In connection with the degree of band flattening, the two-dimensional surface localization of a vertically elongated orbital suggests a new design principle towards flat bands with nearly zero dispersion along all directions. Viewed more broadly, these observations suggest that the surface of a magnetic flat band material, being situated in an electromagnetic environment distinct from that of the bulk, has a potential to host a flat band with unique orbital and spin characters. In addition, given the surface-localized nature of this flat band, it is expected to have pronounced effect when embedded into heterostructure-based devices for spintronic applications.

Chapter 5

Anisotropic flat band and non-Fermi-liquid state in Ni_3In

One of the key design principles in material realization of the kagome lattice model is the physical separation between the consecutive kagome layers by an insertion of spacer layers. In this chapter, we focus on a different class of kagome metals with no spacer layer between them. We describe a gradual collapse of the kagome-derived band features and a concurrent emergence of a new type of anisotropic flat band upon increased inter-kagome hybridization. Ni_3In is a model compound that harbors such a band structure with the flat band at the Fermi level. We stabilize thin films of Ni_3In and identify physical properties which deviate from the canonical Fermi liquid expectations. By tracking the key energy scales of the non-Fermi-liquid state in response to various control parameters, we reveal the relevance of the flat band and the associated quantum fluctuations to the observed anomalies.

5.1 Electronic structure evolution from TM to T_3M ($T = 3d$ transition metal ; M = Ge, Sn, In)

Ni_3In belongs to a broad family of kagome metals T_3M ($T = 3d$ transition metal; M = Ge, Sn, In), consisting of AB-stacked two-dimensional networks of T_3M kagome

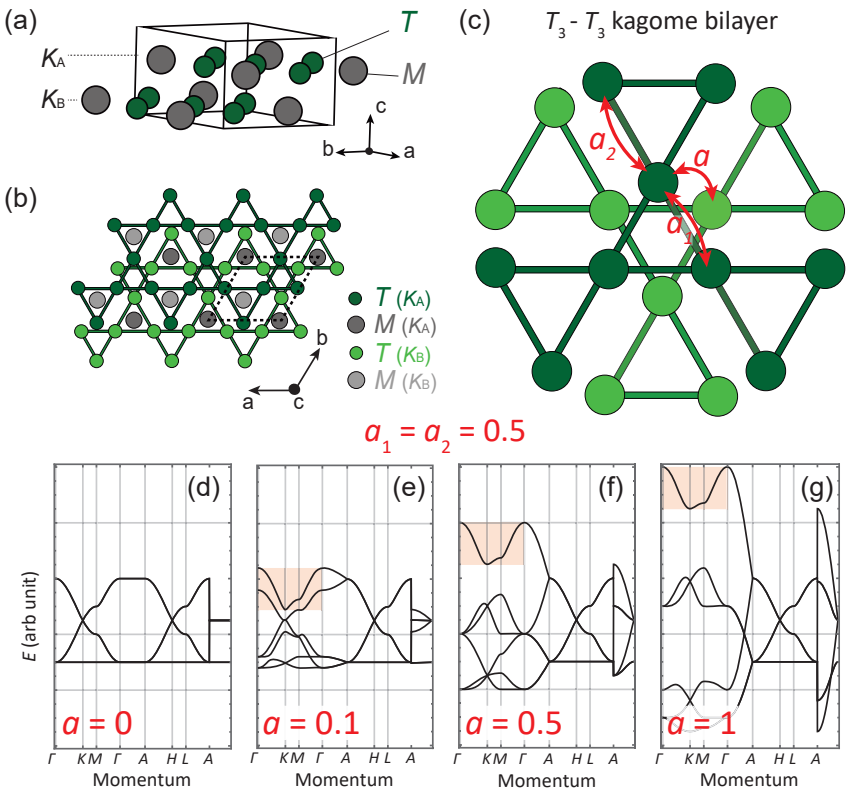

Figure 5-1: **AB-stacked kagome bilayer in T_3M**

(a) Schematic crystal structure and (b) the top view of T_3M. (c) Schematic of a T_3 - T_3 kagome bilayer. M atoms are not yet included here. The red arrows denote hopping pathways for a, a_1, and a_2. (d)-(f) Tight binding band structures with different values of a ($a_1 = a_2 = 0.5$ fixed). The bands of interest are orange-shaded.

layers (Fig. 5-1(a),(b)). Among this family exists a recently highlighted non-collinear antiferromagnet Mn_3(Ga:Ge:Sn), a time reversal symmetry broken Weyl semimetal [56, 57]. In terms of structure, the T_3M has three prominent distinctions from TM (*e.g.* FeSn). (i) The M_2 spacer layer is absent in T_3M, putting the consecutive kagome layers in direct contact with each other and giving rise to inter-kagome hybridization. (ii) The characteristic atomic distribution within the unit cell of T_3M, pertaining to its AB-stacking sequence, accompanies a breathing distortion in which certain clusters of T atoms expand/compress with respect to others. (iii) The orbital-specific hopping anisotropy of d-electrons creates a phase interference between the intra-kagome and inter-kagome hopping pathways − such a phenomenon is less relevant in TM where the inter-kagome hopping itself is reduced. Below, we track the systematic electronic

structure evolution from TM to T_3M by incorporating the three key structural traits of T_3M to a tight binding Hamiltonian of the kagome lattice.

Fig. 5-1(c) shows the schematic of an AB-stacked T_3 kagome bilayer, the most fundamental building block of our tight binding model with M atoms not yet included. The A and B layers in the AB-stack are color-coded dark and light green, respectively. The three simplest nearest neighbor (NN) hopping parameters are: $a_1 = a_2 =$ (intra-layer NN hopping) and $a =$ (inter-layer NN hopping). The simplest case of $a_1 = a_2 = 0.5$ and $a = 0$ realizes the single layer kagome band structure (Fig. 5-1(d)) as the two layers within the unit cell do not hybridize. Each dispersion is four-fold degenerate due to spin and layer degrees of freedom.

As the inter-layer hybridization increases ($|a| > 0$), the layer degeneracy becomes lifted and the bands split along k_z (see the bifurcating branches along the Γ-A line in Fig. 5-1(d)-(g)). This splitting can be viewed as an energy difference between the bonding and anti-bonding phase configurations within the bilayer unit cell (and also analogous to the zone folding effect from unit cell doubling). In the $a \to 1$ limit, the band structure is significantly deformed from its original morphology. Hereon, we focus primarily on the orange-shaded band in Fig. 5-1(d)-(g), originating from the Dirac branch in the $a = 0$ state.

The model becomes more realistic when M atoms are inserted into the lattice. From the top view of the structure (Fig. 5-2(a)), we identify two sets of T_3 trimers placed under distinct chemical environments: one with M atoms at the center and the other with voids. The former experiences a negative chemical pressure from the M atoms and expand in size, whereas the latter shrinks. This generate a mismatch between the two NN bond lengths within the T_3M kagome layer. In Ni_3In, for example, the bond lengths for the expanded trimer and the compressed trimer are 0.28 nm and 0.25 nm, respectively. This phenomenon is referred to as a breathing distortion and is reflected in the tight binding model as $a_1 \neq a_2$. By varying a_2 from 0.5 to 0.3 ($a_1 = 0.5$ and a=1 fixed), we find that the band of interest becomes flatter (Fig. 5-2(b),(c)). This evidences that the Wannier function of this band resides predominantly on the compressed trimers with enhanced degree of localization from the

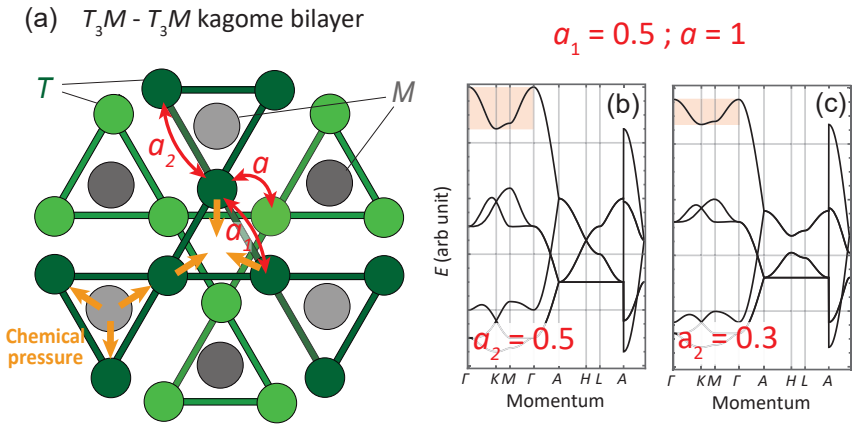

Figure 5-2: **Breathing distortion in** T_3M

(a) Schematic of a T_3M - T_3M kagome bilayer. The red arrows denote hopping pathways for a, a_1, and a_2. The orange arrows denote the directions of chemical pressure. (b),(c) Tight binding band structures with different values of a_2 ($a_1 = 0.5$, $a = 1$ fixed). The bands of interest are orange-shaded.

breathing distortion.

In incorporating higher order hoppings, it is important to consider the characteristic hopping anisotropy of each d-orbital; see Fig. 5-3(a) for the relevant hopping parameters a_3 = (inter-layer NNN hopping) and a_4 = (inter-layer NNNN hopping), where NNN and NNNN denote next and next-next nearest neighbors. In previous studies on Ni_3In, the orbital origin of its valence electrons have been identified as the d_{xz}-orbital with an X-shaped lobes protruding out-of-plane along the direction tilted from the z (Fig. 5-3(b),(c)) [60]. Such lobe orientation makes a_3 and a_2 to have comparable amplitudes, reflected in the model in a simplified fashion as $a_3 = a_2 = 0.3$. Additionally, taking into account the phase relation of each lobe, a_4 is expected to have an opposite sign and a reduced amplitude with respect to a_2 or a_3. Fig. 5-3(e)-(g) plot the band structures as a_4 is varied from -0.1 to -0.2. An intriguing observation is made in Fig. 5-3(f) when a_4 = -0.15 and $a_2 + 2a_4 = 0$ condition is satisfied: the band of interest attains a zero bandwidth within the plane, indicating the perfect destructive interference of relevant hopping pathways. Given that its localization site is the compressed trimer, the interference involves one intra-layer hopping and two inter-layer hoppings, thus constituting $a_2 + 2a_4 = 0$ (Fig. 5-2(d)).

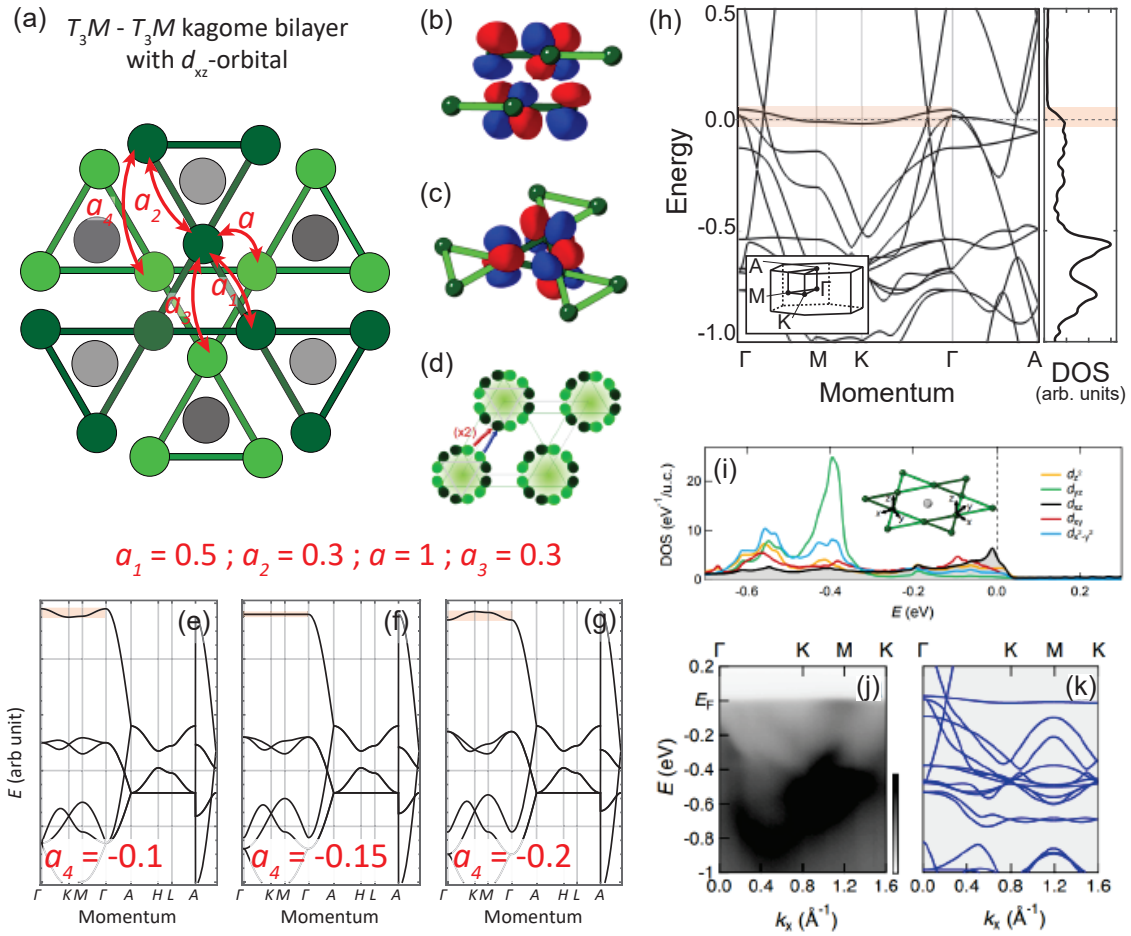

Figure 5-3: **Destructive phase interference of hopping pathways in** T_3M

(a) Schematic of a T_3M - T_3M kagome bilayer with higher order hoppings included. The red arrows denote hopping pathways for a, a_1, a_2, a_3, and a_4. (b)-(d) Schematic orientation and hopping pathways for the d_{xz}-orbital in T_3M. (e)-(g) Tight binding band structures with different values of a_4 ($a_1 = 0.5$, $a_2 = 0.3$, $a = 1$, $a_3 = 0.3$ fixed). (h) Density functional theory (DFT) band structure and density of states (DOS) of Ni_3In. The bands of interest are orange-shaded in (e)-(h). (i) Orbital-projected DOS of Ni_3In. (j) Photoemission measurements on bulk single crystal Ni_3In and (k) a DFT calculation for comparison with (j). (b-d) and (i-k) are from [60]. The calculations for (h) are performed by S. Fang.

The band is perfectly flat within the plane, but still maintains dispersiveness along k_z. We therefore call this band an anisotropic flat band.

While our tight binding approach is purely phenomenological, it captures key aspects of the actual electronic structure of T_3M. For example, density functional theory (DFT) band structure of Ni_3In in Fig. 5-3(h) reveals at the Fermi level (E_F) an anisotropic flat band of the identical origin as the one we constructed (a recent photoemission measurement of bulk single crystal Ni_3In has experimentally confirmed the validity of this calculation; see Fig. 5-3(i)-(k) from [60]). The Dirac and flat bands in FeSn (TM; T = Fe; M = Sn) are born out of the kagome lattice geometry within the Fe-kagome layers; the anisotropic flat band in Ni_3In (T_3M; T = Ni; M = In) can be ascribed to its characteristic lattice structure harboring the three key elements discussed above. Being lattice-driven in nature, it can be identified in a variety of T_3M compounds such as Fe_3Sn or Cu_3Sn. Among them, Ni_3In is special in that its E_F crosses the flattest part of the flat band (*i.e.* at the $k_z = 0$ plane near its top band edge) from which a mini-peak is generated in the d_{xz}-orbital projection of the density of states (DOS) (Fig. 5-3(i)). A critical question is the influence of these flat band electrons in driving correlated phenomena. In the following sections, we demonstrate our works on synthesis and characterization of Ni_3In thin films, from which we uncover anomalous transport and thermodynamic properties.

5.2 Synthesis and characterization of Ni_3In epitaxial thin films

5.2.1 Epitaxial thin film synthesis of Ni_3In

This section provides descriptions of synthesizing high quality Ni_3In thin films with molecular beam epitaxy (MBE). Ni_3In thin films are grown on lattice-matched $SrTiO_3$ (111) substrates (+2.8% mismatch). The substrates are prepared and preannealed the same way as explained in section 3.2.1. During film deposition, the substrate temperature is fixed at T_d and Ni and In are evaporated from solid source effusion

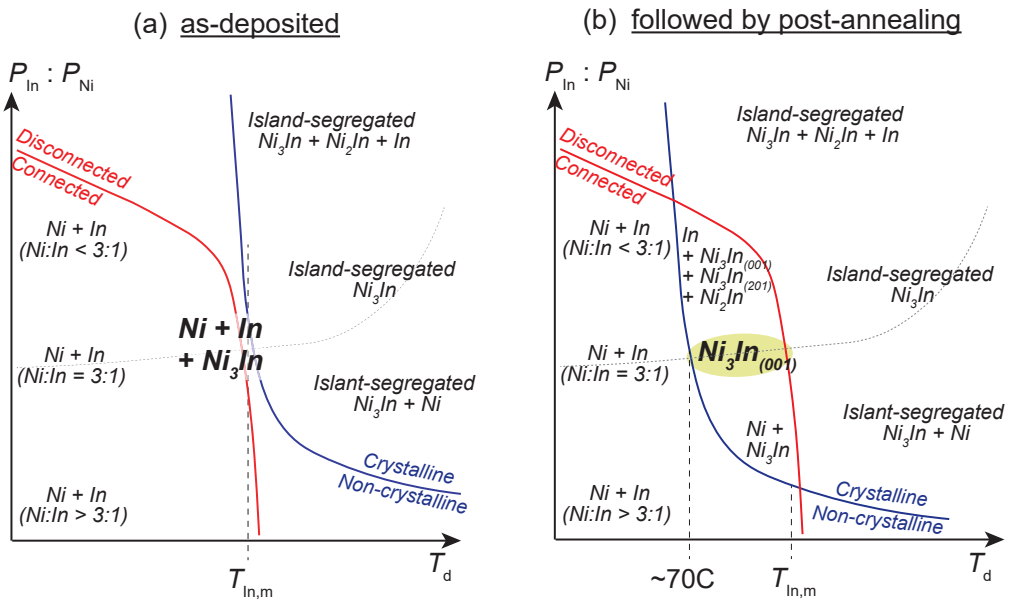

Figure 5-4: **Optimization of Ni_3In thin film synthesis**

Schematic growth phase diagrams of (a) as-deposited and (b) post-annealed Ni_3In thin films. An optimized film has high crystallinity (above the blue boundary), connected in-plane morphology (below the red boundary), and 3:1 stoichiometry (along the black dashed line). The region that satisfies these conditions is yellow-shaded.

cells. The ratio of beam-equivalent pressures (BEPs) for Ni (P_{Ni}) and In (P_{In}) are calibrated before each growth. After the deposition, most of the films are post-annealed at T_{a} for 1 h.

The synthesis of high quality Ni_3In requires precise calibrations of T_{d}, $P_{\mathrm{In}} : P_{\mathrm{Ni}}$, and T_{a}. Each of these growth parameters is optimized following the same methodology presented in section 3.2.1; the growth phase diagrams with and without the post-annealing treatment are summarized in Fig. 5-4(a) and (b), respectively. Similar to the case of FeSn above the Sn melting point, Ni_3In films tend to manifest enhanced crystallinity as well as island-segregated morphology when deposited above the In melting point $T_{\mathrm{m,In}} = 156.6$ °C. The case of Ni_3In is distinguished from FeSn, however, in that there does not exist an available growth phase space within which sufficient crystallinity and connected morphology are simultaneously attained in as-deposited films; note that the red boundary (connected vs. disconnected) and the blue boundary (crystalline vs. non-crystalline) in Fig. 5-4(a) do not intersect.

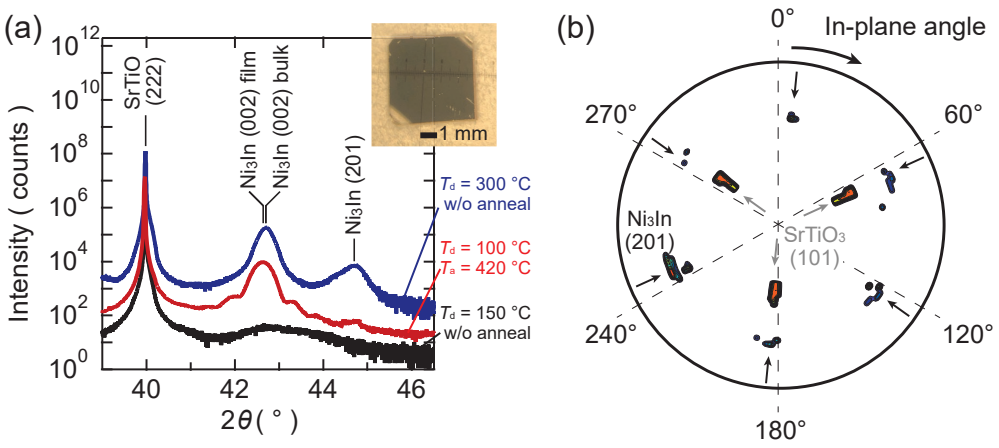

Figure 5-5: **X-ray measurements on Ni_3In films**

(a) X-ray diffraction spectra of Ni_3In films with (red) and without (black, blue) the post-annealing treatment. Inset: optical micrograph of a Ni_3In film (scale bar: 1 mm). (b) Pole figure of a Ni_3In film, showing the in-plane crystallographic orientation of the film with respect to that of the $SrTiO_3$ substrate.

When the films are post-annealed at 350 °C $\leq T_a \leq$ 450 °C, a relatively large growth phase space becomes available; see the yellow region between the red and blue boundaries in Fig. 5-4(b). We first deposit films with connected morphology (but low quality) at 70 °C $\leq T_a \leq$ 140 °C. After post-annealing, they eventually manifest high crystallinity while preserving the original connected morphology. $T_a \ll$ 350 °C does not give sufficient crystallinity and $T_a \gg$ 450 °C segregates the films into islands. Within this allowed growth phase space, $P_{In} : P_{Ni}$ is optimized to ensure the correct 3:1 stoichiometry (see the grey dashed line in Fig. 5-4(b)).

5.2.2 Structural characterizations

Figure 5-5(a) shows the X-ray diffraction (XRD) spectra of samples with (red; optimized) and without (black, blue; unoptimized) the post-annealing treatments. The samples have 20 nm film thickness (t_{Ni3In}) and the wavelength of the incident X-ray beam is $\lambda = 0.154$ nm. In vicinity of $SrTiO_3$ (222) XRD peak at $2\theta = 39.98°$, film XRD peaks are observed. The film deposited at $T_d = 140$ °C shows a broad and low-intensity peak around $2\theta = 42.70°$, the (002) XRD peak position for bulk Ni_3In

(Fig. 5-5(a), black). This indicates the formation of a c-axis oriented low quality Ni_3In film. On the other hand, the film deposited at T_d = 300 °C show a well-defined and high-intensity peak at $2\theta = 42.70°$ together with another satellite peak at $2\theta = 44.70°$ (Fig. 5-5(a), blue). The position of the latter is the (201) XRD peak position of bulk Ni_3In, suggesting the formation of a high crystalline but less singly oriented Ni_3In film. The film deposited with an optimized growth condition of (T_d, T_a) = (100 °C, 420 °C) shows a well-defined peak at $2\theta = 42.65°$ (0.1% deviated from $2\theta_{bulk,(002)}$) and a suppressed intensity at $2\theta_{bulk,(201)} = 44.70°$ (Fig. 1(d), red). Laue interference fringes are observed on both sides of the film peak, indicating sharp interfaces.

The epitaxial relation between Ni_3In and $SrTiO_3$ is characterized by asymmetric XRD measurements. A collection of Ni_3In (201) diffraction peaks and $SrTiO_3$ (101) diffraction peaks are shown in the pole figure in Fig. 5-5(b). The Ni_3In (201) peaks (black arrows in Fig. 5-5(b)) manifest six-fold rotation symmetry as expected from the hexagonal crystal symmetry, whereas the $SrTiO_3$ (101) peaks (grey arrows in Fig. 5-5(b)) manifest three-fold rotation symmetry as expected from the trigonal symmetry of the (111) facet of a cubic crystal. The in-plane angles of the Ni_3In (201) peaks are matched with those of the $SrTiO_3$ (101) peaks, indicating epitaxial alignment of in-plane crystallographic orientations between the two layers.

Figure 5-6(a),(b) are cross-section transmission electron microscopy (TEM) images of a t_{Ni3In} = 16 nm sample. The low magnification image (Fig. 5-6(a)) reveals a conformally coated film morphology and the actual t_{Ni3In} is estimated to be 15.3 nm, $\sim$ 4% deviated from the calibrated t_{Ni3In}. The higher magnification image (Fig. 5-6(b)) visualizes more clearly the atomic arrangements in both Ni_3In film and $SrTiO_3$ substrate. In agreement with the X-ray measurements, Ni_3In c-axis is aligned with the film normal direction and the inter-kagome distance is found to be $d_{c,TEM}$ = 2.03 Å. This is close to the inter-kagome distance in bulk Ni_3In ($d_{c,bulk}$ = 2.10 Å).

Additionally, we conduct electron energy loss spectroscopy (EELS) measurements for an element-specific chemical identification. Each element is color-coded in Fig. 5-6(d)-(e) and Fig. 5-6(c) is their superposition. Across the sharp film−substrate interface, Ni and In are present only in the top layer (Fig. 5-6(d),(e)), whereas Sr,

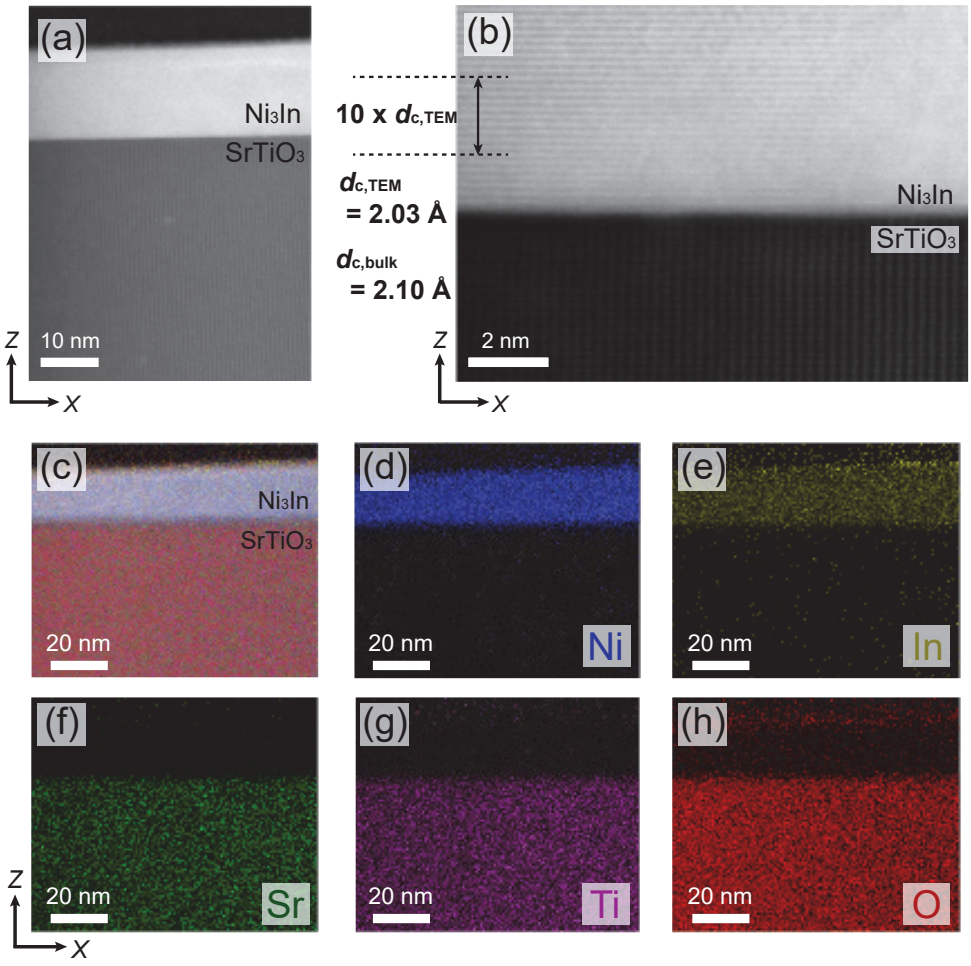

Figure 5-6: **Cross-section structural analysis of a Ni_3In film**

Cross-sectional transmission electron microscopy (TEM) image of a Ni_3In film with (a) high and (b) low magnifications. (c) Electron energy loss Spectroscopy (EELS) measurement and (d-h) element-specific mappings of Ni, In, Sr, Ti, O.

Ti, and O can be found only in the bottom layer (Fig. 5-6(f)-(h)). As expected from the 3:1 stoichiometry, the intensity from Ni is stronger than that from In. At the top surface of Ni_3In film is observed a finite intensity from O, which we hypothesize to be a thin layer of surface oxidation from air exposure.

5.2.3 Electrical characterizations

Electrical transport properties of Ni_3In films are characterized down to 1.8 K in a He-4 cryostat and down to 0.3 K in a He-3 cryostat. Figure 5-7(a) shows the temperature dependent electrical resistivity $\rho_{xx}(T)$ of a $t_{\rm film} = 15$ nm sample grown with ($T_{\rm d}$, $T_{\rm a}$) = (90 °C, 400 °C) (sample $S\#1$ henceforth). The overall temperature dependence at $\mu_0 H = 0$ T reveals a metallic character with decreasing ρ_{xx} as T decreases. The resistivity at $T = 300$ K and 0.3 K are 82.8 $\mu\Omega$ cm and 41.2 $\mu\Omega$ cm, respectively, giving the residual resistivity ratio of $RRR = 2.01$.

Within 100 K $\leq T \leq$ 300 K, $\rho_{xx}(T)$ shows a nonlinear temperature dependence with larger $d\rho_{xx}/dT$ at lower temperature (*i.e.* $d^2\rho_{xx}/dT^2 < 0$). This tendency can also be extracted from the resistivity exponent α, assuming $\rho_{xx} \propto T^{\alpha}$ (Fig. 5-7(c), red). α is inferred from the relation $\alpha = T(d\rho_{xx}/dT)/(\rho_{xx} - \rho_{xx,0})$, where $\rho_{xx,0}$ is the projected ρ_{xx} value at $T = 0$ K. The sublinear exponent ($\alpha < 1$) at $T \geq 100$ K is consistent with $d^2\rho_{xx}/dT^2 < 0$ within this T range. At $T < 100$ K, T-linearity is approximately restored and it persists down to $T \sim 1$ K, much lower than the temperature below which T^2-dependence is observed in conventional metals. With $\rho_{xx}(T)$ deviated significantly from the canonical Fermi liquid (FL) expectation, we identify this 1K $< T \ll 100$ K regime to stabilize a non-Fermi-liquid (NFL) state in Ni_3In. A closer inspection of the NFL state reveals another inflection-like feature in $\rho_{xx}(T)$. As T drops below 20 K, $d\rho_{xx}/dT$ increases additionally by a small amount (Fig. 5-7(b), red). This behavior is also manifested as a small dip in α within a narrow T range around 20 K: $\alpha < 1$ within the dip and $\alpha \sim 1$ above and below that, reflecting two distinct linear slopes. As will be described further below, the feature at 20 K reflects a crucial energy scale of the NFL state. Entering the $T \leq 1$ K regime, $\rho_{xx}(T)$ eventually recovers a FL-like T^2 rollover, which can also be seen from

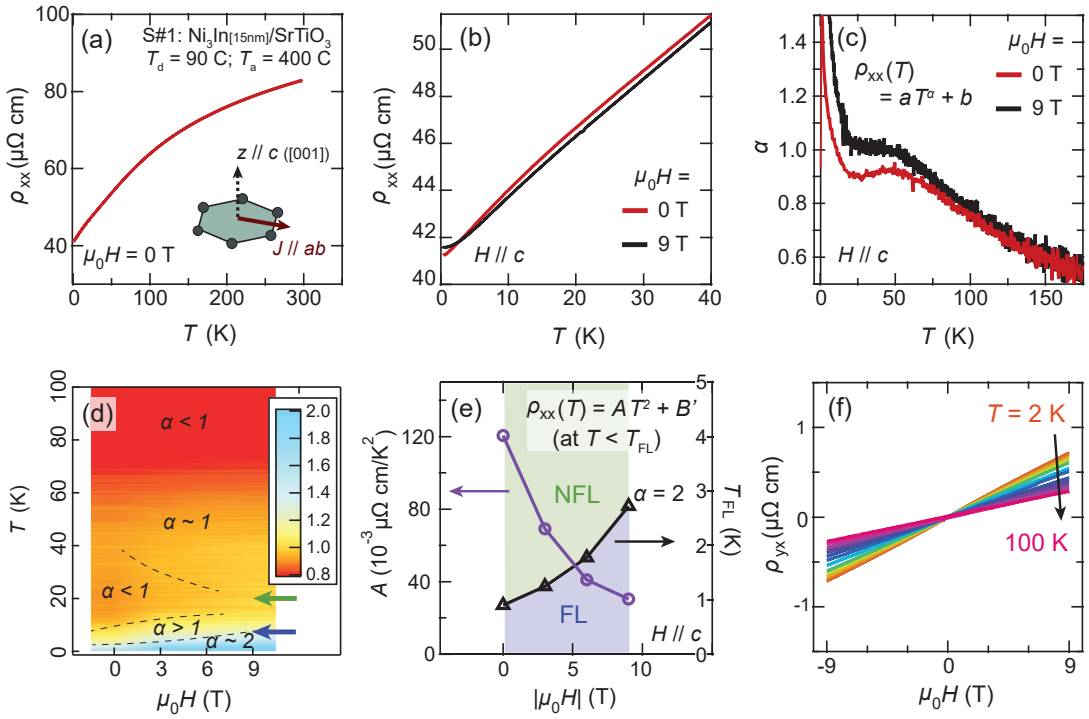

Figure 5-7: **Temperature dependent electrical transport of a Ni_3In film**

(a) Temperature dependent electrical resistivity $\rho_{xx}(T)$ of a Ni_3In film ($S\#1$). (b) Magnified view of (a) in the low temperature regime under 0 T (red) and 9 T (black). (c) Temperature dependent resistivity exponent α under 0 T (red) and 9 T (black). (d) Color plot of α in temperature−field phase space. Dashed lines are guide to the eye for boundaries across which α changes above or below 1. (e) Magnetic field dependent A-coefficient and the NFL-to-FL transition temperature ($T_{\rm FL}$). (f) Hall effect at selected temperatures.

the abrupt increase in α around 1 K (Fig. 5-7(b),(c), red). This crossover signifies a NFL-to-FL transition across $T_{\rm FL} = 1$ K. Within the framework of quantum criticality, quantum fluctuations and their derived NFL behaviors are believed to be enhanced when a system is situated near a quantum critical point (QCP), the zero temperature phase boundary between an ordered phase and a disordered phase [120–123]. The observation of NFL behaviors down to anomalously low temperature evidences that Ni_3In may be positioned in close proximity to a suspected QCP.

We find that the NFL-to-FL transition can be tuned with magnetic field. Both $\rho_{xx}(T)$ and α at $\mu_0 H = 9$ T (H // c) indicate $T_{\rm FL} \sim 3$ K, increased from that for $\mu_0 H = 0$ T (Fig. 5-7(b),(c), black). The overall behavior of α in (T, $\mu_0 H$) phase space is

depicted in Fig. 5-7(d), manifesting the increase in T_{FL} (blue arrow) as well as the dilution of the feature at 20 K (green arrow) under magnetic field. The field-tuning of T_{FL} suggests that fluctuating magnetic moments may be related to the quantum fluctuations that give rise to the Fermi surface breakdown. To examine the framework of field-tuned quantum criticality, we extract the A-coefficient of resistivity, acquired by fitting $\rho_{xx}(T)$ to $AT^2 + B'$ at $T < T_{\mathrm{FL}}$. A number of quantum critical systems have manifested divergence of the A-coefficient at the QCP. In the case of Ni_3In, the A-coefficient systematically decreases as the NFL state becomes suppressed with increasing magnetic field (Fig. 5-7(e)). This supports a consistent scenario that Ni_3In shifts away from the suspected QCP as magnetic field suppresses the spinful quantum fluctuations in the system.

The electrical transport responses in Fig. 5-7(a)-(e) qualitatively agree with those observed in bulk single crystal Ni_3In, even matching the key temperature scales of the NFL state [60]. In bulk, the Hall response was found to be linear within 9 T with hole-like Hall coefficients (R_{H}) monotonically increasing as T decreases. There, one of the interpretations was that an anomalous Hall contribution to R_{H}, arising from the field-polarized magnetic moments in the system (those also responsible for the quantum fluctuations in the zero-field state), increases at lower T as moments grow in size − this is phenomenologically similar to the Hall responses in heavy fermion Kondo systems [124–126]. In our films, a qualitatively similar response is observed (Fig. 5-7(f)). Given the multi-band nature of the system, however, further studies are required to confirm this argument.

In addition to the NFL-to-FL transition, other features in $\rho_{xx}(T)$ across the extended temperature range can be explained in relation to the spin fluctuations. For this purpose, we characterize magnetoresistance (MR $\equiv (\rho_{xx}(H) - \rho_{xx}(H = 0))/\rho_{xx}(H = 0)$) of another $t_{\mathrm{Ni3In}} = 20$ nm sample grown with (T_{d}, T_{a}) = (95 °C, 420 °C) (sample $S\#2$ henceforth). S#2 manifests a similar $\rho_{xx}(T)$ to S#1 though with different ρ_{xx} and RRR values (Fig. 5-8(a)). Figure 5-8(b) shows the MR of S#2 within 2 K $\leq T \leq$ 300 K (H // c). At $T = 300$ K, we see a small positive MR with 0.002% amplitude at $\mu_0 H = 9$ T, likely originating from the Lorentz-force deflection

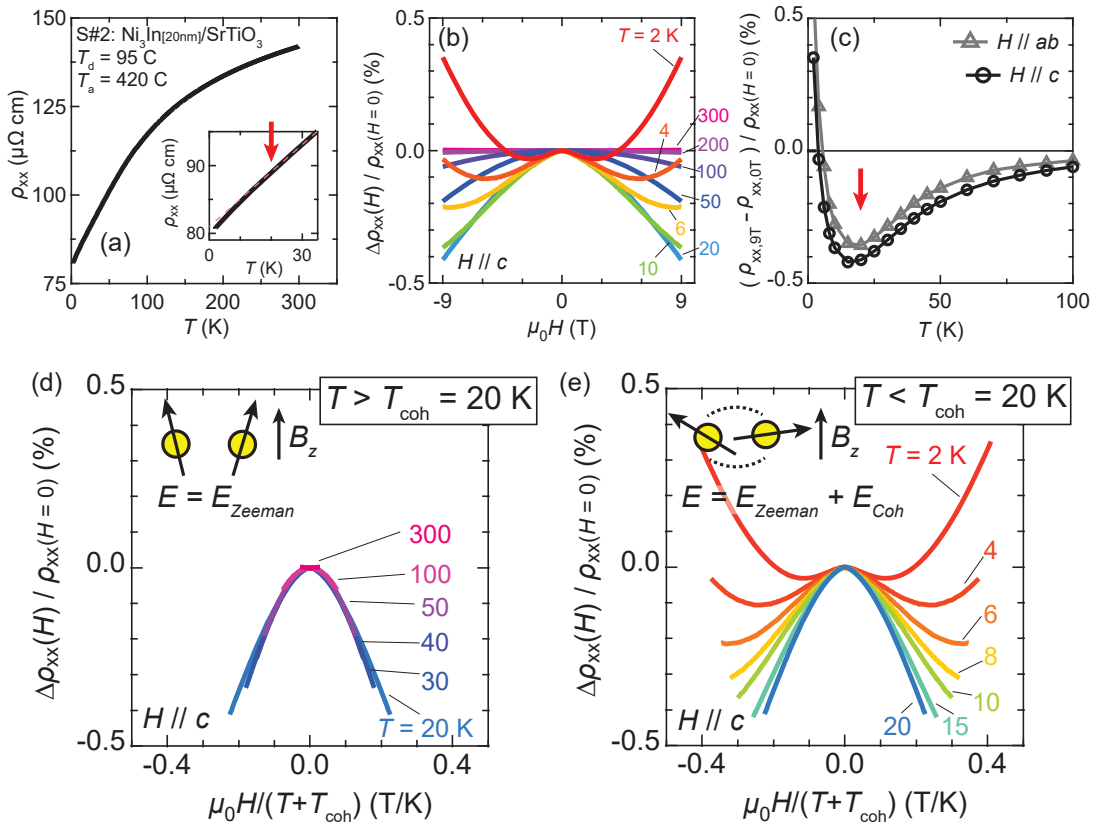

Figure 5-8: **Magnetoresistance of a Ni_3In film**

(a) Temperature dependent electrical resistivity $\rho_{xx}(T)$ of a Ni_3In film ($S\#2$). Inset: magnified view of (a) in the low temperature regime. (b) Magnetoresistance (MR) at selected temperatures with H // c. (c) 9 T MR at different temperatures with H // c (black) and H // ab (grey). Red arrows in (a),(c) mark the features at T = 20 K. The MR traces in (b) plotted against $\mu_0 H/(T+T_{\rm coh})$ for (d) $T \geq 20$ K and (e) $T \leq 20$ K. $T_{\rm coh}$ = 20 K is used for this analysis.

of electrons' trajectory. As T decreases, it gives way to a small negative MR with -0.002% amplitude at $\mu_0 H = 9$ T at $T = 250$ K. The onset of negative MR at $T < 300$ K can be ascribed to the formation of localized magnetic moments and subsequent field-suppression of their fluctuations. This may also account for the nonlinear $\rho_{xx}(T)$ in the 100 K $\leq T \leq$ 300 K regime, within which the local moments become increasingly well-defined at lower T and generate a nonmonotonic temperature dependence of scattering cross-sections for conduction electrons.

The quadratic negative MR enhances as T decreases, reaching up to -0.42% at $\mu_0 H$

= 9 T at $T = 20$ K. At $T < 20$ K, however, the MR begins to manifest a non-quadratic field dependence. This non-quadraticity likely originates from the superposition of the positive MR component (diverging due to higher electronic mobility at lower T) and the negative MR component (diverging due to higher moment size at lower T). As a result of the two competing contributions, the net MR response below 20 K changes from negative (*i.e.* $d\rho_{xx}/dH < 0$) in the low field regime to positive (*i.e.* $d\rho_{xx}/dH > 0$) in the high field regime. The positive MR component tends to dominate more strongly at lower T and the 9 T MR at 2 K becomes positive with 0.35% amplitude. Figure 5-8(c) summarizes the 9 T MR at different T for H // c (black) and H // ab (grey). Qualitatively similar trends are observed for both field orientations, but the H // c trace is consistently more negative than the H // ab trace. In bulk Ni_3In, χ_c and χ_{ab} showed a Curie-Weiss-type temperature dependence with $\chi_c > \chi_{ab}$ within 2 K $\leq T \leq$ 300 K, where χ_c (or χ_{ab}) denote magnetic susceptibility under H // c (or H // ab) [60]. The former observation is consistent with the presence of local magnetic moments in Ni_3In and the latter suggests more effective field-suppression of magnetic fluctuations when H // c, consistent with our observation that the negative MR component is larger for H // c.

The gradual crossover from the net negative MR response ($T > 20$ K) to the net positive MR response ($T < 20$ K) can be understood as an emergence of spin-spin coherence − the possibility also raised in the bulk study of Ni_3In [60]. To examine this hypothesis, we scale the MR with respect to $\mu_0 H/(T+T_{\rm coh})$ akin to the incoherent spin fluctuation model frequently applied in analyzing the MR responses of heavy fermion systems, where $T_{\rm coh}$ is the temperature above/below which spins are incoherent/coherent [127–130]. Recently, the scope of this model has been expanded to describing in general the effects of local moments on MR responses in metallic systems, not restricted to those from the f-electrons [131–134]. Here, $T_{\rm coh} = 20$ K is used for this analysis under an assumption that the inflection-like feature in $\rho_{xx}(T)$ at $T = 20$K is also a signature of this. Within 20 K $\leq T \leq$ 250 K, the MR traces at different T, when plotted against $\mu_0 H/(T+T_{\rm coh})$, overlay nearly perfectly onto each other (Fig. 5-8(d)). The success of this scaling analysis at $T > T_{\rm coh}$ indicates

that the system in the zero-field state in fact contains an ensemble of incoherently fluctuating spins. In contrast, the MR traces below 20 K deviate significantly from the scaling curves above 20 K (Fig. 5-8(e)). The failure of this scaling analysis at $T < T_{\mathrm{coh}}$ suggests the insufficiency of the incoherent spin fluctuation model in fully accounting for the MR response in this T regime. As depicted in the inset of Fig. 5-8(e), it is hypothesized that the spin-spin coherence energy (E_{coh}) counteracts the field-polarization of individual spins (driven by the Zeeman energy E_{Zeeman}), leading to the suppression of the negative MR component and enabling the positive MR component to dominate the net response.

5.2.4 Magnetic characterization

From the electrical transport measurements, we have gained an insight that Ni_3In may harbor fluctuating local moments likely responsible for the breakdown of the FL state. Having identified the magnetic origin of the quantum fluctuations, we directly probe the magnetic properties of Ni_3In films with torque magnetometry. The sample used for this measurement has $t_{\mathrm{film}} = 20$ nm and is synthesized with (T_{d}, T_{a}) = (97 °C, 427 °C) (sample $S\#3$ henceforth).

Figure 5-9(a) shows the magnetic field dependent torque ($\tau(H)$) at different temperatures. At $T \geq 80$ K, $\tau(H)$ reveals a small but non-quadratic response likely originating from complex background contributions. The background signal depends heavily on cantilever material/shape as well as sample quality/condition. As T drops below 60 K, a relatively well defined quadratic $\tau(H)$ is observed as Ni_3In starts to develop a sizable magnetic susceptibility (χ). We note as a clarification that the quantity being measured is the torque susceptibility χ_τ (or torque magnetization M_τ) that is related to the anisotropy of χ (or M) rather than its absolute value. Despite this distinction, the amplitudes of χ and χ_τ are positively correlated in general. τ monotonically increases as T decreases, reflecting the divergence of χ observed in bulk Ni_3In (Fig. 5-9(e)).

As T decreases further, however, $\tau(H)$ tends to show a linear or even saturating behavior. Such non-quadraticity in $\tau(H)$ reflects the nonlinear magnetic response

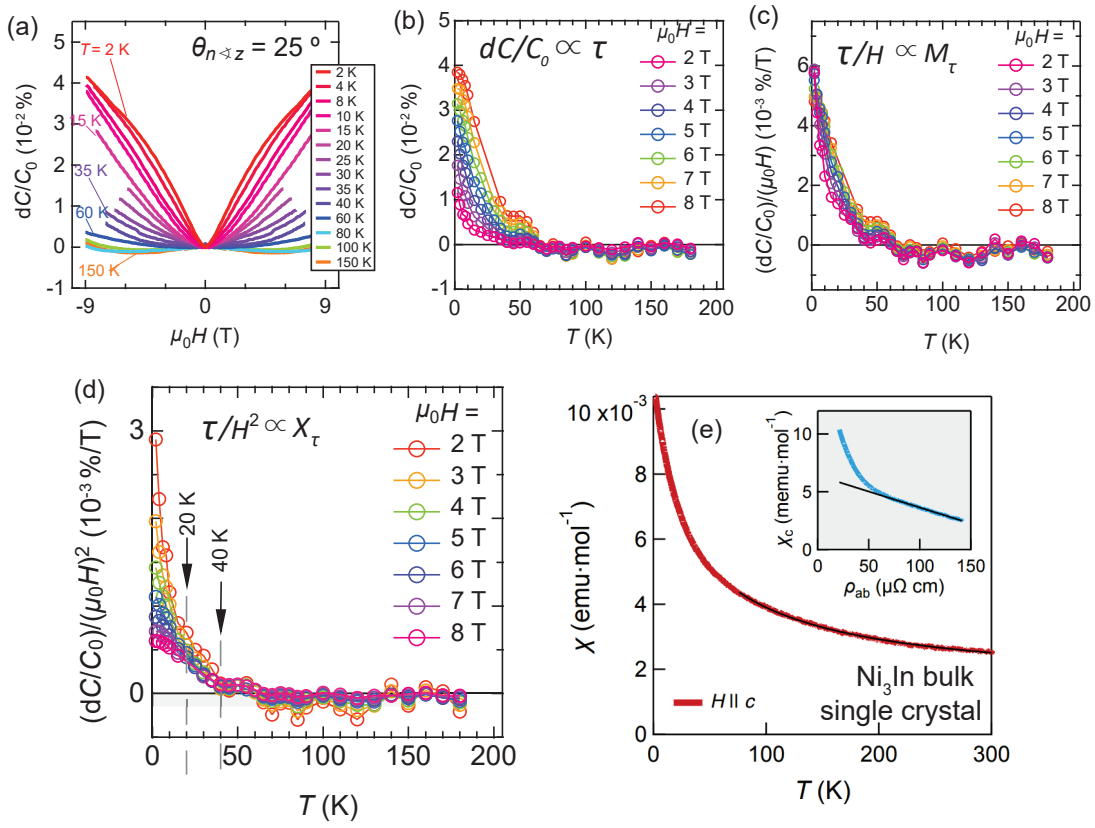

Figure 5-9: **Magnetic torque of a Ni_3In film**

(a) Magnetic torque τ of a Ni_3In film ($S\#3$). Temperature dependent (b) τ, (c) torque magnetization (M_τ), and (d) torque susceptibility (χ_τ) at selected magnetic fields. (e) Temperature dependent magnetic susceptibility of bulk Ni_3In (from [60]).

of Ni_3In at low temperatures. Fig. 5-9(b),(c),(d) show temperature dependent τ, M_τ, χ_τ, respectively, for different values of magnetic field. χ_τ develops a mild field dependence below $\sim$ 40 K, which grows exponentially below $\sim$ 20 K. Considering the nearly identical temperature scale, we hypothesize that the emergence of spin-spin coherence ($T_{\rm coh}$ = 20 K) may be related to the onset of nonlinear magnetic response. At T = 2 K, we find that χ_τ is significantly suppressed by magnetic field. This recalls the MR response at T = 2 K in which the positive MR component always dominates the negative MR component as $\mu_0 H \rightarrow 9$ T. With the magnetic susceptibility rapidly decreasing as a function of magnetic field, the negative MR component can no longer counterbalance the positive MR in the high field regime.

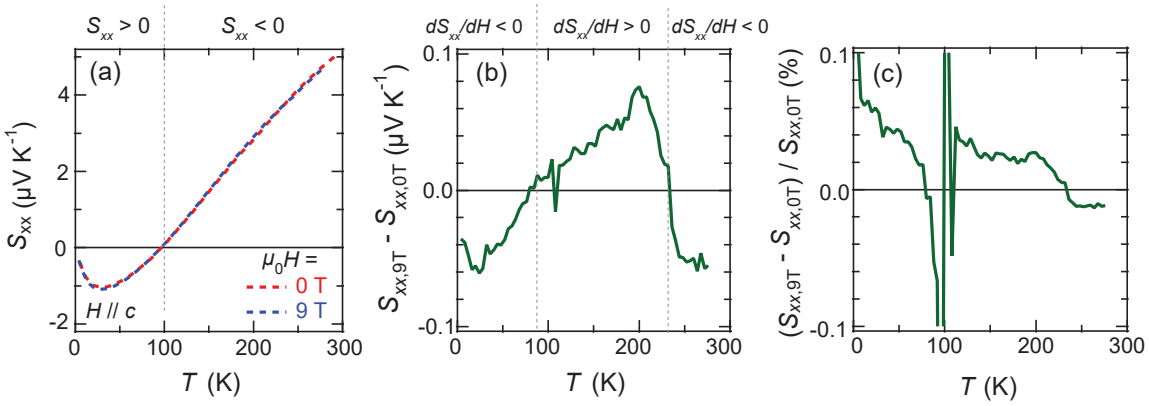

Figure 5-10: **Thermoelectric response of a Ni_3In film**

(a) Temperature dependent Seebeck coefficient S_{xx} of a Ni_3In film ($S\#1$) at 0 T (red) and 9 T (blue). (b),(c) Magneto-Seebeck response. (b) plots the difference between the 9 T trace and the 0 T trace in (a). (c) plots the percentage change of (b) with respect to the 0 T trace.

5.2.5 Thermoelectric characterization

Lastly, we characterize the thermoelectric properties of $S\#1$ within 4 K $\leq T \leq$ 300 K and compare them with its electrical transport properties. Fig. 5-10(a) displays the temperature dependent Seebeck coefficients (S_{xx}) at $\mu_0 H = 0$ T (red) and 9 T (blue). They shows sign reversing behaviors with hole-like/electron-like characters above/below 100 K. The switching of the effective carrier polarity does not agree with the monotonically hole-like Hall response in Fig. 5-7(f), indicating that the band that dominates electrical conduction does not coincide with the band that drives thermal diffusion. Approaching the lowest T, S_{xx} converge to 0 as anticipated from the Mott relation $S_{xx} \propto T$ (*i.e.* thermal diffusion is frozen out at $T = 0$ K) [135].

To capture the effects of magnetic field, we plot in Fig. 5-10(b),(c) the magneto-Seebeck (MS) response at $\mu_0 H = 9$ T. Within 4 K $\leq T \leq$ 230 K, MS is positive with S_{xx} increasing in amplitude without changing sign under magnetic field (note that MS is ill-defined near $T = 100$ K where S_{xx} crosses 0). In contrast, above 230 K, the tendency is reversed and the positive S_{xx} decreases in amplitude under magnetic field. The positive MS response at $T \leq 230$ K is in agreement with the negative MR response at $T \leq 250$ K – electrons flow more easily when the spin fluctuations

disappear. Likewise, the negative MS response at $T > 230$ K is consistent with the positive MR response at $T = 300$ K, the T regime where the moments are significantly diminished in size.

5.2.6 Discussion: anisotropic non-Fermi-liquid state

A combination of electrical transport, magnetic torque, and Seebeck coefficient constructs an insightful viewpoint on the NFL state in Ni_3In. A critical question is: "how relevant is the flat band to this anomaly?" Recalling the high degree of anisotropy of the flat band, it is necessary to examine the anisotropy of the NFL state. In this section, we introduce an interpretation by L. Ye *et al*. based on bulk experiments and revisit the transport responses of the films.

Fig. 5-11(a) shows the reported temperature dependent electrical resistivity of bulk Ni_3In in [60] with the current within the *ab*-plane ($\rho_{xx}(T)$) and along the *c*-axis ($\rho_{zz}(T)$). Compared to $\rho_{xx}(T)$, $\rho_{zz}(T)$ shows a T^2 rollover at an order of magnitude higher temperature. This suggests that the quantum fluctuations have a lesser impact for electrons traveling out-of-plane and the A-coefficient is expected to be smaller when extracted from $\rho_{zz}(T)$. As well as scattering-originated quantities, thermodynamic quantities are extracted from heat capacity. The heat capacity measurement on bulk Ni_3In from [60] manifest a response which deviates from a FL-like response in its cousin compound Ni_3Sn. From here, the Sommerfeld coefficient γ can be estimated.

The extracted A and γ are mapped onto the Kadowaki-Woods ratio plot ($KW \equiv A_c/\gamma^2$) originally compiled in [136] (Fig. 5-11(c)). A number of heavy fermion systems, each harboring distinct A and γ values, belong to the same class with $KW \sim 10$ $\mu\Omega$ mol^2 K^2 J^{-1}. By comparison, transition metals belong to a different class with $KW < 1$ $\mu\Omega$ mol^2 K^2 J^{-1}. Ni_3In is situated in an unusual position in this plot. For in-plane conduction, $KW_{ab} = A_{ab}/\gamma^2 = 226$ $\mu\Omega$ mol^2 K^2 J^{-1}, an order of magnitude larger than the ratio for heavy fermion materials. On the other hand, for out-of-plane conduction, $KW_c = A_c/\gamma^2 \sim 0.65$ $\mu\Omega$ mol^2 K^2 J^{-1}, closer to the ratio for transition metals. While γ is not directly measured in our films, we assume that the films have the same KW_{ab} with the bulk. Using the A_{ab} values extracted in

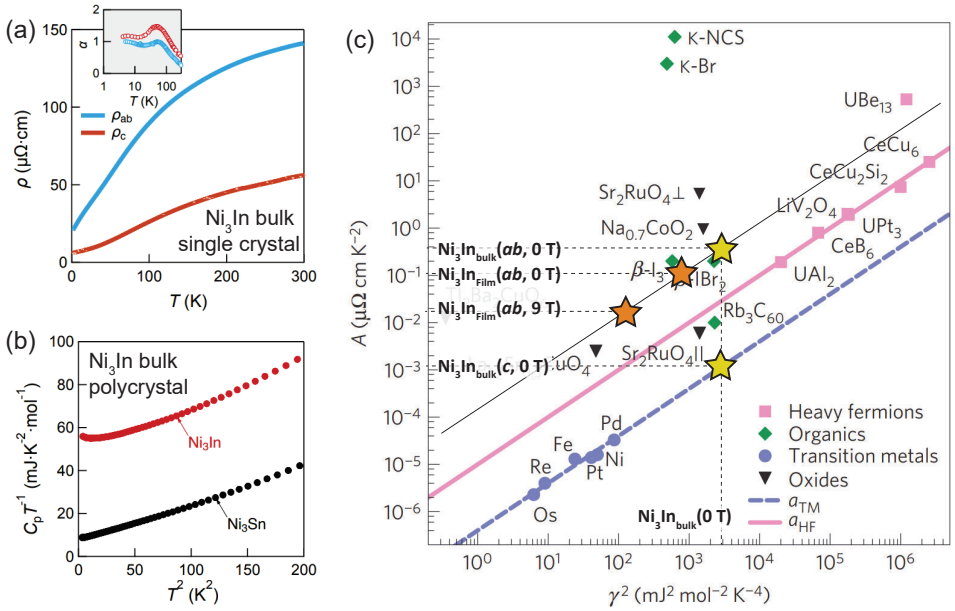

Figure 5-11: **Kadowaki-Woods ratio of Ni_3In**

(a) Temperature dependent electrical resistivity for in-plane (blue) and out-of-plane conductions (red) in bulk Ni_3In. (b) Heat capacity measurements for bulk Ni_3In and bulk Ni_3Sn. (a),(b) are from [60]. (c) Kadowaki-Woods ratios of various compounds compiled in [136]. The yellow stars and orange stars mark the parameters extracted from bulk Ni_3In in [60] and thin film Ni_3In in this work, respectively.

section 5.2.3, we mark $S\#1$ at $\mu_0 H = 0$ T and 9 T on this plot (orange stars in Fig. 5-11(c)). The observation of $KW_{ab}/KW_c \sim 350$ suggests an intriguing aspect of the NFL state in Ni_3In: for a given quasiparticle density, electrons traveling within the plane experience a scattering more than two orders of magnitude stronger than those traveling out of plane.

L. Ye *et al.* have proposed that the flat band in Ni_3In can account for this extremely anisotropic KW [60]. Being localized within the *ab*-plane and delocalized along the *c*-axis, the flat band electrons are expected to act as *f*-electron-like (or *d*-electron-like) scatterers for other conduction electrons traveling within the plane (or out of plane). Furthermore, in the context of the spin fluctuation framework discussed in section 5.2.3 - 5.2.5, the strong in-plane localization of the flat band satisfies one of the key requirements in making local moments [16, 137]. Throughout this section, we have assembled a number of evidence to correlate the NFL behaviors, the anisotropic

flat band, and the fluctuating local moments. We remark that further studies are required to reinforce the connections between them by *e.g.* resolving the mechanism of local moment formation or identifying the nature of the ordered phase beyond the suspected QCP.

5.3 Tuning non-Fermi-liquid behaviors in Ni_3In

To understand better the NFL state in Ni_3In, we apply different experimental control parameters to our Ni_3In films and track the changes in the electrical transport properties. In section 5.3.1, we modify the MR response of Ni_3In via spin injection. In section 5.3.2, we tune the key energy scales of the NFL state by intercalating alkali metal atoms into Ni_3In.

5.3.1 Heterointerfacial spin injection

To engineer the magnetic scattering processes in Ni_3In, we deposit magnetic insulators on Ni_3In films and inject spinful quasiparticles across the interfaces. The film used for this experiment is a $t_{\mathrm{film}} = 15$ nm sample grown with (T_{d}, T_{a}) = (80 °C, 375 °C) and capped with a 190 nm thick antiferromagnetic insulator NiO (sample $S\#4$ henceforth). Fig. 5-12(b) displays the XRD spectrum of $S\#4$ (black), showing a comparable quality to a bare Ni_3In film grown in the same manner (green). As NiO is insulating, the electrical transport of $S\#4$ reflects the intrinsic properties of Ni_3In, nearly identical to those observed in $S\#1$ and $S\#2$ (Fig. 5-13(a)).

A vertical temperature gradient (ΔT) is generated so that quasiparticles in the NiO layer can diffuse into the Ni_3In layer [138–140]. The setup is similar to that for thermoelectricity measurements (Fig. 5-12(a)). To vary ΔT while maintaining the Ni_3In layer at a desired temperature T_{film}, the temperatures of the hot end (T_{hot}) and the cold end (T_{cold}) are independently controlled. Fig. 5-13(b) shows the temperature dependent 9 T MR under different ΔT. The $\Delta T = 0$ trace (red) reproduces the behavior expected for a bare Ni_3In film (see section 5.2.3). In the $\Delta T = 1$ K (green), 2 K (blue), 3 K (purple) traces, however, the negative MR amplitudes systematically

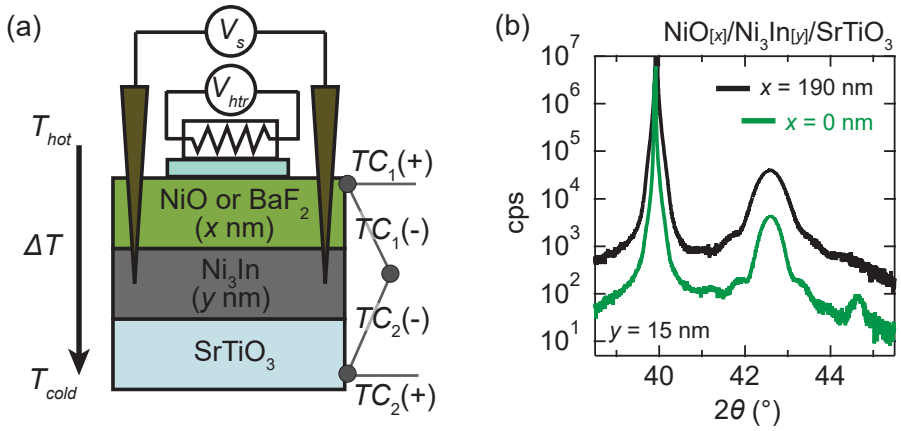

Figure 5-12: **Fabrication of NiO/Ni_3In heterostructure**

(a) Schematic of a NiO/Ni_3In heterostructure with a heater and thermocouples attached. (b) X-ray diffraction spectra of a NiO/Ni_3In heterostructure (S#4; black) and a bare Ni_3In film (reference; green).

suppress with increasing ΔT. This tendency monotonically intensifies down to 20 K, below which it becomes less pronounced; the full MR responses at $T_{\text{film}} \sim 20$ K are presented in Fig. 5-13(c) as an example. These observations are also summarized in Fig. 5-13(d), where we plot the percentage suppression of MR amplitude at each T_{film} and ΔT. As described above, the MR changes most dramatically around 20 K.

As a control experiment, we perform the same set of measurements on a thicker sample with $t_{\text{Ni3In}} = 35$ nm and confirm that MR is nearly unaffected by ΔT (Fig. 5-14(a)). The strong dependence on t_{Ni3In} suggests that the observed effect is an interface-originated one. When $t_{\text{Ni3In}} \gg \xi$, where ξ is the characteristic quasiparticle decay length, the quasiparticles do not propagate deep into the bulk part of the film and the electrical transport will remain unchanged. Comparing the results from $t_{\text{Ni3In}} = 15$ nm and $t_{\text{Ni3In}} = 35$ nm, we expect that $\xi \ll 35$ nm and reduction of t_{film} below 15 nm may further enhance the ΔT dependence of MR. Another control experiment is performed on a sample with $t_{\text{Ni3In}} = 15$ nm, but capped with nonmagnetic BaF_2. In this case, the injected quasiparticles are not spinful and MR is does not change appreciably under $\Delta T \neq 0$ (Fig. 5-14(b)). This indicates that the modification of MR is associated with the magnetic nature of the injected quasiparticles.

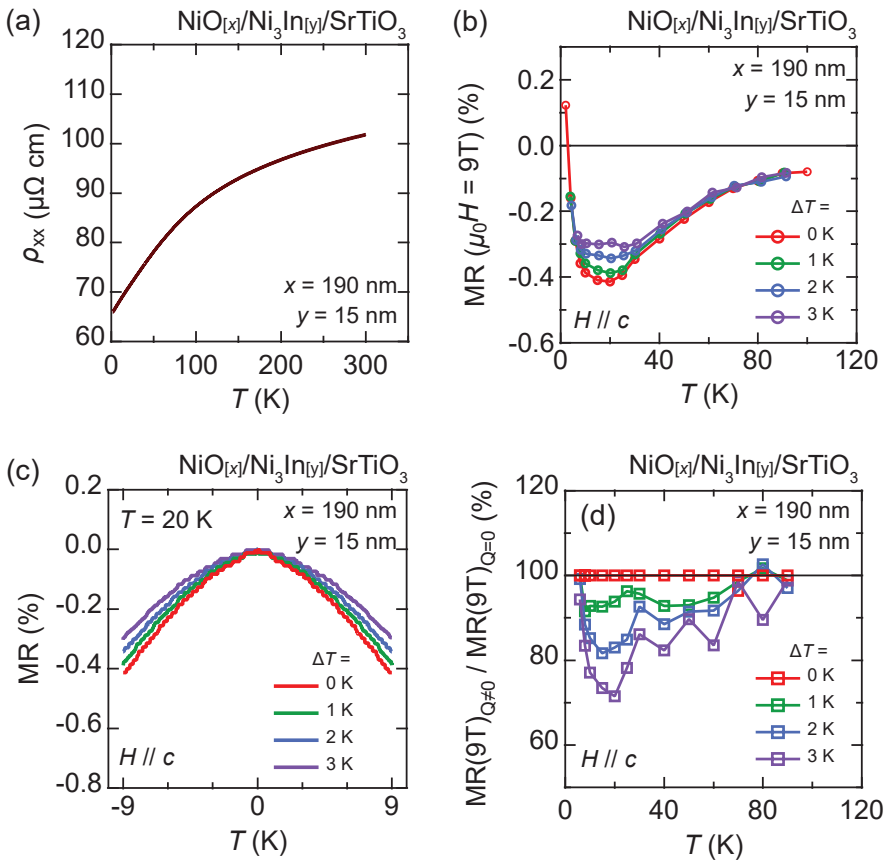

Figure 5-13: **NiO/Ni_3In under thermal gradient**

(a) Temperature dependent electrical resistivity of a NiO/Ni_3In heterostructure (S#4). (b) 9 T MR at different temperatures under different thermal gradients (ΔT). (b) MR traces under different ΔT with the Ni_3In layer fixed at $\sim$ 20 K. (d) Percentage change of 9 T MR under different ΔT.

Based on these findings, we discuss a possible interpretation for the suppression of negative MR. In general, one of the major decay pathways for magnetic quasiparticles is a spin-non-preserving scattering process. This gives rise to a rapid decay of spin current when injected into a ferromagnet with opposite spin polarization direction (*i.e.* giant magnetoresistance) [141] or into a heavy metal with large spin-orbit interactions (*e.g.* Pt, Ta, W) [142]. Ni_3In does not belong to either of these material classes, but is suspected to contain fluctuating local moments. We hypothesize that the magnetic scattering with the intrinsic local local moments in Ni_3In may be the dominant decay pathway for the injected quasiparticles. This quasiparticle−moment

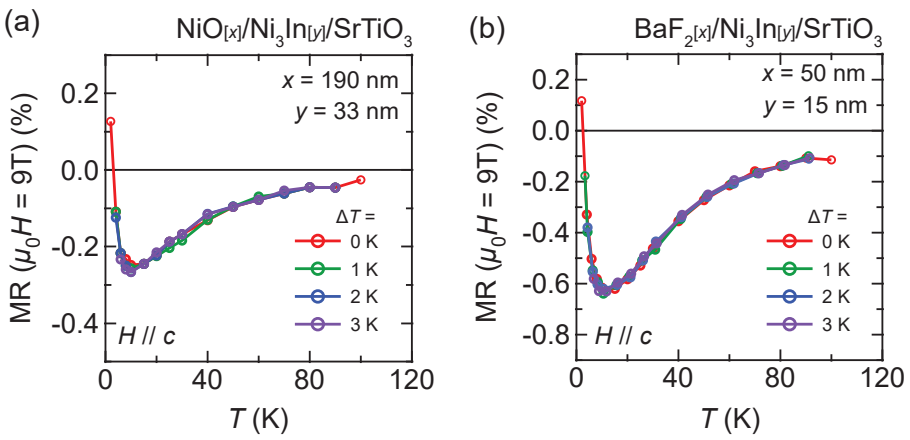

Figure 5-14: **Other heterostructures under thermal gradient**

9 T MR at different temperatures under different thermal gradients in other heterostructures. (a) Results for a sample with the identical structure as $S\#4$, but thicker Ni_3In layer. (b) Results for a sample with the same Ni_3In layer thickness as $S\#4$, but capped with BaF_2.

scattering will simultaneously modify the lifetime and degeneracy of the local moments and eventually affect their interactions with the existing conduction electrons in Ni_3In, incurring a significant change in the MR response as observed here. This interpretation can account for other aspects of the data. The enhancement of MR modification at lower T_{film} can be explained as the quasiparticle−moment scattering manifesting more clearly when thermal fluctuation is reduced. Below $T_{\mathrm{film}} = 20$ K, the local moments are seen to be impervious to the quasiparticles. Recalling that this temperature scale coincides with $T_{\mathrm{coh}} = 20$ K, we anticipate that a coherent many-body ensemble of the local moments is more robust against external magnetic scatterings that lift the degeneracy of individual spins. Similarly as the coherence energy counteracts the Zeemen energy under magnetic field, it is suspected to resist against the interaction energy with the NiO quasiparticles.

5.3.2 Alkali metal intercalation

In section 5.3.1, we engineered the nature of quantum fluctuations in Ni_3In via spin injection and made a stronger tie between the NFL state and the local moments. In

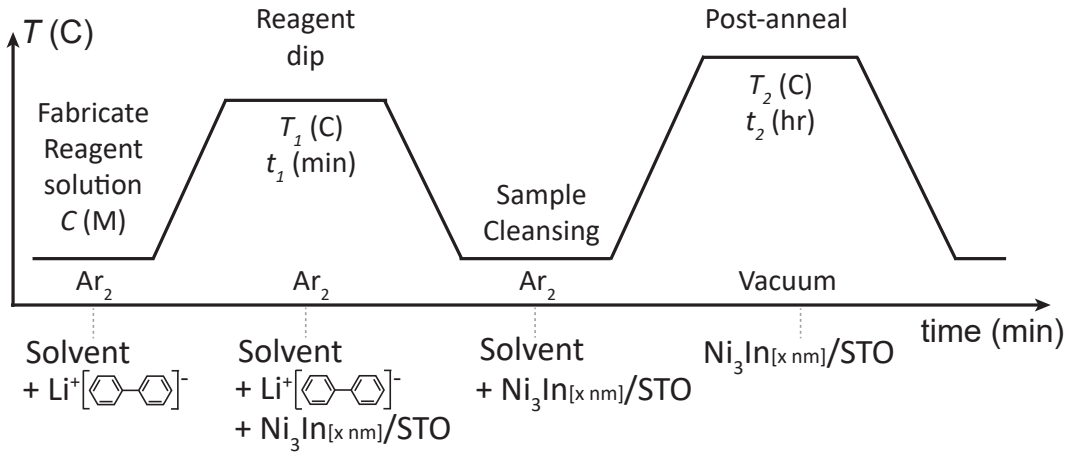

Figure 5-15: **Schematic experimental sequence for alkali intercalation**

this section, a different approach is taken. We intercalate alkali metal atoms into our Ni_3In films and track the changes in the key energy scales of the NFL state. Whereas bulk crystals with macroscopic sample dimensions show highly inhomogeneous intercalant distributions even after prolonged synthesis, thin films with a few nm thickness facilitate homogeneous intercalant distribution within a reasonable experiment time. Furthermore, it is known that chemical pressure from intercalants tend to pulverize bulk samples [143]. Thin films, however, are known to maintain their single crystallinity owing to the film−substrate epitaxial energy.

We intercalate Li and K into Ni_3In through diffusion-mediated approach frequently used for processing Li-ion battery electrodes [144]. Fig. 5-15 is the schematic experimental procedure. For lithiation, we first prepare a reagent solution by dissolving 1M Li metal and 1M Biphenyl (BP) in Dimethoxyethane (DME) solvent. The solution turns dark blue as Li atoms and BP molecules bind to form $Li^{1+}BP^{1-}$ complexes with optical energy gaps. Then, Ni_3In films are dipped into the reagent solution at temperature 25 °C $\leq T_1 \leq$ 75 °C for t_1 (min). When the chemical potential of lithiated Ni_3In (Li_xNi_3In) is lower that that of the reagent solution, Li atoms spontaneously unbind from BP and diffuse into Ni_3In matrix. The relative chemical potential of Li_xNi_3In with respect to that of Li−BP/DME solution is determined by a number of factors including Li concentration, stabilization from Li−Ni_3In chemical reaction, and

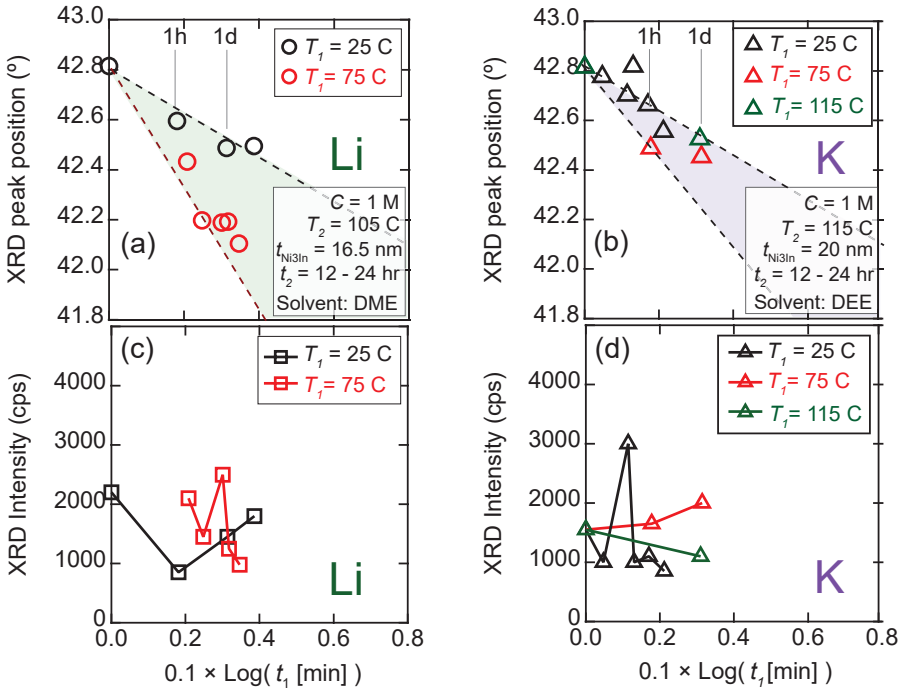

Figure 5-16: **X-ray diffraction of alkali intercalated Ni_3In films**

Intercalation-induced changes in the Ni_3In (002) X-ray diffraction (XRD) peak. XRD peak positions in (a) lithiated and (b) potassiated Ni_3In films. XRD peak intensities in (c) lithiated and (d) potassiated Ni_3In films.

destabilization from Li-induced chemical pressure. We find empirically that Li_xNi_3In forms spontaneously at room temperature and the rate of reaction can be boosted at elevated T_1. After the reagent dip, the samples tend to have higher/lower Li concentration near the top/bottom surface and manifest asymmetric XRD peaks. To distribute the intercalants uniformly, the films are post-annealed at $T_2 = 105$ °C for t_2 (hr) and the XRD peaks restored symmetric shapes. To obtain potassiated Ni_3In (K_xNi_3In), Diethoxyethane (DEE) is used for the reagent solution and a similar synthesis protocol is followed.

In response to intercalation, the (002) XRD peak of Ni_3In shifts systematically. As shown in Fig. 5-16(a),(b), the shift is roughly proportional to $\log(t_1)$, reflecting an exponential slow down of the reaction as the chemical potential of Li_xNi_3In or K_xNi_3In changes as x increases. As inferred from the direction of the shift, the c-axis lattice constant of Ni_3In expands as a consequence of negative chemical pressure from Li or

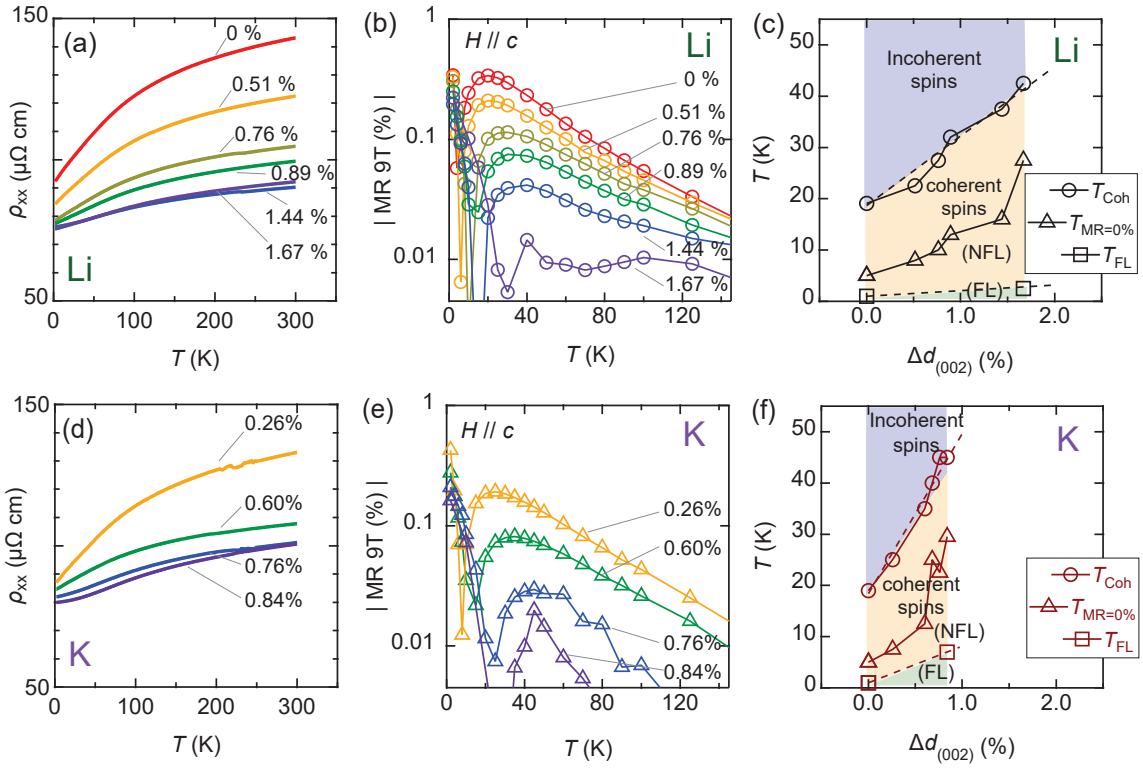

Figure 5-17: **Electrical transport of alkali intercalated Ni_3In films**

(a) Temperature dependent electrical resistivity and (b) 9 T MR (absolute value) for lithiated Ni_3In films with different percentage changes in the c-axis lattice constant (Δd_c). (c) Δd_c-dependent changes in the key energy scales, including the coherence temperature ($T_{\rm coh}$), the zero MR temperature ($T_{\rm MR=0\%}$), and the NFL-to-FL transition temperature ($T_{\rm FL}$). (d)-(f) are the same measurements/analyses as (a)-(c) for potassiated Ni_3In films.

K. By varying t_1 and T_1, we stabilize a wide range of intercalated states as denoted by the phase space shaded green and purple in Fig. 5-16(a) and (b), respectively. Across the entire range of intercalation, the XRD peak intensity maintains the same order of magnitude (except for the fluctuations due to beam alignment and sample size effects), indicating the sample quality does not deteriorate significantly with respect to the pristine state (Fig. 5-16(c),(d)).

We characterize the electrical transport properties of Li_xNi_3In and K_xNi_3In. Fig. 5-17(a) shows $\rho_{xx}(T)$ of Li_xNi_3In with different percentage changes in the c-axis lattice constant (Δd_c). The RRR decreases from 1.55 at $\Delta d_c = 0\%$ to 1.21 at $\Delta d_c = +1.67\%$, likely originating from the increased scattering centers at the Li sites. For $\Delta d_c \sim 0$,

$\rho_{xx}(T)$ is approximately linear down to the lowest T measured, while for $\Delta d_c \rightarrow 1.67\%$ T^2 rollover is observed from $\sim$ 2.5 K, higher than $T_{\mathrm{FL}} = 1$ K in pristine Ni_3In. This suggests another type of NFL-to-FL transition driven by lithiation. Fig. 5-17(b) shows the temperature dependent 9 T MR amplitudes for different values of Δd_c. All samples manifest qualitatively similar trends, but the positive and negative MR components simultaneously decrease as Δd_c increases. Furthermore, the temperature at which the negative MR is maximized − corresponding to T_{coh} in pristine Ni_3In − gradually increases from $\sim$ 20 K at $\Delta d_c = 0\%$ to $\sim$ 42 K at $\Delta d_c = +1.67\%$. Fig. 5-17(c) summarizes the changes in T_{FL} (squares) and T_{coh} (circles) as a function of Δd_c. Also plotted in this phase diagram is the temperature at which the 9 T MR crosses 0% ($T_{\mathrm{MR=0\%}}$; triangles), increasing from $\sim$ 5 K at $\Delta d_c = 0\%$ to $\sim$ 27 K at $\Delta d_c = +1.67\%$. A collection of T_{FL}, T_{coh}, and $T_{\mathrm{MR=0\%}}$ constitute a phase diagram which highly resembles a phase diagram of a system shifting away from a QCP with all relevant energy scales increasing. The same set of measurements are performed on K_xNi_3In (Fig. 5-17(d),(e)) and an analogous phase diagram is constructed (Fig. 5-17(f)). While the phase diagrams of Li_xNi_3In and K_xNi_3In show similar NFL-to-FL transitions, we find that the rate at which the system moves away from the suspected QCP is approximately two times faster for K_xNi_3In when plotted against Δd_c. As K generates a stronger negative chemical pressure than Li, the discrepancy between the two phase diagrams is expected to be larger when plotted against doping concentration. These suggest that neither unit cell size nor doping capacity alone can fully account for the observed quantum critical tuning.

We therefore investigate the effects of local bond distortions at a sub-unit cell scale. Structural stability calculations suggest that alkali atoms favor the centers of compressed Ni_3 trimers in Ni_3In, the localization sites for the flat band electrons. This as a result disrupts the hopping interference condition in pristine Ni_3In and increases the in-plane bandwidth of the flat band. Being approximately twice as large as Li, K is expected to impose more drastic deformations to the flat band wavefunction and suppress the NFL state more rapidly. In a broader perspective, the lattice engineering of Ni_3In via intercalation can help manipulate the flat band morphology in a designer

approach. We propose that driving the flat band to the zero bandwidth state may push the system across the suspected QCP and stabilize a possible ordered phase.

5.4 Conclusions and outlook

In this chapter, we have investigated the electronic structure and physical properties of an AB-stacked paramagnetic kagome metal Ni_3In. By taking into account some of the key structural aspects, we identified a disappearance of the kagome-derived band singularities and a concurrent emergence of a new type of anisotropic flat band. We stabilized Ni_3In in epitaxial thin film form with MBE and characterized its properties significantly deviated from the FL expectations, suggestive of a QCP in the proximate phase space. The field dependence of the NFL state implies that fluctuating local moments, potentially originating from the flat band in the band structure, may be account for the quantum fluctuations that give rise to Fermi surface breakdown. We enriched this understanding by engineering the NFL behaviors via heterointerfacial spin injection and alkali metal intercalation, through which the connections between the NFL behaviors, the fluctuating local moments, and the flat band are examined.

Looking forward, we anticipate that epitaxial strain, electrostatic gating, quantum confinement, and chemical doping can all be applied to thin films of Ni_3In and its related systems so that the nature of their quantum criticality can be elucidated. Along this line, one of the theoretical advances that can be made is to decipher the mechanism through which local moments can be born out of the anisotropic flat band. Last but not least, as well as the physics of quantum criticality, the anisotropic flat band discussed herein represents only one among numerous pathways of designing a flat band. This study proposes that a concerted action of stacking sequence, lattice distortion, and orbital degrees of freedom can generate different types of flat bands starting from building block atoms and layers that originally do not support a flat band in the energy spectrum.

Chapter 6

Band engineering of antiferromagnetic semimetal GdBi

In the previous chapters, we have investigated different types of topological and correlated electronic states in the kagome lattice placed under various symmetry conditions and electromagnetic environments. The purpose of this chapter is to provide a perspective on commingling topology and correlation in a non-kagome-derived platform and compare it with the kagome-derived approaches taken in chapter 3 - 5. Here, we present our works on synthesis and characterization of epitaxial thin film GdBi – a member of rare-earth monopnictides (RX) in which topologically nontrivial Dirac electrons interact with the internal magnetic order. Whereas the kagome metals accomplish the above by the characteristic lattice geometry of the constituent layers and their stacking sequences, RX does so by the spatial coexistence of localized f-electrons and spin-orbit coupled p-electrons, the former providing spin degrees of freedom and the latter driving band inversion. We realize the films down to the two-dimensional limit in a degradation-free manner and drive them across a metal-to-insulator transition via quantum confinement, while preserving the magnetic order and topological character. Finally, we propose a possible higher Chern number state realizable in the monolayer limit of this compound.

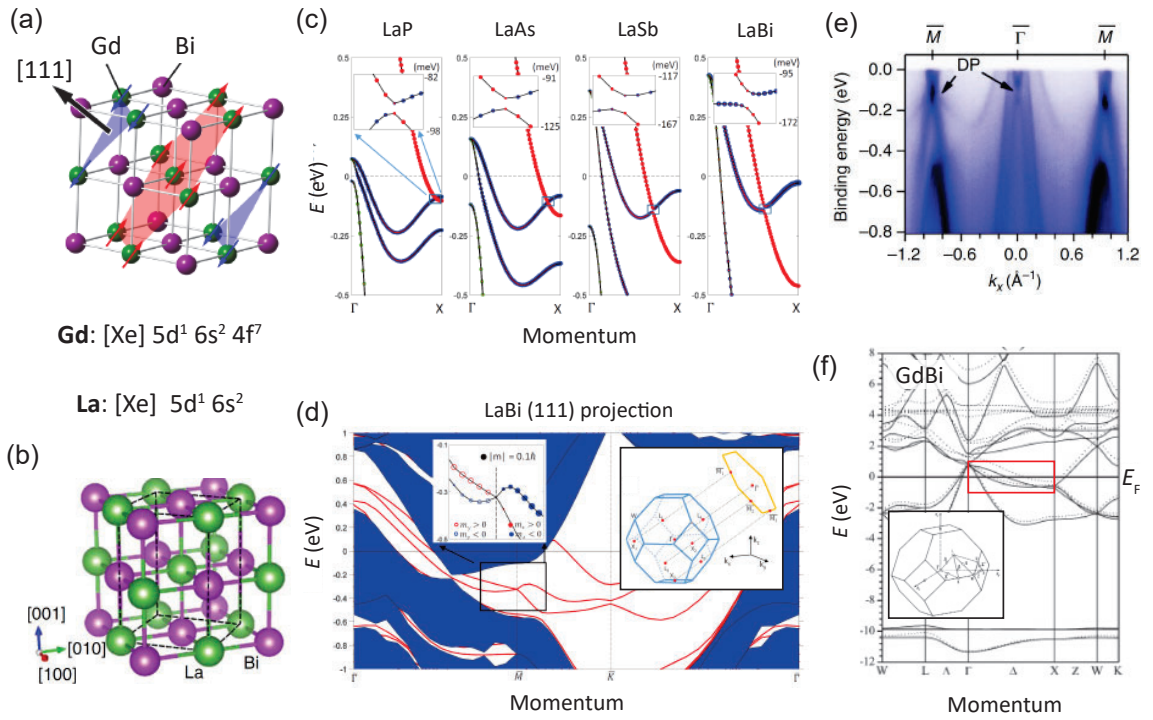

Figure 6-1: **Properties of LaBi and GdBi**

Schematic crystal structures of (a) GdBi and (b) LaBi. The spin structure is also depicted in (a). (c) Band structures of LaX (X = P, As, Sb, Bi). (d) (111)-projected band structure of a LaBi slab, manifesting a topological Dirac surface state. (e) Photoemission spectrum of bulk single crystal LaBi. (f) Band structure of GdBi in the antiferromagnetic state. (c),(d) are adapted from [145]. (b),(e) are from [146]. (f) is adapted from [147].

6.1 Properties of (La:Gd)Bi

The rare-earth monopnictides (RX, R: rare-earth; X: pnictogen) are a class of materials which host a rich variety of magnetic and electronic phases [147]. RX crystallizes in a rocksalt structure with R and X each occupying one of the sublattices. With spin-orbit coupled (SOC) p-electrons in X atoms and localized f-electrons in R atoms coexisting in a single material, RX has been identified as a potential platform to study the interplay of nontrivial band topology and electronic correlation.

GdBi is a member of RX (R = Gd; X = Bi) that stabilizes a type-II antiferromagnetic order below $T_N = 28$ K, in which Gd spins polarize ferromagnetically within

each (111) plane with the easy-plane moment directions and arrange antiferromagnetically along the [111] vector [148]; the spin structure is depicted in Fig. 6-1(a). LaBi plays a crucial role in understanding the electrical properties of GdBi (Fig. 6-1(b)). As La does not contain f electron, distinguished from other R = Ce - Lu, LaX (X = P, As, Sb, Bi) typically serve as reference systems in extracting the effects of p-f interactions in other RX. Given that the valance configuration of Gd is [Xe]$5d^16s^24f^7$, seven $4f$-orbitals added to La ([Xe]$5d^16s^2$), GdBi is expected to harbor an electronic structure qualitatively similar to that of LaBi but with additional f-bands far below the Fermi level (E_{F}). These localized f-electrons give rise to magnetism, but cannot contribute directly to electrical transport.

Density functional theory (DFT) band structures of LaX reveal semimetallic band structures with conduction bands from X p-orbitals and valence bands from La d-orbitals at E_{F} (Fig. 6-1(c)) [145]. The conduction and valence bands intersect along the $\Gamma - X$ line and open up a SOC gap, through which a band inversion occurs. As a consequence of nontrivial band topology in the bulk, the (111) surface of LaBi is predicted to have a topological Dirac surface state as presented in Fig. 6-1(d). Following these theoretical insights, photoemission experiments on bulk single crystal LaBi have verified the existence of surface Dirac bands (Fig. 6-1(e)) [146, 149, 150]. As shown in Fig. 6-1(f), the band structure of GdBi in the antiferromagnetic state manifests a nearly identical morphology to that of LaBi. While its topological character has not been reported, a similar band degeneracy is present along the $\Gamma - X$ line and a SOC gap of the same origin as in LaBi is anticipated (note that GdBi is listed in a catalogue of topological materials recently compiled based on high-throughput computations [151–153]). Sharing key aspects of the LaBi band structure, GdBi is also expected to have Dirac surface states, which upon onset of the antiferromagnetic order may interact with spin degrees of freedom.

A challenge in selectively probing these surface states (and further exploring their couplings to magnetism) in GdBi is the presence of large bulk bands from negative indirect band gap of $\sim$ -1 eV. However, theoretical calculations of RX systems in the ultrathin limit suggest that quantum confinement has a potential to push away the

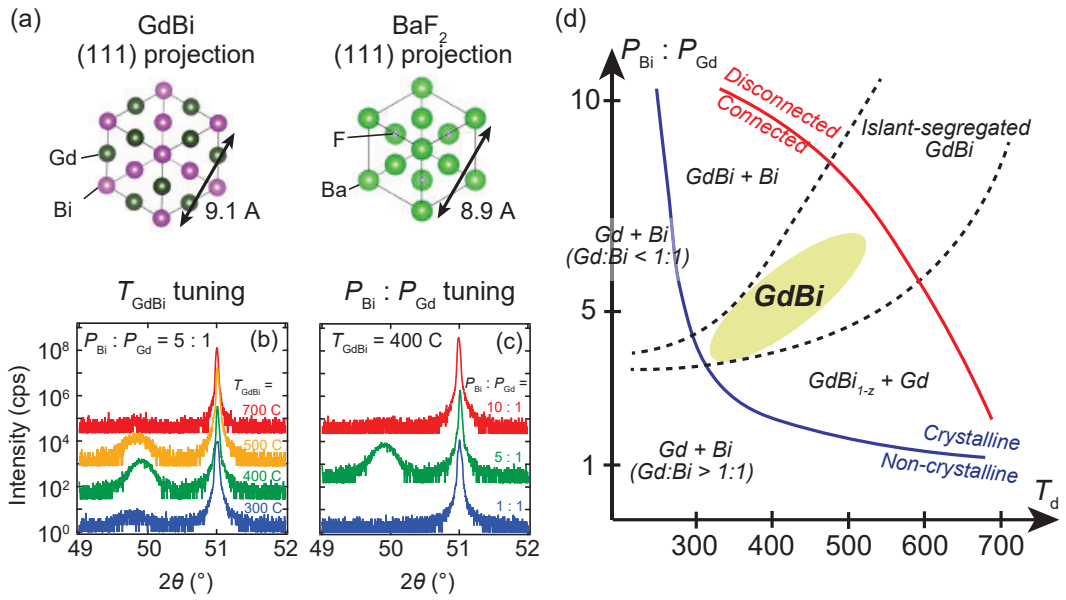

Figure 6-2: **Optimization of GdBi thin film synthesis**

(a) Schematic atomic arrangements on the GdBi (111) plane (left) and the BaF_2 (111) plane (right). X-ray diffraction spectra of GdBi films synthesized (c) at different deposition temperatures and (d) with different BEP ratios. (d) Schematic growth phase diagram of GdBi thin films. An optimized film has high crystallinity (above the blue boundary), connected in-plane morphology (below the red boundary), and 1:1 stoichiometry (along the black dashed line). The region that satisfies these conditions is shaded yellow.

bulk bands from E_F and energetically isolate the surface bands [154]. In the following sections, we present our studies on synthesis, characterization, and thickness-tuning of GdBi thin films conducted with a goal of realizing the bulk insulating state with its topological and magnetic characters preserved.

6.2 Synthesis and characterization of GdBi epitaxial thin films

6.2.1 Epitaxial thin film synthesis of GdBi

GdBi is deposited on the (111) surface of cubic BaF_2 with lattice constant $a_{\mathrm{BaF2}} = 6.20$ Å, well-matched with that of GdBi ($a_{\mathrm{GdBi}} = 6.32$ Å). The inter-atom distance of

the Ba network on (111) planes of BaF_2 is 8.9 Å, 2.2% smaller than that of the Bi (or Gd) network on (111) planes of GdBi (9.1 Å). The identical in-plane crystallographic symmetry and the reasonable match between the two relevant inter-atom distances enable stabilization of GdBi (111) film on BaF_2 (111) substrate (Fig. 6-2(a)).

Without any chemical or thermal treatment, we load as-received BaF_2 substrates (Crystal GmbH) to the molecular beam epitaxy (MBE) chamber and pre-anneal them at 450 °C for 1.5 h. Then, the substrate temperature is changed to 765 °C for deposition of a 200 nm thick epitaxial BaF_2 (111) buffer layer in order to prepare flat and step-terraced surface morphology. Following the buffer layer deposition, GdBi (111) film is deposited at temperature $T_\mathrm{d} = 400$ °C. The beam-equivalent pressures (BEPs) for Gd (P_Gd) and Bi (P_Bi) are calibrated before each growth with an *in-situ* flux monitor. After the film deposition, the samples are capped with 40−100 nm thick BaF_2 to suppress degradation when taken out of the chamber.

The synthesis of high quality GdBi requires fine calibration of T_d and $P_\mathrm{Bi} : P_\mathrm{Gd}$. In the case of FeSn (chapter 3, 4) or Ni_3In (chapter 5), where the sticking coefficients of constituent elements are comparable to each other at a selected T_d range, an extremely precise BEP tuning is required to ensure the intended stoichiometry. The case of GdBi is different in that it realizes an absorption-limited growth due to high vapor pressure of Bi. As the sticking coefficient of Bi is orders of magnitude smaller than that of Gd within the optimized T_d range, synthesis under a Bi-rich environment stabilizes GdBi relatively easily and any surplus Bi desorbs from the substrate. This tendency also helps enlarge the growth phase space for connected films. In absorption-limited growth, island segregation tends to occur at temperature much higher than the melting point of Bi ($T_\mathrm{Bi,melt} = 271$ °C).

Fig. 6-2(b) shows the X-ray diffraction (XRD) spectra of four samples grown with different T_d ($P_\mathrm{Bi} : P_\mathrm{Gd} = 5 : 1$ fixed). The wavelength of the incident X-ray beam was $\lambda = 0.154$ nm and all traces show the BaF_2 (222) XRD peaks at $2\theta = 51.10°$. For 350 °C $\leq T_\mathrm{d} \leq$ 550 °C, pronounced film peaks are observed around the XRD peak position of GdBi (222) ($2\theta_\mathrm{GdBi,(222)} = 50.02°$). Films grown outside this T_d range have either low crystallinity ($T_\mathrm{d} \ll 350$ °C) or disconnected film morphology ($T_\mathrm{d} \gg 550$ °C). Fig.

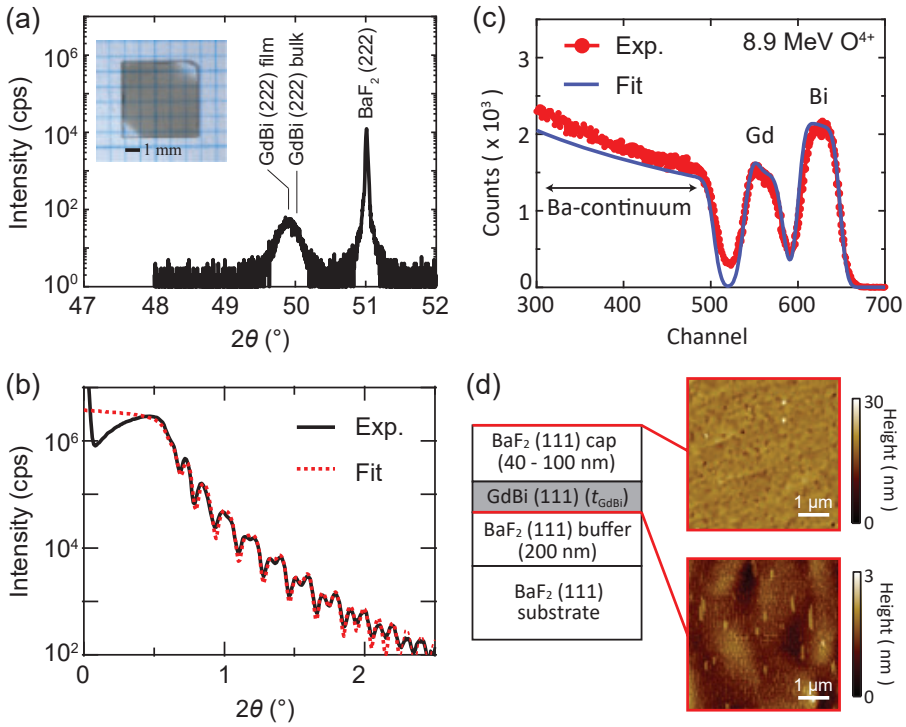

Figure 6-3: **Structural characterizations of GdBi films**

(a) X-ray diffraction spectrum of an optimized GdBi film. Inset: optical micrograph of a GdBi film (scale bar: 1 mm). (b) X-ray reflectivity oscillation (black) and the best fit to the data (red). (c) Rutherford backscattering spectrum from an 8.9 MeV O^{4+} beam experiment (red) and the best fit to the data (blue). (d) Schematic sample structure (left) and atomic force microscopy images of the BaF_2 capping layer (top right) and the BaF_2 buffer layer (bottom right).

6-2(c) shows the XRD spectra of three samples deposited at different $P_{Bi} : P_{Gd}$ (T_d = 400 °C fixed). A pronounced film peak is observed for $P_{Bi} : P_{Gd} = 5 : 1$ and the BEP ratios excessively deviated from this fail to stabilize GdBi. The resultant growth phase diagram for GdBi is depicted in Fig. 6-2(d) with the optimized growth phase space shaded in yellow.

6.2.2 Structural characterizations

Figure 6-3(a) shows the XRD spectrum of an optimized GdBi film synthesized with T_d = 400 °C and $P_{Bi} : P_{Gd} = 5 : 1$, where a pronounced XRD peak is identified at $2\theta = 49.90°$ ($\sim 0.2\%$ deviated from the bulk reference position). The thicknesses

of the GdBi layer (t_{GdBi}) and the BaF_2 capping layer ($t_{\mathrm{BaF2-cap}}$) are calibrated by fitting the X-ray reflectivity (XRR) oscillation to a model structure simulation (Fig. 6-3(b)) and t_{GdBi} = 40 nm and $t_{\mathrm{BaF2-cap}}$ = 42 nm are obtained. To further confirm the sample structure, we perform a Rutherford backscattering (RBS) measurement on a GdBi film with the calibrated thickness of 100 nm. Fig. 6-3(c) shows the RBS spectrum from an 8.9 MeV O^{4+} ion beam experiment, manifesting pronounced peaks from Gd and Bi as well as Ba continuum from the substrate contributions. By fitting the spectrum to the simulated trace, we obtain t_{GdBi} = 105 nm and 1.06 : 0.94 atomic ratio between Gd and Bi, both within the uncertainties of fit from the calibrated thickness and stoichiometry. The atomic force microscopy images in Fig. 6-3(d) display flat surface morphologies of the BaF_2 cap (top) and the BaF_2 buffer (bottom). The surface morphology of the GdBi layer is not directly visualized as it rapidly degrades in air unless capped *in-situ* immediately after growth.

6.2.3 Magnetic characterizations

To probe signatures of a magnetic transition, we characterize a GdBi film with t_{GdBi} = 40 nm using a commercial superconducting quantum interference device (SQUID). Figure 6-4(a) shows the temperature dependence of the magnetic moment m in the GdBi film (red, blue) as well as the magnetic susceptibility χ_{bulk} in GdBi bulk single crystal (green). At the reported T_{N} = 28 K, the bulk measurement manifests a kink in $\chi_{\mathrm{bulk}}(T)$. While for the film there is a relatively large background signal, there are small but discernible features near $T \sim T_{\mathrm{N}}$ for both field orientations.

In order to detect the magnetic response of the films with higher resolution, we perform torque magnetometry. The magnetic field dependent torque $\tau(H)$ is shown in Fig. 6-4(b). At T = 100 K, we observe a quadratic response typical of a paramagnetic susceptibility. This response is enhanced at T = 30 K, while a prominent dip at intermediate H develops at the lowest T = 4 K. In Fig. 6-4(c) we plot the corresponding torque magnetization $M_\tau \equiv \tau/(\mu_0 H) = M_{\mathrm{plane}}$ - M_{norm}, where M_{plane} and M_{norm} are the magnetization parallel and normal to the sample plane, respectively. Here, the trend of an approximately linear M_τ at high T giving way to a strong nonlinear

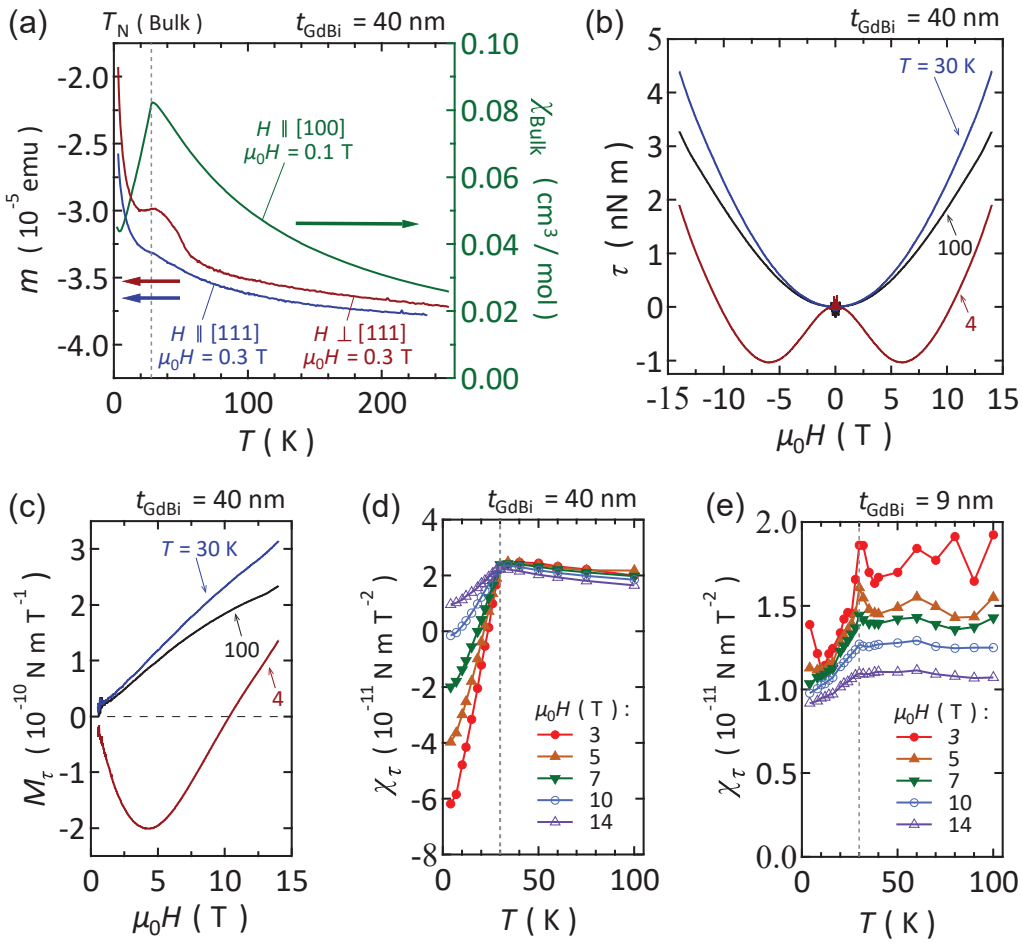

Figure 6-4: **Magnetic characterizations of GdBi films**

(a) Temperature dependence of the magnetic moment m in a GdBi film ($t_{\mathrm{GdBi}} = 40$ nm) (red and blue, left axis) and the magnetic susceptibility χ_{bulk} in GdBi bulk single crystal (green, right axis), both measured from SQUID. Magnetic field dependent (b) torque τ and (c) torque magnetization M_τ of a GdBi film ($t_{\mathrm{GdBi}} = 40$ nm) at selected temperatures. (d),(e) Temperature dependent torque susceptibility χ_τ at fixed magnetic fields for (d) a $t_{\mathrm{GdBi}} = 40$ nm sample and (e) a $t_{\mathrm{GdBi}} = 9$ nm sample.

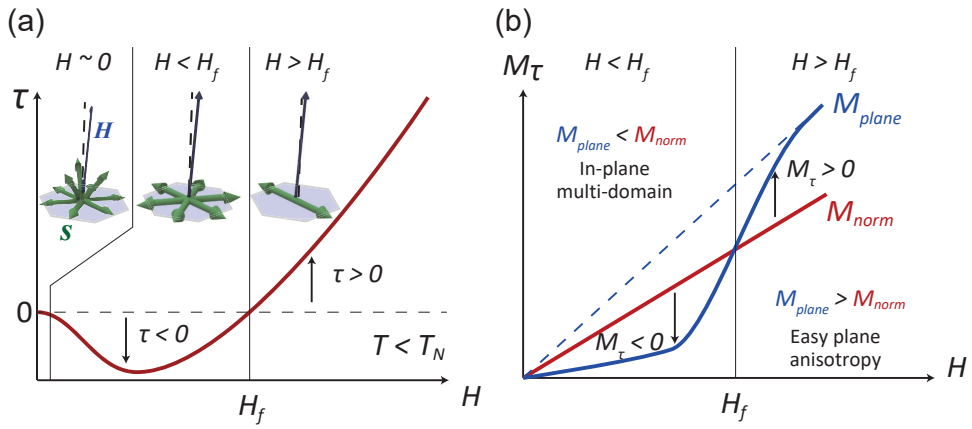

Figure 6-5: **Origin of the magnetic torque response**

(a) Schematic of the low temperature torque response in GdBi. Inset: schematic spin orientations in different magnetic field regimes. (b) Schematic behaviors of $M_{\rm plane}$ and $M_{\rm norm}$ in different magnetic field regimes. $M_{\rm plane}$ - $M_{\rm norm}$ in (b) determines the sign and magnitude of τ in (a).

response at low T can be observed.

The onset of non-quadratic $\tau(H)$ (Fig. 6-4(b)) and nonlinear $M_\tau(H)$ (Fig. 6-4(c)) at low T can be naturally explained by the development of magnetic anisotropy in the magnetic phase. In the absence of H, GdBi forms multiple antiferromagnetic domains with the q-vectors along four equivalent [111] vectors in a cubic crystal (Fig. 6-5(a), $H \sim 0$). An application of small magnetic field, however, stabilizes a single domain state with the q-vector along one of the [111] vectors parallel to the film normal direction (Fig. 6-5, $H < H_{\rm f}$). In this low field state, Gd spins are confined within the film plane due to easy-plane anisotropy, but directed along three different high symmetry directions. Such three-fold degeneracy suppresses $M_{\rm plane}$ and generates $M_\tau < 0$. Upon entering the high field regime, the Zeeman energy eventually dominates and Gd spins flop towards the direction perpendicular to both in-plane and out-of-plane components of H (Fig. 6-5, $H > H_{\rm f}$). In this high field state, $M_\tau > 0$ is obtained due to inherent easy-plane anisotropy of GdBi.

As described above, the complex competition of domain energy, anisotropy energy, and Zeeman energy generates a nonlinear and sign-changing $M_\tau(H)$ response in GdBi. Such response can also be used to probe the Neel temperature of the film ($T_{\rm N,film}$). We

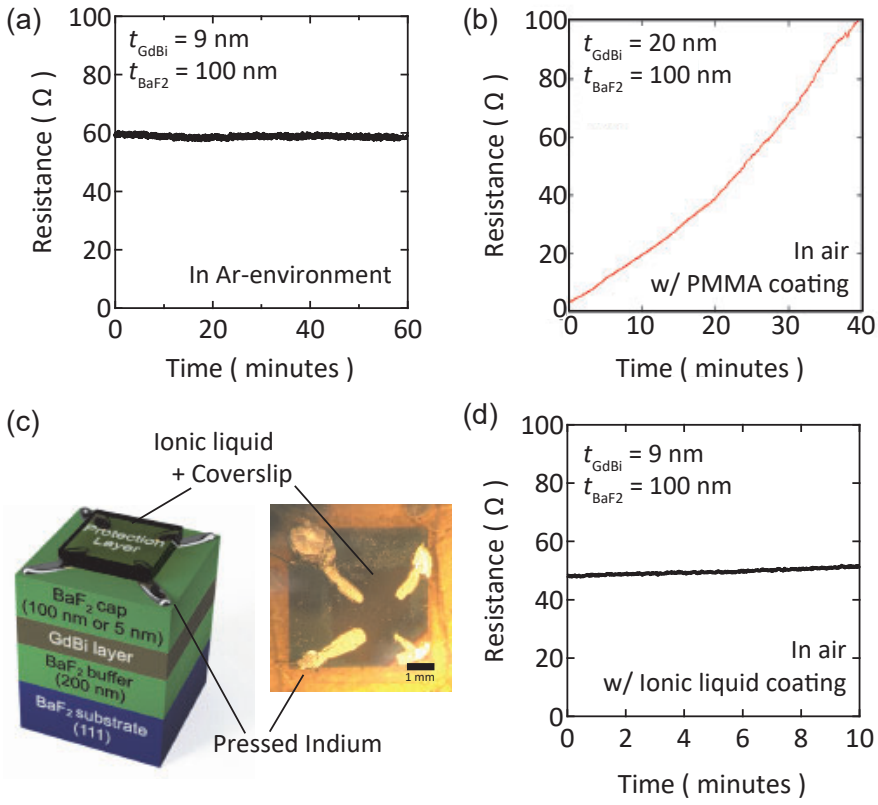

Figure 6-6: **Degradation-free sample preparation**

Time dependent resistance of GdBi films (a) inside the glovebox without additional coating and (b) outside the glovebox with a PMMA coating. (c) Schematic structure of a sample covered with an ionic liquid and a coverslip (left) and an optical micrograph of a sample in that structure. (d) Time dependent resistance of a GdBi film embedded in the structure in (c). It shows a relatively stable behavior in air.

plot the temperature dependent torque susceptibility $\chi_\tau \equiv \chi_{\text{plane}} - \chi_{\text{norm}} = M_\tau/(\mu_0 H)$ in Fig. 6-4(d) for different H and identify $T_{\text{N,film}} \sim 30$ K. A similar $T_{\text{N,film}}$ is observed from a film with $t_{\text{GdBi}} = 9$ nm (Fig. 6-4(e)). The high resolution magnetometry reveals the persistence of the original type-II antiferromagnetic order with nearly identical transition temperature in our GdBi films.

6.3 Confinement-driven metal-insulator crossover

Having confirmed the structural and magnetic properties of our GdBi films, we now explore their electrical transport properties. Critical to this, especially in the ultra-

thin limit, is preventing films from degrading in air. In section 6.3.1, we describe the experimental methodologies developed to preserve the film quality in ambient conditions. In section 6.3.2, we utilize these techniques to observe the thickness-tuned metallicity of the films.

6.3.1 Degradation-free transport sample preparation

Even in bulk form, RX are known to be highly air-sensitive. Within a few minutes in air, surfaces of RX oxidize, which themselves act as protection layers for further permeation of oxygen and moisture into the inner parts of the crystal. The volume of the oxidation layer is generally negligible compared to that of the bulk.

In RX films, however, the entirety of the sample is much thinner than the typical thickness of the oxidation layer. Even with a BaF_2 cap, GdBi films degrade in air within a time scale of seconds and their physical properties change dramatically. To preserve sample properties, we transfer as-grown films directly from the MBE to an Argon-filled glovebox without any air exposure (see section 2.1). As shown in Fig. 6-6(a), the resistance of a $t_{\mathrm{GdBi}} = 9$ nm sample inside the glovebox stays nearly constant for a prolonged period of time. When taken out of the glovebox, however, it immediately oxidizes and turns insulating. This can be slowed by coating the samples with polymethyl methacrylate (PMMA), but the resistance still increases by $\sim$ 10-fold within $\sim$ 20 min (Fig. 6-6(b)).

A number of non-aqueous or hydrophobic liquids have been tested in terms of sample protection performance and a properly degassed ionic liquid has proven the most effective. By adding a droplet of ionic liquid and covering it additionally with a coverslip, we are able to slow down sufficiently the rise in sample resistance for $>$ 10 min in air (Fig. 6-6(c),(d)). In the present sample configuration, the conduction channel is defined by the region underneath the ionic liquid droplet; the area outside the droplet immediately becomes insulating in air and do not contribute to electrical transport. To remove any source of degradation, pressed indium contacts are used instead of conductive epoxies.

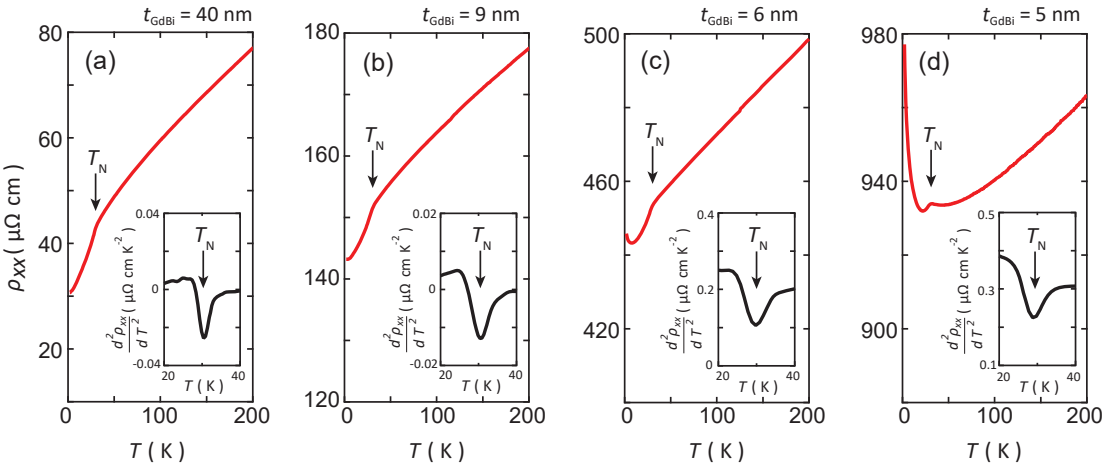

Figure 6-7: **Thickness-tuned longitudinal resistivity in GdBi films**

Temperature dependent electrical resistivity of GdBi films with (a) 40 nm, (b) 9 nm, (c) 6 nm, and (d) 5 nm thicknesses. Insets: second derivatives of (a)-(d). The kink-like features are marked in (a)-(d).

6.3.2 Thickness-tuned electrical transport

Figure 6-7 shows the temperature dependent longitudinal resistivity $\rho_{xx}(T)$ of GdBi films with different t_{GdBi}. For the thickest film with t_{GdBi} = 40 nm, $\rho_{xx}(T)$ reveals a metallic response for all T with a kink near T= 30 K, the latter more clearly observed in the second derivative $d^2\rho_{xx}/dT^2$ (Fig. 6-7(a)). This matches the $T_{\mathrm{N,film}}$ = 30 K identified from the magnetic torque response, suggesting it is a signature of the antiferromagnetic transition. We note that a qualitatively similar feature is also observed in FeSn across its antiferromagnetic transition (see chapter 3). For all measured thicknesses down to t_{GdBi} = 5 nm, the kink is consistently observed around T= 30 K, indicating the preservation of the identical antiferromagnetic order with unchanged T_{N} down to at least five crystallographic unit cells of GdBi. While the magnetism stays nearly thickness-independent, the overall electrical response changes from metallic to non-metallic with decreasing t_{GdBi}; the low T slope $d\rho_{xx}/dT$ changes from positive in t_{GdBi} = 40 nm to negative in t_{GdBi} = 5 nm. This crossover reflects a possible band rearrangement taking place as the system is driven towards the ultrathin limit with significant confinement effects. We note that a similar metal-to-insulator

crossover has been observed as semimetallic Bi thin films are driven to a few nm thickness limit [155, 156].

In order to examine the thickness dependence, we first investigate more thoroughly the properties of a relatively thick film that does not harbor appreciable confinement energy. The black traces in Fig. 6-8 display the magnetic field dependent longitudinal ($\rho_{xx}(H)$) and Hall resistivity ($\rho_{yx}(H)$) of the $t_{\mathrm{GdBi}} = 40$ nm sample at $T = 2$ K. $\rho_{xx}(H)$ shows a non-saturating quadratic field dependence with approximately 10% increase at $\mu_0 H = 9$ T (disregarding the cusp-like feature near $H = 0$ from the superconductivity of the Indium electrodes), whereas $\rho_{yx}(H)$ shows a nonlinear and sign-changing Hall slopes. We analyze these behaviors using the two-band model, in which ρ_{xx} and ρ_{yx} are given by

$$\begin{aligned}
\rho_{xx} &= \frac{\sigma^{\mathrm{e}}_{xx} + \sigma^{\mathrm{h}}_{xx}}{\left(\sigma^{\mathrm{e}}_{xx} + \sigma^{\mathrm{h}}_{xx}\right)^2 + \left(\sigma^{\mathrm{e}}_{xy} + \sigma^{\mathrm{h}}_{xy}\right)^2}, \\
\rho_{yx} &= \frac{\sigma^{\mathrm{e}}_{xy} + \sigma^{\mathrm{h}}_{xy}}{\left(\sigma^{\mathrm{e}}_{xx} + \sigma^{\mathrm{h}}_{xx}\right)^2 + \left(\sigma^{\mathrm{e}}_{xy} + \sigma^{\mathrm{h}}_{xy}\right)^2}, \\
\sigma^{\mathrm{e}}_{xx} &= \frac{e n_e \mu_e}{1 + \mu_e^2 \left(\mu_0 H\right)^2}, \\
\sigma^{\mathrm{e}}_{xy} &= -\frac{e n_e \mu_e^2}{1 + \mu_e^2 \left(\mu_0 H\right)^2} \mu_0 H, \\
\sigma^{\mathrm{h}}_{xx} &= \frac{e n_h \mu_h}{1 + \mu_h^2 \left(\mu_0 H\right)^2}, \\
\sigma^{\mathrm{h}}_{xy} &= \frac{e n_h \mu_h^2}{1 + \mu_h^2 \left(\mu_0 H\right)^2} \mu_0 H,
\end{aligned} \tag{6.1}$$

where n_h (n_e) and μ_h (μ_e) are the carrier density and electronic mobility of the hole (electron) band, respectively. We set n_e, μ_e, and μ_h as fit parameters and apply the constraint $e\left(n_e \mu_e + n_h \mu_h\right) = \sigma_{xx,0}$ to extract n_h, where $\sigma_{xx,0}$ is the measured zero-field longitudinal conductivity.

The best fit is acquired by minimizing the deviation between the experimental traces and the calculated curves, which gives $n_e = 2.5 \times 10^{20}$ cm^{-2}, $\mu_e = 389$ cm^2 V^{-1} s^{-1}, $n_h = 3.0 \times 10^{20}$ cm^{-2}, and $\mu_h = 349$ cm^2 V^{-1} s^{-1} (Fig 6-8, red). We note that these parameters are close but not identical to the values extracted from bulk single crystal

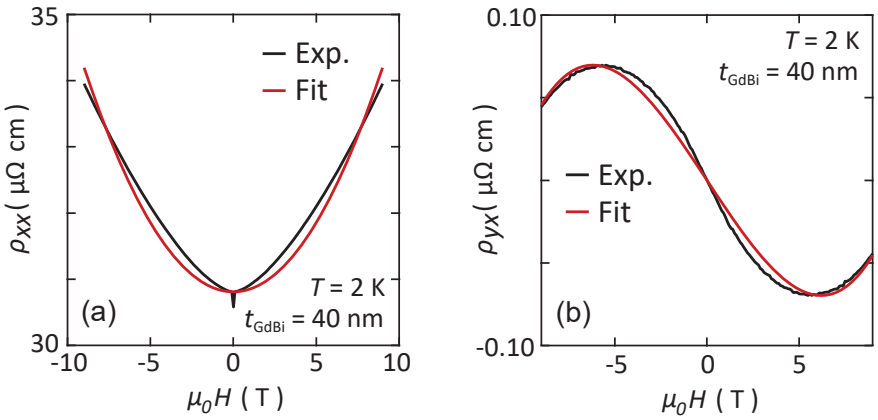

Figure 6-8: **Multi-band analysis of magnetotransport**

Magnetic field dependent (a) longitudinal and (b) Hall resistivity. Black and red traces are the experimental data and the multi-band fittings, respectively.

GdBi [157]. A number of RX systems have shown non-saturating magnetoresistance (MR) response similar to that seen here but with significantly larger amplitudes [157–162]. Provided that non-saturating MR requires a nearly perfect compensation of n_e and n_h, the suppressed $\rho_{xx}(H)$ amplitude in our films may reflect the deviation from the $n_e/n_h \sim 1$ condition.

Starting from the typical semimetallic band structure in the $t_{\mathrm{GdBi}} = 40$ nm sample, we now revisit the thickness dependent electrical transport properties. For this, we measure $\rho_{yx}(H)$ across a broad range of T and t_{GdBi}. As shown in Fig. 6-9(a), the $t_{\mathrm{GdBi}} = 40$ nm sample manifest a nonlinear, sign-changing $\rho_{yx}(H)$ at low T and linear, positive $\rho_{yx}(H)$ at high T. The strong temperature dependence suggests a competition of conductivity contributions between the electron and hole bands. With decreasing t_{GdBi} (Figs. 6-9(b)-(d)), a linear response emerges at low T suggestive of a hole-like single-band transport. For $t_{\mathrm{GdBi}} \leq 6$ nm, the temperature dependence also becomes nearly quenched, consistently suggesting the disappearance of the competing electron band contribution to the Hall response (Fig. 6-9(c),(d)).

This observed multi-to-single band crossover can be explained in light of the confinement-driven band shift as depicted schematically in the upper insets of Fig. 6-9(a)-(d). Upon reducing t_{GdBi}, confinement energy quantizes the allowed momentum

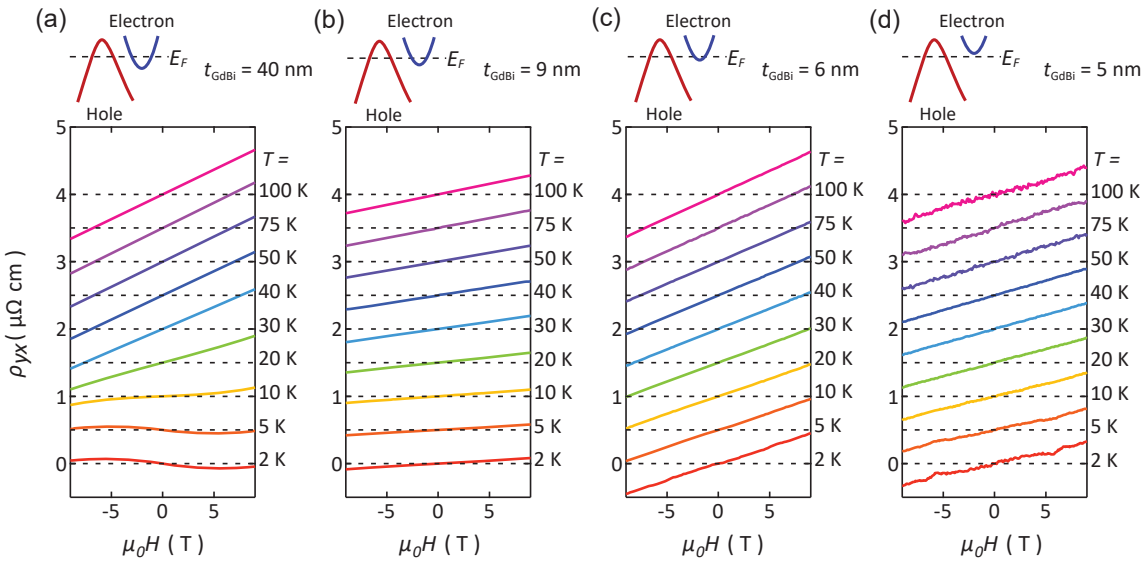

Figure 6-9: **Thickness-tuned Hall effect in GdBi films**

Hall effect of GdBi films with (a) 40 nm, (b) 9 nm, (c) 6 nm, and (d) 5 nm thicknesses measured at selected temperatures. The traces are offset vertically for clarity. The upper inset in each panel is a schematic of the bulk band arrangement.

values along the film normal direction and the band edges of the originally three-dimensional electron/hole bands shift upward/downward. This band shift effectively decreases the semimetallic band overlap at E_{F} and the negative indirect band gap gradually decreases in magnitude. Approaching $t_{\mathrm{GdBi}} = 5$ nm, the bottom edge of the electron band is expected to shift above E_{F}, leaving the hole band to solely dominate the transport response. This framework is also consistent with the crossover from metallic to mildly insulating behavior in $\rho_{xx}(T)$ shown in Fig. 6-7; there, the hole band remains metallic but the upwards shifted electron band produces a parallel thermally activated conduction generating an increasing resistivity contribution at lower T. Within this interpretation, we anticipate that stabilizing films thinner than 5 nm will further enhance quantum confinement and eventually generate a positive band gap across the entire Brillouin zone − a truly bulk insulating state.

In suppressing the bulk electrical conductivity, Anderson localization in the two-dimensional limit will cooperate with the confinement-induced band shifts in diminishing the mobility of bulk carriers [163, 164]. To understand the relevance of lo-

calization effects in the ultrathin limit, we probe the thickness dependence of MR response. Figure 6-10(a) shows the $T = 2$ K MR responses for different t_{GdBi}. As t_{GdBi} decreases from 40 nm to 6 nm, the non-saturating MR rapidly changes to saturating MR with reduced amplitude, likely arising from (i) further deviation of the band parameters from the perfect carrier compensation condition as a result of the confinement-induced band rearrangements and (ii) the suppression of mobility. Unlike in other samples, the MR for the $t_{\mathrm{GdBi}} = 5$ nm sample quickly increases in the low field regime ($|\mu_0 H| < 3T$) until it saturates beyond a shoulder-like feature around 4 T (also plotted in Fig. 6-10(b) in the unit of conductance quantum). This behavior cannot be explained within the Drude model of magnetotransport and we therefore ascribe it to the weak antilocalization (WAL) effect. According to the Hikami-Larkin-Nagaoka (HLN) theory [165], correction of conductivity due to WAL is given by:

$$\begin{aligned}\frac{\Delta\sigma}{(e^2/\pi h)} &= \ln\left(\frac{H}{H_{\mathrm{SO}}+H_\phi}\right)+\psi\left(\frac{1}{2}+\frac{H_{\mathrm{SO}}+H_\phi}{H}\right)\\ &- \frac{1}{2}\ln\left(\frac{H}{H_\phi}\right)-\frac{1}{2}\psi\left(\frac{1}{2}+\frac{H_\phi}{H}\right)\\ &+ \frac{1}{2}\ln\left(\frac{H}{2H_{\mathrm{SO}}+H_\phi}\right)+\frac{1}{2}\psi\left(\frac{1}{2}+\frac{2H_{\mathrm{SO}}+H_\phi}{H}\right), \end{aligned} \tag{6.2}$$

assuming negligible spin-flip scattering and diffusive transport regime. H_{SO} and H_ϕ are the characteristic fields for spin-orbit scattering and phase coherence, respectively, and ψ is the digamma function. The fit results of this formula are shown as black dotted lines in Fig. 6-10(b) and the associated length scales for spin-orbit scattering $l_{\mathrm{SO}} = (\hbar/4e\mu_0 H_{\mathrm{SO}})^{1/2}$ and phase coherence length $l_\phi = (\hbar/4e\mu_0 H_\phi)^{1/2}$ are plotted in Fig. 6-10(c). l_ϕ increases rapidly below $T_{\mathrm{N}} = 28$ K potentially stemming from the suppressed scattering by magnetic fluctuations. As the effects of WAL is generally enhanced in low dimensions, the observation of WAL only in our thinnest films evidences that they are in fact approaching the two-dimensional limit. $l_{\mathrm{SO}}, l_\phi > t_{\mathrm{GdBi}} = 5$ nm also supports this interpretation.

Stabilization of thinner films will simultaneously intensify the confinement effects and the localization effects, both contributing to the realization of a bulk insulat-

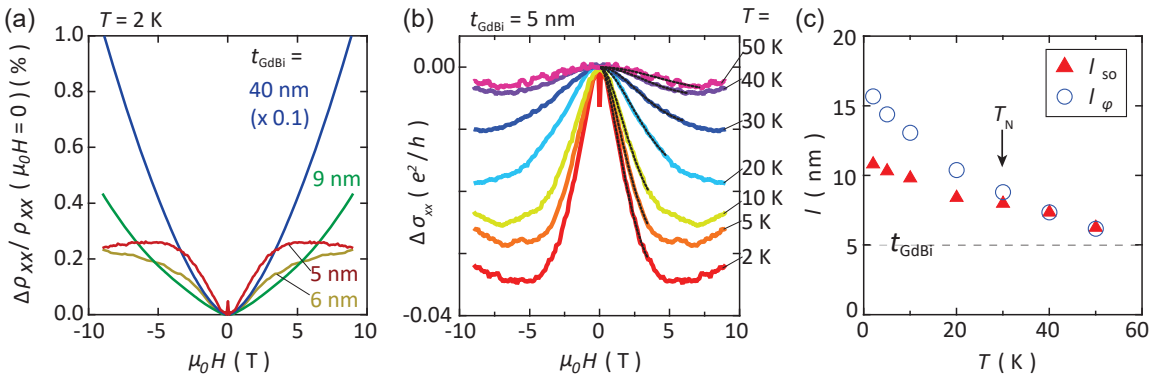

Figure 6-10: **Thickness-tuned magnetoresistance in GdBi films**

(a) Magnetoresistance of GdBi films with different thicknesses (t_{GdBi}). The measurements are conducted at $T = 2$ K and the data for $t_{\mathrm{GdBi}} = 40$ nm are scaled by a factor of 0.1. (b) Field-modulation of conductivity in the $t_{\mathrm{GdBi}} = 5$ nm sample at selected temperatures. Low field region of the data is fitted to the Hikami-Larkin-Nagaoka theory and the best fits to the data are shown as the black dotted lines. (c) Temperature dependence of the spin-orbit scattering length (l_{SO}) and the phase coherence length (l_ϕ) extracted from the fittings in (b).

ing state in GdBi. In such a limit, the transport is anticipated to be driven by the topological Dirac surface states (or edge modes if the Dirac point gaps out in the magnetic phase). This prediction, however, assumes that GdBi maintains a topologically nontrivial character all the way down to the ultrathin limit. Below, we examine the validity of this assumption.

6.3.3 Discussion: metallicity and topology of monolayer GdBi

Here we provide theoretical perspectives on the metallicity and topology of bulk and monolayer GdBi. Figure 6-11(a) shows the bulk band structure of antiferromagnetic GdBi (111) in the hexagonal unit cell with SOC. It exhibits an indirect negative band gap of about -1 eV between the Bi-derived valence band at the Γ-point and the Gd-derived conduction band at the M-points. This band structure matches well with the previous calculations on (La:Gd)Bi presented in section 6.1. From the orbital-projection analysis, we confirm that the bands are inverted at the M-point, giving rise to nontrivial topology.

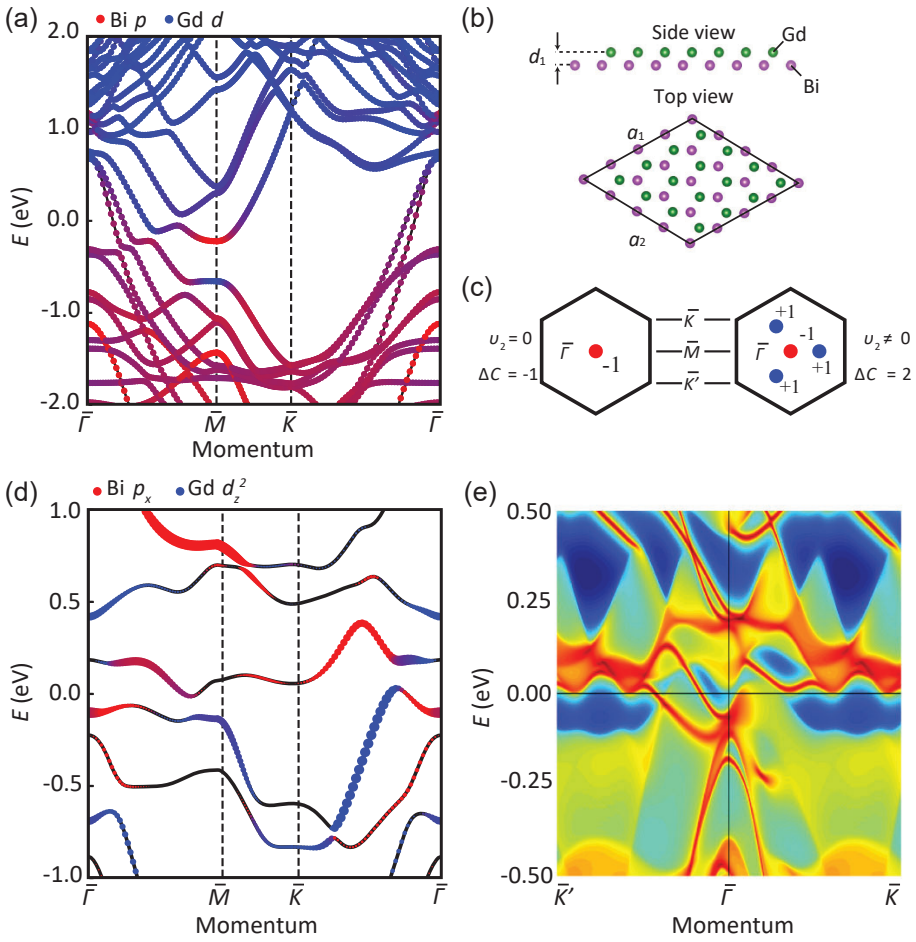

Figure 6-11: **Band structures of bulk and monolayer GdBi**

(a) Band structure of bulk GdBi (111) in the antiferromagnetic state with spin-orbit coupling (SOC). (b) Schematic crystal structure of monolayer GdBi (111). d_1 is the distance between the Bi layer and the Gd layer and a_1, a_2 are the in-plane lattice constants. (c) Schematic Brillouin zone of monolayer GdBi (111). Color of the circle denotes the change in the Chern number ΔC across the topological phase transition, contributed by each Dirac point: -1 for red and $+1$ for blue. (d) Band structure of monolayer GdBi (111). Orbital projections in (b),(d) are color-coded red (Bi p) and blue (Gd d). (e) Edge states of monolayer GdBi (111) along the Zigzag direction, exhibiting a pair of edge modes around the $\overline{\Gamma}$ point. The calculations for (a),(d),(e) are performed by M. Hu and J. Liu in [76].

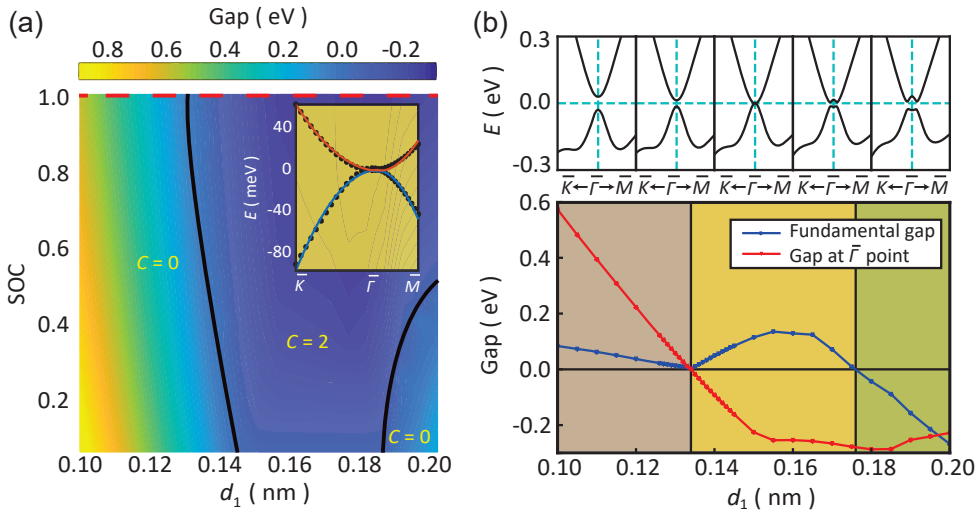

Figure 6-12: **Topological phase diagram of monolayer GdBi (111)**

(a) Topological phases in monolayer GdBi (111) at different values of the inter-layer distance d_1 and the SOC strength λ. The color represents the direct gap size and the negative value indicates inverted band ordering. The inset shows the fitting results of the $k \cdot p$ Hamiltonian (solid line) to the first-principles calculations (empty circle) around the critical point $d_1 = 0.134$ nm. (b) Strain induced topological phase transition in monolayer GdBi (111). The top and bottom panels respectively show the band evolution and energy gap as a function of d_1. In the bottom panel, the red line represents the direct gap at the $\overline{\Gamma}$ point and the negative value means the Chern state with $C = 2$. The blue line represents the fundamental gap in the whole Brillouin Zone and the negative value denotes a semimetallic band overlap. The calculations here are performed by M. Hu and J. Liu in [76].

We then consider a monolayer GdBi (111), consisting of a pair of single atomic layers of Gd and Bi, separated by the lattice spacing d_1 from each other (Fig. 6-11(b)); this corresponds to the half of the magnetic unit cell in GdBi. The band structure of monolayer GdBi (111) is calculated using $d_1 = 0.182$ nm (the bulk value) and assuming ferromagnetic spin texture (Fig. 6-11(d)). From the overall band morphology, we observe that the size of the negative indirect gap is nearly lifted, while a positive direct gap can be identified at every momentum. The orbital-projection analysis reveals a band inversion between the Gd d_{z2}-orbital and the Bi p_x-orbital at the $\overline{\Gamma}$ point, implying a nontrivial band topology persisting down to the monolayer limit (Fig. 6-11(d)). Intriguingly, from the edge-projected band structure in Fig. 6-11(e),

we find within the inverted gap two copies of topological edge modes, suggesting a non-ordinary $C = 2$ state.

To understand this high Chern number state better, we track the topological character of the system while varying d_1 and SOC. As shown in Fig. 6-12(a), the phase diagram contains only two distinct phases with $C = 0$ and $C = 2$, with no intermediate $C = 1$ phase. This indicates that the gap in fact realizes a high Chern number state rather than consisting of two overlapping $C = 1$ gaps. Furthermore, at the phase boundary between the two is realized a quadratic band touching, a typical signature of a higher order topological phase transition (Fig. 6-12(a), inset). The top panel in Fig. 6-12,(b) shows the evolution of the energy gap Δ at the $\overline{\Gamma}$ point as a function of d_1. A trivial Δ monotonically decreases to 0 as d_1 increases up to $d_1 = 0.134$ nm and a nontrivial Δ opens beyond that. The nontrivial topology is indicated as a negative-valued gap ($\Delta < 0$) in the red trace in Fig. 6-12(b). Across this topological phase transition, the fundamental gap is consistently positive (Fig. 6-12(b), blue). At $d_1 > 0.176$ nm, however, the system recovers a semimetallic behavior, in which a negative indirect gap is restored in other parts of the Brillouin zone. While the $C = 2$ gap is expected at the $\overline{\Gamma}$-point in real monolayer GdBi ($d_1 = 0.182$ nm), parallel bulk conduction may obscure its direct detection. Based on these results, we propose that driving the system towards $0.134 \text{ nm} \leq d_1 \leq 0.176$ nm via *e.g.* epitaxial strain may realize a perfectly bulk insulating state with two chiral edge modes circulating around the sample.

6.3.4 Discussion: symmetry analysis on the $C = 2$ state

We track the symmetry-origin of the $C = 2$ gap in monolayer GdBi (111) by considering the low energy band structure near the $\overline{\Gamma}$-point. Monolayer GdBi (111) has three-fold rotation symmetry C_3. Given a ferromagnetic spin texture, both time-reversal symmetry (T) and mirror symmetry with the mirror plane perpendicular to y-direction (M_y) are broken, whereas the combined TM_y is preserved. We therefore construct a generic $k \cdot p$ Hamiltonian that obeys the little group containing C_3 and

TM_y symmetries:

$$H\left(k_x, k_y\right) = m_1\sigma_z + m_2(k_x^2 + k_y^2)\sigma_z + v_1\left(k_x\sigma_y - k_y\sigma_x\right) + v_2\left(2k_xk_y\sigma_y - \left(k_x^2 - k_y^2\right)\sigma_x\right) + v_3\left(k_x^2 + k_y^2\right)I, \tag{6.3}$$

where σ is the pseudo-spin representing the conduction and valence bands, m_1 and m_2 are mass parameters, k_x and k_y are the crystal momenta, and v_1, v_2, and v_3 are velocity parameters. We set $v_3 = 0$ here as it gives the same energy shift for both conduction and valence bands and does not affect the topological properties.

We first consider the simplest case with $m_2 = v_2 = 0$, where the $k \cdot p$ Hamiltonian reduces to the typical massive Dirac Hamiltonian. For $m_1 \neq 0$, a gap opens at the $\overline{\Gamma}$-point (red circle in Fig. 6-11(c), left) with ΔC = -1 expected between $m_1 > 0$ and $m_1 < 0$ (*i.e.* band inversion). We then turn to the case of small $v_2 \neq 0$ and $m_2 = 0$, in which Dirac cones appear at four different points in the Brillouin zone: one at the $\overline{\Gamma}$-point (red circle in Fig. 6-11(c), right) and the other three at equivalent points along the $\overline{\Gamma} - \overline{M}$ lines (blue circles in Fig. 6-11(c), right). As m_1 flips sign, the net change in the Chern number is $\Delta C = 2$, ΔC = -1 from the Dirac point at the $\overline{\Gamma}$ and the $\Delta C = 3$ from the other three. As v_2 increases (with $m_2 = 0$ fixed), the three Dirac points along the $\overline{\Gamma} - \overline{M}$ lines converge to the zone center and eventually merge with the one at the $\overline{\Gamma}$-point in the $v_2 \gg v_1$ limit to create a quadratic band touching. Despite changes in the band morphology, $\Delta C = 2$ is maintained across a wide range of v_2. We find that inclusion of non-zero m_2 can generate via more complex band distortions intermediate phases with ΔC = -1 or 3. Their phases space areas (δ), however, is approximately $\delta = |m_2|\,(\frac{v_1}{v_2})^2$, indicating practical absence of such phases in the regime of small m_2 and small $(\frac{v_1}{v_2})$.

Fitting all $k \cdot p$ parameters to the actual low energy band structure near the $\overline{\Gamma}$-point calculated with the critical value $d = 1.34$ (Fig. 6-12(a), inset), we find v_1 = -0.3, v_2 = 37.2, v_3 = -7.1, and $|m_2| < 0.1$. This parameter set situates real monolayer GdBi in the regime with negligibly $\delta = |m_2|(\frac{v_1}{v_2})^2 \sim 10^{-5}$ and no intermediate Chern state is expected between the $C = 0$ state and the $C = 2$ state. The successful explanation

of the first-principles calculation with a generic $k \cdot p$ model conveys a message that the identified $C = 2$ state is a general feature of a Hamiltonian that shares the same symmetry properties with monolayer GdBi. This realization proposes that material tunings of the SOC strength and the lattice parameters may help navigate the discussed phase space and realize different types of high Chern number states.

6.4 Conclusions and outlook

In this chapter, we have investigated the structural, magnetic, and electrical properties of antiferromagnetic topological semimetal GdBi stabilized in epitaxial thin film form. We discovered that bringing GdBi to the ultrathin limit does not suppress the original magnetic order but drives the system towards a bulk insulating regime as a result of confinement-driven band shifts. In conjunction with first principles calculations, we also predicted that monolayer GdBi potentially harbors an inverted gap that supports the $C = 2$ state. Stabilization of mono-to-few layer thick GdBi films and subsequent engineering via epitaxial strain or electrostatic gating will help realize the bulk insulating high Chern number state in a real material. In addition, the experimental methodologies developed herein can be used to stabilize thin films of other RX with more complex magnetic properties, allowing exploration of a wide variety of symmetry broken phases interacting with topologically nontrivial band structures [147, 166–168].

As a final remark, we compare these results to the kagome-originated approaches taken in the previous chapters. The idea of opening a topological gap at the lattice-derived Dirac points in kagome metals (*e.g.* FeSn) is conceptually analogous to the original proposals on the honeycomb lattice. A Dirac point, being at the pinchpoint of any type of gap opening, provides a natural starting point for this. By comparison, in Bi-based compounds like GdBi, the nontrivial topology is attained by the SOC-driven band inversion. The process of band inversion, though not lattice-driven as in the kagome lattice, can also be viewed as a closing of a trivial gap and a reopening of a nontrivial gap passing through an intermediate "Dirac-like" band touching

point. These two complementary but conceptually similar approaches constitute important design principles for topological materials: (i) realizing the kagome lattice with sufficiently heavy atoms, with relaxed requirements for their SOC strength or (ii) realizing an arbitrary lattice with extremely heavy mass atoms, not limited to its lattice structure.

Chapter 7

Concluding remarks

In this thesis, we have explored emergent quantum phenomena arising from the characteristic electronic structure of the kagome lattice realized embedded in a class of intermetallic compounds called the kagome metals. Their crystal structures were constructed by layer-by-layer stacking of the two-dimensional kagome/honeycomb networks of transition metal elements. Different choices of the constituent elements and the layer stacking sequences gave rise to a varierty of electronic structures with the key band features of the original lattice model preserved or collapsed. Among different candidate materials, we have stabilized two representative kagome metals, FeSn and Ni_3In, in epitaxial thin film forms using molecular beam epitaxy and, by engineering their material parameters with various experimental tuning knobs, uncovered the connections between the salient band features therein to the observed topological and correlated physical properties.

FeSn is an antiferromagnetic kagome metal with the kagome-derived Dirac and flat bands manifested in its quasi-two-dimensional electronic structure. With the systematic chemical doping across a large energy range, we have driven FeSn thin films towards heavily electron- and hole-doped regimes where the lattice-driven band singularities can be brought to the Fermi level (E_{F}). Taking advantage of the complete tunability over the chemical potential and spin structure, we were able to control fully on-demand either massless or massive Dirac electrons to govern the transport response of the system − an important step towards designing high temperature Dirac states,

the quantum spin Hall state, and the quantum anomalous Hall state all derived from a single parent compound with appropriate stoichiometric modifications. As well as the Dirac physics, we also elucidated the flat band driven nature of magnetism in this compound, which in a broader context formulates a design principle that fine engineering of the intra-kagome flat band instability and the inter-kagome exchange coupling can generate a rich variety of emergent phases.

The heterointerface of FeSn film and $SrTiO_3$ substrate was identified as a unique platform to study the fate of the kagome band structure upon broken inversion symmetry. From planar tunneling spectroscopy across a Schottky heterointerface of FeSn and Nb-doped $SrTiO_3$, we have observed a local band structure reconstruction at the interfacial kagome layer formed immediately above the top-most layer of the substrate. One of its most conspicuous consequences was the generation of a two-dimensional surface/interface flat band not expected in the bulk of FeSn. With further analyses, we have discovered the Dirac origin of this flat band though manifested in a dramatically deformed morphology. This conveys a crucial message that a surface-driven anomalous band flattening effects on Dirac bands may offer an alternative pathway to realize a topological flat band; one can either make a flat band to become topological or make a topological band to become flatter.

As a counterpart for FeSn, Ni_3In provides a model case in which the kagome layers actively hybridize which each other and produce a three-dimensional band structure with the lattice-driven Dirac and flat bands hardly visible. Accompanied with this electronic dimensional crossover was an emergence of an anisotropic flat band inherent to the characteristic stacking sequence of this compound. We synthesized epitaxial thin films of Ni_3In and identified with various experimental probes the non-Fermi-liquid (NFL) behaviors potentially originating from the intrinsic spin fluctuations in the system. By spin injection experiments and alkali metal intercalation experiments, we also engineered the key energy scales of the NFL state in Ni_3In, through which the connections between the anisotropic flat band, the fluctuating local moments, and the Fermi surface breakdown were reinforced.

In chapter 6, we introduced briefly a non-kagome-originated approach in com-

mingling topology and correlation. We synthesized epitaxial thin films of GdBi, an antiferromagnetic topological semi-metal, and manipulated the metallicity of the bulk via quantum confinement while their magnetic and topological characters remained unperturbed. We compared the band-inversion-based approach in designing topological materials to the kagome-based approaches discussed in chapter 3 - 5.

This thesis research inspires a number of future research prospects. We summarize below some of the major directions:

- (i) *Stabilization of ultrathin kagome films*

  One of the long standing goals in the field is to stabilize a mono-layer kagome material, the most faithful realization of the original lattice model. While we have focused primarily on > 10 nm thick films in this thesis, dramatic changes in the physical properties are anticipated in the mono-to-few layer thickness regimes of these compounds.

  ⋆ Mono-layer regime (*i.e.* ≤ 0.5 nm): Being free of any inter-layer coupling, the flat band in a mono-layer kagome film is expected to restore its zero-bandwidth state predicted in the original lattice model. The flat band in bulk FeSn have shown a tendency to induce ferromagnetism within the kagome plane (see chapter 3) − the situation predicted from the Hubbard model on a partially flat band with non-singular density of states peak [37–40]. The realization of a perfect flat band, however, would further enhance the correlation strength and potentially lead to the observations of other predicted phases, including the spin liquid phase and the fractional quantum Hall phase [32–36]. In addition, the regime of (surface-to-bulk ratio) = 1 is where the two-dimensional surface/interface flat band in FeSn (see chapter 4) can govern the global transport and thermodynamic properties. A variety of bulk-sensitive probes, originally inapplicable for detecting the surface flat band in thick films, can be used to track the changes in physical properties of the films as the flat band position and morphology are manipulated via *e.g.* substrate engineering or adlayer deposition.

  ⋆ Few-layer regime (*i.e.* $\leq$ 2 - 5 nm): The films in the few-layer regime will represent the evolution of physical properties from the monolayer to the bulk.

In FeSn films with n kagome layers (n = 2, 3, 4, ...), for example, their inherent antiferromagnetic inter-layer coupling will quench the net magnetization when n = 2, 4, 6, ... $\in$ (even numbers) whereas it cannot do so when n = 3, 5, 7, ... $\in$ (odd number), which in the latter case would let the system behave like a weak ferromagnet macroscopically. Such alternation of symmetry conditions for even vs. odd layer numbers would help stabilize distinct topological phases realized under higher/lower symmetry conditions. Similar observations have been made in the few layer limit of magnetic topological insulator $MnBi_xTe_y$ (x:y = 2:4, 4:7, 6:10), in which either the Chern insulator phase or the Axion insulator phase was observed at zero-field depending on the even-ness or odd-ness of the layer number [169–171]. Unlike in quasi-two-dimensional kagome metals, electronic structures of three-dimensional kagome metals are expected to modify significantly in the few-layer thickness regime. In Ni_3In films, for example, the anisotropic flat band with strong k_z dispersion will quantize into multiple subbands. In the limit the confinement energy is larger than the in-plane bandwidth, the anisotropic flat band will evolve into a nearly isotropic flat band with suppressed dispersions along all three directions. It is of significant interest to study the evolution of the NFL behaviors as the electronic dimensionality of the anisotropic flat band is altered.

$\star$ Synthesis strategies: Utilizing the conventional growth mode of MBE, we have attained high quality films with a minimum thickness of $\sim$ 5nm in this thesis (films thinner than this showed lower quality). We anticipate that further reduction of film thickness down to the mono-to-few layer regime may be facilitated by more advanced growth optimizations, surfactant-mediated growth [172], van der Waals epitaxy [173], or confinement heteroepitaxy [174].

- (ii) *Incorporation of optimally tuned kagome metal films to spintronic devices*
  Recent studies have shown exceptionally high spin-orbit torque generation efficiencies of spin-orbit coupled Dirac electrons and flat band electrons [175–179]. In chapter 3, we have demonstrated a capability to tune E_F of a kagome

metal film to any desired energy in the kagome band structure via ultra-precise chemical doping. Some of the optimally tuned films, when incorporated into device geometry, would help evaluate spintronic performances of the lattice-driven band singularities.

- (iii) *Stabilization of artificial kagome heterostructures*
  Artificial kagome heterostructures with highly metastable stacking sequences (those not found in bulk materials) may help realize more exotic variants of the kagome band structure − similarly as the FeSn/Nb:STO interfacial layer produces the flat band nonexistent in bulk of FeSn. This approach has given rise to developments of electronic/magnetic phase spaces in complex oxide superlattices [180] and Kondo superlattices [181].

- (iv) *Proximity effects*
  Films can also be interfaced (either epitaxially or non-epitaxially) with heterogeneous materials and be proximitized various electronic correlations from the neighboring layers. For example, the Dirac electrons in kagome metal films, if proximitized a superconducting pairing interaction, may stabilize unconventional order parameters predicted in section 1.3.3 [41–43].

To conclude, the material designs and thin film engineerings of kagome metals provide crucial insights and useful methodologies for exploring the interplay of topology and correlation in lattice-model-based platforms. We anticipate that the scientific findings and interpretations presented herein would make an important step towards realizing thus-far-unexplored topological and correlated electronic states as well as incorporating some of the candidate compounds into functional electronic/spintronic devices operating at high temperatures.

Appendix A

Magnetic transitions in doped FeSn films

In section 3.3.4, we have discussed the doping dependence of Neel temperatures (T_{N}) in $(Fe_{1-x-y}Mn_xNi_y)Sn$ films. T_{N} at each doping concentration was extracted from kinks/inflections in the temperature dependent electrical resistivity (see Fig. 3-22). Here, we present additional experimental signatures of the magnetic phase transitions in doped FeSn films.

A.1 Seebeck coefficients in $(Fe_{1-y}Ni_y)Sn$ films

We perform the Seebeck coefficient ($S_{xx} \equiv \Delta V_{xx}/\Delta T$) measurements on $(Fe_{1-y}Ni_y)Sn$ films. Fig. A-1(a) shows the thermal conductivity $\kappa \equiv (Q\ d)/(A\ \Delta T)$ measured from a FeSn/$SrTiO_3$ sample, where Q is heat load, d is sample length, A is sample cross-section. The measured κ is determined by the intrinsic thermal conductivity of $SrTiO_3$ substrate and a similar behavior has been observed in bulk single crystal $SrTiO_3$ [182]. Given a ΔT determined by the $SrTiO_3$ substrate, S_{xx} is generated solely by the FeSn film. Fig. A-1(b) and (c) display the temperature dependent S_{xx} of an undoped FeSn film and a $(Fe_{0.75}Ni_{0.25})Sn$ film, respectively. For both films, S_{xx} is negative and decreases in magnitude as T decreases. This is consistent with T-linear suppression of S_{xx} predicted from the Mott formalism of thermoelectricity

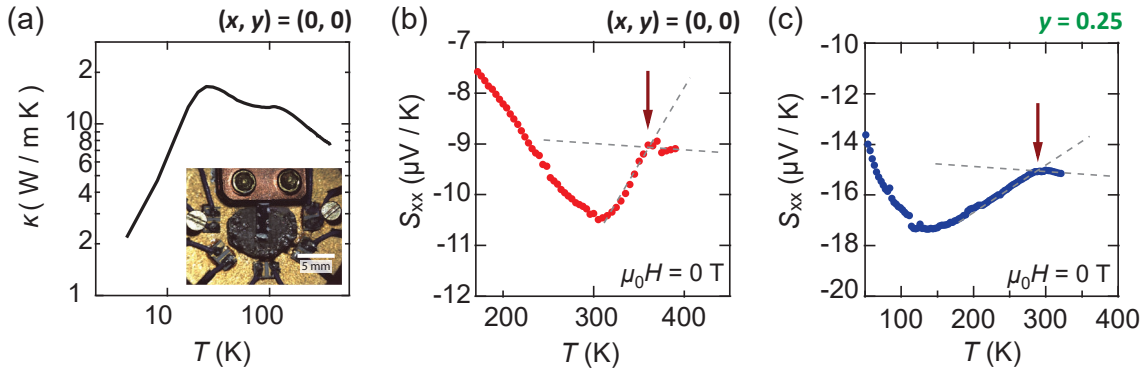

Figure A-1: **Temperature dependent Seebeck coefficient in $(Fe_{1-y}Ni_y)Sn$**

(a) Thermal conductivity κ measured from a FeSn/$SrTiO_3$ sample (inset: optical micrograph of the measurement setup). Temperature dependent Seebeck coefficients of (b) an undoped FeSn film and (c) a $(Fe_{0.75}Ni_{0.25})Sn$ film measured at $\mu_0 H = 0$ T. The arrows in (b),(c) mark the magnetic transition temperatures.

[135]. In addition to the overall temperature dependence, kink-like anomalies are observed at high temperature. For the FeSn film, the kink occurs at $T \sim 360$ K, nearly identical to the intrinsic T_N of FeSn (Fig. A-1(b)). For the $(Fe_{0.75}Ni_{0.25})Sn$ film, the kink with qualitatively similar form as in Fig. A-1(b) is observed at $T \sim 290$ K (Fig. A-1(c)). This is proximate to the temperature at which an anomaly was observed in the electrical resistivity of $(Fe_{0.75}Ni_{0.25})Sn$ ($T \sim 288$ K; see Fig. 3-22). We therefore identify this as the magnetic transition temperature of $(Fe_{0.75}Ni_{0.25})Sn$, suppressed from that of undoped FeSn. The T_N values extracted from the Seebeck coefficient measurements are reflected in Fig. 3-21.

A.2 Canting-induced hysteresis onset temperatures in $(Fe_{1-y}Ni_y)Sn$ films

Magnetic phase transitions in heavily doped films are accompanied by the onset of field hysteresis, potentially arising from spin-canting effects in the disordered regime of an antiferromagnet [90]. Fig. A-2 shows the temperature dependent coercive fields (H_{coer}) in $(Fe_{1-y}Ni_y)Sn$ films. H_{coer} is defined as the field at which the hysteresis loop

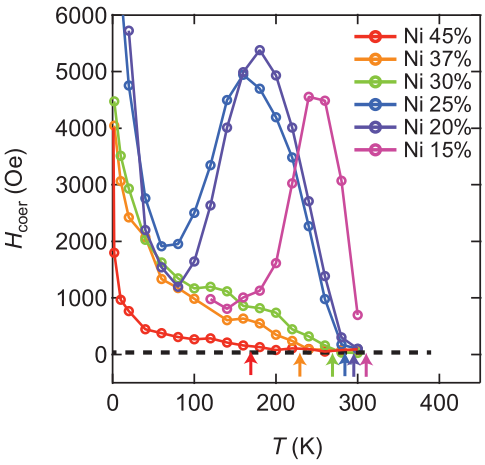

Figure A-2: **Canting-induced coercive fields in $(Fe_{1-y}Ni_y)Sn$**

Coercive field (H_{coer}) in $(Fe_{1-y}Ni_y)Sn$ films ($0.15 \leq y \leq 0.45$) at different temperatures. The arrows mark the approximate hysteresis onset temperatures.

crosses zero (different definitions of H_{coer} give qualitatively similar traces). When the magnetic phase sets in, H_{coer} also acquires a non-zero value. The hysteresis onset temperature for each doping concentration matches T_N extracted from the electrical resistivity (Fig. 3-22) and the Seebeck coefficient (Fig. A-1). The T_N values inferred from Fig. A-2 are reflected in the Fig. 3-21.

While the hysteresis persists down to the lowest T, H_{coer} exhibited a nonmonotonic temperature dependence. H_{coer} rapidly increases below T_N until it gives way to a sudden decrease, forming a broad peak-like feature. As T decreases further, H_{coer} begins to increase again approaching $T \to 0$. Such behavior is observed across the entire range of y, though the peak-like features become less prominent hump-like features at higher y. This nonmonotonic behavior is reminiscent of a cascade of spin reorientation transitions within the antiferromagnetic phase of Co-doped FeSn bulk single crystals [87]. There, the magnetic easy axis rotated from axial (along the c-axis) in the high temperature regime to planar (within the ab-plane) in the low temperature regime. Though its exact origin has not been clearly identified, a similar change in magnetic anisotropy may potentially account for the observed temperature dependence of H_{coer} in $(Fe_{1-y}Ni_y)Sn$ films.

Bibliography

[1] J. Weis and K. v. Klitzing. Metrology and microscopic picture of the integer quantum Hall effectl. *Phil. Trans. R. Soc. A*, 369:3954, 2011.

[2] K. v. Klitzing. The quantized Hall effect. *Rev. Mod. Phys.*, 58:519, 1986.

[3] I. M. Singer and J. A. Thorpe. *Lecture Notes on Elementary Topology and Geometry*. New York: Springer-Verlag, 1996.

[4] K. v. Klitzing, G. Dorda, and M. Pepper. New method for high-accuracy determination of the fine-structure constant based on quantized Hall conductance. *Phys. Rev. Lett.*, 45:494, 1980.

[5] D. J. Thouless, M. Kohmoto, M. P. Nightingale, and M. den Nijs. Quantized Hall conductance in a two-dimensional periodic potential. *Phys. Rev. Lett.*, 49:405, 1982.

[6] A. H. Castro Neto, F. Guinea, N. M. R. Peres, K. S. Novoselov, and A. K. Geim. Electronic properties of graphene. *Rev. Mod. Phys.*, 81:109, 2009.

[7] C. L. Kane and E. J. Mele. Quantum spin Hall effect in graphene. *Phys. Rev. Lett.*, 95:226801, 2005.

[8] F. D. M. Haldane. Model for a quantum Hall effect without Landau levels: condensed-matter realization of the "parity anomaly". *Phys. Rev. Lett.*, 61:2015, Oct 1988.

[9] J. O. Island, X. Cui, C. Lewandowski, J. Y. Khoo, E. M. Spanton, H. Zhou, D. Rhodes, J. C. Hone, T. Taniguchi, K. Watanabe, L. S. Levitov, M. P. Zaletel, and A. F. Young. Spin-orbit-driven band inversion in bilayer graphene by the van der Waals proximity effect. *Nature*, 571:85, 2019.

[10] I. T. Witting, F. Ricci, T. C. Chasapis, G. Hautier, and G. J. Snyder. The thermoelectric properties of n-type bismuth telluride: bismuth selenide alloys $Bi_2Te_{3-x}Se_x$. *Research*, 2020:4361703, 2020.

[11] Y. Xia, D. Qian, D. Hsieh, L. Wray, A. Pai, H. Lin, A. Bansil, D. Grauer, Y. S. Hor, R. J. Cava, and M. Z. Hasan. Observation of a large-gap topological-insulator class with a single Dirac cone on the surface. *Nat. Phys.*, 5:398, 2009.

[12] B. A. Bernevig, T. L. Hughes, and Zhang. S.-C. Quantum spin Hall effect and topological phase transition in HgTe quantum Wells. *Science*, 314:1757, 2006.

[13] M. Z. Hasan and C. L. Kane. Colloquium: topological insulators. *Rev. Mod. Phys.*, 82:3045, Nov 2010.

[14] D. Hsieh, D. Qian, L. Wray, Y. Xia, Y. S. Hor, R. J. Cava, and M. Z. Hasan. A topological Dirac insulator in a quantum spin Hall phase. *Nature*, 452:970, 2008.

[15] M. König, S. Wiedmann, C. Brüne, A. Roth, H. Buhmann, L. W. Molenkamp, X.-L. Qi, and S.-C. Zhang. Quantum spin Hall insulator state in HgTe quantum wells. *Science*, 318:766, 2007.

[16] P. Coleman. *Introduction to many-body physics*. Cambridge University Press, 2015.

[17] R. Skomski. Finite-temperature depolarization in half metals. *J. Phys.: Condens. Matter*, 19:315202, 2007.

[18] J. Spalek, A. Ślebarski, J. Goraus, L. Spalek, K. TOmala, A. Zarzycki, and A. Hackemer. From Kondo semiconductor to a singular non-Fermi liquid via a quantum critical point: the case of $CeRhSb_{1-x}Sn_x$. *Phys. Rev. B*, 72:155112, 2005.

[19] H. L. Stormer. Two-dimensional electron correlation in high magnetic fields. *Physica B*, 177:401, 1992.

[20] Y. Cao, V. Fatemi, A. Demir, S. Fang, S. L. Tomarken, J. Y. Luo, J. D. Sanchez-Yamagishi, K. Watanabe, T. Taniguchi, E. Kaxiras, R. C. Ashoori, and Pablo Jarillo-Herrero. Correlated insulator behaviour at half-filling in magic-angle graphene superlattices. *Nature*, 556:80, 2018.

[21] Y. Cao, V. Fatemi, S. Fang, K. Watanabe, T. Taniguchi, E. Kaxiras, and P. Jarillo-Herrero. Unconventional superconductivity in magic-angle graphene superlattices. *Nature*, 556:43, 2018.

[22] B Sutherland. Localization of electronic wave functions due to local topology. *Phys. Rev. B*, 34:5208, 1986.

[23] E. H. Lieb. Two theorems on the Hubbard model. *Phys. Rev. Lett.*, 62:1201, 1989.

[24] D. Leykam, A. Andreanov, and S. Flach. Artificial flat band systems: from lattice models to experiments. *Adv. Phys.: X*, 3:1473052, 2018.

[25] K. Sun, Z. Gu, H. Katsura, and S. Das Sarma. Nearly flatbands with nontrivial topology. *Phys. Rev. Lett.*, 106:236803, 2011.

[26] F. Wang and Y. Ran. Nearly flat band with Chern number $C = 2$ on the lattice. *Phys. Rev. B*, 84:241103(R), 2011.

[27] N. Regnault, Y. Xu, M. R. Li, D. S. Ma, M. Jonanovic, A. Yazdani, S. S. P. Parkin, C. Felser, L. M. Schoop, N. P. Ong, R. J. Cava, L. Elcoro, Z. D. Song, and A. Bernevig. Catalogue of flat-band stoichiometric materials. *Nature*, 603:824, 2022.

[28] R. L. Johnston and R. Hoffmann. The kagomè net: band theoretical and topological aspects. *Polyhedron*, 9:1901, 1990.

[29] D. L. Bergman, C. Wu, and L. Balents. Band touching from real-space topology in frustrated hopping models. *Phys. Rev. B*, 78:125104, 2008.

[30] G. Xu, B. Lian, and S.-C. Zhang. Intrinsic quantum anomalous Hall effect in the kagome lattice $Cs_2LiMn_3F_{12}$. *Phys. Rev. Lett.*, 115:186802, 2015.

[31] H.-M. Guo and M. Franz. Topological insulator on the kagome lattice. *Phys. Rev. B*, 80:113102, 2009.

[32] L. Balents. Spin liquids in frustrated magnets. *Nature*, 464:199, 2010.

[33] S. Yan, D. A. Huse, and S. R. White. Spin-liquid ground state of the $S = 1/2$ kagome Heisenberg antiferromagnet. *Science*, 332:1173, 2011.

[34] S. Depenbrock, I. P. McCulloch, and U. Schollowöck. Nature of the spin-liquid ground state of the $S = 1/2$ Heisenberg model on the kagome Lattice. *Phys. Rev. Lett.*, 109:067201, 2012.

[35] S. Sachdev. Kagomé- and triangular-lattice Heisenberg antiferromagnets: ordering from quantum fluctuations and quantum-disordered ground states with unconfined bosonic spinons. *Phys. Rev. B*, 45:12377, 1992.

[36] E Tang, J.-W. Mei, and X.-G. Wen. High-temperature fractional quantum Hall states. *Phys. Rev. Lett.*, 106:236802, Jun 2011.

[37] H. Tasaki. Ferromagnetism in Hubbard Models. *Phys. Rev. Lett.*, 75:4678, 1995.

[38] A. Tanaka and H. Ueda. Stability of ferromagnetism in the Hubbard model on the kagome Lattice. *Phys. Rev. Lett.*, 90:067204, 2003.

[39] A. Mielke. Ferromagnetism in single-band Hubbard models with a partially flat band. *Phys. Rev. Lett.*, 82:4312, 1999.

[40] A. Mielke. Ferromagnetism in the Hubbard model on line graphs and further considerations. *J. Phys. A: Math. Gen.*, 24:3311, 1992.

[41] I. I. Mazin, H. O. Jeschke, F. Lechermann, H. Lee, M. Fink, R. Thomale, and R. Valenti. Theoretical prediction of a strongly correlated Dirac metal. *Nat. Commun.*, 5:2461, 2014.

[42] S.-L. Yu and J.-X. Li. Chiral superconducting phase and chiral spin-density-wave phase in a Hubbard model on the kagome lattice. *Phys. Rev. B*, 85:144402, 2012.

[43] L. Fu and C. L. Kane. Superconducting proximity effect and Majorana fermions at the surface of a topological insulator. *Phys. Rev. Lett.*, 100:096407, 2008.

[44] M. Kang, L. Ye, S. Fang, J.-S. You, A. Levitan, M. Han, J. I. Facio, C. Jozwiak, A. Bostwick, E. Rotenberg, M. K. Chan, Chan, R. D. McDonald, D. Graf, K. Kaznatcheev, E. Vescovo, D. C. Bell, E. Kaxiras, J. van den Brink, M. Richter, M. P. Ghimire, J. G. Checkelsky, and R. Comin. Dirac fermions and flat bands in the ideal kagome metal FeSn. *Nat. Mater.*, 19:163, 2020.

[45] M. Kang, S. Fang, L. Ye, H. C. Po, J. Denlinger, C. Jozwiak, A. Bostwick, E. Rotenberg, E. Kaxiras, J. G. Checkelsky, and R. Comin. Topological flat bands in frustrated kagome lattice CoSn. *Nat. Commun.*, 11:4004, 2020.

[46] Z. Liu, Q. Li, M. Wang, G. Wang, C. Wen, K. Jiang, X. Lu, S. Yan, Y. Huang, D. Shen, J.-X. Yin, Z. Wang, Z. Yin, H. Lei, and S. Wang. Orbital-selective Dirac fermions and extremely flat bands in frustrated kagome-lattice metal CoSn. *Nat. Commun.*, 11:4002, 2020.

[47] M. Ochi, R. Arita, M. Matsumoto, H. Kono, and T. Miyake. Robust flat bands in $R\mathrm{Co}_5$ (R = rare earth) compounds. *Phys. Rev. B*, 91:165137, 2015.

[48] B. R. Ortiz, S. M. L. Teicher, Y. Hu, J. L. Zuo, P. M. S. Sarte, E. C. Schueller, A. M. Milinda Abeykoon, M. J. Krogstad, S. Rosenkranz, R. Osborn, R. Seshadri, L. Balents, J. He, and S. D. Wilson. $\mathrm{CsV_3Sb_5}$: a Z_2 topological kagome metal with a superconducting ground state. *Phys. Rev. Lett.*, 125:247002, 2020.

[49] B. R. Ortiz, P. M. Sarte, E. M. Kenney, M. J. Graf, S. M. L. Teicher, R. Seshadri, and S. D. Wilson. Superconductivity in the Z_2 kagome metal $\mathrm{KV_3Sb_5}$. *Phys. Rev. Mater.*, 5:034801, 2021.

[50] J.-X. Yin, W. Ma, T. A. Cochran, X. Xu, S. S. Zhang, H.-J. Tien, N. Shumiya, G. Cheng, K. Jiang, B. Lian, Z. Song, G. Chang, I. Belopolski, D. Multer, Litskevich, M., Z.-J. Cheng, X. P. Yang, B. Swidler, H. Zhou, H. Lin, T. Neupert, Z. Wang, T.-R. Yao, N. Chang, S. Jia, and M. Z. Hasan. Quantum-limit Chern topological magnetism in $\mathrm{TbMn_6Sn_6}$. *Nature*, 583:533, 2020.

[51] S. Fang, L. Ye, M. P. Ghimire, M. G. Kang, J. Liu, M. Han, L. Fu, M. Richter, J. van den Brink, E. Kaxiras, R. Comin, and J. G. Checkelsky. Ferromagnetic helical nodal line and Kane-Mele spin-orbit coupling in kagome metal $\mathrm{Fe_3Sn_2}$. *Phys. Rev. B*, 105:035107, 2022.

[52] L. Ye, M. Kang, J. Liu, F. von Cube, C. R. Wicker, T. Suzuki, C. Jozwiak, A. Bostwick, E. Rotenberg, D. C. Bell, L. Fu, R. Comin, and J. G. Checkelsky. Massive Dirac fermions in a ferromagnetic kagome metal. *Nature*, 555:638, 2018.

[53] L. Ye, M. K. Chan, R. D. McDonald, D. Graf, M. Kang, J. Liu, T. Suzuki, R. Comin, L. Fu, and J. G. Checkelsky. de Haas-van Alphen effect of correlated Dirac states in kagome metal Fe_3Sn_2. *Nat. Commun.*, 10:4870, 2019.

[54] Z. Li, J. Zhuang, L. Wang, H. Feng, Q. Gao, X. Xu, W. Hao, X. Wang, C. Zhang, K. Wu, S. X. Dou, L. Chen, Z. Hu, and Y. Du. Realization of flat band with possible nontrivial topology in electronic Kagome lattice. *Sci. Adv.*, 4:aau4511, 2018.

[55] J.-X. Yin, S. S. Zhang, H. Li, K. Jiang, G. Chang, B. Zhang, B. Lian, C. Xiang, I. Belopolski, H. Zheng, T. A. Cochran, S.-Y. Xu, G. Bian, K. Liu, T.-R. Chang, H. Lin, Z.-Y. Lu, Z. Wang, S. Jia, W. Wang, and M. Z. Hasan. Giant and anisotropic many-body spin-orbit tunability in a strongly correlated kagome magnet. *Nature*, 562:91, 2018.

[56] A. K. Nayak, J. E. Fischer, Y. Sun, B. Yan, J. Karel, Alexander C. Komarek, Chandra Shekhar, Nitesh Kumar, Walter Schnelle, Jürgen Kübler, Claudia Felser, and S. S. P. Parkin. Large anomalous Hall effect driven by a nonvanishing Berry curvature in the noncolinear antiferromagnet Mn_3Ge. *Sci. Adv.*, 2:e1501870, 2016.

[57] K. Kuroda, T. Tomita, M.-T. Suzuki, C. Bareille, A. A. Nugroho, P. Goswami, M. Ochi, M. Ikhlas, M. Nakayama, S. Akebi, R. Noguchi, R. Ishii, N. Inami, K. Ono, H. Kumigashira, A. Varykhalov, T. Muro, T. Koretsune, R. Arita, S. Shin, T. Kondo, and S. Nakatsuji. Evidence for magnetic Weyl fermions in a correlated metal. *Nat. Mater.*, 16:1090, 2017.

[58] N. Morali, R. Batabyal, P. K. Nag, E. Liu, Q. Xu, Y. Sun, B. Yan, C. Felser, N. Avraham, and H. Beidenkopf. Fermi-arc diversity on surface terminations of the magnetic Weyl semimetal $Co_3Sn_2S_2$. *Science*, 365:1286, 2019.

[59] A. A. Burkov and L. Balents. Weyl semimetal in a topological insulator multilayer. *Phys. Rev. Lett.*, 107:127205, 2011.

[60] L. Ye, M. G. Fang, S. Kang, J. Kaufmann, Y. Lee, J. Denlinger, C. Jozwiak, A. Bostwick, E. Rotenberg, E. Kaxiras, D. C. Bell, O. Janson, R. Comin, and J. G. Checkelsky. A flat band-induced correlated kagome metal. *arXiv:2106.10824*, 2021.

[61] M. Uchida, Y. Nakazawa, S. Nishihaya, K. Akiba, M. Kriener, Y. Kozuka, A. Miyake, Y. Taguchi, M. Tokunaga, N. Nagaosa, Tokura Y., and M. Kawasaki. Quantum Hall states observed in thin films of Dirac semimetal Cd_3As_2. *Nat. Commun.*, 8:2274, 2017.

[62] A. A. Taskin, H. F. Legg, F. Yang, S. Sasaki, Y. Kanai, K. Matsumoto, A. Rosch, and Y. Ando. Planar Hall effect from the surface of topological insulators. *Nat. Commun.*, 8:1340, 2017.

[63] J. Zhang, C.-Z. Chang, Z. Zhang, J. Wen, X. Feng, K. Li, M. Liu, K. He, L. Wang, X. Chen, Q.-K. Xue, X. Ma, and Y. Wang. Band structure engineering in $(Bi_{1-x}Sb_x)_2Te_3$ ternary topological insulators. *Nat. Commun.*, 2:574, 2011.

[64] Burganov. B., C. Adamo, A. Mulder, M. Uchida, King. P. D. C., J. W. Harter, D. E. Shai, A. S. Gibbs, A. P. Mackenzie, R. Uecker, M. Bruetzam, M. R. Beasley, C. J. Fennie, and K. M. Schlom, Shen. Strain control of fermiology and many-body Interactions in two-dimensional ruthenates. *Phys. Rev. Lett.*, 116:197003, 2016.

[65] D. Li, K. Lee, B. Y. Wang, M. Osada, S. Crossley, H. R. Lee, Y. Cui, Y. Hikita, and H. Y. Hwang. Superconductivity in an infinite-layer nickelate. *Nature*, 572:624, 2019.

[66] C. Zhang, Y. Zhang, X. Yuan, S. Lu, J. Zhang, A. Narayan, Y. Liu, H. Zhang, Z. Ni, R. Liu, E. S. Choi, A. Suslov, S. Sanvito, L. Pi, H.-Z. Lu, A. C. Potter, and F. Xiu. Quantum Hall effect based on Weyl orbits in Cd_3As_2. *Nature*, 565:331, 2019.

[67] C.-Z. Chang, J. Zhang, X. Feng, J. Shen, Z. Zhang, M. Guo, K. Li, Y. Ou, P. Wei, L.-L. Wang, Z.-Q. Ji, Y. Feng, S. Ji, X. Chen, J. Jia, X. Dai, Z. Fang, S.-C. Zhang, K. He, Y. Wang, L. Lu, X.-C. Ma, and Q.-K. Xue. Experimental observation of the quantum anomalous Hall effect in a magnetic topological insulator. *Science*, 340:167, 2013.

[68] J. G. Checkelsky, R. Yoshimi, A. Tsukazaki, K. S. Takahashi, Y. Kozuka, J. Falson, M. Kawasaki, and Y. Tokura. Trajectory of the anomalous Hall effect towards the quantized state in a ferromagnetic topological insulator. *Nat. Phys.*, 10:731, 2014.

[69] R. Yoshimi, A. Tsukazaki, Y. Kozuka, J. Falson, K. S. Takahashi, J. G. Checkelsky, N. Nagaosa, M. Kawasaki, and Y. Tokura. Quantum Hall effect on top and bottom surface states of topological insulator $(Bi_{1-x}Sb_x)_2Te_3$ films. *Nat. Commun.*, 6:6627, 2015.

[70] A. Ohtomo and H. Y. Hwang. A high-mobility electron gas at the $LaAlO_3/SrTiO_3$ heterostructure. *Nature*, 427:423, 2004.

[71] A. Soumyanarayanan, M. Raju, A. L. Gonzalez Oyarce, A. K. C. Tan, M.-Y. Im, P. Petrović, Ho, K. H. Khoo, M. Tran, C. K. Gan, F. Ernult, and C. Panagopoulos. Tunable room-temperature magnetic skyrmions in Ir/Fe/Co/Pt multilayers. *Nat. Mater.*, 16:898, 2017.

[72] M. Mogi, T. Nakajima, V. Ukleev, A. Tsukazaki, R. Yoshimi, M. Kawamura, K. S. Takahashi, T. Hanashima, K. Kakurai, T.-H. Arima, M. Kawasaki, and Y. Tokura. Large anomalous Hall effect in topological Insulators with proximitized ferromagnetic insulators. *Phys. Rev. Lett.*, 123:016804, 2019.

[73] H. Inoue, M. Han, L. Ye, T. Suzuki, and J. G. Checkelsky. Molecular beam epitaxy growth of antiferromagnetic kagome metal FeSn. *Appl. Phys. Lett.*, 115:072403, 2019.

[74] M. Han, H. Inoue, S. Fang, C. John, L. Ye, M. K. Chan, D. Graf, T. Suzuki, M. P. Ghimire, W. J. Cho, E. Kaxiras, and J. G. Checkelsky. Evidence of two-dimensional flat band at the surface of antiferromagnetic kagome metal FeSn. *Nat. Commun.*, 12:5345, 2021.

[75] M. Han, C. John, M. P. Ghimire, S. Fang, M. Richter, H. Inoue, J. van den Brink, E. Kaxiras, and J. G. Checkelsky. Complete control of kagome spectrum in thin film 3*d*-stannides. *preprint*, 2022.

[76] H. Inoue, M. Han, M. Hu, T. Suzuki, J. Liu, and J. G. Checkelsky. Band engineering of a magnetic thin film rare-earth monopnictide: a platform for high Chern number. *Phys. Rev. Mater.*, 3:101202(R), 2019.

[77] M. Mayer. A simulation program for the analysis of NRA, RBS and ERDA. *AIP Conf. Proc.*, 475:541, 1999.

[78] IBANDL database, IAEA (2019), http://www-nds.iaea.org/ibandl/.

[79] C. Bergmann. 'Fermi surface measurements.' In *Encyclopedia of condensed matter physics*, Academic Press, pp.185-192 (2005).

[80] O. Hartmann and R. Wäppling. Muon spin precession in the hexagonal antiferromagnet FeSn. *Phys. Scr.*, 35:499, 1987.

[81] L. Häggström, T. Ericsson, R. Wäppling, and K. Chandra. Studies of the magnetic structure of FeSn using the Mössbauer effect. *Phys. Scr.*, 11:47, 1975.

[82] H. Yamamoto. Mössbauer effect measurement of intermetallic compounds in Iron-Tin system: Fe_5Sn_3 and FeSn. *J. Phys. Soc. Jpn.*, 21:1058, 1966.

[83] S. K. Kulshreshtha and P. Raj. ^{57}Mössbauer studies of the $(Fe_{1-x})Sn$ system for $0 \leq x \leq 0.2$: estimation of the anisotropy of the hyperfine coupling tensor. *J. Phys. F. Met. Phys.*, 11:281, 1981.

[84] B. Stenström. The electrical resistivity of FeSn single crystals. *Phys. Scripta*, 6(4):214, 1972.

[85] M. Kakihana, K. Nishimura, D. Aoki, A. Nakamura, M. Nakashima, Y. Amako, T. Takeuchi, T. Kida, T. Tahara, M. Hagiwara, H. Harima, M. Hedo, T. Nakama, and Y. Onuki. Electronic states of antiferromagnet FeSn and Pauli paramagnet CoSn. *J. Phys. Soc. Jpn.*, 88:014705, 2019.

[86] K. Usami. Magnetoresistance in antiferromagnetic metals. *J. Phys. Soc. Jpn.*, 45(2):466, 1978.

[87] W. R. Meier, J. Yan, M. A. McGuire, X. Wang, A. D. Christianson, and B. C. Sales. Reorientation of antiferromagnetism in cobalt doped FeSn. *Phys. Rev. B*, 100:184421, 2019.

[88] R. Dingle, H. L. Stormer, A. C. Gossard, and W. Wiegmann. Electron mobilities in modulation-doped semiconductor heterojunction superlattices. *Appl. Phys. Lett.*, 33:665, 1978.

[89] Q. Wang, K. Neubauer, C. Duan, Q. Yin, S. Fujitsu, H. Hosono, F. Ye, R. Zhang, S. Chi, K. Krycka, H. Lei, and P. Dai. Field-induced topological Hall effect and double-fan spin structure with a *c*-axis component in the metallic kagome antiferromagnetic compound YMn_6Sn_6. *Phys. Rev. B*, 103:014416, 2021.

[90] S. K. Pradhan, B. Dalal, and S. K. De. Exchange bias effect in a finite site disordered canted antiferromagnet. *J. Phys.: Condens. Matter.*, 30:365801, 2018.

[91] K. S. Novoselov, A. K. Geim, S. V. Morozov, D. Jiang, Y. Zhang, S. V. Dubonos, I. V. Grigorieva, and A. A. Firsov. Electric field effect in atomically thin carbon films. *Science*, 306:666, 2004.

[92] K. S. Novoselov, A. K. Geim, S. V. Morozov, D. V. Jiang, M. I. Katsnelson, I. V. Grigorieva, S. V. Dubonos, and A. A. Firsov. Two-dimensional gas of massless Dirac fermions in graphene. *Nature*, 438:197, 2005.

[93] Y. Zhang, Y.-W. Tan, H. L. Stormer, and P. Kim. Experimental observation of the quantum Hall effect and Berry's phase in graphene. *Nature*, 438:201, 2005.

[94] S. Nishihaya, M. Uchida, Y. Nakazawa, M. Kriener, Y. Kozuka, Y. Taguchi, and M. Kawasaki. Gate-tuned quantum Hall states in Dirac semimetal $(Cd_{1-x}Zn_x)_3As_2$. *Sci. Adv.*, 4:eaar5668, 2018.

[95] R. S. K. Mong, A. M. Essin, and J. E. Moore. Antiferromagnetic topological insulators. *Phys. Rev. B*, 81:245209, 2010.

[96] N. J. Ghimire, R. L. Dally, L. Poudel, D. C. Jones, D. Michel, N. Thapa Magar, M. Bleuel, M. A. McGuire, J. S. Jiang, J. F. Mitchell, J. W. Lynn, and I. I. Mazin. Competing magnetic phases and fluctuation-driven scalar spin chirality in the kagome metal YMn_6Sn_6. *Sci. Adv.*, 6:eabe2680, 2020.

[97] B. C. Sales, J. Yan, W. R. Meier, A. D. Christianson, S. Okamoto, and M. A. McGuire. Electronic, magnetic, and thermodynamic properties of the kagome layer compound FeSn. *Phys. Rev. Mater.*, 3:114203, 2019.

[98] Y. Xie, L. Chen, T. Chen, Q. Wang, Q. Yin, J. R. Stewart, H. Feng, E. Cao, H. Lei, Z. Yin, and P. MacDonald, A. H. Dai. Spin excitations in metallic kagome lattice FeSn and CoSn. *Commun. Phys.*, 4:240, 2021.

[99] H. Yamada and S. Takada. Negative magnetoresistance of ferromagnetic metals due to spin fluctuations. *Prog. Theor. Phys.*, 48:1828, 1972.

[100] N. Nagaosa, J. Sinova, S. Onoda, A. H. MacDonald, and N. P. Ong. Anomalous Hall effect. *Rev. Mod. Phys.*, 82:1539, 2010.

[101] D. Khadka, T. R. Thapaliya, S. H. Parra, J. Wen, R. Need, J. M. Kikkawa, and S. X. Huang. Anomalous Hall and Nernst effects in epitaxial films of topological kagome magnet Fe_3Sn_2. *Phys. Rev. Mater.*, 4:084203, 2020.

[102] G. Bihlmayer, O. Rader, and R. Winkler. Focus on the Rashba effect. *New J. Phys.*, 17:050202, 2015.

[103] J. Falson and M. Kawasaki. A review of the quantum Hall effects in MgZnO/ZnO heterostructures. *Rep. Prog. Phys.*, 81:056501, 2018.

[104] R. Yoshimi, A. Tsukazaki, K. Kikutake, J. G. Checkelsky, K. S. Takahashi, M. Kawasaki, and Y. Tokura. Dirac electron states formed at the heterointerface between a topological insulator and a conventional semiconductor. *Nat. Mater.*, 13:253, 2014.

[105] J. W. Conley and G. D. Mahan. Tunneling spectroscopy in GaAs. *Phys. Rev.*, 161:681, 1967.

[106] Y. Kozuka, T. Susaki, and H. Y. Hwang. Rectifying $NdNiO_3$/Nb:$SrTiO_3$ junctions as a probe of the surface electronic structure of $NdNiO_3$. *Appl. Phys. Lett.*, 88:142111, 2006.

[107] G. Binnig and H. E. Hoenig. Energy gap of the superconducting semiconductor $SrTiO_{3-x}$ determined by tunneling. *Solid State Commun.*, 14:597, 1974.

[108] Y. Hikita, L. F. Kourkoutis, T. Susaki, D. A. Muller, H. Takagi, and H. Y. Hwang. Negative differential resistance induced by Mn substitution at $SrRuO_3$/Nb:$SrTiO_3$ Schottky interfaces. *Phys. Rev. B*, 77:205330, 2008.

[109] C. Park, Y. Seo, J. Jung, and D.-W. Kim. Electrode-dependent electrical properties of metal/Nb-doped $SrTiO_3$ junctions. *J. Appl. Phys.*, 103:054106, 2008.

[110] P. K. Hansma. *Tunneling Spectroscopy.* Plenum Press, 1982.

[111] T. Yamamoto, S. Suzuki, H. Suzuki, K. Kawaguchi, K. Takahashi, and Y. Yoshisato. Effect of the field dependent permittivity and interfacial layer on $Ba_{1-x}K_xBiO_3$/Nb-doped $SrTiO_3$ Schottky junctions. *Jpn. J. Appl. Phys.*, 36:L390, 1997.

[112] H. E. Weaver. Dielectric properties of single crystals of $SrTiO_3$ at low temperatures. *J. Phys. Chem. Solids*, 11:274, 1959.

[113] E. Mikheev, B. D. Hoskins, D. B. Strukov, and S. Stemmer. Resistive switching and its suppression in Pt/Nb:$SrTiO_3$ junctions. *Nat. Commun.*, 5:3990, 2014.

[114] T. Shimizu and H. Okushi. Intrinsic electrical properties of $Au/SrTiO_3$ Schottky junctions. *J. Appl. Phys.*, 85:7244, 1999.

[115] T. Fujii, M. Kawasaki, A. Sawa, Y. Kawazoe, H. Akoh, and Y. Tokura. Electrical properties and colossal electroresistance of heteroepitaxial $SrRuO_3/SrTi_{1-x}Nb_xO_3$ ($0.0002 \leq x \leq 0.02$) Schottky junctions. *Phys. Rev. B*, 75:165101, 2007.

[116] A. G. Swartz, H. Inoue, T. A. Merz, Y. Hikita, S. Raghu, T. P. Devereaux, S. Johnston, and H. Y. Hwang. Polaronic behavior in a weak-coupling superconductor. *Proc. Natl. Acad. Sci. U.S.A.*, 115:1475, 2018.

[117] S. M. Sze and K. K. Ng. *Physics of Semiconductor Devices, 2nd ed.* Wiley, 1981.

[118] J. G. Simmons. Generalized formula for the electric tunnel effect between similar electrodes separated by a thin insulating film. *J. Appl. Phys.*, 34:1793, 1963.

[119] W. Witczak-Krempa, G. Chen, Y. B. Kim, and L. Balents. Correlated quantum phenomena in the strong spin-orbit regime. *Annu. Rev. Condens. Matter Phys.*, 5:57, 2014.

[120] P. Coleman and A. J. Schofield. Quantum criticality. *Nature*, 433:226, 2005.

[121] G. R. Stewart. Non-Fermi-liquid behaviors in d- and f-electron metals. *Rev. Mod. Phys.*, 73:797, 2001.

[122] Q. Si and F. Steglich. Heavy fermions and quantum phase transitions. *Science*, 329:1161, 2001.

[123] H. v. Löheneysen, A. Rosch, M. Vojta, and P. Wöfle. Fermi-liquid instabilities at magnetic quantum phase transitions. *Rev. Mod. Phys.*, 79:1015, 2001.

[124] E. Cattaneo. Hall effect of Ce intermetallic compounds. *Z. Phys. B Cond. Mat.*, 64:305, 1986.

[125] S. Paschen, T. Lühmann, S. Wirth, P. Gegenwart, O. Trovarelli, C. Geibel, F. Steglich, P. Coleman, and Q. Si. Hall-effect evolution across a heavy-fermion quantum critical point. *Nature*, 432:881, 2004.

[126] S. Paschen, T. Lühmann, S. Wirth, O. Trovarelli, C. Geibel, and F. Steglich. Anomalous Hall effect in $YbRh_2Si_2$. *Physica B*, 359:44, 2005.

[127] E. Cattaneo. Kondo effect in a magnetic field and the magnetoresistivity of Kondo Alloys. *Phys. Rev. Lett.*, 85:1504, 2000.

[128] D. Kaczorowski, B. Andraka, R. Pietri, T. Cichorek, and V. I. Zaremba. Heavy-fermion behavior in YbPtIn. *Phys. Rev. B*, 61:15255, 2005.

[129] A. Malinowski, M. F. Hundley, C. Capan, F. Ronning, R. Movshovich, N. O. Moreno, J. L. Sarrao, and J. D. Thompson. c-axis magnetotransport in $CeCoIn_5$. *Phys. Rev. B*, 72:184506, 2005.

[130] B. Batlogg, D. J. Bishop, E. Bucher, B. Golding, A. P. Ramirez, Z. Fisk, J. L. Smith, and H. R. Ott. Superconductivity and heavy fermions. *J. Magn. Magn. Mater.*, 63, 64:441, 1987.

[131] C. Liu, V. F. C. Humbert, T. M. Bretz-Sullivan, G. Wang, D. Hong, F. Wrobel, J. Zhang, J. D. Hoffman, J. E. Pearson, J. S. Jiang, C. Chang, A. Suslov, N. Mason, M. R. Norman, and A. Bhattacharya. Observation of an antiferromagnetic quantum critical point in high-purity $LaNiO_3$. *Nat. Commun.*, 11:1402, 2020.

[132] A. Patra, K. P. Maity, and V. Prasad. Influence of orbital two-channel Kondo effect on anomalous Hall effect in ferrimagnetic composites of ferrimagnetic composites of $LaNiO_3$ and $CoFe_2O_4$. *J. Phys.: Condens. Matter*, 31:255702, 2019.

[133] V. Hien-Hoang, N.-K. Chung, and H.-J. Kim. Electrical transport properties and Kondo effect in $La_{1-x}Pr_xNiO_{3-\delta}$ thin films. *Sci. Rep.*, 11:5391, 2021.

[134] R. P. Khosla and J. R. Fischer. Magnetoresistance in degenerate CdS: localized magnetic moments. *Phys. Rev. B*, 2:4084, 1970.

[135] M. Jonson and G. D. Mahan. Mott's formula for the thermopower and the Wiedemann-Franz law. *Phys. Rev. B*, 21:4223, 1980.

[136] A. C. Jacko, J. O. Fjrestad, and B. J. Powell. A unified explanation of the Kadowaki-Woods ratio in strongly correlated metals. *Nat. Phys.*, 5:422, 2009.

[137] A. Housoel, M. Karolak, E. Sasioglu, A. Lichtenstein, K. Held, A. Katanin, A. Toschi, and G. Sangiovanni. Local magnetic moments in iron and nickel at ambient and Earth's core conditions. *Nat. Commun.*, 8:16062, 2017.

[138] K. Uchida, S. Takahashi, K. Harii, J. Ieda, W. Koshibar, K. Ando, S. Maekawa, and E. Saitoh. Observation of the spin Seebeck effect. *Nature*, 455:778, 2008.

[139] H. Adachi, K.-I. Uchida, E. Saitoh, and S. Maekawa. Theory of the spin Seebeck effect. *Rep. Prog. Phys.*, 76:036501, 2008.

[140] S. M. Rezende, A. Azevedo, and R. L. Rodríguez-Suárez. Introduction to antiferromagnetic magnons. *J. Appl. Phys.*, 126:151101, 2019.

[141] M. N. Baibich, J. N. Broto, A. Fert, F. Nguyen Van Dau, F. Petroff, P. Etienne, G. Creuzet, A. Friederich, and J. Chazelas. Giant Magnetoresistance of (001)Fe/(001)Cr Magnetic Superlattices. *Phys. Rev. Lett.*, 61:2472, 1988.

[142] M. I. Dyakonov and V. I. Perel. Current-induced spin orientation of electrons in semiconductors. *Phys. Lett. A*, 35:459, 1971.

[143] Z. Yi, Z. Wang, Y. Cheng, and L. Wang. Sn-based intermetallic compounds for Li-ion batteries: structures, lithiation mechanism, and electrochemical performances. *Energy Environ. Mat.*, 1:132, 2018.

[144] G. Wang, F. Li, D. Liu, D. Zheng, Y. Luo, D. Qu, T. Ding, and D. Qu. Chemical prelithiation of negative electrodes in ambient air for advanced lithium-ion batteries. *ACS Appl. Mater. Interfaces*, 11:9, 2019.

[145] M. Zeng, C. Fang, G. Chang, Y.-A. Chen, T. Hsieh, A. Bansil, H. Lin, and L. Fu. *arXiv:1504.03492*, 2015.

[146] J. Nayak, S.-C. Wu, N. Kumar, C. Shekhar, S. Singh, J. Fink, E. E. D. Rienks, G. H. Fecher, S. S. P. Parkin, B. Yan, and C. Felser. Multiple Dirac cones at the surface of the topological metal LaBi. *Nat. Commun.*, 8:13942, 2017.

[147] C.-G. Duan, R. F. Sabirianov, W. N. Mei, P. A. Dowben, S. S. Jaswal, and E. Y. Tsymbal. Electronic, magnetic and transport properties of rare-earth monopnictides. *J. Phys. Condens. Matter*, 19:315220, 2007.

[148] C.-G. Duan, R. F. Sabiryanov, W. N. Mei, P. A. Dowben, S. S. Jaswal, and E. Y. Tsymbal. Magnetic ordering in Gd monopnictides: Indirect exchange versus superexchange interaction. *Appl. Phys. Lett.*, 88(18):182505, 2006.

[149] R. Lou, B. B. Fu, Q. N. Xu, P. J. Guo, L. Y. Kong, L. K. Zeng, J. Z. Ma, P. Richard, C. Fang, Y. B. Huang, S. S. Sun, Q. Wang, L. Wang, Y. G. Shi, H. C. Lei, K. Liu, H. M. Weng, T. Qian, H. Ding, and S. C. Wang. Evidence of topological insulator state in the semimetal LaBi. *Phys. Rev. B*, 95:115140, 2017.

[150] B. Feng, J. Cao, M. Yang, Y. Feng, S. Wu, B. Fu, M. Arita, K. Miyamoto, S. He, K. Shimada, Y. Shi, T. Okuda, and Y. Yao. Experimental observation of node-line-like surface states in LaBi. *Phys. Rev. B*, 97(15):155153, 2018.

[151] Topological materials database (2022), https://topologicalquantumchemistry.org/.

[152] B. Bradlyn, L. Elcoro, J. Cano, M. G. Vergniory, Z. Wang, C. Felser, M. I. Aroyo, and B. A. Bernevig. Topological quantum chemistry. *Nature*, 547:298, 2017.

[153] M. G. Vergniory, L. Elcoro, C. Felser, N. Regnault, B. A. Bernevig, and Z. Wang. A complete catalogue of high-quality topological materials. *Nature*, 566:480, 2019.

[154] Z. Li, J. Kim, N. Kioussis, S. Y. Ning, H. Su, T. Iitaka, T. Tohyama, X. Yang, and J. X. Zhang. GdN thin film: Chern insulating state on square lattice. *Phys. Rev. B*, 92:201303(R), 2015.

[155] S. Xiao, D. Wei, and X. Jin. Bi(111) thin film with insulating interior but metallic surfaces. *Phys. Rev. Lett.*, 109:166805, 2012.

[156] F. Gity, L. Ansari, M. Lanius, P. Schuffelgen, G. Mussler, D. Grutmacher, and J. C. Greer. Reinventing solid state electronics: harnessing quantum confinement in bismuth thin films. *App. Phys. Lett.*, 110:093111, 2017.

[157] L. Ye, T. Suzuki, C. R. Wicker, and J. G. Checkelsky. Extreme magnetoresistance in magnetic rare-earth monopnictides. *Phys. Rev. B*, 97(8):081108(R), feb 2018.

[158] N. Kumar, C. Shekhar, S.-C. Wu, I. Leermakers, O. Young, U. Zeitler, B. Yan, and C. Felser. Observation of pseudo-two-dimensional electron transport in the rock salt-type topological semimetal LaBi. *Phys. Rev. B*, 93:241106(R), 2016.

[159] F. F. Tafti, Q. D. Gibson, S. K. Kushwaha, N. Haldolaarachchige, and R. J. Cava. Resistivity plateau and extreme magnetoresistance in LaSb. *Nat. Phys.*, 12:272, 2016.

[160] P.-J. Guo, H.-C. Yang, B.-J. Zhang, K. Liu, and Z.-Y. Lu. Charge compensation in extremely large magnetoresistance materials LaSb and LaBi revealed by first-principles calculations. *Phys. Rev. B*, 93(23):235142, 2016.

[161] J. He, C. Zhang, N. J. Ghimire, T. Liang, C. Jia, J. Jiang, S. Tang, S. Chen, Y. He, S.-K. Mo, C. C. Hwang, M. Hashimoto, D. H. Lu, B. Moritz, T. P. Devereaux, Y. L. Chen, J. F. Mitchell, and Z.-X. Shen. Distinct electronic structure for the extreme magnetoresistance in YSb. *Phys. Rev. Lett.*, 117:267201, 2016.

[162] F. F. Tafti, M. S. Torikachvili, R. L. Stillwell, B. Baer, E. Stavrou, S. T. Weir, Y. K. Vohra, H.-Y. Yang, E. F. McDonnell, S. K. Kushwaha, Q. D. Gibson, R. J. Cava, and J. R. Jeffries. Tuning the electronic and the crystalline structure of LaBi by pressure: from extreme magnetoresistance to superconductivity. *Phys. Rev. B*, 95:014507, 2017.

[163] P. W. Anderson. Absence of diffusion in certain random lattices. *Phys. Rev.*, 109:1492, 1958.

[164] K. Nomura and N. Nagaosa. Surface-quantized anomalous Hall current and the magnetoelectric effect in magnetically disordered topological insulators. *Phys. Rev. Lett.*, 106:166802, 2011.

[165] S. Hikami, A. I. Larkin, and Y. Nagaoka. Spin-orbit interaction and magnetoresistance in the two Dimensional random system. *Prog. Theor. Phys*, 63:707, 1980.

[166] K. Kuroda, M. Ochi, H. S. Suzuki, M. Hirayama, M. Nakayama, R. Noguchi, C. Bareille, S. Akebi, S. Kunisada, T. Muro, M. D. Watson, H. Kitazawa, Y. Haga, T. K. Kim, M. Hoesch, S. Shin, R. Arita, and T. Kondo. Experimental Determination of the Topological Phase Diagram in Cerium Monopnictides. *Phys. Rev. Lett.*, 120:086402, 2018.

[167] J. Rossat-Mignod, P. Burlet, S. Quezel, J. M. Effantin, D. Delacôte, H. Bartholin, O. Vogt, and D. Ravot. Magnetic properties of cerium monopnictides. *J. Magn. Magn. Mater.*, 31-34:398, 1983.

[168] F. Hulliger, H. R. Ott, and T. Siegrist. Low temperature behaviour of HoBi. *J. Less Common Met.*, 96:263, 1984.

[169] Y. Deng, Y. Yu, M. Z. Shi, Z. Guo, Z. Xu, J. Wang, X. H. Chen, and Zhang. Y. Quantum anomalous Hall effect in intrinsic magnetic topological insulator $MnBi_2Te_4$. *Science*, 367:895, 2020.

[170] C. Hu, K. N. Gordon, P. Liu, J. Liu, X. Zoue, P. Hao, D. Narayan, E. Emmanouilidou, H. Sun, Y. Liu, H. Brawer, A. P. Ramirez, L. Ding, H. Cao, Q. Liu, D. Dessau, and Ni. N. A van der Waals antiferromagnetic topological insulator with weak interlayer magnetic coupling. *Nat. Commun.*, 11:97, 2020.

[171] S. Tian, S. Gao, S. Nie, Y. Qian, C. Gong, Y. Fu, H. Li, W. Fan, P. Zhang, T. Kondo, S. Shin, J. Adell, H. Fedderwitz, H. Ding, Z. Wang, T. Qian, and H. Lei. Magnetic topological insulator $MnBi_6Te_{10}$ with a zero-field ferromagnetic state and gapped Dirac surface states. *Phys. Rev. B*, 102:035144, 2020.

[172] E. A. Paisley, M. D. Losego, B. E. Gaddy, J. S. Tweedie, R. Collazo, Z. Sitar, D. L. Irbing, and J.-P. Maria. Surfactant-enabled epitaxy through control of growth mode with chemical boundary conditions. *Nat. Commun.*, 2:461, 2011.

[173] A. Koma. Van der Waals epitaxy for highly lattice-mismatched systems. *J. Cryst. Growth*, 202:236, 1999.

[174] N. Brigg, B. Bersch, Y. Wang, J. Jiang, R. J. Koch, N. Nayir, K. Wang, M. Kolmer, W. Ko, A. De La Fuente Duran, S. Subramanian, C. Dong, J. Shallenberger, M. Fu, Q. Zou, Y.-W. Chuang, Z. Gai, A.-P. Li, A. Bostwick, C. Jozwiak, C.-Z. Chang, E. Rotenberg, J. Zhu, A. C. T. van Duin, V. Crespi, and J. A. Robinson. Atomically thin half-van der Waals metals enabled by confinement heteroepitaxy. *Nat. Mater.*, 19:637, 2020.

[175] A. R. Mellnik, J. S. Lee, A. Richardella, J. L. Grab, P. J. Mintun, M. H. Fischer, A. Vaezi, A. Manchon, E. A. Kim, N. Samarth, and D. C. Ralph. Spin-transfer torque generated by a topological insulator. *Nature*, 511:449, 2014.

[176] J. Han, A. Richardella, S. A. Siddiqui, J. Finley, N. Samarth, and L. Liu. Room-temperature spin-orbit torque switching induced by a topological insulator. *Phys. Rev. Lett.*, 119:077702, 2017.

[177] N. Roschewsky, E. S. Walker, P. Gowtham, S. Muschinske, F. Hellman, S. R. Bank, and S. Salahuddin. Spin-orbit torque and Nernst effect in Bi-Sb/Co heterostructures. *Phys. Rev. B*, 99:195103, 2019.

[178] N. D. Reynolds, S. Chatterjee, G. M. Stiehl, J. A. Mittelstaedt, S. Karimeddiny, A. J. Buser, D. G. Schlom, K. M. Shen, and D. C. Ralph. Strong, temperature-dependent spin-orbit torques in heavy fermion $YbAl_3$. *arXiv:2004.03678*, 2020.

[179] I. Lyalin, S. Cheng, and R. K. Kawakami. Spin-orbit torque in bilayers of kagome ferromagnet Fe_3Sn_2 and Pt. *Nano Lett.*, 21:6975, 2021.

[180] E. J. Monkman, C. Adamo, J. A. Mundy, D. E. Shai, J. W. Harter, D. Shen, B. Burganov, D. A. Muller, D. G. Schlom, and K. M. Shen. Quantum many-body interactions in digital oxide superlattices. *Nat. Mater.*, 11:855, 2012.

[181] H. Shishido, T. Shibauchi, K. Yasu, H. Kontani, T. Terashima, and Y. Matsuda. Tuning the dimensionality of the heavy fermion compound $CeIn_3$. *Science*, 327:980, 2010.

[182] V. Martelli, J. L. Jimenez, M. Continentino, E. Baggio-Saitovitch, and K. Behnia. Thermal transport and phonon hydrodynamics in strontium titanate. *Phys. Rev. Lett.*, 120:125901, 2018.